Harmonic generation in gases using Bessel-gauss beams

Caron, Christian Frédéric Roger Caron

Harmonic Generation in Gases using Bessel-Gauss Beams

by

Christian Frédéric Roger Caron
Diplom-Physiker
(Universität Karlsruhe, Germany)

A thesis submitted to the University of Durham in
candidature for the degree of Doctor of Philosophy

Physics Department
May 1998

This thesis is dedicated to my wife Françoise and my parents. Without their love, support and understanding, this effort would not have been possible.

"... was nicht umbringt, stärkt." (T.P.)

Declaration

I declare that the work contained in this thesis has not previously been submitted for a degree, either at this university or at any other. All the work presented herein was conducted by the author, unless explicitly stated otherwise.

C F R Caron

May 1998

Acknowledgements

It is a pleasure to thank Drs Jim McCann and Robert Potvliege for accepting me as their PhD student and for their unabating support throughout my time spent in the Atomic and Molecular Physics Group at the University of Durham. I am particularly indebted to Dr Robert Potvliege for his relaxed but vigilant supervision of the work out of which the present thesis has grown. I have greatly benefited from many fruitful discussions with Dr Carlo Altucci (Naples, Italy), Dr Philippe Balcou (Palaiseau, France), Dr Martin Dörr (Berlin, Germany), Prof. Anne L'Huillier (Lund, Sweden), and Dr Victor Peet (Tartu, Estonia) and was privileged to enjoy the kind hospitality of the Department of Physics at the Lund Institute of Technology (Lund, Sweden) and the Laboratoire d'Optique Appliquée (Palaiseau, France) during my visits there.

I wish to thank all the members of the Atomic and Molecular Physics group in Durham, Dr Charles Adams, Prof. David Flower, Dr Lydia Heck, Dr Martin Plummer, Dr Krzysztof Szymaniec, and, of course, my 'companions-in-misfortune', Hilary Davies, Brian Jackson and Richard Whitehead, for their company, encouragement and help. I'm particularly grateful to my former officemates, Dr Henry Day and Dr Emine Meşe, for their lasting friendship. My special thanks go to Dr Lydia Heck for her communicative enthusiasm in solving every conceivable computational problem and for her unfailing cheerfulness.

Further, I would like to acknowledge generous financial support from various sources: a three-year scholarship granted by the Deutscher Akademischer Austauschdienst (DAAD) and financed by the German Federal Ministry for Research and Technology and financial support from the University of Durham covering a large part of the tuition fees, from the EC HCM network for attending their conferences in Paris and Crete, from the EC TMR programme for my visit to the Laboratoire d'Optique Appliquée in Palaiseau, France, and from the Atomic and Molecular Physics Group at the University of Durham for my visit to the Lund Institute of Technology, Sweden.

My last, but sincere thanks, are offered to the unknown taxpayer, who made this adventure possible. May the present thesis be a worthy, if small retribution for his/her trust.

Abstract

The generation and propagation of harmonics in an atomic gas are described for the case of an incident Bessel-Gauss beam. Theoretical expressions are derived for the far-field amplitude of the harmonic field by solving the propagation equation using an elaborate integral formalism. We establish simple rules which determine the optimum Bessel-Gauss beam with respect to phase-matching as a function of the medium properties, such as the dispersion and the gas density. Target depletion due to photoionization and refractive index variations originating from both free electrons and dressed linear atomic susceptibilities are taken into account. The intensity-dependent complex atomic dipole moment is calculated using nonperturbative methods.

Numerical propagation calculations for hydrogen, xenon and argon are presented. For hydrogen we consider the third harmonic of a 355-nm, 15-ps pump beam up to 3×10^{13} W/cm^2 intensity, similarly for xenon, but at lower intensities. For argon we consider the 17^{th} and 19^{th} harmonic of a 810-nm, 30-fs pump beam around 10^{14} W/cm^2 intensity. We compare conversion efficiencies and both spatial and temporal far-field profiles for an optimized Bessel-Gauss beam with respect to a Gaussian beam of same power and/or peak focal intensity. For the case of hydrogen, we investigate the effect of an ac-Stark-shift induced atomic resonance. We find all results in good agreement with our theoretical predictions.

We conclude from our studies that Bessel-Gauss beams can perform better in terms of conversion efficiency than a comparable Gaussian beam. We find this to originate essentially from the more flexible phase-matching conditions for Bessel-Gauss beams. Bessel-Gauss beams also allow for spatial separation of the harmonic and the incident field in the far-field region, owing to the conical shape of their spatial far-field profile. Both features make Bessel-Gauss beams an attractive alternative to Gaussian beams in a limited but substantial number of experimental conditions.

Contents

Chapter 1

About Harmonic Generation

1.1 Introduction

Harmonic generation in gases is by now a well established and continously expanding field of nonlinear optics. Its rapid development is spurred by the prospect of constructing table-top coherent X-ray sources based on this process, for applications in spectroscopy and biological imaging, and, of course, by its fascinating intrinsic physical interest. Though many aspects of the harmonic generation process are now well understood, conversion efficiencies, especially for higher-order harmonics, are still low. In this thesis we will therefore be mainly concerned with this particular aspect about harmonic generation. More specifically, we shall investigate the possibility of increasing the conversion efficiency through better phase-matching by considering a different type of laser beam geometry, namely the Bessel-Gauss beam, and compare it to the Gaussian beam which is traditionally used in harmonic generation experiments. We will show the Bessel-Gauss beam to be of particular interest for harmonic generation processes in a negatively dispersive atomic gas. We will come back in more detail to the organization of the material in the present work at the very end of this chapter, after having exposed the basic physics and methods of harmonic generation. The following sections are also meant to clarify how the work presented in this thesis is embedded in past, current and future research about generation of harmonic radiation (in gases) through nonlinear optical processes.

1.2 The basics of harmonic generation

1.2.1 The perturbative regime

Roughly speaking, to generate harmonics, all that is needed is a photon field interacting nonlinearily, i.e. with sufficient intensity for multiphotonic processes to happen, with some matter system coupling to the electromagnetic force. This system then absorbs simultaneously an integer number N of photons out of the incident photon field and, as one of all possible energy-conserving processes, emits a single photon carrying the total energy of the incident N photons. Accordingly, this emitted photon is called the N-th harmonic. Not surprisingly, owing to the generality of the mechanism outlined above, nearly all matter systems can in principle emit harmonic photons or, macroscopically speaking, harmonic radiation. The simplest system, perhaps, is a free electron. Interestingly enough, it is even more straightforward to compute the harmonic spectrum using the relativistic wave equations, because it is possible to find, in this particular case, exact wavefunctions for the electron in the photon field without having to restrict to the dipole approximation[1] as appears to be necessary in the nonrelativistic case. Detailed calculations have been performed in the relativistic case, both classically [198, 199, 221] and using quantum field theory [34, 41]. However, harmonic generation by free electrons is very inefficient and the first experimental observation of the second harmonic from free electrons dates from 1983 [74]. This is more than twenty years after the very first observation of second harmonic generation by Franken *et al.* in 1961 [80], who irradiated a crystal with one of the first laser beams available. Indeed, for efficient harmonic generation to happen, it is customary to use targets such as gases and solids, consisting of bound electrons which have to be promoted to an excited state or to the continuum by absorbing several photons[2]. The corresponding polarizability of the bound system is then, in general, a measure of how efficiently harmonics

[1] The well known dipole approximation $\exp(i\boldsymbol{k}\cdot\boldsymbol{r}) \approx 1$ neglects the momentum of the photon and is valid as long as the wavelength is long compared to the dimensions of the matter system. This is no constraint in practical applications where atomic and molecular systems are irradiated by infrared, optical or even ultraviolet frequencies.

[2] Other states of matter have also been considered, such as plasmas in Ref. [60,126] and atomic clusters in Ref. [219,220]. For liquids, see, e.g., Ref. [191].

can be generated in this way. Low-order harmonic generation at moderate intensities has quickly become a standard textbook subject and good introductions to this field can be found in Boyd [33], Butcher and Cotter [40], Mills [141], Reintjes [191], Shen [203], Hanna, Yuratich and Cotter [92] and Delone and Krainov [64]. The emission of a given harmonic in this regime is successfully described by leading-order perturbation theory, with the immediate consequence, that the probability of generating a harmonic decreases with the order of the process, N. Systems with inversion symmetry, such as atoms in their ground states, some molecules (e.g., diatomic ones) and certain crystal classes, emit dominantly odd harmonics while all others systems may in principle radiate both odd and even harmonic orders. We will give a simple explanation of the first assertion by recalling that the wavefunction of a system with inversion symmetry can be taken a parity eigenstate. The interaction term in the dipole approximation and length gauge of the active electron with (odd-parity) position operator $\mathbf{x}$ with a light field of amplitude $\boldsymbol{E}$ is well known to be proportional to $\boldsymbol{E} \cdot \mathbf{x}$. Following the 'prescription' of harmonic generation given above, we have to consider the following amplitude, written for the sake of clarity as

$$\sum_{I_1,\ldots,I_N} \langle 0|\mathbf{x}|I_N\rangle\langle I_N|\mathbf{x}|I_{N+1}\rangle \ldots \langle I_2|\mathbf{x}|I_1\rangle\langle I_1|\mathbf{x}|0\rangle\,, \tag{1.1}$$

where the sum over the intermediary states I_i has to be taken and $|0\rangle$ is the initial state. Starting from the right in Eq. (1.1), the amplitudes will not vanish only if the two states involved are of opposite parity. But then, if N is even, $|I_N\rangle$ and $|0\rangle$ have the same parity and the first amplitude in Eq. (1.1) vanishes. Clearly this result needs not to hold for higher-order transitions, e.g., electric-quadrupole transitions, but those contributions, if any, are much smaller. Even harmonic orders can be observed in atomic vapors, if the symmetry is broken by additional fields. Kim *et al.* [111] observed second harmonic generation in a potassium vapor and could show the ionization-induced space charge creating a dc-field within the medium to be at the origin of this effect. Even-order harmonics could in principle also be observed due to the presence of free electrons or through sum- or difference-frequency mixing processes of the fundamental with the odd-order harmonics, but the latter processes are, in general, forbidden to the same extent than direct even-order harmonic gen-

eration. In the following we shall however concentrate on harmonic generation in rare gases by a single incident laser beam, and only odd-order harmonics will considered. In the perturbative regime, the harmonic spectrum thus consists in general of a series of more or less rapidly decreasing peaks located at odd multiples of the laser frequency.

1.2.2 The nonperturbative regime

A new era in the field of harmonic generation opened when, with increasing intensity on target, the breakdown of perturbation theory was revealed[3]. The first experiment to show a modification in the harmonic spectra was carried out by Ferray *et al.* in 1988 [78]. In contrast to most of the previous works (see references in [78]), these authors used a fundamental of long wavelength, namely 1064-nm radiation from a Nd:YAG laser, which they focused into various rare gases (argon, krypton and xenon). The main features they noticed have now become the 'trademark' of the nonperturbative regime: The harmonic spectrum typically begins with a rapid decrease for the first few harmonics, followed by an extended plateau, where the harmonics are generated roughly at equal strength, the plateau ending more or less abruptly after some harmonic order is reached (cut-off). As we shall see later it was essentially passing to longer wavelengths (for a given intensity) which made it possible to enter the new regime of harmonic generation.

In such an experiment, harmonic radiation from a large number of emitters is recorded. Thus, the first question to be elucidated was whether the particular form of the harmonic spectrum was already determined by the response of every single atom in the laser field (the single-atom response), or whether the propagation of the harmonics in the nonlinear medium in which they were generated would affect the shape of the spectrum. Soon after the experiment of Ref. [78], Kulander and Shore [115] performed numerical calculations, showing that the harmonic spectra observed by Ferray *et al.* could be essentially traced back to the single-atom re-

[3]In fact, this had already been realized earlier for a related process, namely above threshold ionization (ATI), see Ref. [151] for a review.

sponse, provided the calculation was done nonperturbatively. For this, they solved the 3D-time-dependent Schrödinger equation (TDSE) for a model xenon atom, using otherwise the same parameters (intensity and wavelength of the fundamental) as in Ref. [78]. About the same time, similar results were found for calculations in atomic hydrogen by Potvliege and Shakeshaft [175], who solved the Schrödinger equation using the Floquet method (see chapter 2). A typical calculation is shown in Fig. 1.1, which nicely shows the formation of a plateau, followed by a pronounced cut-off, as the intensity increases.

The state of the field of harmonic generation in rare gases around 1990 was reviewed in detail by L'Huillier *et al.* in Refs. [129,130], leaving still open the question of the origin of the shape of the harmonic spectrum. In the early 1990's, Krause *et al.* [113], after extensive numerical simulations, suggested an universal law that determines the position (that is, the harmonic order $N_{\max}$) of the cut-off, namely[4]

$$N_{\max} \approx \frac{I_p + 3.2U_p}{\hbar\omega}. \tag{1.2}$$

Here, I_p is the ionization potential of the atomic species considered, ω the laser (angular) frequency and U_p the ponderomotive energy. The latter is the time-averaged kinetic energy of an electron freely oscillating in a (linearily polarized) laser field,

$$U_p\,(\text{a.u.}) = E_0^2/4\omega^2, \tag{1.3}$$

$$U_p\,(\text{eV}) = 9.33 \times 10^{-20}\, I_L[\text{W/cm}^2]\,\lambda^2\,[\text{nm}] \tag{1.4}$$

where E_0 is the electric field amplitude and I_L is the intensity of the laser field[5]. From Eq. (1.2) is apparent that the width of the plateau can be influenced in various ways. The width increases for increasing laser intensity and increasing wavelength, as $U_p/\omega \propto \lambda^3$. A larger ionization potential I_p is also helpful[6] though the efficiency of harmonic generation starts to suffer from a lower atomic polarizability. On the other hand, I_p determines the saturation intensity I_S, that is essentially the maximum value of I_L for which harmonic generation can be obtained before the atom is ionized. Obviously, the higher I_p the higher I_S and consequently the higher the value of U_p

[4]The unit systems used throughout this thesis are the international system of units (SI) and atomic units (a.u.). If the latter are used, this will be clearly stated.

[5]The expression for U_p will be derived in Chapter 2.

[6]Helium has the highest available ionization potential, $I_p = 24.59$ eV.

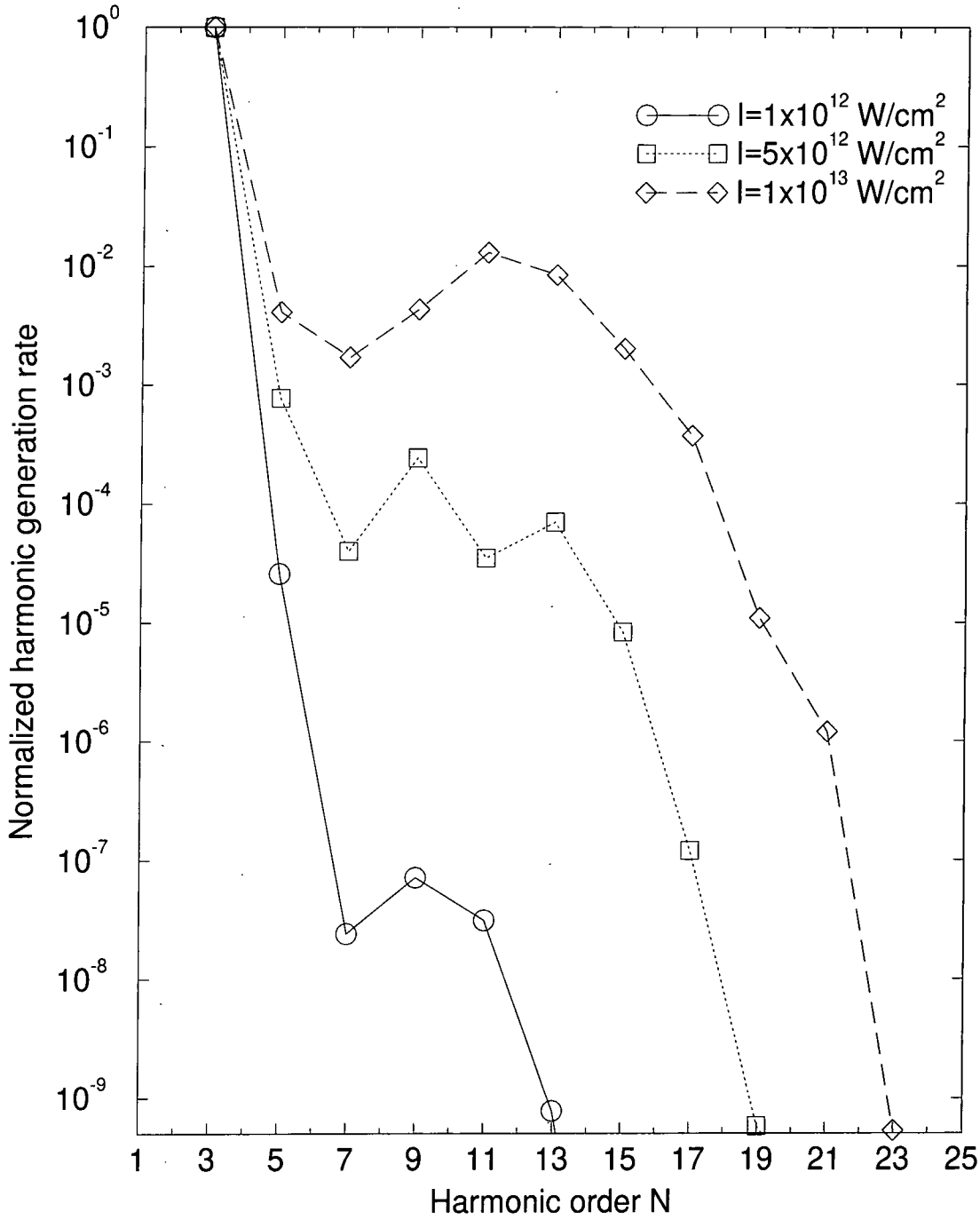

Figure 1.1: Harmonic generation rates for atomic hydrogen for various intensities versus the harmonic order N [172]. The rates are normalized to the value for $N = 3$. The wavelength is $\lambda = 1064$ nm. Only odd harmonics are produced due to the parity selection rules. The 9^{th} and 11^{th} harmonics are often singled out when considering 1064-nm radiation in hydrogen, as the energy of the 9^{th} harmonic corresponds roughly to the (field-free) 1s-2p transition, while for the 11^{th} harmonic a strong influence of the Rydberg series is to be expected.

that can be effectively used[7]. A comparative study highlighting these various aspects has been carried out for several atomic and molecular gases[8] by Lynga *et al.* [127]. In the case $I_p \gg U_p$, Chin and Golovinski [46], using theoretical arguments, suggested the harmonic yields Y_1 and Y_2 of two atomic or molecular systems with respective static polarizabilities α_1 and α_2 to be related by

$$Y_2/Y_1 = (\alpha_2/\alpha_1)^N , \tag{1.5}$$

where N is the harmonic order. They found this prediction to agree well with experimental data.

More generally, I_p and U_p can be used to distinguish the two regimes mentioned above, where two different physical pictures have to be invoked to explain the harmonic generation process. The relevant parameter,

$$\gamma = \sqrt{\frac{I_p}{2U_p}} , \tag{1.6}$$

has, in fact, been introduced a long time ago by Keldysh [110] to distinguish multiphoton ionization (MPI, $\gamma \gg 1$) and tunnel ionization (TI, $\gamma \ll 1$) in atomic systems. In the former case, the initially bound electron is promoted into the continuum through absorbtion of several photons while in the latter case, typically for high intensities and low frequencies, the Coulomb wall is periodically tilted and lowered, allowing the electron to tunnel out every half-cycle through the oscillating barrier. An extreme case is reached when the barrier is suppressed at very high intensities. The electronic wavepacket can then simply flow over the barrier into the continuum [11]. This regime has subsequently become known as over-the-barrier ionization (OBI). It is worth noting that harmonic generation is again suppressed in this regime, therefore setting an upper limit on the efficiency of the tunneling mechanism [148]. At such high intensities, solid targets appear to be a more interesting source of high-order harmonics than rare gases (see, e.g., Ref. [93] and references therein).

[7] That is, the maximum value of U_p that enters the determination of $N_{\max}$ in Eq. (1.2) is roughly given by $I = I_S$ though I_L might be nominally higher.

[8] Organic molecules (butane and butadiene) have been used as targets in harmonic generation experiments by Fraser *et al.* [81].

With the help of the TI mechanism, the factor of 3.2 appearing in Eq. (1.2) was explained in a simple way by Kulander *et al.* [117] and Corkum [54] using classical dynamics. According to their two-step model, the electron appears in the continuum with zero velocity close to the nucleus, is accelerated in the laser-field and, provided the electron returns to the nucleus, emits a harmonic photon when falling back into the ground state. The maximum photon energy obtained in this way is thus $N_{\max}\hbar\omega = I_p + T_{\max}$, where $T_{\max}$ is the maximum kinetic energy acquired by the electron in the continuum. We give a brief account, on how $T_{\max}$ can be easily computed. For linear polarization, one can restrict to 1D, having to solve

$$\ddot{x}(t) = -E_0 \cos(\omega t + \phi) \qquad \text{(in a.u.)}, \tag{1.7}$$

subject to the initial conditions $\dot{x}(0) = 0$ and $x(0) = 0$. ϕ is the phase at $t = 0$ of the laser field of amplitude E_0. The solution of Eq. (1.7) is

$$x(t) = (E_0/\omega^2)\,[\cos(\omega t + \phi) - \cos\phi + \omega t \sin\phi]. \tag{1.8}$$

Computing the kinetic energy, we arrive at the following expression,

$$T = 8\cos^2(u/2 + \phi)\,\sin^2(u/2)\,, \tag{1.9}$$

in units of U_p, where $u = \omega t$. We have to find the maximum of T, subject to the constraint $x = 0$ (the electron must be back at the nuclear position), which can be written as

$$2\,\sin(u/2)\sin(\phi + u/2) = u\sin\phi\,. \tag{1.10}$$

Searching for $u(\phi)$ satisfying Eq. (1.10) for $\phi \in [0, \pi]$ and inserting the solution into Eq. (1.9) leads to the graph shown in Fig. 1.2. Clearly, a distinct maximum appears around $\phi \approx 18°$, with $T_{\max} \approx 3.17(U_p)$, thus corroborating the famous cut-off rule Eq. (1.2).

Using classical arguments it is also easy to understand why the harmonic yield decreases with increasing ellipticity of the laser field polarization, as was confirmed by Budil *et al.* [35]. Indeed, imparting some angular momentum to the electron deviates its trajectory, thereby reducing the probability of rescattering with the nucleus. Quantum-mechanically, taking for simplicity the case of circular polarization

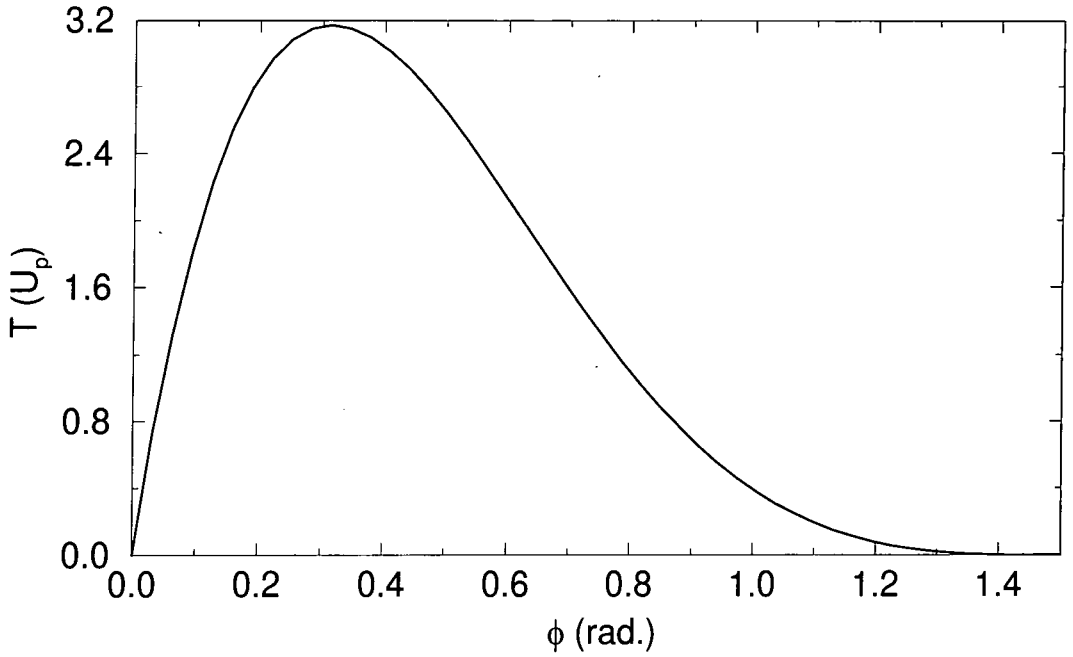

Figure 1.2: Kinetic energy T gained by an electron released into the continuum at $t = 0$ at the origin with zero velocity and returning to the origin after one return time, plotted versus the phase of the field at $t = 0$.

in the multiphoton ionization regime, the dipole selection rules require the magnetic quantum number $|m|$ to be increased by one unit for each photon absorbed, thus making it impossible for the electron to fall back into the ground state by emitting just one photon in the dipole approximation ($|\Delta m| \leq 1$). The detailed dependence of harmonic generation on ellipticity is very complicated, though. Burnett *et al.* [39] found the dependence of the harmonic yield on the ellipticity of the incident beam to be markedly different for harmonic energies below and above the ionization potential (in neon). Weihe *et al.* [230] measured the ellipticity of harmonics generated by intense laser pulses and found the axis of polarization rotated with respect to the axis of the elliptically polarized fundamental. They did not find any pressure dependence for this effect and concluded the single atom response to be the origin of the offset angle. This was confirmed by Meşe and Potvliege [137] who carried out numerical simulations in atomic hydrogen to determine both the offset angle and change in ellipticity for various harmonics with respect to the fundamental. The dependence of the harmonic yield on the ellipticity can be used to control harmonic generation spatially with the use of birefringent optics. Mercer *et al.* [135] found

in this way, that the harmonics dominantly created in regions of linear polarization lead to annular harmonic beams whose angle of divergence could be continously varied.

Many suggestions have been made on how to extend the plateau beyond the prediction Eq. (1.2). They include the application of an ultrastrong magnetic field such as to confine the electronic wavepacket, enhancing the probability of the electron returning to the nucleus[9] [21, 235], and the double plateau predicted by Watson *et al.* [229], which arises when the atom is prepared initially in a superposition of states. Two plateaus can also appear when using the H_2^+ molecular ion as target as shown by Zuo *et al.* [236], owing to the additional degrees of freedom in a molecule (vibrational states)[10]. Another suggestion was put forward by Moreno *et al.* [149, 150]. It is based on the observation from Eq. (1.9) that the maximum energy gained by the electron in the tunneling regime would be $8U_p$ (e.g., for $u = \pi$ and $\phi = \pi/2$) and not $3.2U_p$, if the electron were not restricted to rescatter with the nucleus. The authors thus argued that in a partially ionized medium, dense enough for neighbouring ions to be close enough to the ionizing atom [within a few times the electron's quiver amplitude, see Eq. (4.36)], the electron could be captured by one of the surrounding ions and emit harmonics of higher orders than predicted by Eq. (1.2).

Soon after the quasi-classical explanation of the cut-off law Eq. (1.2), a quantum-mechanical version of the two-step model was implemented by Lewenstein *et al.* [132], validating the results from the corresponding classical model. Systematic experimental studies in the tunneling regime, such as the one carried out by Miyazaki and Takada [147], confirmed the basic understanding of the mechanisms underlying the (high-order) harmonic generation process. It is worth pointing out yet another simple physical picture describing the harmonic generation process in which the (time) periodic scattering of the electron with the atomic core is responsible for harmonic generation: a single encounter generates a broad bremsstrahlung spec-

[9] It should be stressed that the magnetic induction required is about $B \sim 10^3 - 10^4$ T compared to typically 10-15 T achievable with standard laboratory equipment.

[10] Because the H_2^+ molecular ion is the simplest one-electron system beyond hydrogen-like atoms, harmonic generation has been extensively investigated in this system (see, e.g., Ref. [170] and references therein).

trum which evolves into a typical harmonic spectrum after a sufficient number of rescattering processes [186].

1.2.3 Recent developments

Nowadays, attention has focused on the control of (high-order) harmonic generation in view of possible application as a new source of light (see section 1.5). For this, the coherence properties are, besides the overall conversion efficiency, the most important aspects to study. Ditmire *et al.* [65] performed the first measurement of the spatial coherence of high-order harmonics, carrying out a Young's two-slit type experiment. They found a good fringe visibility and concluded that the spatial coherence of the harmonics was significantly better than the one of similar radiation emitted by current soft X-ray lasers. A different but related experiment was reported by Zerne *et al.* [233]. The authors made two beams of harmonic radiation from independent sources to interfere by splitting the incoming fundamental beam and focusing the two parallel beams in the same gas jet but at different locations. The good fringe visibility of the interference pattern led to the conclusion that the two harmonic beams were locked in phase, despite the strong intensity-dependence of the phases in the generation process (see section 1.4.1). The coherence properties of high-order harmonics have been extensively reviewed by Salières *et al.* [201].

Most of the investigations carried out over the past few years have in common a continous trend towards the use of ultrashort pulses, down to a few cycles per pulse [108]. Indeed, because the shorter the pulse duration the higher is the saturation intensity. As a consequence the atoms can experience a high effective ponderomotive potential U_p before ionizing thereby allowing for the generation of very high harmonic orders. This was confirmed for very short pulses (< 100 fs), where harmonic orders higher than those predicted by the cut-off law were observed by Zhou *et al.* [234] using 25 fs laser pulses. Comparative studies for different pulselengths in the range 25-200 fs by the same authors [48] showed an increase of the maximum harmonic order by about twenty in argon when decreasing the pulselengths from 100 fs down to 25 fs, keeping the peak intensity constant. Additionally, part of the enhancements reported

in [48,234] could be attributed to the significant change of the laser intensity during an optical cycle of the laser field the electron returning to the nucleus experiences, a feature which is also not taken into account when deriving Eq. (1.2). These two effects, which do depend explicitly on the short pulse duration, are therefore usually called nonadiabatic.

Ultrashort pulses made it possible to observe the highest harmonic orders up to date. Using a Ti:sapphire laser system (780 nm), Spielmann *et al.* [212] reached down to less than 4.4 nm harmonic wavelength in helium. Similar results for the same gas were obtained by Chang *et al.* [45], who, using the same laser system at 800 nm, observed harmonic radiation down to 2.7 nm. While the harmonics were discernible as peaks up to order 221, an X-ray continuum was observed above this order. The continuum extended to a maximum photon energy of 460 eV corresponding to a maximum order of 297. Neon, with the second highest ionization potential after helium, was also used in this experiment with similar results.

A related topic is the possibility of generating ultrashort, attosecond harmonic pulses. This is in analogy to the mode-locking of a laser where various modes amplified by the oscillator are forced to have a fixed phase-relationship, creating a series of pulses with well defined pulselength and pulse separation (see, e.g., Ref. [205]). The feasability of harmonic attosecond pulses has been predicted by Antoine *et al.* [6]. Though the harmonics are not phase-locked in the single-atom response, propagation effects were shown to be able to provide the necessary mode-locking. One way of selecting a single attosecond pulse out of a train of pulses makes use of a time-dependent degree of ellipticity (recall that increasing ellipticity strongly suppresses harmonic generation). Many authors have pointed out this as the route to follow [7,101]. It is worth mentioning, that the generation and detection of such short X-ray pulses poses numerous technical problems, including the lack of suitable optical materials, but also require new measurement methods for the duration of these pulses [53,84].

Another possibility of generating very high harmonics is the use of a short fundamental wavelength as less harmonic orders are needed to reach high energies. The

disadvantage of ionizing more rapidly the medium can sometimes be compensated by the onset of harmonic generation from ions [227]. Preston *et al.* [184] reported wavelengths down to 6.7 nm using a 248.6 nm KrF laser focused into a helium gas jet, corresponding to the 37^{th} harmonic of the fundamental wavelength. They could identify the He^+-ion to be responsible for the highest harmonics generated. This was also found by Krause *et al.* [113] in numerical simulations, who could show the He^+-ion to be the source of an extended plateau. Again, this is due to a higher saturation intensity of the ion with respect to the corresponding neutral atom, thus allowing very high intensities to be used in experiments (up to 4×10^{17} W/cm^2 in Ref. [184]).

The tunability of harmonics by tuning the fundamental wavelength itself has rarely been studied, and if so, then seemingly only in connection with atomic resonances. Mittleman *et al.* [145] showed the wavelength of the harmonic radiation to follow smoothly the corresponding variations of the fundamental in N_2 (at constant gas pressure and pulse energy) while dramatic changes were observed in xenon due to resonances close to the 7^{th} harmonic under investigation. Peet [164] has studied resonantly enhanced multiphoton ionization close to the 6s resonance of xenon by an internally created third harmonic field over a range of wavelengths spanning the width of the resonance (see chapter 3 for more details).

An even wider range of effects can be studied when the atomic gas is interacting with two (or more, see Ref. [224]) laser modes. In most cases, two modes have been considered, in particular a coherent superposition of the fundamental with one of its harmonics. This case offers the possibility of coherence control of harmonic generation through the variation of the relative phase between the two fields. This idea is based on the simple quantum-mechanical fact that two different paths leading to a given final have to be added up in terms of amplitudes and may thus interfere. This has been investigated theoretically by Potvliege and Smith [178, 179] for hydrogen. They found that sometimes even a weak harmonic could significantly affect the ionization rate. The impact is equally significant on harmonic generation, as calculated both by Telnov *et al.* [216] for hydrogen and by Meşe [136] for a Yukawa potential

using the same theoretical approach[11]. Meşe and Potvliege [138] have also computed the same processes for two incommensurate frequencies[12] and found little influence of the added weak field on the harmonic yield. Milošević and Piraux [143] have generalized the quantum-mechanical two-step model of harmonic generation introduced previously to bichromatic fields. In the region of parameters investigated, they predicted a strongly enhanced harmonic yield and a lower cut-off than compared to the monochromatic case. Bichromatic fields of perpendicular polarization can also be used to obtain the time-dependent elliptical polarization used to generate ultrashort pulses as described above [8].

Instead of a second ac-field, the effect of additional dc-fields can be studied. Bao and Starace [22] investigated the effects of a static electric field on harmonic generation in atomic systems, H^- in particular. The strong static field (10^7 V/m) severely breaks the initial inversion symmetry of the unperturbed atom and the harmonic spectrum peaks at both odd and even harmonic frequencies of comparable strength. The authors also found the odd harmonics in the plateau to be strongly enhanced in the presence of the static field. The latter result is somewhat contested by more recent calculations by Meşe and Potvliege [139] and work towards the resolution of this question is in progress [140]. The inclusion of a static magnetic field occurs usually in connection with calculations in the relativistic domain (typically reached for intensities above 10^{18} W/cm^2), where the magnetic field component of the laser field also comes into play [52, 109]. While most of the earlier studies have been carried out using classical methods, the use of relativistic wave equations is a new trend in strong laser-atom interaction physics, though still limited to 1D or 2D calculations (see, e.g., Ref. [119, 190]). The quantum-mechanical approach is also necessary if spin dynamics are to be taken into account.

Despite all these spectacular advances, the conversion efficiency in a typical short pulse (< 1 ps) higher harmonic generation experiment remains generally low. Ditmire *et al.* [66] reported conversion efficiencies of up to 10^{-7} in helium in the spectral range 31.0-17.0 nm (corresponding to the 17^{th} -31^{st} harmonics of 526.4-nm radia-

[11]The Sturmian-Floquet approach introduced in chapter 2.

[12]That is, the ratio of the two frequencies is not expressible as a (simple) rational number.

tion), while Preston *et al.* [185] measured conversion efficiencies of up to 5×10^{-6} in helium and neon in the spectral range 35.5-19.1 nm (corresponding to the 7^{th} -13^{th} harmonic of 248.6-nm radiation). Recently, attention has thus also turned to the generation of short pulses of low-order harmonics [12] and a conversion efficiency of up to 0.1 % into the third harmonic of 800-nm radiation in air and argon has been reported by Peatross *et al.* [163].

1.3 Single-atom response

1.3.1 Theoretical approaches

The need of having to treat the electron dynamics nonperturbatively in order to account satisfactorily for the harmonic spectra in the tunneling regime has led to the development of various techniques. The most straightforward approach is the numerical solution of the time-dependent Schrödinger equation (TDSE), or more generally, of the time-dependent Hartree-Fock equation (TDHF) for complex atoms. Kulander *et al.* [116] have approached this problem by replacing the nonlocal term in the TDHF by a suitable local potential, reducing the calculations to the evaluation of single-electron orbitals. Erhard and Gross [76] used time-dependent density functional theory to yield a local approximation for the exchange term. Taylor *et al.* [215] attempted to solve the TDHF without approximations for helium using massively-parallel supercomputers. Lappas *et al.* [120], using a 1D model of helium, investigated the role of electronic correlation. They found no major difference between the fully correlated calculation and the single-active electron approach for harmonic generation. In the limiting case of a purely harmonic time-dependence (that is, neglecting the temporal envelope of the laser pulse), the Floquet method is another exact approach, allowing the time-dependent equations to be rewritten as an infinite system of coupled time-independent equations. This approach has been coupled with the R-matrix theory for describing complex atoms in intense electromagnetic fields and has become known as R-matrix-Floquet theory. We will turn to the Floquet method in some more detail in chapter 2. For completeness we men-

tion that a nonrelativistic QED version of harmonic generation in a n-level atom based on the Floquet method has been developed by Compagno *et al.* [51]. They related the harmonic spectrum to the hyper-Raman spectrum and suggested that the plateau observed in the harmonic spectrum could be due to the interference of both spectra.

Semi-analytical models suffer from the lack of an analytical expression for the wave-function of an electron in the combined potentials of the binding system and the light field. Though efforts have been made towards finding approximative analytical solutions to this problem [71, 192], they are not of much help in actual calculations. The Lewenstein model, introduced in Ref. [132] and developed in Refs. [5, 123], makes the following assumptions: The laser parameters are chosen such as to be in the tunneling regime. It is then possible to restrict essentially the atom to a single bound state (the ground state) which is coupled to the continuum when a strong external field is applied. Neglecting thus excited atomic states but also (possible) electronic correlation and the long-range part of the atomic binding potential, the Schrödinger equation becomes amenable to semi-analytical treatment, the integrals over the electronic momenta being evaluated using the saddle-point method (see, e.g., Ref. [29]). The saddle-points are derived from the requirement of the stationarity of the classical action of the electron oscillating in the external field (neglecting the binding potential in this step). To this respect, the approach is thus also to some extent semi-classical, the quantum aspect being essentially determined by the number of saddle-points taken into account, to account for the interference of the different possible trajectories of the electron. Another semi-analytical model is that developed by Becker *et al.* [24–26], who used a delta-type potential to model short-range potentials. Because of their similar assumptions and range of validity, both models can be shown to have common theoretical roots [27].

Of course, a myriad other attempts such as, e.g., purely classical methods or one-dimensional models (see, e.g., Ref. [193]) exist and they have proven to yield useful insight into the physics of harmonic generation. But for all the useful information that has been drawn from them, one ultimately has to use one of the more sophisticated approaches outlined above for a realistic modelling of all aspects of harmonic

generation and for providing sufficiently accurate atomic data that can be used as an input for further calculations, e.g., the propagation of harmonic radiation through various media. We shall thus be content with mentioning a recent modelling of harmonic generation by a degenerate two-level system by Burlon *et al.* [37], who were able to give simple analytical formulas for the onset of the plateau, its width and the position of the cut-off of the harmonic spectrum, within the limits of this simplified atomic model. Balcou *et al.* [18] used a confining anharmonic potential ('Duffing' oscillator) to investigate both classically and quantum-mechanically high harmonic generation. It emerges from those studies, that the formation of a plateau ending with a sharp cut-off is a quite general feature of any strongly driven nonlinear system.

1.3.2 The harmonic spectrum

The harmonic spectra are usually calculated semi-classically in the sense that the classical value for the dipole acceleration is replaced by its quantum-mechanical expectation value. Starting from the quantized radiation field, Sundaram and Milonni [213] (see also the Appendix of Ref. [27]) were able to show the validity of the semi-classical approach provided interatomic correlations could be neglected. Moreover, quantum fluctuations are also neglected in this way and only the mean dipole is taken into account [82]. The harmonic spectrum is thus essentially given by the Fourier transform (FT) of the single-atom dipole acceleration

$$S(\Omega) \propto \mathrm{FT}\left\{ \left| \frac{d^2}{dt^2} \langle \psi(\mathbf{x},t) | \mathbf{x} | \psi(\mathbf{x},t) \rangle \right|^2 \right\} . \tag{1.11}$$

This expression reduces in the Floquet limit of a purely harmonic time-dependence (or whenever contributions from the laser field envelope can be neglected) to

$$S(\Omega) \propto \Omega^4 \,\mathrm{FT}\left\{ \left| \langle \psi(\mathbf{x},t) | \mathbf{x} | \psi(\mathbf{x},t) \rangle \right|^2 \right\} , \tag{1.12}$$

where the Fourier transform consists of a sum of delta functions $\delta(\Omega - N\omega)$ at (odd) multiples of the laser frequency ω. To evaluate the dipole acceleration it is possible to apply Ehrenfest's theorem to the Hamiltonian of the atomic system, written here

in the velocity gauge as

$$H = \frac{\boldsymbol{p}^2}{2m} - V_{\rm at}(\mathbf{x}) + \frac{e}{mc}\boldsymbol{A}(t)\cdot\boldsymbol{p} + \frac{e^2}{2mc^2}\boldsymbol{A}^2(t)\,, \tag{1.13}$$

and describing an optically active electron in a local, space-dependent binding potential $V_{\rm at}(\mathbf{x})$ subjected to a laser field (in dipole approximation) and to evaluate the dipole acceleration as

$$\frac{d^2}{dt^2}\langle\mathbf{x}\rangle = \frac{1}{m}\frac{d}{dt}\left(\langle\boldsymbol{p}\rangle + \frac{e}{c}\boldsymbol{A}\right)\,. \tag{1.14}$$

This has been done in Ref. [42] within the framework of the Lewenstein model of Refs. [123, 132]. It was found in Ref. [42] that most integrals could be solved analytically without the saddle-point method, by a suitable analytical fit of the ground-state momentum distribution to simple transcendental functions. Eq. (1.14) is not the only way to calculate the dipole acceleration using the Ehrenfest theorem. The dipole acceleration can also be written as

$$\frac{d^2}{dt^2}\langle\mathbf{x}\rangle = \frac{e}{mc}\frac{d}{dt}\boldsymbol{A}(t) - \frac{1}{m}\langle\nabla V_{\rm at}(\mathbf{x})\rangle\,. \tag{1.15}$$

This form has been introduced in calculations by Burnett *et al.* [38]. It is particularly advantageous in numerical calculations as the wave function needs to be accurately known only close to the nucleus, where the electron experiences the strongest force due to the binding potential. In contrast, the length form Eq. (1.11) requires a good knowledge of the wavefunction even far from the nucleus and additionally requires a double numerical differentiation with respect to time.

Besides harmonic spectra, recent interest has focused on time profiles, which can be obtained through analysis of the dipole acceleration [9]. Time profiles from the two-step model predictions and from the numerical solution of the TDSE have been compared by Faria *et al.* [77] and found to be generally in good (qualitative) agreement. For short pulses, the increasingly nonadiabatic regime leads to the observation of pulse-shape effects: Watson *et al.* [227] found the harmonics to be increasingly blueshifted when the peak laser intensity was increased. As already pointed out before, the nonadiabatic effects originate in the intensity variations seen by an electron returning to the nucleus. This was subsequently confirmed by the same authors in a later study [228].

Note finally that for the single-atom response the phase of the emitted harmonics is not of importance as the spectrum depends only on the modulus of the dipole acceleration as given by Eq. (1.11). It is, however, never the single atom response which is observed in experiments but the collective response from a macroscopic target. Only for sufficiently thin targets (the harmonic radiation being emitted rather from a plane than from a volume) is the macroscopic yield reflecting the single-atom response. Therefore, the phase of the atomic reponse can be of importance when considering the propagation of the harmonic fields through the medium in which they have been generated. We turn now to the investigation of the influence of propagation on the harmonic radiation that will eventually be emitted from the atomic gas.

1.4 The propagation aspect

1.4.1 General considerations

A typical harmonic generation experiment we will be dealing with uses a (rare) gas target, confined to a gas cell or in form of a gas jet. A strong laser beam is focused into the gas, usually, but not necessarily, with the focal plane placed at the center of the medium. The type of focusing lenses together with the spatial intensity profile of the laser field determine the interaction geometry. For a Gaussian type of beam (see, e.g., Ref. [142,207]), for which the vast majority of harmonic generation experiments have been carried out, loose focusing designates the case where the confocal parameter b is much larger than the medium length L. A Gaussian beam can often be approximated by a plane wave in this limit. The opposite case is called tight focusing limit. There, the spatial intensity profile varies appreciably over the medium dimensions and the harmonic output generally reflects the behaviour of a small volume of atoms subjected to very strong fields [145]. The harmonics generated by the incident field have first to travel through the medium and might be modified in their characteristics during this propagation period, essentially through constructive or destructive interference with harmonics created at different points in

space and time. Formally, this stems from the fact that it is the amplitude (and not the modulus) of the single-atom response which enters the propagation equations as source term (see chapter 4). As a result, the phases of the harmonics within the medium will play a crucial role in what will be the measurable output in the far-field. There, the harmonics have further to be separated from the nearly undepleted, thus very intense fundamental laser mode (considering the generally low conversion efficiencies). They are analyzed using various types of spectrometers, due to the vast range of wavelengths that is covered when generating harmonics up to very high orders.

The presence of the phases leads above all to a discrepancy between the wavenumber at which the harmonic is allowed to travel according to Maxwell's equations, namely[13] k_q, which is determined by the medium properties at the q^{th} harmonic frequency (dispersion), and the wavenumber which is imprinted on the q^{th} harmonic, when it is generated through the nonlinear process. We will write the latter quantity, for the sake of clarity, as $qk_1 - K$, where k_1 is the wavenumber of the laser field at the fundamental frequency. K is, in general, a very complicated function of time and space. It includes phases of the following origin: firstly, a geometric phase which depends only on the laser beam geometry and vanishes in the plane wave limit $b \gg L$. To illustrate its dependence on focusing, we state here a simple approximation to this phase factor [204],

$$K_{\text{geo}} L \equiv \Delta\Phi_{\text{geo}} \approx 2(q-1)\tan^{-1}(2L/b)\,. \tag{1.16}$$

The geometric phase is thus largest in the tight focusing limit $b \ll L$ and increases with the harmonic order q. K consists secondly of the atomic phase (sometimes called dynamically induced phase of the atomic polarization), which we had introduced briefly in the previous section. The atomic phase has been studied within the framework of the two-step model by Lewenstein *et al.* [124]. The authors found a very general expression for the intensity-dependence of this phase, namely a piecewise linear function, of slope $-3.2U_p/\hbar\omega$ for intensities in the cut-off region (recall that $U_p \propto I_L$), and of slope $-5.8U_p/\hbar\omega$ in the plateau region. At any rate, the

[13]For the harmonic order we also use the symbol q as N might be confused with the density when considering propagation aspects.

atomic phase varies very rapidly at high intensities which is of particular importance in the tight focusing limit. Intensity-dependent atomic phase effects in high harmonic generation have been subject to experimental investigation by Peatross and Meyerhofer [159, 160], who could show them to affect the spatial far-field profiles of emitted harmonics by adding broad wings to the otherwise narrow central peak around the propagation axis. On the other hand, use of this effect could be made by adjusting the laser focus position with respect to the nonlinear medium in order to control the temporal and spatial profiles of the emitted harmonics. Playing the geometric phase against the atomic phase, Salières *et al.* [200] could demonstrate this control by focusing the laser sufficiently before the medium. Turning back to k_1 and k_q, we find that they depend on space and time through the atomic density and linear atomic susceptibility and through the corresponding electronic quantities if ionization is to be taken into account. In fact, at sufficiently high intensities and for not too short pulses the free electrons will determine the refractive index and thus most of the medium properties.

1.4.2 Phase-matching

From the point of view of conversion efficiency, the most important aim is to reduce the difference between k_q and $qk_1 - K$ to a minimum over the whole nonlinear medium (and at all times during the laser pulse), so that the harmonic field can build up efficiently in the medium. The quantity

$$\Delta k = k_q - qk_1 + K \equiv \Delta k_{\text{disp}} + K \tag{1.17}$$

is known as the *phase-mismatch* and *phase-matching* remains possibly the last problem to be solved in the field as it is the key to high conversion efficiencies and, eventually, will determine whether in the future (high-order) harmonic generation can compete with the development of other X-ray sources, especially X-ray lasers. The heart of the problem lies in the fact that the dispersive phase-mismatch Δk_{disp} is often positive for neutral gases (and even more so if free electrons are present) while the geometric phase factor $\Delta\Phi_{\text{geo}}$ entering K is positive too. Phase-matching is generally worst in the tight focusing limit as follows from Eq. (1.16) and it espe-

cially affects the higher harmonic orders. In experiments this effect can be traced by moving gradually from the plane wave to the tight focusing limit, resulting in a modification of the harmonic cut-off law (1.2), where the factor of 3.2 decreases down to approximately a factor of 2 [72, 132, 226], thus limiting the maximum harmonic order which can be effectively generated.

Owing to its central importance, phase-matching has been thoroughly studied (for recent work on this subject, see, e.g., Refs. [15,16,19,130,161] and references therein) and numerous methods have been suggested to circumvent the intrinsic limits it sets to an efficient production of harmonic radiation. Widely used traditional methods [191] include the use of gas mixtures with a dispersion of opposite sign, such that $\Delta k_{\text{disp}} = \Delta k^{(1)}_{\text{disp}} + \Delta k^{(2)}_{\text{disp}} = 0$ in a plane wave geometry or a negatively dispersive atomic gas such as to offset the positive geometric phase in a more focused geometry. These techniques are useful for low-order harmonic generation in the perturbative regime where analytical expressions exist for optimum phase-matching conditions from which the values of the parameters necessary to achieve phase-matching can be inferred. They are less useful for high-intensity high-order harmonic generation because the outcome of an experiment can at best be 'predicted' by a full numerical simulation. Some recent suggestions include those by Shkolnikov *et al.* [204] who proposed the use of density-modulated media so as to cut out the regions of space within the medium where the harmonics interfere destructively[14]. The same authors also pointed out that in plasmas high-order difference-frequency mixing would be a better phase-matched process than high-order harmonic generation and thus a more efficient way of generating short wavelengths[15]. This approach however was shown to have inherent limitations by Kan *et al.* [107]. Another interesting method of eliminating out-of-phase harmonic generation was put forward by Peatross *et al.* [162]. These authors suggested the use of counter-propagating light to suppress out-of-phase harmonic generation in specific regions of the focus. The key point

[14]The principle of this method dates also back to the early days of harmonic generation and is commonly called *quasi-phase-matching.*

[15]That is, instead of obtaining the desired high frequency through harmonic generation of order q, $\omega = q\omega_0$, one uses the process $\omega = m\omega_1 - l\omega_2$, with $\omega_1 \gg \omega_2$, $m > l$, as a process of order $m + l$. Note that this process can also be used to tune harmonic generation: ω_1 is then the frequency of a high power laser and ω_2 the frequency of a less powerful but tunable laser [72].

is that this can be achieved with a relatively weak (counterpropagating) field, so as not to induce further nonlinear processes. Finally, in determining the optimum focusing geometry for high-order harmonic generation, Balcou *et al.* [19] could show a graphical method monitoring the variation of the phases over the medium dimensions to be very helpful.

1.5 Harmonic radiation in applications

Possibly the main interest in studying harmonic generation lies in its potential applications as a bright, coherent source of X-ray light, a domain which is traditionally reserved to synchroton radiation and powerful X-rays lasers (usually designed to support fusion experiments). Both sources require huge facilities and can be afforded only on a national or international level. All the more desirable is therefore the design of a table-top X-ray source[16].

Harmonics have been used as a source of light on their own right since the early 1990's. Haight and Peale [89] examined semiconductor surface states in Ge(111):As, recording the spectra of photoelectrons ejected from the samples by short UV pulses. For this they created harmonics in a krypton gas up the the 11^{th} harmonic of a 610-nm (2.03 eV) dye laser and focused the resulting UV light into the germanium sample. Harmonics as a source of light in spectroscopy have been used to measure radiative lifetimes of helium [121] and autoionizing states in krypton [17]. Balcou *et al.* [17] have also measured single-photon ionization cross sections of rare gases over the range 10 to 110 eV using higher harmonics (11^{th} to 69^{th}) from a 825-nm Cr:LiSAF laser and found them to be in good agreement with existing data obtained using different methods. Two-photon ionization in argon with third harmonic photons from a 248.6-nm KrF laser was observed by Xenakis *et al.* [232] which was, according to the authors, the first multiphoton process using XUV photons. Hässner *et al.* [93] have used high-order harmonics from a solid target (a thin poly-

[16]For the characterisation of spectral wavelength ranges we follow Ref. [134]: ~2-20μm: mid-infrared (IR), 700-2000nm: near IR, 400-700nm: visible, 200-400nm: near ultraviolet (UV), 100-200nm: vacuum UV (VUV), 10-100nm: extreme UV (XUV), <10nm: X-ray.

carbonate foil) created at very high intensities (exceeding 10^{18} W/cm^2) to probe high-density plasma conditions. Indeed, high frequencies should only be transmitted through the plasma if larger than the plasma frequency, the latter being dependent on the plasma density. Possibly the most important application of very high-order harmonic generation will be the X-ray imaging of living cells and micro-organisms. For imaging purposes one must achieve a good contrast between carbon-based organic structures embedded in a surrounding fluid, consisting essentially of water (thus oxygen). The region of interest lies in the narrow range between 2.3 nm and 4.4 nm, the so-called water window, where X-rays are absorbed by carbon but not yet by oxygen [45, 202, 212].

1.6 Conclusions and aim of the present thesis

In the present thesis, we shall be mainly concerned with the improvement of the conversion efficiency in a typical harmonic generation experiment. We have seen in the preceeding sections that it is phase-matching which controls the coherent built-up of the single-atom response within the nonlinear medium and therefore determines the overall, measurable harmonic yield. Several methods, of which we have mentioned a few and each having their own range of applicability, exist for improving the phase-matching conditions. The aim of the present work is to thoroughly investigate yet another possible method by considering Bessel-Gauss beams, a very general class of solutions of the paraxial wave equation containing the Gaussian beam as limit case. We will show Bessel-Gauss beams to induce a noncollinear phase-matching geometry, making use of the fact, that Eq. (1.17), in fact is a vector relation, reducing essentially to the scalar limit for Gaussian beams. The range of applicability will turn out to be restricted to negatively dispersive media. Regions of negative dispersion in atomic systems can be found close to resonances or above the first ionization threshold. Calculations in the vicinity of an atomic resonance at high intensities make it necessary to account (nonperturbatively) for ac-Stark-shifts in determining the atomic properties. We have therefore chosen, as a starting point, to use atomic hydrogen as nonlinear medium, essentially because it is possibly to

perform very accurate nonperturbative calculations for this system. Data of comparable accuracy for more complex atoms is presently lacking or can only be gained with considerable computational effort. The emphasis in applications is on general concepts, however, and the conclusions we draw from this study are valid for atomic gases in general. Chapter 2 is thus devoted to the nonperturbative calculation of the single-atom response for atomic hydrogen. Chapter 3 introduces Bessel type beams in general and Bessel-Gauss beams in particular. Chapter 4 gives a detailed derivation of the harmonic far-field from which the measurable characteristics, such as conversion efficiency and spatio-temporal profiles, can be gained. Chapter 5 presents an extensive review of the propagation calculations performed for atomic hydrogen up to high intensities involving the effects of the $1s-2p$ resonance. Chapter 6 deals with analytical formulas for predicting the optimum Bessel-Gauss beam in the perturbative regime and supporting propagation calculations in both hydrogen and xenon. Chapter 7 reports a high-order harmonic generation calculation in argon which has been carried out in connection with an ongoing experiment at the Laboratoire d'Optique Appliquée (LOA) in Palaiseau, France. We will draw our final conclusions from the material presented in chapters 5,6 and 7 thereafter. The appendices contain, amongst others, the description of an experimental realization of a Bessel type beam, which we have carried out during a visit at the LOA (Appendix D) and a presentation of the propagation code, which has been conceived and written as part of this thesis (Appendix E).

Chapter 2

Floquet Calculations in Hydrogen at 355 nm

2.1 Introduction

For most of the calculations presented in this work, the basic atomic properties have been calculated using the Floquet method. This approach is based on a theorem from mathematics of the same name which discusses the general structure of solutions to differential equations with periodic coefficient functions (see, e.g., Ref. [96]). We take the Hamiltonian Eq. (1.13) as a starting point and consider a time-periodic, linearly polarized laser field with a vector potential given by $\boldsymbol{A}(t) = -\hat{\boldsymbol{e}}A_0 \sin(\omega t + \varphi)$. Hence, the laser field amplitude is given by $\boldsymbol{E}(t) = -(\partial \boldsymbol{A}/\partial t)/c = \hat{\boldsymbol{e}}E_0 \cos(\omega t + \varphi)$, where $E_0 = A_0\omega/c$. We can remove the term proportional to $A^2(t)$ from the Schrödinger equation

$$i\hbar\frac{\mathrm{d}}{\mathrm{d}t}|\Psi(t)\rangle = H(t)|\Psi(t)\rangle \tag{2.1}$$

by the transformation

$$|\Psi(t)\rangle = \exp\left[-\frac{ie^2}{2\hbar mc^2}\int^t \boldsymbol{A}^2(\tau)\mathrm{d}\tau\right]|\psi(t)\rangle \equiv \exp\left[-\frac{i}{\hbar}F(t)\right]|\psi(t)\rangle, \tag{2.2}$$

where $F(t)$ is found to be given by

$$F(t) = U_p t - \frac{e^2E_0^2}{8m\omega^3}\sin[2(\omega t + \varphi)]\,. \tag{2.3}$$

The time average of the derivative of $F(t)$ is simply

$$\langle F'(t)\rangle_t = U_p\,, \tag{2.4}$$

which is the ponderomotive energy as introduced in Eq. (1.3). The Schrödinger equation can now be written as

$$i\hbar\frac{\mathrm{d}}{\mathrm{d}t}|\psi(t)\rangle = [H_{\rm at} + V(t)]|\psi(t)\rangle, \tag{2.5}$$

where we have introduced the atomic Hamiltonian

$$H_{\rm at} = \frac{\boldsymbol{p}^2}{2m} - V_{\rm at}(\mathbf{x})\,, \tag{2.6}$$

and the interaction term V(t), written as

$$V(t) = V_- \exp[i(\omega t+\varphi)] + V_+ \exp[-i(\omega t+\varphi)]\,, \tag{2.7}$$

with

$$V_- = i\frac{eE_0}{2m\omega}\,\hat{\boldsymbol{e}}\cdot\boldsymbol{p}\,, \qquad\qquad V_+ = V_-^\dagger\,. \tag{2.8}$$

The Floquet ansatz reads

$$|\psi(t)\rangle = \exp(-i\mathcal{E}t/\hbar)\sum_{N=-\infty}^{N=+\infty}\exp[-iN(\omega t+\varphi)]|\Phi_N\rangle\,, \tag{2.9}$$

and transforms the Schrödinger equation (2.5) into an infinite set of time-independent coupled equations which determine the wavefunction and the quasienergy $\mathcal{E}$ of the atomic system, namely

$$(\mathcal{E} + N\hbar\omega - H_{\rm at})|\Phi_N\rangle = V_+|\Phi_{N-1}\rangle + V_-|\Phi_{N+1}\rangle\,, \tag{2.10}$$

for all N. This set of equations is expanded on a basis set of known functions. It is usually rather inconvenient to use the atomic basis set of bound and continuum states. Indeed, basis sets such as, e.g., B-Splines or Sturmian functions cover more readily coordinate space with a (necessarily) finite number of functions than does the atomic basis set. The program employed in this work uses a Sturmian basis set [181], that is

$$\langle\mathbf{x}|\Phi_N\rangle = \sum_{nlm} C_{nlm}^{(N)} Y_{lm}(\hat{\boldsymbol{r}})S_{nl}^{\kappa}(r)/r\,, \tag{2.11}$$

where

$$S_{nl}^{\kappa}(r) = \mathcal{N}_{nl}\,(-2i\kappa r)^{l+1}\exp(i\kappa r)\;{}_1F_1(l+1-n, 2l+2, -2i\kappa r)\,. \tag{2.12}$$

${}_1F_1(a,b,c)$ is the confluent hypergeometric function [1] and the Y_{lm} are the well known spherical harmonics. The parameter κ can be chosen freely to optimize the calculations as long as $0 < \arg(\kappa) < \pi/2$, which is imposed by the boundary conditions for an outgoing wave that is exponentially damped as $r \to +\infty$. The eigenvalues and eigenvectors of a subset of the system of coupled equations above (that is, for a finite number N of 'Floquet blocks') are then determined, e.g., by inverse iterations [176]. The convergence of the calculations is obtained both by including more and more basis functions n and angular momenta l in the sum (2.11) and by increasing the number of Floquet blocks N, until a specified accuracy is reached. The quasi-energy $\mathcal{E}$ is complex and given by

$$\mathcal{E} = E_{\rm at} + \Delta_{\rm ac} - i\hbar\Gamma/2\,. \tag{2.13}$$

The real part is the sum of the energy of the field-free atom, $E_{\rm at}$, and the ac-Stark-shift, $\Delta_{\rm ac}$. The imaginary part is proportional to the ionization rate Γ, $\Gamma = -2\,\mathrm{Im}\mathcal{E}/\hbar$. The quasi-energy (2.13) is only part of the total energy $\mathcal{E}_{\rm tot}$ of the atomic system in the laser field, owing to the initial transformation (2.2) which had removed the energy shift induced by the $A^2(t)$-term. Thus, to describe the full system in terms of a time-independent energy, we let

$$\mathcal{E}_{\rm tot} = \mathcal{E} + \langle F'(t)\rangle_t = \mathcal{E} + U_p\,. \tag{2.14}$$

In the case of a two-colour field consisting of a coherent superposition of the fundamental field (amplitude $E_1 > 0$, phase φ) and its q^{th} harmonic (amplitude $E_q > 0$, phase ϕ), both polarized co-linearily,

$$E(t) = [E_1\,\cos(\omega t + \varphi) + E_q\,\cos(q\omega t + \phi)]\,\hat{\mathbf{e}}\,, \tag{2.15}$$

we have to replace Eq. (2.7) by

$$\begin{aligned} V(t) &= V_{1+}\exp(-i\omega t - i\varphi) + V_{1-}\exp(i\omega t + i\varphi) \\ &+ V_{q+}\exp(-iq\omega t - i\phi) + V_{q-}\exp(iq\omega t + i\phi)\,, \end{aligned} \tag{2.16}$$

and Eq. (2.10) by

$$\begin{aligned}(\mathcal{E} + N\hbar\omega - H_{\rm at})|\Phi_N\rangle &= V_{1+}|\Phi_{N-1}\rangle + V_{1-}|\Phi_{N+1}\rangle \\ + V_{q+}\exp(-i\phi + iq\varphi)|\Phi_{N-q}\rangle &+ V_{q-}\exp(i\phi - iq\varphi)|\Phi_{N+q}\rangle\,.\end{aligned} \tag{2.17}$$

Recalling from section 1.3.2 that the atomic response to the driving laser field is sought in form of the atomic dipole moment, we obtain within the framework of Floquet theory [175]

$$\boldsymbol{d}(t) = \exp(-\Gamma t)\left\{d_0 + \sum_{N>0}\mathrm{Re}\left[2\,d_N\,\exp(-iN\omega t)\right]\right\}\hat{\boldsymbol{e}}\,, \tag{2.18}$$

where we have defined the Fourier components of the dipole moment as

$$d_N \equiv d_N(E_1, E_q, \varphi, \phi) = \left[\sum_{M=-\infty}^{M=+\infty}\langle\Phi_{M-N}|e\mathbf{x}|\Phi_M\rangle\right]\exp(-iN\varphi)\,. \tag{2.19}$$

In close analogy to the evaluation of the dipole acceleration with the help of the Ehrenfest theorem (section 1.3.2), it is possible to evaluate the dipole moment in different ways: in length form, as given by Eq. (2.19), in velocity form, with the position operator replaced by the momentum operator, and in acceleration form, with the position operator replaced by the gradient of the atomic binding potential[1]. This provides additional tests for the accuracy of the numerical calculations to follow. Assuming perturbation theory to hold with respect to the field strength of the harmonic, E_q, we can express the dependence of $d_{N=q}$ on the field strengths as

$$\begin{aligned}d_q(E_1, E_q, \varphi, \phi) &= [d_q(E_1) + \epsilon_0\chi(q\omega, E_1)E_q\exp(-i\phi + iq\varphi)]\exp(-iq\varphi) \\ &= d_q(E_1)\exp(-iq\varphi) + \epsilon_0\chi(q\omega, E_1)E_q\exp(-i\phi)\,.\end{aligned} \tag{2.20}$$

The first term is responsible for the generation of the q^{th} harmonic and will serve as source term in the propagation equation as discussed in chapter 4. This term is nonperturbative in the sense that all orders of E_1 are taken into account. In the weak field limit it reduces to the well known power law

$$d_q(E_1) = \epsilon_0\chi^{(q)}(-q\omega; \omega, ..., \omega)E_1^q\,. \tag{2.21}$$

[1]Note that the form of dipole moment is not related to the gauge. All calculations (wavefunction, quasienergy) are performed in velocity gauge, that is, V_- and V_+ are functions of the momentum operator $\boldsymbol{p}$ as given in Eq. (2.8).

The second term of Eq. (2.20) is linear in E_q and hence $\chi(q\omega, E_1)$ is the linear atomic susceptibility which determines the refractive index at the frequency $q\omega$. This susceptibility, however, is dependent on the (strong) fundamental field which dresses the atom. That is, expanding this quantity into powers of E_1, we obtain the well known expression,

$$\chi(q\omega, E_1) = \chi^{(1)}(-q\omega; q\omega) + \chi^{(3)}(-q\omega; q\omega, -\omega, \omega)E_1^2 + ... \qquad (2.22)$$

where the second term in this expansion is the so-called Kerr nonlinearity, leading to an intensity-dependent refractive index[2]. The atomic susceptibility at a given field strength E_1 is then formally evaluated as

$$\chi(q\omega, E_1) = \frac{1}{\epsilon_0}\exp(i\phi)\frac{\partial d_q(E_1, E_q)}{\partial E_q}, \qquad \chi(\omega, E_1) = \left.\frac{\partial d_1(E)}{\partial E}\right|_{E=E_1}. \qquad (2.23)$$

Note that because we need only the term linear in E_q, the atomic susceptibility is effectively independent of the phase ϕ.

The application of the Floquet method to nonperturbative calculations in hydrogen has been developed by Chu and Reinhardt [50] in the late 1970's and independently by Potvliege and Shakeshaft [173] in the late 1980's. For exhaustive details about the method and applications to hydrogen within the Sturmian-Floquet approach used in this work we refer to Refs. [62, 136, 175–177] and references therein. A possible approach for more complex atoms is the R-matrix-Floquet theory [36, 106]. The R-matrix theory distinguishes two regions of space, an inner region where the correlation between all electrons is taken into account, and an outer region, where, when it is reached by one of the electrons under the influence of the external field, the exchange effects of this particular electron with those remaining in the inner region can be neglected. The R-matrix is then essentially the mathematical expression for the matching conditions at the boundaries of the two regions and all information about the atomic system can be gained from this matrix.

Clearly, effects depending crucially on the temporal shape of the laser field envelope, such as those discussed in section 1.3.2 (e.g., the blueshifting of the harmonics), can-

[2]The prefactor of $\chi^{(3)}$ in expansion (2.22) is a matter of convention and we have set it to unity for simplicity, as we do not calculate the terms on the right hand side individually. In fact, the power expansion is not at all valid in our case as the atomic levels entering the calculation of $\chi^{(k)}$ depend on E_1 as well (see next section).

not be accounted for by the Floquet approach. A possible exception are resonantly coupled states, which can be described by appropriately coupling the corresponding time-independent Floquet states with time-dependent coefficients [62]. For a sufficiently long pulse however - typically a few tens or hundreds of cycles when away from resonances, a few thousand cycles when close to a resonance - a single Floquet state yields a very good description of the strongly driven atom. Indeed, the atom then follows adiabatically the quasienergy trajectory leading from the bare atomic to the dressed Floquet state.

2.2 The third harmonic order

We will now apply the theory outlined in the previous section to the calculation of the atomic properties of hydrogen for an incident field of wavelength λ =355 nm, which corresponds to a photon energy of about 3.49 eV. For the calculation of the atomic data, the code of Ref. [181] is used, applying a single-colour field (oscillating at the fundamental frequency) for the calculation of the quasienergies and the atomic dipole moment responsible for the generation of the harmonics, and a two-colour field for determining the dressed atomic susceptibility at the harmonic frequencies[3]. The energy of the third harmonic (λ_3=118.3 nm) is somewhat in excess of the (field-free) 1s-2p transition in hydrogen (at about λ=121.5 nm). From the quasi-energy curves $\mathcal{E} = \mathcal{E}(I_1)$ of the dressed 1s and 2p states, we find that with increasing intensity the 1s state moves downwards due to an increasing ac-Stark shift, while the 2p state moves in the opposite direction (see Fig. 2.1). Both states are resonantly coupled around $I_1 = 1.15 \times 10^{13}$ W/cm^2 , shifting off resonance at higher intensities [175]. The atomic data could only be determined up to $I_1 = 3 \times 10^{13}$ W/cm^2 , because the 4-photon threshold is reached at about $I_1 = 2.94 \times 10^{13}$ W/cm^2 . Indeed, at this intensity the ac-Stark shift of the dressed ground state is $\Delta_{ac} \simeq -0.014$ a.u. $\simeq -0.375$ eV and $N_{ion} = |(-13.6 - 0.375)|/3.49 = 4$ photons

[3]For the determination of the atomic data we can obviously let $\phi = 0$ and $\varphi = 0$ in Eq. (2.20), as the linear atomic susceptibility does not depend on ϕ and the atomic dipole moment is only determined up to an overall phase factor $\exp(-iq\varphi)$. The phase φ will be used to accomodate for the local phase of the field within the nonlinear medium in connection with the propagation equations (section 4.2).

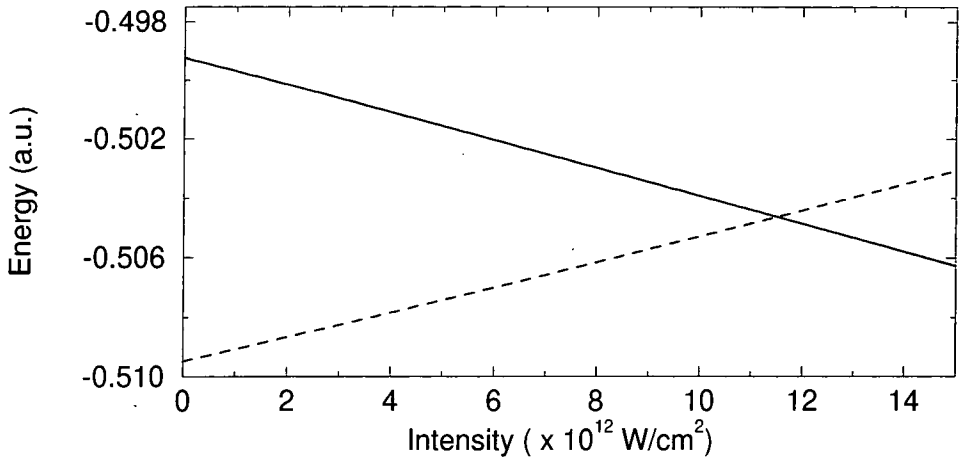

Figure 2.1: Energy levels ($\mathrm{Re}\mathcal{E}$) = $E_{\mathrm{at}}+\Delta_{\mathrm{ac}}$ showing the ac-Stark shift in atomic hydrogen as a function of the intensity for a 355-nm field. Solid line: $1s$ state, dashed line: $2p$ state. For better visualisation of the crossing, the 2p-level is shown shifted down by three times the photon energy. The field-free transition energy is $\Delta E_{1s-2p} \approx 10.2$ eV, while $3\hbar\omega \approx 10.5$ eV. The crossing occurs around $I_1 = 1.15 \times 10^{13}$ W/cm^2 .

are required to ionize the hydrogen atom. As a result of the nearby threshold, the Sturmian-Floquet method becomes inadequate as no finite basis set can fully represent the coupling to all the Rydberg states when the threshold is crossed. Note finally the value of the Keldysh parameter, from Eq. (1.6),

$$\gamma = \frac{2.4 \times 10^7}{\sqrt{I_L\,[\mathrm{W/cm^2}\,]}}. \tag{2.24}$$

At the highest peak intensity considered, $I_{\mathrm{f}} = 3\times 10^{13}$ W/cm^2 , we find $\gamma \approx 4.4$. We are therefore essentially in the multiphoton ionization regime. We have calculated the nonperturbative dipole moments and the dressed atomic susceptibilities for the harmonics q =3, 5, 7 and 9. However most of the propagation calculations were carried out for the third harmonic and we will present detailed results in later chapters only for this particular case. We thus defer a short presentation of the atomic data for q =5, 7, and 9 until the last section of this chapter.

In a first step, we test the assumption of Eq. (2.20), which allows us to determine the linear atomic susceptibilies. For this, we rewrite Eq. (2.20) in terms of intensities as

$$\log_{10}[|d_q(I_1, I_q) - d_q(I_1, I_q = 0)|^2] = \log_{10}[|C(I_1)|^2] + \log_{10}(I_q)\,, \tag{2.25}$$

which is independent of the phases φ and ϕ. The result is shown for in Fig. 2.2 for

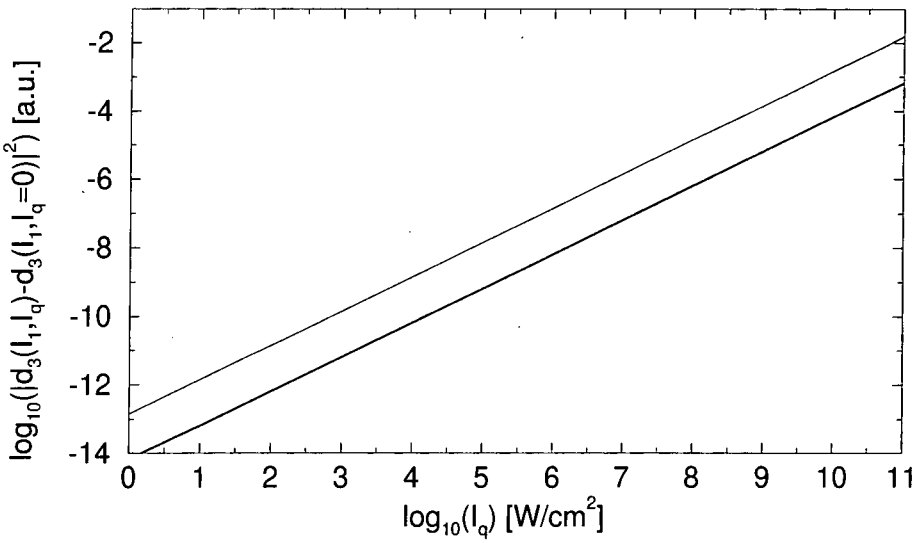

Figure 2.2: Test of assumption Eq. (2.20) for $q = 3$ as described in the text. The thin solid line is for $I_1 = 1 \times 10^{13}$ W/cm^2 , the thick solid line for $I_1 = 3 \times 10^{13}$ W/cm^2 .

$q = 3$. There is no noticeable deviation from a slope of unity, up to intensities $I_q \approx 10^{-2} I_1$, well beyond the harmonic intensities considered in this work, $I_q < 10^{-3} I_1$.

Fig. 2.3 shows the dipole moment as a function of the intensity of the fundamental. Perturbation theory, characterized by a power law dependence as stated in Eq. (2.21), is valid roughly up to $I_1 = 10^{12}$ W/cm^2 . At resonance, the modulus of the dipole moment is enhanced compared to the perturbative value but quickly saturates and decreases as the states shift off resonance at higher intensities. A very remarkable feature is the smooth variation of the phase of the atomic dipole in the vicinity of the resonance. For comparison we have shown on the same graph the corresponding phase of the 9^{th} harmonic of a fundamental field with $\lambda = 1064$ nm which has a wavelength very close to the third harmonic of $\lambda = 355$ nm. The 1064-nm results vary much more rapidly owing to ac-Stark-shift induced resonances with low-lying Rydberg states[4].

Fig. 2.4 shows the dressed atomic polarizabilities for various wavelengths of the incident field and how the profile of the resonance and the intensity at which it occurs do vary as the wavelength of the incident laser field is varied. It is apparent that with a lower wavelength the resonance could have been reached at a higher intensity but

[4]This fast variation over a significant range of intensities would be a major cause for an unpredictable phase-mismatch at higher intensities. Recall that the atomic phase is entering the term K in expression (1.17) for the phase-mismatch. This will be discussed in more detail in section 5.5.

with a less pronounced resonance effect (Fig. 2.4c). Conversely a stronger resonance could have been obtained at lower intensities with a third harmonic wavelength closer to the field-free transition frequency (Fig. 2.4a). The magnitude of the polarizability for $I_1 \to 0$ is however limited by the width of the field free 1s-2p resonance due to various line broadening effects, including the natural linewidth due to spontaneous emission, all of which are not included in the Floquet formalism. In Appendix C we have therefore compared the Floquet results with the corresponding results from linear dispersion theory in the zero-intensity limit, taking the width into

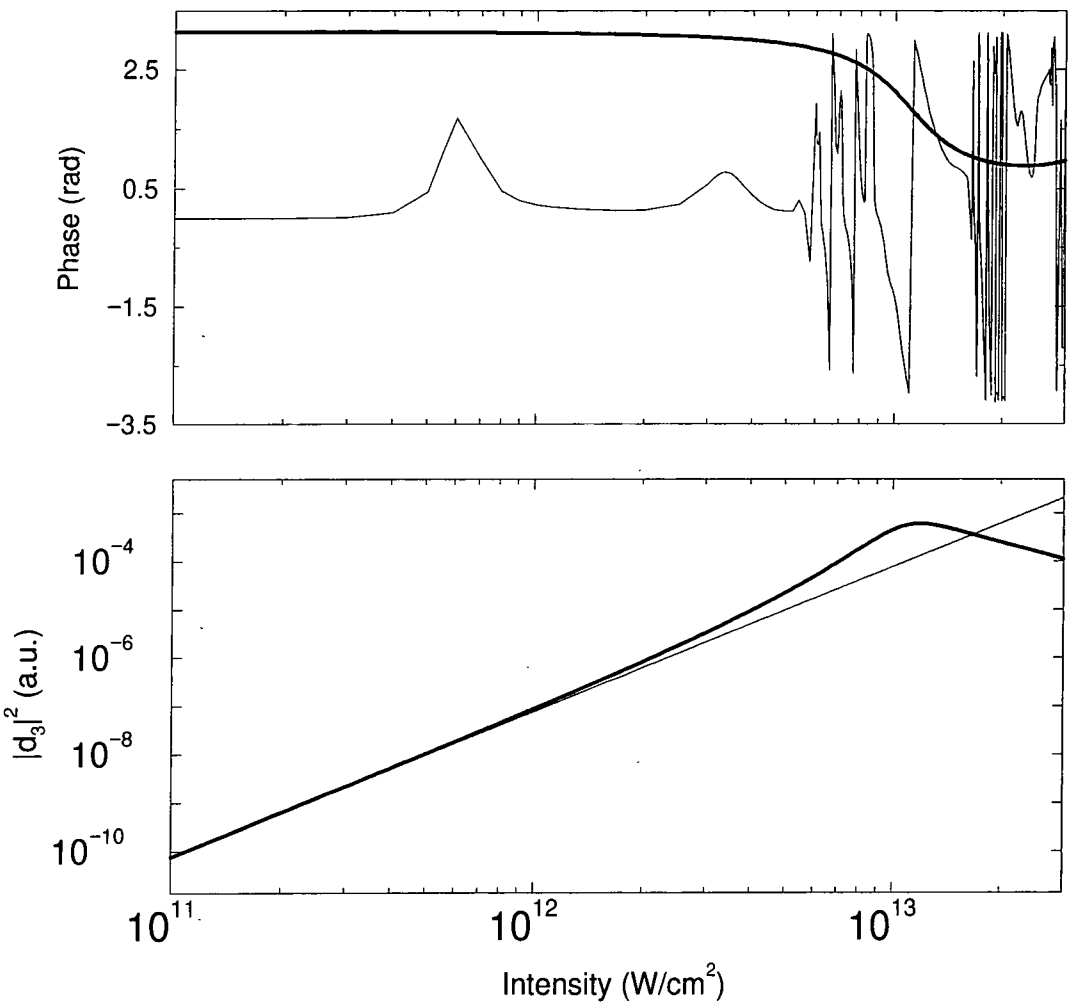

Figure 2.3: Top: Phase of the atomic dipole moment at the third harmonic of $\lambda = 355$ nm (thick line) and at the ninth harmonic of $\lambda = 1064$ nm (thin line). Bottom: Modulus square of the atomic dipole moment at the third harmonic of $\lambda = 355$ nm (thick line) and the corresponding perturbative power-law curve (thin line). In order to avoid confusion it should be stressed that the phase at the 9^{th} harmonic shown only appears to oscillate rapidly because its values are restricted to the interval $[-\pi, \pi]$. In fact, the phase is (essentially) continously decreasing with increasing intensity.

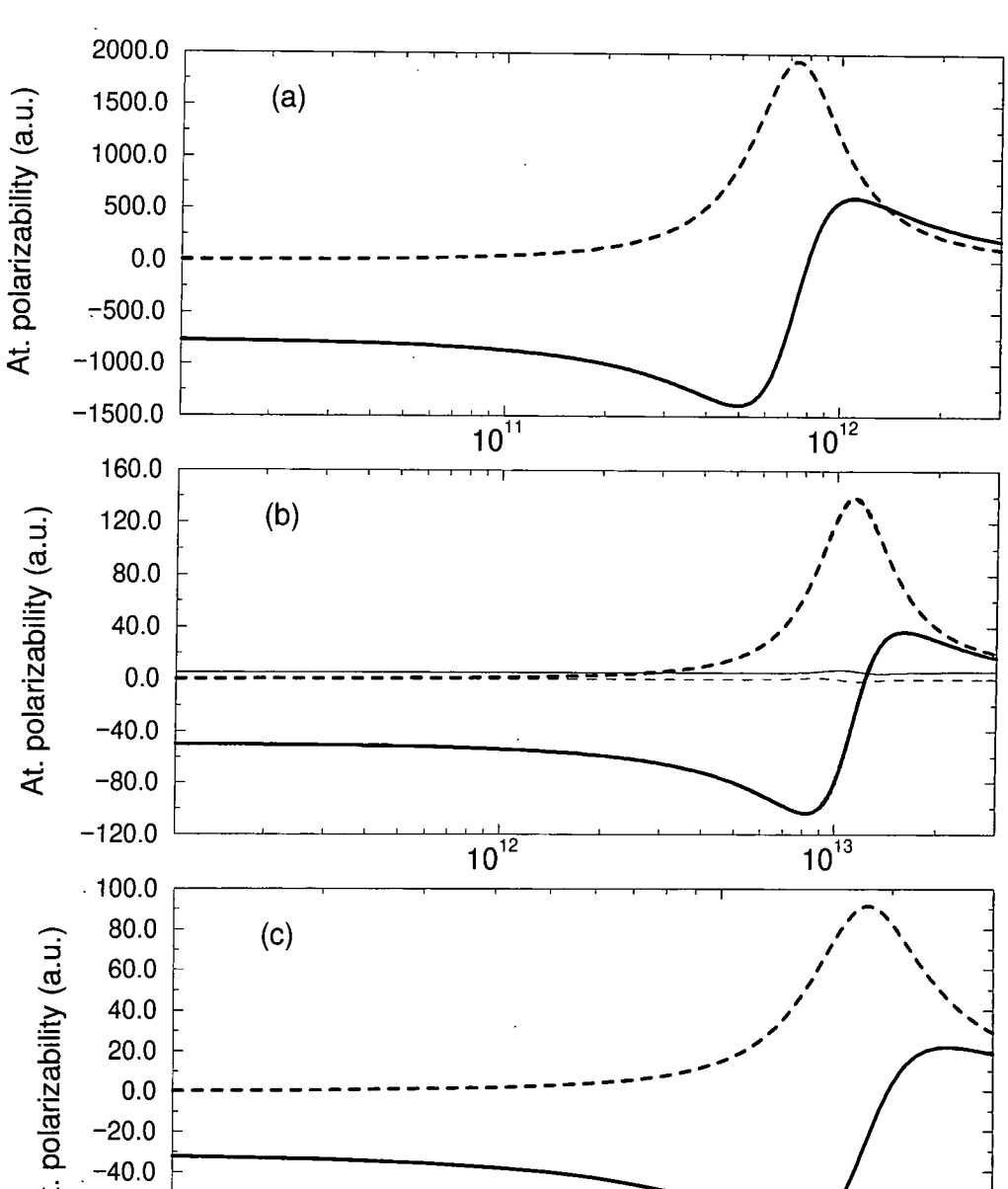

Figure 2.4: From top to bottom: real (solid lines) and imaginary parts (dashed lines) of the dressed linear atomic polarizability at the third harmonic frequency of the fundamental wavelengths (a) $\lambda = 364$ nm, (b) $\lambda = 355$ nm and (c) $\lambda = 350$ nm, respectively. The thin lines for $\lambda = 355$ nm show the corresponding polarizability at the fundamental frequency. The polarizabilities are given in a.u. and are related to the atomic susceptibilities (in SI) by a simple conversion factor, given in Appendix A.

account. The choice of the third harmonic of $\lambda = 355$ nm is thus based on the fact that, besides being very close to the 9^{th} harmonic of $\lambda = 1064$ nm, we achieve a good compromise between a sufficiently large region of intensity for which the medium is negatively dispersive and the magnitude of this dispersion, $\chi(\omega, E_1) - \chi(q\omega, E_1)$. The latter is essentially dictated by the behaviour of $\chi(q\omega, E_1)$, as $\mathrm{Re}[\chi(\omega, E_1)] \approx 5$ a.u. throughout the whole range of intensities (Fig. 2.4b). Additionally, $\lambda = 355$ nm as fundamental wavelength has been used several times in harmonic generation experiments in gases in the past (see Refs. [118, 237] and the discussion in chapter 5).

As mentioned earlier, it is also apparent from Fig. 2.4, that the intensity-dependence of the dressed linear atomic susceptibility cannot be described by the simple perturbative expansion (2.22). This is due to the fact that close to resonance the quantities entering the calculation of the susceptibilities (e.g., the oscillator strengths) on the right hand side of Eq. (2.22) depend strongly on the laser intensity themselves.

Calculations of atomic properties at the third harmonic frequency similar to ours have been performed for atomic helium: Van Enk *et al.* [75] have studied possible schemes of enhancing the third-order nonlinear susceptibility $\chi^{(3)}(-3\omega; \omega, \omega, \omega)$ within the framework of perturbation theory via double resonances (involving an autoionizing state). The dressed linear atomic susceptibility has been studied using a nonperturbative approach by Cormier and Lambropoulos [55], who used a single active electron (pseudo-potential) model for helium and solved the corresponding TDSE.

2.3 Two-colour ionization rate

The harmonic fields generated in the medium might be strong enough to modify the ionization process induced by the strong fundamental. Two-colour multiphoton ionization of hydrogen by an intense laser field and its third harmonic has been thoroughly discussed in Refs. [178, 179] for various wavelengths of the fundamental field and in the following similar results will be presented for $\lambda = 355$ nm. It is

Table 2.1: Ionization rate $\Gamma_{2c} = -2\mathrm{Im}\mathcal{E}$ (in a.u.) for a two-colour calculation as a function of the ratio $\xi = I_3/I_1$ of the intensities of the harmonic and fundamental field, respectively. Three values for the phase, $\phi = 0°, 90°, 180°$ and four values for the laser field intensity, $I_L = 1 \times 10^{12}, 5 \times 10^{12}, 1.15 \times 10^{13}, 3 \times 10^{13}$ W/cm^2 have been considered. The numbers in parenthesis indicate powers of ten.

	$\frac{I_3}{I_1} = 0$	$\frac{I_3}{I_1} = 10^{-5}$	$\frac{I_3}{I_1} = 10^{-4}$	$\frac{I_3}{I_1} = 10^{-3}$
$I_1 = 1 \times 10^{12}$ W/cm^2				
$\phi = 0°$	9.36(-11)	5.04(-10)	2.56(-09)	1.95(-08)
$\phi = 90°$	9.36(-11)	2.64(-10)	1.79(-09)	1.71(-08)
$\phi = 180°$	9.36(-11)	2.20(-11)	1.03(-09)	1.47(-08)
$I_1 = 5 \times 10^{12}$ W/cm^2				
$\phi = 0°$	1.21(-7)	2.06(-7)	4.66(-7)	1.99(-6)
$\phi = 90°$	1.21(-7)	1.33(-7)	2.36(-7)	1.26(-6)
$\phi = 180°$	1.21(-7)	5.94(-8)	4.32(-9)	5.34(-7)
$I_1 = 1.15 \times 10^{13}$ W/cm^2				
$\phi = 0°$	8.58(-6)	1.15(-5)	1.96(-5)	5.92(-5)
$\phi = 90°$	8.58(-6)	8.80(-6)	1.08(-5)	3.12(-5)
$\phi = 180°$	8.58(-6)	6.04(-6)	2.08(-6)	3.48(-6)
$I_1 = 3 \times 10^{13}$ W/cm^2				
$\phi = 0°$	1.08(-5)	1.25(-5)	1.68(-5)	3.54(-5)
$\phi = 90°$	1.08(-5)	1.09(-5)	1.17(-5)	1.93(-5)
$\phi = 180°$	1.08(-5)	9.30(-6)	6.58(-6)	3.14(-6)

important to assess the impact of the harmonic field on the ionization rate as the far-field method used in the work for calculating the propagation of the harmonics does not yield the harmonic fields inside the medium. Table 2.1 shows the two-colour ionization rates for various laser intensities I_1, ratios $\xi = I_3/I_1$ and phases ϕ.[5] It is apparent from those results that the single-colour ionization rate is strongly influenced by the harmonic field. The ionization rate obtained considering the fundamental field alone is lower in most of the cases compared to the corresponding two-colour rate. This is particularly severe for small values of ϕ, whereas for values $\phi \approx 180°$ the two-colour rate can be smaller than the single-colour rate [180].

To assess more accurately the influence of the harmonic field on the ionization process, we compute in the following the ionization probability at the end of a laser

[5] We have set $\varphi = 0$ in those calculations. In fact, it can be shown that for the calculation of the time-independent two-colour ionization rate, φ and ϕ may be replaced by $\tilde{\varphi} = 0$ and $\tilde{\phi} = \phi - q\varphi$, respectively [179]. For the simplicity of notation we will continue to use ϕ.

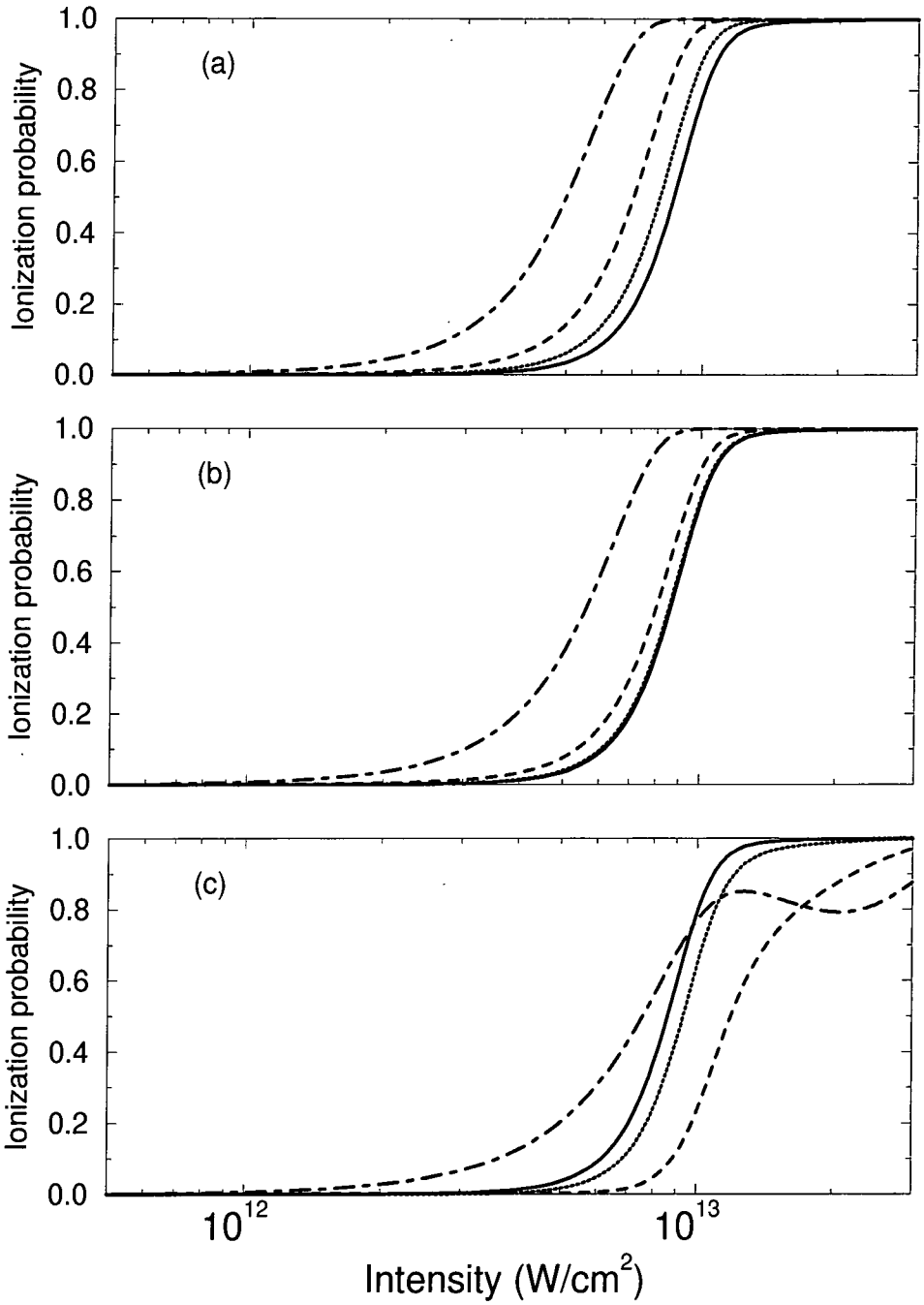

Figure 2.5: From top to bottom: ionization probabilities for (a) $\phi = 0°$, (b) $\phi = 90°$ and (c) $\phi = 180°$ as obtained from Eq. (2.26). The solid lines show the one-colour calculation for a 355-nm field. Results for the two-colour calculations are shown by dotted lines ($\xi = 10^{-5}$), dashed lines ($\xi = 10^{-4}$) and dot-dashed lines ($\xi = 10^{-3}$).

pulse, defined by

$$f_{\rm ion}(I_1,\xi) = 1 - \exp\left\{-\int_{-\infty}^{+\infty} \Gamma_\xi[I_1 \exp(-4\ln 2t^2/\tau^2)]{\rm d}t\right\}, \qquad (2.26)$$

where I_1 is the laser (peak) intensity at the position of the atom and τ is the pulse-length defined as the FWHM of the temporal intensity profile, which we assume to be Gaussian. We will take $\tau = 15$ ps in the following. The period of the fundamental being $T \approx 1.2$ fs, the pulse thus contains over 12,500 cycles within the FWHM of the intensity envelope. For such a large number of cycles, the Floquet calculation using a single dressed state (namely the dressed 1s ground state) can be shown to be in very good agreement with time-dependent methods even at resonance [182]. This, because all the population that is resonantly transferred to the dressed 2p state is rapidly ionized and contributions from this state are therefore negligible. Results are shown in Fig. 2.5, for the same phases ϕ and the same ratios ξ than in Table 2.1. Clearly it is the resonance which is responsible for the strong influence of the harmonic on the ionization process. However its influence results at the same time in a very rapid increase of the ionization probability in a narrow range of intensities, thus limiting the range of variation of the ionization probability. The single- and two-colour ionization probabilities start to differ significantly for conversion efficiencies larger than $10^{-5} - 10^{-4}$. For $\phi = 0°$ and 90° the single-colour calculation underestimates the ionization probability (Fig. 2.5a and b), while it essentially overestimates it for $\phi = 180°$ (Fig. 2.5c). The behaviour of the curve for $\xi = 10^{-3}$ in (Fig. 2.5c) comes from the fact, that the two-colour ionization rate is significantly higher than the single-colour rate below the resonance but lower at and beyond the resonance (see Table 2.1).

2.4 Higher harmonic orders

In this section, we shall give a brief overview of the atomic properties for the harmonic orders q =5, 7, and 9. As the fifth harmonic is already above the ionization threshold ($5\hbar\omega \approx 17.5$ eV $> I_p = 13.6$ eV) we expect quite generally the linear atomic susceptibilities for $q > 3$ not to be affected by any resonance structure, in

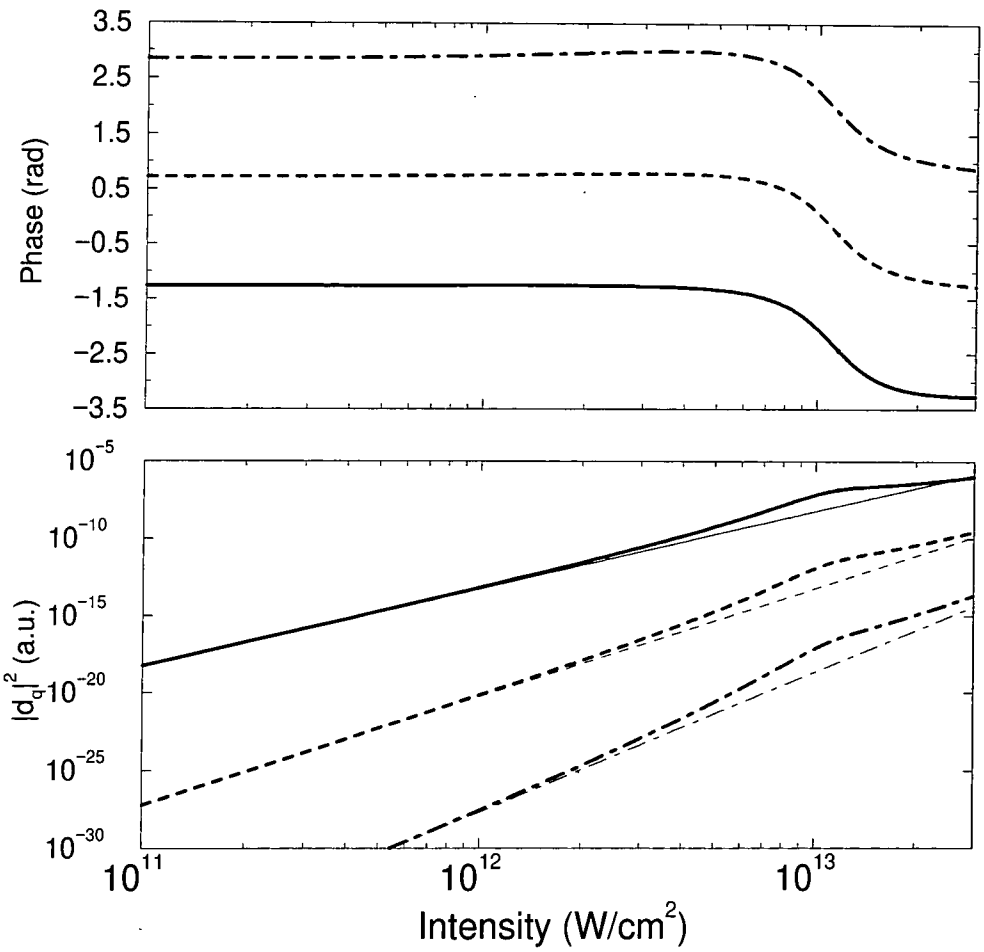

Figure 2.6: Atomic dipole moments of the 5^{th} (solid lines), 7^{th} (dashed lines) and the 9^{th} (dot-dashed lines) harmonics of 355-nm radiation. Top: Phase of the atomic dipole moments. Bottom: Modulus square of the atomic dipole moments, the thin lines indicate the corresponding perturbative power law curves.

contrast to the dipole moments for which the 3-photon 1s-2p transition constitutes now an intermediate resonance.

This is indeed shown in Fig. 2.6, where the modulus and phase of the atomic dipole moments display a behaviour similar to those for $q = 3$. The effect of saturation after the resonance is passed becomes less pronounced as the harmonic order q increases. As expected, the atomic polarizabilities are virtually constant over the whole range of intensities, as can be seen from Fig. 2.7. The magnitude of the negative dispersion is much smaller than for $q = 3$ and decreases further with increasing harmonic order.

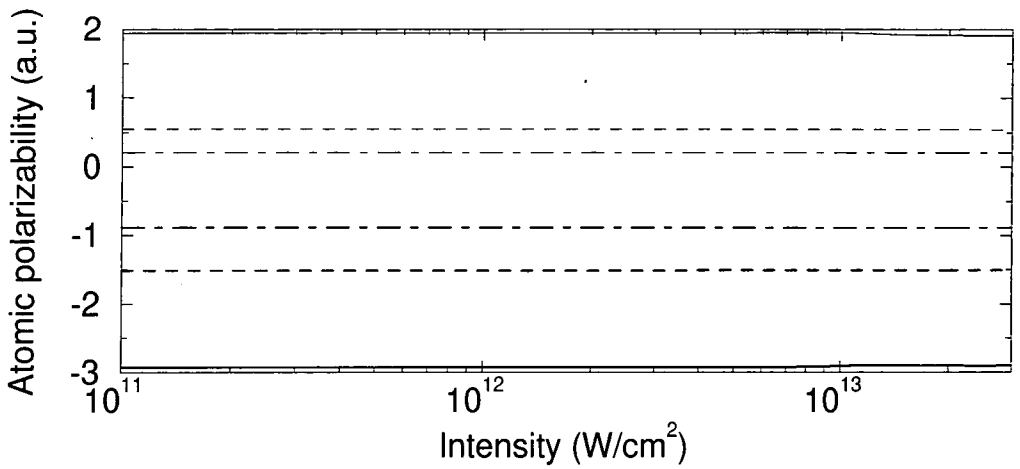

Figure 2.7: Dressed linear atomic polarizabilities at the 5^{th} (solid lines), 7^{th} (dashed lines) and the 9^{th} (dot-dashed lines) harmonic frequencies of 355-nm radiation. The thick lines represent the real part, the thin lines the imaginary part of the polarizabilities. The polarizabilities are given in a.u. and are related to the atomic susceptibilities (in SI) by a simple conversion factor, given in Appendix A.

In fact, the problem of determining the atomic properties for higher-order harmonics can be much more cumbersome if strong low-order harmonics are present, especially when resonance enhancement has to be reckoned with, as it is the case here. If the third harmonic is sufficiently strong, we expect, e.g., for the generation of the 5^{th} harmonic besides the direct term[6] $\chi^{(5)}(-5\omega;\omega,\omega,\omega,\omega,\omega)E_1^5$ also the term $\chi^{(3)}(-5\omega;3\omega,\omega,\omega)E_1^2E_3$ to contribute. Similarly, the propagation of the 5^{th} harmonic will not only involve the terms $\chi^{(1)}(-5\omega;5\omega)$ and $\chi^{(3)}(-5\omega;5\omega,-\omega,\omega)E_1^2$ but also $\chi^{(3)}(-5\omega;5\omega,-3\omega,3\omega)E_3^2$ and $\chi^{(5)}(-5\omega;5\omega,-3\omega,\omega,\omega,\omega)E_1^3E_3$, etc. Even a higher harmonic order can contribute if resonantly enhanced or well phase-matched, recall also that harmonics in the plateau region of the harmonic spectrum are generated at roughly equal strengths. Hence, e.g., the 7^{th} harmonic could contribute to the generation of the 5^{th} harmonic via the term $\chi^{(3)}(-5\omega;7\omega,-\omega,-\omega)E_1^2E_7$.

In the case of a very strong third harmonic, the quantities above have to be computed nonperturbatively, that is $d_5(E_1,E_3)$ for the dipole moment and $\chi(5\omega,E_1,E_3)$ for the linear atomic susceptibility dressed by both the fundamental and the third harmonic fields. In the following we have computed $|d_{5,7,9}(I_1,I_3)|^2$ for $I_1 = 10^{13}$

[6]For the sake of clarity we have omitted all phases in the following.

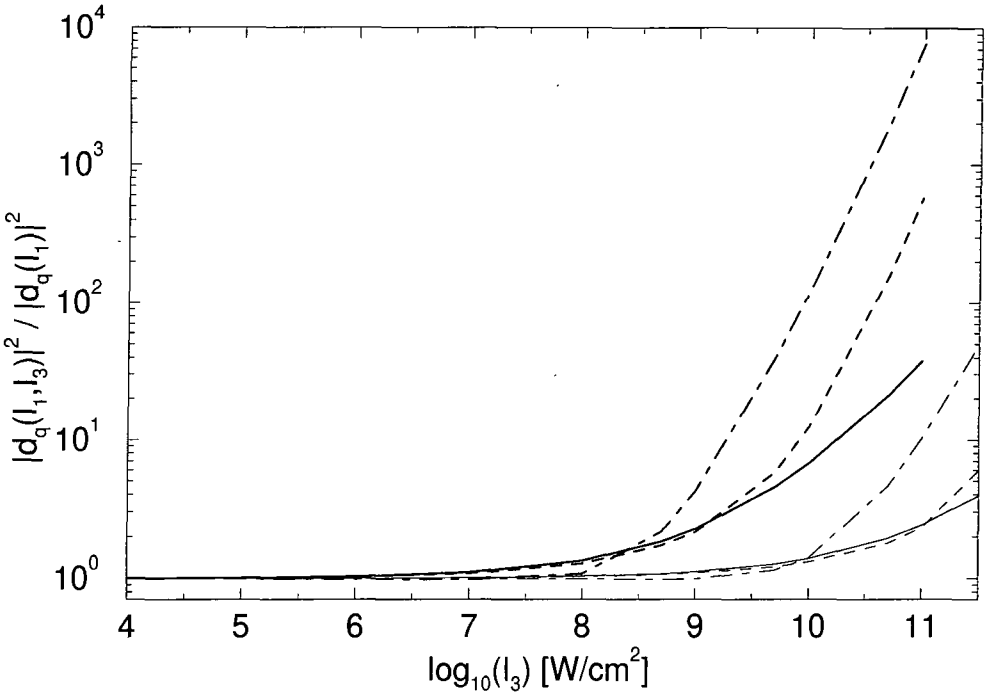

Figure 2.8: Modulus square of the atomic dipole moments for the harmonic orders $q = 5$ (solid lines), $q = 7$ (dashed lines) and $q = 9$ (dot-dashed lines) versus the intensity of the third harmonic: comparison between single- and two-colour calculation, for two values of the intensity of the incident laser field, $I_1 = 1 \times 10^{13}$ W/cm^2 (thick lines) and $I_1 = 3 \times 10^{13}$ W/cm^2 (thin lines).

W/cm^2 and $I_1 = 3 \times 10^{13}$ W/cm^2 , and a range of intensities for the third harmonic up to $I_3 \approx 10^{-2} I_1$. The calculations thus assume implicitly that none of the harmonics $q = 5, 7$ and 9 is affected by the others. The result of this calculation is shown in Fig. 2.8. The deviation of the two-colour results from the single-colour results is very marked for I_1 close to the resonance intensity (thick lines), but much less pronounced away from it (thin lines), and the magnitude of the enhancement increases with harmonic order. It would be interesting to investigate the effect of the enhanced dipole moments of the higher harmonics on the conversion efficiency but the calculation of the corresponding linear atomic susceptibilities necessitates a nonperturbative three-colour code. The phase relationship between the fundamental and the third harmonic would also have to be addressed. In the following, wave mixing processes will be neglected. Close to resonance and at high intensities, we will only consider third-order harmonic generation. We will point out wave mixing effects whenever required in connection with calculations done in this thesis.

Chapter 3

Bessel-Gauss Beams

3.1 Introduction

The output of a laser, generating a TEM_{00} mode, is generally well described by a Gaussian beam of order zero, and, in the limit of a large confocal parameter, a description of the beam in terms of plane waves is sufficient for most applications. Consequently the vast majority of all investigations of laser-matter interactions until the late 1980's have used Gaussian or plane wave amplitudes to describe the electrical field of the laser beam.

In 1987 a new type of beam, solution to the homogenous Helmholtz equation, was introduced by Durnin [68] and, soon afterwards, realized experimentally [69]. This beam has become known as *Bessel beam* owing to its transverse structure which is given by a Bessel function of the first kind and of order zero (J_0) in this particular case. We will describe its properties in greater detail later when introducing the Bessel-Gauss beam. Indeed, both the Bessel and the Gaussian beam will then simply emerge as special cases of the Bessel-Gauss beam.

The Bessel beam introduces two very important features compared to the Gaussian beam: first, it is a diffraction-free beam in the sense that its intensity profile does not dependent on the coordinate in propagation direction, but only on the transverse coordinate. Second, its momentum (wavenumber) has both a longitudinal and a

radial component. It is easy to imagine that this is likely to be of utmost interest in all cases, where this type of beam is used to generate secondary radiation in wave mixing processes where phase-matching is not limited to one dimension (that is, the propagation direction).

For a long time research into the applications of Bessel beams had focused essentially on the nondiffracting aspect, concentrating on various experimental realizations and investigating about the length of diffraction-free propagation that could be achieved, and how the Bessel beam did compare to a Gaussian beam with respect to power-transport efficiency [70]. In the original experiment by Durnin and co-workers [69] the Bessel beam was created by placing a thin circular slit in the focal plane of a lens while in Ref. [102] a confocal resonator with an annular active medium was used. Other methods for obtaining (near) diffraction-free beams include the development of an algorithm suitable for designing transmission filters yielding the desired beam structure [194], the use of axicons (to be discussed later) or spherical lenses showing aberration [94], holographic methods [57, 133, 195, 223], the use of Fabry-Pérot interferometers [58, 98] and periodic gratings with circular symmetry [152, 222]. Higher-order Bessel beams have also been created to optimize applications in optical metronomy (e.g., precision alignment over long distances). Indeed, rather than using the bright central spot of a zero-order Bessel beam it was suggested that greater accuracy could be achieved by using the narrower dark central spot of a higher order beam (recall $J_n(0) = \delta_{n0}$). In Ref. [61] such beams have been created using magneto-optic spatial light modulators. It is worth pointing out that the latter study, besides the usual intensity profile measurements, also includes the measurement of the phase of these beams. Usually, if the interest lies in a long diffraction-free zone, apodization of the beam has to be considered. Indeed, though all methods mentioned earlier generate the transverse Bessel profile to some extent, the axial intensity exhibits generally oscillations which have to be smoothed out [31, 59, 95, 104]. In Appendix D, we will report in some detail on yet another simple method by which we have experimentally generated a Bessel type beam.

Bessel beam generators can also be classified according to their efficiency. The loss of incident energy is quite severe in the set-up of Ref. [69] (see above), while the

efficiency of holograms depends on the specific type considered, e.g., around 40 % efficiency for the hologram used in Ref. [133]. The most straightforward and most efficient optical element to generate a Bessel beam, perhaps, is the conical lens, or axicon [94]. The term axicon designates generally every optical element which produces a focal line rather than a focal point[1]. A serious disadvantage of the axicon lies in the difficulty of manufacturing a conically shaped lens of suitable optical quality and explains why axicons are hardly available commercially. The literature abounds with reports on research on axicon design and we refer the interested reader to Refs. [209, 210] and references therein. Fig. 3.1 shows how a conical lens works in principle, the light rays having been drawn according to the laws of geometrical optics. If γ is the base angle of the lens and α is the angle at which the rays

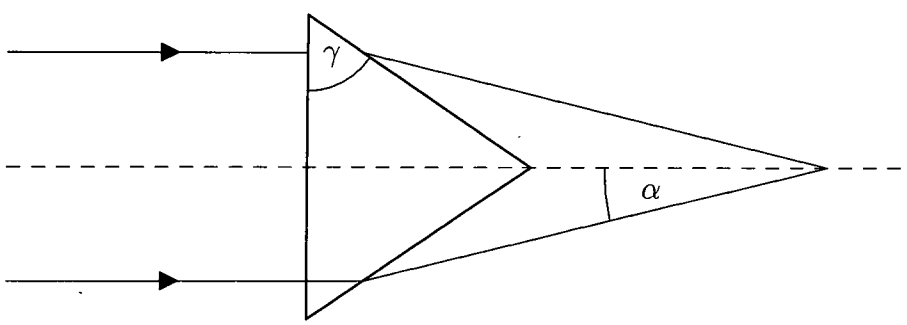

Figure 3.1: Simplified geometric illustration of the optical path through a conical lens (from Ref. [94]).

emerging from the lens intersect the propagation direction, then by Snell's law,

$$\sin(\gamma + \alpha) = n \sin\gamma\,, \tag{3.1}$$

where n is the refractive index of the lens. For small angles α, we obtain from Eq. (3.1) approximately

$$\alpha = (n-1)\tan\gamma\,. \tag{3.2}$$

[1]More specifically, an axicon which transforms a point source into a line focus is called a lensacon [112].

It is easy to see how the Bessel profile is generated in this way. We can decompose the wavenumber of the incident plane wave $\exp(i\boldsymbol{k}\cdot\mathbf{x})$ as

$$\boldsymbol{k}\cdot\mathbf{x} = k_\perp \rho\cos(\phi_k - \phi) + k_\parallel z\,, \tag{3.3}$$

where $\boldsymbol{k} = (k_\perp, k_\parallel, \phi_k)$ and $\mathbf{x} = (\rho, z, \phi)$ are cylindrical coordinates, and

$$k_\perp = k\,\sin\alpha\,, \qquad k_\parallel = k\,\cos\alpha\,, \qquad k_\parallel^2 + k_\perp^2 = \boldsymbol{k}^2 = k^2\,. \tag{3.4}$$

We thus get, by adding up all the amplitudes, that is by integrating over the azimuthal symmetry of the emerging wavevectors lying on the surface of a cone of half-opening angle α,

$$\frac{\exp(ikz\cos\alpha)}{2\pi}\int_0^{2\pi} d\phi\,\exp[ik\rho\sin\alpha\cos(\phi_k-\phi)] = J_0\left(k\rho\sin\alpha\right)\exp(ikz\cos\alpha)\,. \tag{3.5}$$

This is the azimuthally symmetric zero-order Bessel beam. We have not yet discussed the polarization of the scalar amplitude obtained so far and we will come back to this aspect in some detail in section 3.5. We shall henceforth call α the conical half-angle of the beam, or - if there is no confusion possible - the *Bessel angle* for simplicity. It is apparent from Eq. (3.5), that $k\cos\alpha$ is the longitudinal component of the beam's wavevector $\boldsymbol{k}$, while $k\sin\alpha$ is expected to be the transverse component. This can be confirmed by computing the Fourier transform

$$F(\boldsymbol{K}) = \frac{1}{(2\pi)^3}\int \mathrm{d}\mathbf{x}\,J_0\left(k\rho\sin\alpha\right)\exp(ikz\cos\alpha)\exp(-i\boldsymbol{K}\cdot\mathbf{x})\,, \tag{3.6}$$

which, with the help of Bessel function closure relation [10],

$$\int_0^{+\infty}\rho\,\mathrm{d}\rho\,J_0\left(A\rho\right)J_0\left(B\rho\right) = (1/B)\delta(A-B)\,, \tag{3.7}$$

is readily evaluated as

$$F(\boldsymbol{K}) = \frac{1}{2\pi}\delta(K_\parallel - k\cos\alpha)\frac{1}{K_\perp}\delta(K_\perp - k\sin\alpha)\,. \tag{3.8}$$

We also note from expression (3.5), that a pure Bessel beam, very much as the plane wave, cannot be realized in practice as it would carry an infinite amount of energy[2].

[2]This is the reason why both the Bessel and the plane wave amplitude can describe diffraction-free beams [142].

Indeed, each lobe of the J_0^2-profile contains very nearly the same amount of energy. Letting

$$S_j = \int_{\rho_j}^{\rho_{j+1}} d\rho\, \rho\, J_0^2(\rho) = \left[\rho_{j+1}^2 J_1^2(\rho_{j+1}) - \rho_j^2 J_1^2(\rho_j)\right]/2\,, \tag{3.9}$$

where ρ_j and ρ_{j+1} are two consecutive zeros of $J_0(\rho)$ (and defining $\rho_0 = 0$), we get computing the first few values,

$$S_1 = 0.779\,, \qquad S_2 = 0.985\,, \qquad S_3 = 0.995\,, \ldots\,. \tag{3.10}$$

It can be easily shown, using the asymptotic expansion of J_0 and $\rho_{j+1} - \rho_j \to \pi$, that S_j approaches unity as $j \to +\infty$. Recalling $\rho_1 = 2.405$, we find the diameter of the central spot to be given by

$$d \backsimeq \frac{2.405}{\pi \sin\alpha}\,\lambda\,. \tag{3.11}$$

To get a physically realizable Bessel beam in experiments one has to consider an apertured (or windowed) beam profile. As the laser beam incident on a Bessel beam generator typically has a Gaussian transverse profile, two possibilities appear. Either the incident, well collimated beam is truncated so as to simulate plane wave illumination, and a truncated Bessel beam is generated, or the Bessel beam is naturally cut-off in the transverse direction due to the exponentially decaying Gaussian beam profile. The latter beam is known as *Bessel-Gauss beam* [86]. In the paraxial limit, the corresponding field amplitude can be obtained by solving the well known Fresnel integral (see Appendix D),

$$E(\rho, z) = \frac{-ik}{z}\, \mathrm{e}^{i[kz + k\rho^2/2z]} \int_0^R r\, dr\, E_A(r)\, \mathrm{e}^{ikr^2/2z}\, J_0\left(kr\rho/2z\right)\,, \tag{3.12}$$

with

$$E_A(r) = E_0\, J_0\left(kr\sin\alpha\right) \exp(-kr^2/b)\,, \tag{3.13}$$

where b is the confocal parameter. The integral (3.12) can be evaluated in closed form for $R \to +\infty$ [86]. In Section 3.3 we will derive the spatial amplitude of the Bessel-Gauss beam by explicitely solving the paraxial wave equation. A comparative study investigating the long-range propagation characteristics of Bessel-Gauss, Bessel and Gaussian beams using the Fresnel integral technique for a finite aperture

R has been carried out in Ref. [154]. It emerges from this study that a Bessel-Gauss beam has less pronounced axial intensity fluctuations than the truncated Bessel beam but propagates less far than the latter. For our purposes is thus seems that a Bessel-Gauss beam is more appropriate for describing the incident laser beam than a truncated Bessel beam as we are more interested in a high beam quality over fairly short distances (of the order of the medium length).

Before discussing the role of Bessel-type beams in nonlinear optics we will mention briefly here, for completeness, other types of beams discussed in the literature. Indeed, especially since the discovery of Bessel beams, more research has been devoted to finding and describing the properties and possible applications of new beam types. For instance another very interesting type of Bessel beam is obtained when the ordinary Bessel function J_0 (*Bessel-J-beam*) is replaced by the modified Bessel function I_0 (*Bessel-I-beam*). This beam has a radially unbound profile with a minimum on axis ($\rho = 0$) hence its characteristics are strongly dependent on the windowing profile. If the latter one is chosen to be Gaussian, a closed expression can be given for the amplitude on axis [196]. Not only does this Bessel-I-Gauss beam has a slower axial decay than the Gaussian or the Bessel-J-Gauss beam, but also, for some range of the propagation parameters, has a different sign of the geometric phase, which has potentially interesting applications in nonlinear optics (wave mixing processes). *Weber beams* finally make use of the Bessel function of the second kind (or sometimes also called Weber's function), Y_0, which is unbound at the origin and has to be suitably truncated [225].

For Gaussian beams finally, besides the well known Gauss-Hermite and Gauss-Laguerre beams [207], work has been carried out on *flattened Gaussian beams* [13, 87]. It is worth noting, that second-harmonic generation with higher-order Gauss-Laguerre modes has been recently investigated by Courtial *et al.* [56]. There, the second-harmonic photons have twice the orbital angular momentum[3] of the photons of the fundamental field. This leads to interesting possibilities of manipulating microscopic targets by imparting them a large angular momentum [155].

[3]The orbital angular momentum of a photon is associated with the azimuthal component of the Poynting vector.

3.2 Bessel type beams in nonlinear optics

Compared to the application of Bessel beams mentioned above it took much longer to appreciate the possibility of using the Bessel angle as new parameter in optimizing nonlinear processes.

Early descriptions of self-modulating effects of Bessel beams were reported in the late 1980's and were aimed at investigating the creation of long, unbroken laser sparks during the breakdown of a gas (see Ref. [4] and references therein). The first generation of a harmonic by a Bessel beam was reported by Wulle and Herminghaus [231]. In their experiment, the second harmonic of 1064-nm radiation was generated in a KDP crystal and the tunability of phase-matching demonstrated by varying the Bessel angle continously. The Bessel beam was obtained with the help of a specially designed Fresnel-like zone plate. This had the advantage of generating a Bessel beam without too much loss of power as required for driving a nonlinear interaction efficiently. Very much at the same time a similar result was obtained using annular beams by Glushko *et al.* [85]. They created a wide annular beam by blocking a large part of the center of a disk-shaped shield which was then focused in a cone of half-opening angle α into a pure alkali vapor (sodium and rubidium). A large conversion efficiency into the third harmonic of 1064-nm radiation was observed and moreover a certain immunity of the harmonic yield with respect to variations of the atomic density. As pointed out in their work, momentum conservation imposes that the harmonic generated in the atomic vapor also has a conical geometry, with half-opening angle β related to the conical half-angle α by the axial phase-matching condition

$$3\,k(\omega)\cos\alpha = k(3\omega)\cos\beta \tag{3.14}$$

where $k(\omega)$ and $k(3\omega)$ are the wavenumber at the fundamental and at the third harmonic frequencies, respectively. Moreover, for the particular beam geometry considered in their experiment, conservation of the normal components of the momentum could also be achieved for values of β compatible with Eq. (3.14). In fact, the variations of the input parameters translating into variations of the refractive index (either because of the variation of pressure or because of Kerr nonlineari-

ties) could then be shown to be compensated by a varying emission angle β. They called this remarkable effect, which requires a negatively dispersive medium, *self-phase-matching*. A theory of self-phase-matching was developed soon afterwards by Tewari *et al.* [217, 218]. In this work the results of Glushko *et al.* were explained by treating the annular beam used in the experiment as a superposition of several Bessel beams with a narrow range of values for the angle α (see also section D.2) At the same time, the concept of an additional radial phase-matching condition was introduced, expressed as the required overlap of the Bessel profiles of both the fundamental and the harmonic field inside the medium.

These insights were used by Peet and Tsubin [164–166] to investigate thoroughly third harmonic generation and resonant multiphoton ionization in xenon, comparing Gaussian, Bessel and annular beams. It was found that the Bessel beam displayed a broad ionization band owing to the self-phase-matching mechanism which allowed for efficient third-harmonic generation in a large spectral range on the high-frequency side of the 6s resonance, where the medium is negatively dispersive. On the other hand, absorption was very important for the third harmonic field generated close to the resonance by the Bessel beam of large conical half-angle $\alpha = 17°$ (see also section C.3) and the intensity of the Bessel beam, focused by an axicon, was low compared to the intensity of both the Gaussian and the focused annular beam. This resulted in the impossibility of measuring the third harmonic yield outside the medium for the pure Bessel beam. The annular beam, with a range of Bessel angles around $\alpha \approx 3°$, behaved very much like the Bessel beam and its overall efficiency in frequency tripling compared very well to the Gaussian beam in similar conditions.

A recent work proposed the use of Bessel-Gauss beams for probing the nonlinear refractive index of optoelectronic materials [99]. In the so called Z-scan method a tightly focused Gaussian beam induces self-focussing effects due to the intensity dependent refractive index of the medium: namely, when scanning the sample through the focal plane, a characteristic pattern of peaks and dips in the far-field pattern is recorded which permits the inference of the characteristics of the nonlinear refractive index. The authors predicted a significantly enhanced sensitivity of this method (that is a larger ratio of the peaks with respect to the dips) when the Gaussian beam

amplitude is replaced by a Bessel-Gauss beam with a small conical half-angle α.

3.3 The spatial field amplitude

We will now turn to a brief description of the derivation of the Bessel-Gauss amplitude, solving explicitely the paraxial wave equation. We follow closely a similar calculation by Overfelt [153].

Starting from the scalar wave equation in cylindrical coordinates (ρ, z, ϕ), assuming azimuthal symmetry from the outset, we have

$$\left[\frac{1}{\rho}\frac{\partial}{\partial\rho}\left(\rho\frac{\partial}{\partial\rho}\right) + \frac{\partial^2}{\partial z^2} - \frac{1}{c^2}\frac{\partial^2}{\partial t^2}\right] E(\rho, z, t) = 0. \tag{3.15}$$

The ansatz for the solution of this equation is taken to be

$$E(\rho, z, t) = \exp[i(kz - \omega t)]\, \tilde{E}(\rho, z), \tag{3.16}$$

neglecting, as usual in the paraxial approximation, the second-order derivative of the slowly-varying envelope function $\tilde{E}(\rho, z)$ with respect to z. In this way we obtain

$$\left[\frac{1}{\rho}\frac{\partial}{\partial\rho}\left(\rho\frac{\partial}{\partial\rho}\right) + 2ik\frac{\partial}{\partial z}\right] \tilde{E}(\rho, z) = 0. \tag{3.17}$$

The ansatz for the dependence on the spatial coordinates is similar to the one for the Gaussian beam, except for an additional Bessel function. It reads

$$\tilde{E}(\rho, z) = E_{\mathrm{f}}\, J_0\left(\frac{k\rho\sin\alpha}{s(z)}\right) \exp[iP(z)] \exp\left[i\frac{k\rho^2}{2q(z)}\right]. \tag{3.18}$$

Inserting Eq. (3.18) into Eq. (3.17) and using

$$x^2 J_0''(x) + x J_0'(x) = -x^2 J_0(x), \qquad x = k\sin\alpha\rho/s(z)\,, \tag{3.19}$$

we arrive at the following equation

$$\begin{aligned}\left(\frac{k\rho}{q(z)}\right)^2 J_0(x)[q'(z) - 1] \;+\; & \frac{2ik^2\sin\alpha\rho}{s(z)} J_0'(x)\left[\frac{1}{q(z)} - \frac{s'(z)}{s(z)}\right] \\ & + \; J_0(x)\left[\frac{2ik}{q(z)} - 2kP'(z) - \left(\frac{k\sin\alpha}{s(z)}\right)^2\right] = 0\,,\end{aligned}$$

which can be satisfied by requiring the three square brackets to vanish simultaneously. It is a straightforward matter to solve the resulting equations for $s(z), q(z)$ and $P(z)$. The final result is

$$\begin{aligned}\tilde{E}(\rho,z) &= \frac{E_{\rm f}}{\sqrt{1+(2z/b)^2}} J_0\left(\frac{k\rho\sin\alpha}{1+i\,(2z/b)}\right) \\ &\times \exp\left[-\frac{k\rho^2/b}{1+i\,(2z/b)} - \frac{ikz\sin^2\alpha/2}{1+i\,(2z/b)} - i\tan^{-1}(2z/b)\right]. \end{aligned} \tag{3.20}$$

Here, we have introduced the confocal parameter[4] b, making use of the integration constants by requiring the amplitude in the focal plane $z = 0$ to be given by

$$\tilde{E}(\rho, z=0) = E_{\rm f} J_0(k\rho\sin\alpha)\exp[-(\rho/w_0)^2], \tag{3.21}$$

where $w_0 = \sqrt{b/k}$ is the beam waist. $E_{\rm f}$, consequently, is the focal field-strength. It is more convenient, though, to separate more clearly phase and amplitude of the Bessel-Gauss beam and we rewrite Eq. (3.20), including the travelling plane wave part from Eq. (3.16), as

$$\begin{aligned}E_{\rm BG}(\rho,z) &= E_{\rm f}[1+(2z/b)^2]^{-1/2} J_0\left(\frac{k\rho\sin\alpha}{1+i\,(2z/b)}\right) \\ &\times \exp\left\{-k(\rho^2+z^2\sin^2\alpha)/b[1+(2z/b)^2]\right\} \\ &\times \exp\left\{i\left[kz(1-\sin^2\alpha/2) - \tan^{-1}(2z/b)\right]\right\} \\ &\times \exp\left\{ik\,(2z/b)\,(\rho^2+z^2\sin^2\alpha)/b[1+(2z/b)^2]\right\}. \end{aligned} \tag{3.22}$$

While the radial distribution in the focal plane, as given by Eq. (3.21), is simply a damped Bessel profile, the amplitude for $z \gg b/2$ is essentially a Gaussian function located about $\rho = z\sin\alpha$:

$$\begin{aligned}E_{\rm BG}(\rho \gg 2z/kb\sin\alpha, z \gg b/2) &\sim -i\frac{E_{\rm f}}{\sqrt{2\pi(2z/b)k\rho\sin\alpha}} \\ \times \exp\left\{-\left[\frac{kb}{4z^2}(\rho - z\sin\alpha)^2\right]\right. &+ \left. i\left[kz\left(1+\frac{\rho^2}{2z^2}\right)\right]\right\}. \end{aligned} \tag{3.23}$$

That is, in the far-field zone the beam propagates along the surface of a cone of half-opening angle α.

[4] $L_r = b/2$ is also known as Rayleigh length.

E_{BG} reduces to the electric field amplitude of a pure Gaussian beam,

$$E_{\mathrm{G}}(\rho,z) = \frac{E_{\mathrm{f}}}{\sqrt{1+(2z/b)^2}} \exp\left(-\frac{k\rho^2/b}{1+(2z/b)^2}\right) \times \exp\left\{i\left[kz-\tan^{-1}(2z/b)+(2z/b)\frac{k\rho^2/b}{1+(2z/b)^2}\right]\right\}, \quad (3.24)$$

for $\alpha \to 0$, and to the electric field amplitude of a pure Bessel beam,

$$E_{\mathrm{B}}(\rho,z) = E_{\mathrm{f}}\, J_0(k\rho\sin\alpha)\, \exp(ikz\cos\alpha), \quad (3.25)$$

in the loose-focusing limit ($b \to +\infty$) provided $\cos\alpha \approx 1-\sin^2\alpha/2$, which is valid for small angles α up to fourth order in α.[5] This difference can be traced back to the paraxial approximation - while the Bessel-Gauss beam is a solution to the paraxial wave equation, the pure Bessel beam Eq. (3.25) is an exact solution of the wave equation with no restriction on the angle α. We will assume the approximation above to hold and replace $1-\sin^2\alpha/2$ by $\cos\alpha$ in Eq. (3.22).

More general types of Bessel-Gauss beams exist, namely the *higher-order Bessel-Gauss beams*, involving the Bessel function J_n [14], the *modified Bessel-Gauss beams*, involving the Bessel function I_n [14, 196], the *generalized Bessel-Gauss beams*, consisting of a superposition of Gaussian beams at their waist plane and having their centres on a circumference of a given radius and their mean axes lying on the surface of a cone [14], the *Super-Gaussian-Bessel beam* introduced in Ref. [105], where the windowing profile is assumed to have the form $\exp[-(\rho/w_0)^n]$, and, last but not least, vector-beam solutions, that is solutions which are not restricted to the scalar wave equation [90, 91]. We will discuss vector-beam solutions in connection with the polarization properties of Bessel-Gauss beam in section 3.5.

We will restrict ourselves to the zero-order Bessel-Gauss beam as more general Bessel-Gauss beams would be even more difficult to realize experimentally at sufficiently high intensities and there is a priori no advantage to be expected from an azimuthally asymmetric beam with respect to phase-matching.

[5] $(1-\sin^2\alpha/2)-\cos\alpha = \alpha^4/8 +$ higher orders.

3.4 Properties of Bessel-Gauss beams

We can compute the power carried by the Bessel-Gauss beam, Eq. (3.22), by integrating over the radial intensity profile. Using formula 6.633.2 of Ref. [88],

$$\int_0^{+\infty} \mathrm{d}x\, x \exp(-\sigma^2 x^2) J_0(ax) J_0(bx) = \frac{1}{2\sigma^2} \exp\left(-\frac{a^2+b^2}{4\sigma^2}\right) I_0\left(\frac{ab}{2\sigma^2}\right), \quad (3.26)$$

and $J_n(\overline{z}) = \overline{J_n(z)}$[6], a straightforward calculation leads to the z-independent expression

$$P_{\mathrm{BG}}(\alpha) = P_{\mathrm{G}} \exp\left(-\frac{b\pi \sin^2\alpha}{2\lambda}\right) I_0\left(\frac{b\pi \sin^2\alpha}{2\lambda}\right), \quad (3.27)$$

where I_0 is the modified Bessel function of order zero, and

$$P_{\mathrm{G}} = P_{\mathrm{BG}}(\alpha = 0) = \frac{b\lambda}{4} I_{\mathrm{f}} \quad (3.28)$$

is the power carried by a pure Gaussian beam of the same focal intensity. It results from Eqs. (3.27) and (3.28) that the power of a Bessel-Gauss beam with $\alpha \neq 0$ is smaller than that of a Gaussian beam of same focal intensity and confocal parameter. Moreover, taking the derivative with respect to α, is it easy to show, using the properties of modified Bessel functions [1], that $P_{\mathrm{BG}}(\alpha)$ is a strictly monotonically decreasing function of α.

Furthermore, Gaussian and Bessel-Gauss beams of same power have focal intensities and confocal parameters related by

$$I_{\mathrm{G,f}}\, b_{\mathrm{G}} = I_{\mathrm{BG,f}}\, b_{\mathrm{BG}} \exp\left(-\frac{b_{\mathrm{BG}}\pi \sin^2\alpha}{2\lambda}\right) I_0\left(\frac{b_{\mathrm{BG}}\pi \sin^2\alpha}{2\lambda}\right). \quad (3.29)$$

Therefore, a Bessel-Gauss beam has a larger confocal parameter than a Gaussian beam of same power and focal intensity, and a larger peak focal intensity than a Gaussian beam of same power and confocal parameter.

It is very interesting to compare the radial power density of a Gaussian beam and a Bessel-Gauss beam with a large confocal parameter in the focal plane, as shown in Fig. 3.2. With increasing angle α the energy of the incident beam is spread over a large number of oscillations in the Bessel function. Clearly most of the Bessel-Gauss

[6] $\overline{z}$ is the complex conjugate of z.

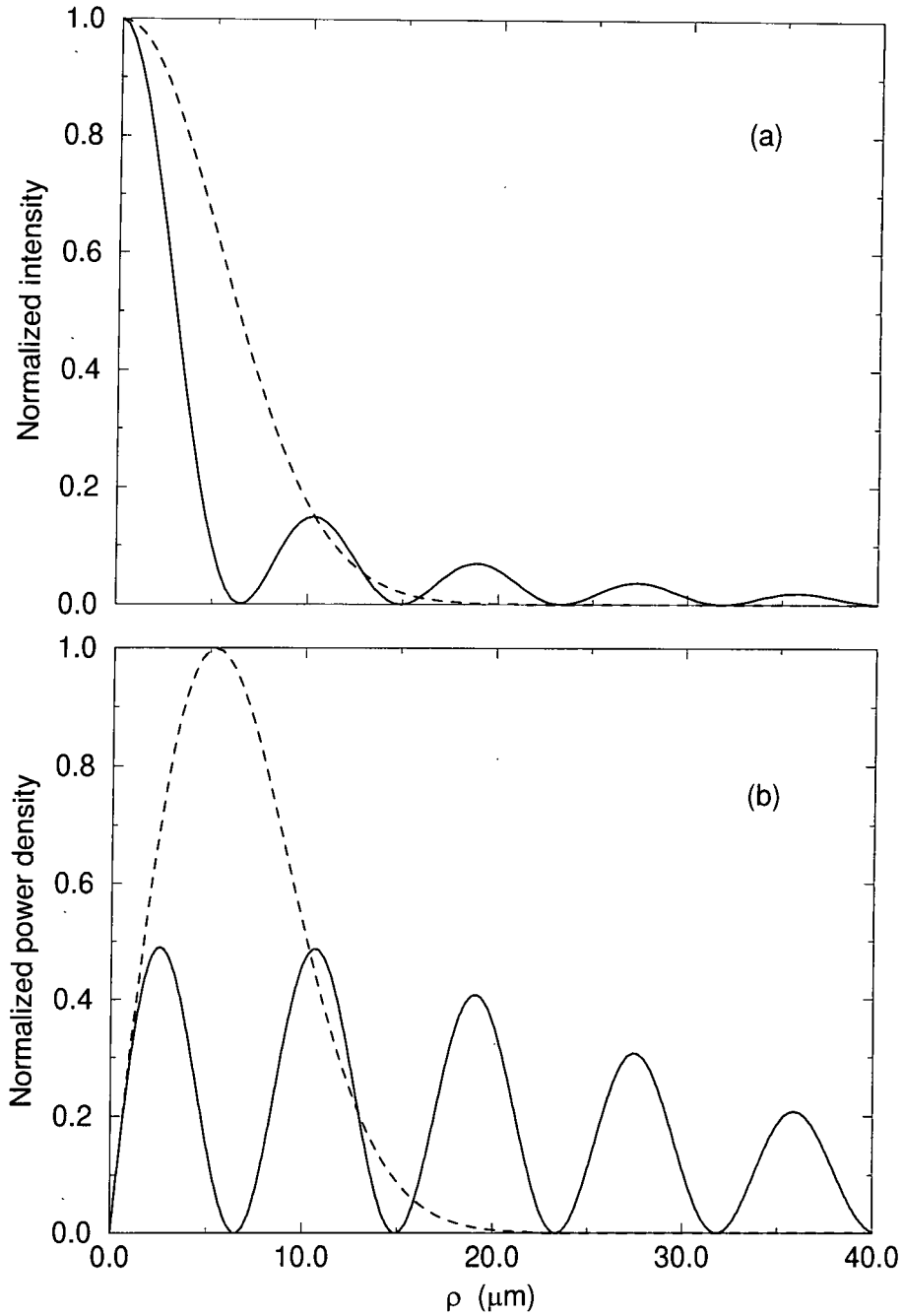

Figure 3.2: (a) Radial intensity profile, $I(z = 0, \rho)$, and (b) radial power density, $2\pi\rho I(z = 0, \rho)$, of a Gaussian beam (dashed line, $\alpha = 0°$) and a Bessel-Gauss beam (solid line, $\alpha = 1.2°$) in the focal plane. The two beams have the same focal intensity, normalized to unity on axis, and the same total power, which is given by the total area enclosed by the curves and the ρ-axis in (b). The confocal parameter of the Gaussian beam has been set to $b_{\mathrm{G}} = 2$ mm, the confocal parameter of the Bessel-Gauss beam is therefore, according to Eq. (3.29), $b_{\mathrm{BG}} = 48.7$ mm.

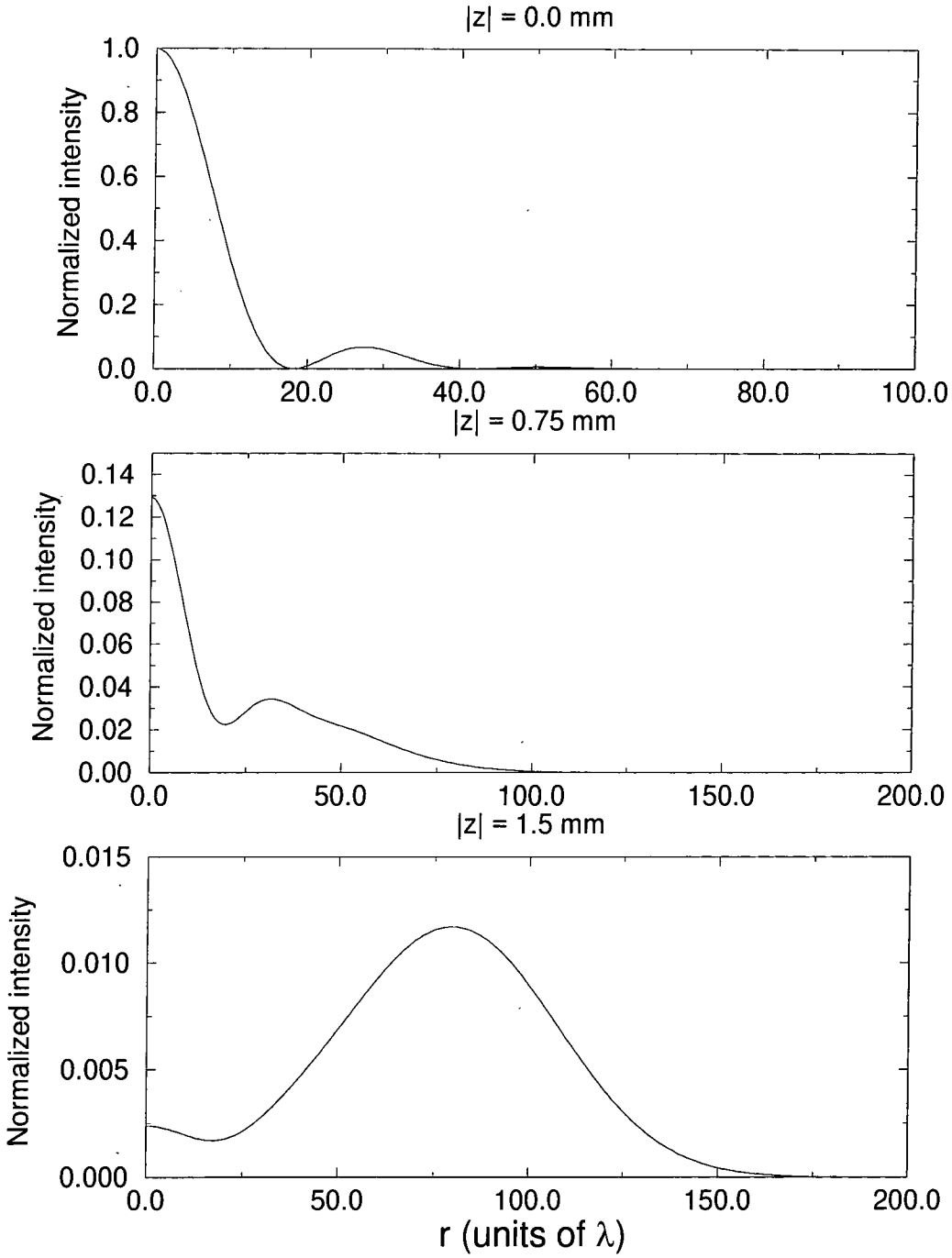

Figure 3.3: Radial intensity profile for various z-positions with $b = 4$ mm and $\alpha = 1.2°$.

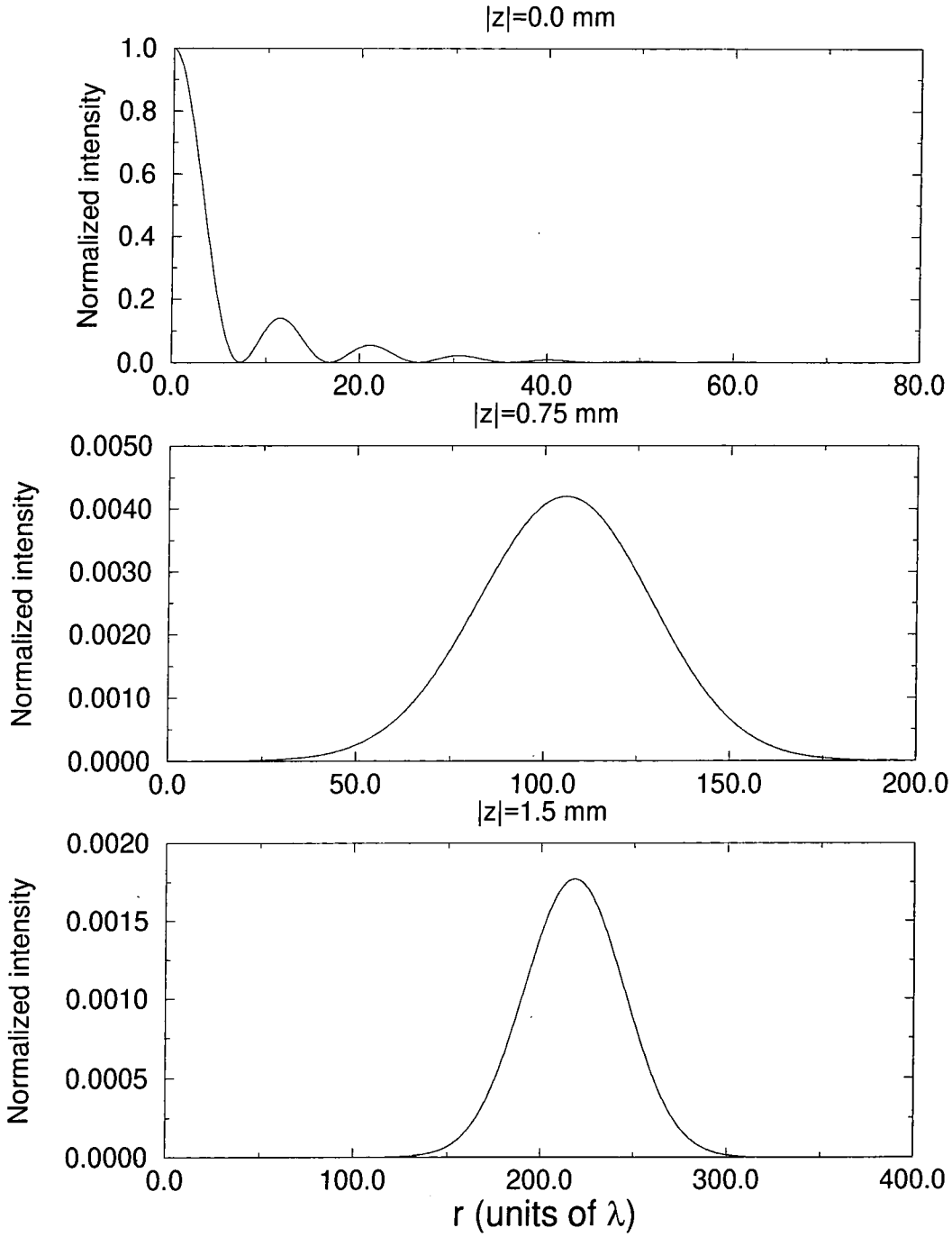

Figure 3.4: Radial intensity profile for various z-positions with $b = 4$ mm and $\alpha = 3.0°$.

beam's power is concentrated in the secondary maxima in strong contrast to the Gaussian beam, where the maximum is close to axis followed by a fast decay.

While for a values of $|z|$ small compared to b the beam shows essentially no diffraction, the transverse profile changes considerably as b becomes smaller for given $|z|$ (and α). In Figs. 3.3 and 3.4 we show the transverse intensity profile of a Bessel-Gauss beam with a confocal parameter $b = 4$ mm for various $|z|$ and α. First note, that for the same Bessel angle as in Fig. 3.2, $\alpha = 1.2°$, in Fig. 3.3 we find less secondary peaks in the focal plane $z = 0$. As $|z|$ increases slowly, the transverse intensity profile approaches quickly the far-field pattern given by Eq. (3.23). This is all the more pronounced as the Bessel angle increases, as shown in Fig. 3.4. Note further that the peak is not exactly located at $\rho = z \sin\alpha$ but slightly before due to the $\rho^{-1/2}$-dependence of the field amplitude in this limit, given by Eq. (3.23).

We conclude this section by simply relating an important quantity for the characterization of a laser beam, the M^2-factor, which characterizes the angular divergence of a beam [208]. It is defined as $M^2 = 2\pi\sigma_0\sigma_\infty$, where σ_0 and σ_∞ are the second-order moments associated with the intensity distribution of the beam at focus and in the far-field, respectively. A closed expression can be obtained for the Bessel-Gauss beam of order n [30], the value for $n = 0$ is

$$M^2 = \sqrt{\left[1 + \gamma \frac{I_1(\gamma)}{I_0(\gamma)}\right]^2 - \gamma^2} \geq 1\,, \tag{3.30}$$

where $\gamma = b\pi \sin^2\alpha/2\lambda$ as in Eq. (3.27). In the Gaussian limit, $\alpha = 0°$, one recovers the well known result $M^2 = 1$. M^2 is continuously increasing with γ and thus with growing confocal parameter and/or Bessel angle and with decreasing wavelength. Recalling the far-field profile (large $|z|$) of the Bessel-Gauss beam from Figs. 3.3 and 3.4, the increase of M^2 is easily understandable. As far as applications of Bessel-Gauss beams in nonlinear optics are concerned, we will see that this feature turns out to be an additional advantage as it will allow to separate spatially the harmonic field from the incident laser field in the far-field region, due to their respectively different cone angles.

3.5 Polarization of the Bessel-Gauss beam

So far we have tacitly assumed that the Bessel-Gauss beams discussed in the previous sections may have any given state of polarization. In fact, it appears that such beams are not divergence-free, that is, they are not solutions of the full set of Maxwell equations. For the Bessel-Gauss beam this had to be expected as it is a well known feature of paraxial solutions of the wave equation [122], such as the Gaussian beam family. In Ref. [122] a power expansion of the Maxwell equations was carried out in terms of λ/b and the Gaussian beam family found to be divergence-free to zeroth order. The same result was obtained for Bessel-Gauss beams in Ref. [91]. It is less obvious that this difficulty should also arise for pure Bessel beams, as they are full solutions of the scalar wave equation. Yet, the reason for this is simple - the vanishing of the divergence remains always an additional constraint on the solutions of the scalar wave equation, though it is used in deriving it.

We are going to investigate this aspect in some detail in the following. Assuming a harmonic time-dependence of the fields, we may, because of the linearity of the Maxwell equations, seek solutions of the form

$$\boldsymbol{E} = \boldsymbol{E}_{\mathrm{S1}}\cos(\omega t) + \boldsymbol{E}_{\mathrm{S2}}\sin(\omega t) = \mathrm{Re}\{2\boldsymbol{E}_{\mathrm{S}}\exp(-i\omega t)\} \tag{3.31}$$

$$\boldsymbol{B} = \boldsymbol{B}_{\mathrm{S1}}\cos(\omega t) + \boldsymbol{B}_{\mathrm{S2}}\sin(\omega t) = \mathrm{Re}\{2\boldsymbol{B}_{\mathrm{S}}\exp(-i\omega t)\} \tag{3.32}$$

where the complex space-dependent amplitudes $\boldsymbol{E}_{\mathrm{S}}$ and $\boldsymbol{B}_{\mathrm{S}}$ are solution of the free-space Maxwell equations

$$\nabla\cdot\boldsymbol{E}_{\mathrm{S}} = 0 \quad (3.33) \qquad \nabla\times\boldsymbol{E}_{\mathrm{S}} = i\omega\boldsymbol{B}_{\mathrm{S}} \quad (3.35)$$

$$\nabla\cdot\boldsymbol{B}_{\mathrm{S}} = 0 \quad (3.34) \qquad \nabla\times\boldsymbol{B}_{\mathrm{S}} = -i(\omega/c^2)\boldsymbol{E}_{\mathrm{S}} \quad (3.36)$$

Deriving the wave equation in the usual way, we obtain the following equivalent set of equations

$$[\nabla^2 + (\omega/c)^2]\boldsymbol{E}_{\mathrm{S}} = 0 \tag{3.37}$$

$$\boldsymbol{B}_{\mathrm{S}} = -i(1/\omega)\nabla\times\boldsymbol{E}_{\mathrm{S}} \tag{3.38}$$

$$\nabla\cdot\boldsymbol{E}_{\mathrm{S}} = 0\,. \tag{3.39}$$

The amplitude Eq. (3.25) for the Bessel beam amplitude can be recovered, provided $\boldsymbol{E}_{\rm S} = E_{\rm S}\hat{\boldsymbol{e}}$ with some space-independent (unit) vector $\hat{e}$. However, because of Eq. (3.39), $\hat{\boldsymbol{e}} \cdot \nabla E_{\rm S} = 0$ is required, which, after a quick glance at Eq. (3.25), obviously does not hold if $\alpha > 0°$. Based on this observation, Mishra [144] showed that it was possible to construct a diffraction-free Bessel beam solution of the Maxwell equations with predominantly linear polarization in a given direction.

More generally, this problem can be avoided by recombining Eqs. (3.37) and (3.39) into

$$\nabla \times \nabla \times \boldsymbol{E}_{\rm S} - (\omega/c)^2 \boldsymbol{E}_{\rm S} = 0\,, \tag{3.40}$$

which is called the vector wave or vector Helmholtz equation, the solutions of which are automatically divergence-free. The general expression for vector Bessel beam solutions of Eq. (3.40) has been given by Bouchal and Olivik [32]. We will rederive the result for linear polarization independently in a simple way by making use of the Bessel beam solution of the scalar wave equation. For this, we note that, letting $k = \omega/c$,

$$\boldsymbol{E}_{\rm S} = \frac{E_0}{2\pi} \int_{u_1}^{u_2} du\, \boldsymbol{A}(u)\, \exp\{ik[xa(u)\sin\alpha + yb(u)\sin\alpha + z\cos\alpha]\} \tag{3.41}$$

is a solution of Eq. (3.37), provided $a^2(u)+b^2(u) = 1$, $u \in [u_1, u_2]$. We specialize here to $u_1 = 0, u_2 = 2\pi$ and $a(u) = -\cos u, b(u) = -\sin u$. Taking the gradient of the exponential leads to $\boldsymbol{k} = k(-\sin\alpha\cos u, -\sin\alpha\sin u, \cos\alpha)$. Hence, for the solution to be divergence-free it is sufficient to find $\boldsymbol{A}(u)$ such that $\boldsymbol{A}(u) \cdot \boldsymbol{k} = 0$ everywhere, which is readily achieved using $\boldsymbol{A}(u) = (1, 0, \tan\alpha\cos u)$. The integral Eq. (3.41) can be solved in closed form and yields, using cylindrical coordinates $x = \rho\cos\phi$, $y = \rho\sin\phi$,

$$E_{S,x} = E_0\, J_0(k\rho\sin\alpha)\, \exp(ikz\cos\alpha) \tag{3.42}$$

$$E_{S,z} = E_0\, (-i)\, \cos\phi\, \tan\alpha\, J_1(k\rho\sin\alpha)\, \exp(ikz\cos\alpha)\,, \tag{3.43}$$

which is identical to the corresponding solution given in Ref. [32]. Clearly, for not too large values of the angle α, we find that describing a linearily polarized Bessel beam using $E_{S,x}$ only, as in Eq. (3.25), is a good approximation. A different but

related matter is how well the solution Eqs. (3.42)-(3.43) can actually be realized experimentally. The authors of Ref. [32] did investigate the tranformation of a linearily polarized plane wave by a linear axicon and found that the beam structure obtained is in good agreement with the one obtained Eqs. (3.42)-(3.43) only if the beam's central spot is much larger than the wavelength. Again, as can be seen from Eq. (3.11), this is tantamount to requiring a reasonably small angle α. The reason for this restriction can be easily explained using our method introduced above. Indeed to simulate a linear axicon we have to require additionally $\boldsymbol{A}(u)$ to be normalized to unity (so as to have a genuine unit vector describing polarization), that is $\boldsymbol{A}(u) = (\cos^2\alpha + \sin^2\alpha\,\cos^2 u)^{-1/2}\,(\cos\alpha, 0, \sin\alpha\cos u)$. This leads of course to yet another divergence-free solution of the scalar wave equation but it reduces to Eqs. (3.42)-(3.43) only in the limit of small α. No closed form of the integral can be given in this case.

We will not pursue these investigations any further within the framework of this thesis but expressedly note as a conclusion from the study above that it is sensible to talk about a linearily polarized Bessel-Gauss beam, the expression for the field amplitude as given in section 3.3, provided the conical half-angle α is not too large. Research into the properties of large-α Bessel beams is currently in progress [167].

3.6 Pulsed beams

If a pulsed beam needs to be described, one can make use of the superposition principle to generate the desired temporal pulse shape. The monochromatic solution of the wave equation is thereby weighted with a frequency spectrum $g(\omega)$,

$$E_{\mathrm{B}}(\rho, z, t) = \int_{-\infty}^{+\infty} \mathrm{d}\omega\, g(\omega)\,[E_f J_0\,(k\rho\sin\alpha)\exp(kz\cos\alpha - \omega t)]\,, \tag{3.44}$$

centered as some carrier frequency ω_0. In Eq. (3.44) we have taken for simplicity the pure Bessel beam of Eq. (3.25). We assume the distribution $g(\omega)$ to be Gaussian,

$$g(\omega) = \frac{\tau}{2\sqrt{2\pi\ln 2}}\,\exp\left[-\frac{(\omega-\omega_0)^2\tau^2}{8\ln 2}\right], \tag{3.45}$$

the prefactor being chosen in such a way as to normalize the integral of $g(\omega)$ to unity. A straightforward calculation then leads to

$$E_{\rm B}(\rho,z,t) = \frac{E_f}{2\pi}\exp[i(k_0 z\cos\alpha-\omega_0 t)\int_0^{2\pi}\mathrm{d}\phi\,\exp(ik_0\sin\alpha\cos\phi) \times \exp\left[-2\ln 2\left(\frac{\rho\sin\alpha\cos\phi+z\cos\alpha}{c\tau}-\frac{t}{\tau}\right)^2\right]. \quad (3.46)$$

In the latter expression, one recognizes the pulselength τ as defined in section 2.3. Clearly, provided $\rho\sin\alpha/(c\tau)\ll 1$, the distortion of the pulse shape due to this term is negligible. This will be the case in all subsequent calculations. Indeed, recalling from the figures in this chapter that $\rho\lesssim 100$ microns and typically $\alpha<5°$, we obtain for a $\tau=15$ ps pulse and a medium length of $L=1$ mm the following orders of magnitude,

$$c\tau=4.5\,\mathrm{mm}\,,\qquad \rho\sin\alpha<10\,\mu\mathrm{m}\,,\qquad z\cos\alpha\lesssim 1\,\mathrm{mm}\,.$$

For the shape of the pulse we will thus simply assume the form

$$\text{pulse shape}=\exp\left[-2\ln 2\left(\frac{z\cos\alpha}{c\tau}-\frac{t}{\tau}\right)^2\right]. \quad (3.47)$$

The Gaussian pulse shape is a very common intensity profile used in propagation calculations (see, e.g., Ref. [131]). The total energy carried by a Bessel-Gauss beam can now be evaluated and it is given by

$$\mathcal{E}_{\rm BG}=\int_{-\infty}^{+\infty}P(t)\mathrm{d}t=\sqrt{\frac{\pi}{4\ln 2}}\,\tau\,P_{\rm BG} \quad (3.48)$$

Ultrashort pulse versions of Bessel beams, so-called *Bessel-X beams*, have been also been introduced (see Ref. [211] and references therein). They are generated from femtosecond laser pulses and meant to allow for diffraction-free transmission of images over large distances. The difficulty that arises when considering very short pulses is the possible dispersion of the Bessel beam generator, e.g., the frequency-dependence of the refractive index of glass in the case of an axicon, resulting in a temporal spread of the pulse. The authors of Ref. [211] have investigated the possibility of compensating this spread by playing the dispersion of the Bessel beam generator against the dispersion of the medium into which the resulting beam is

afterwards focused. An experimental realization of such Bessel-X pulses has been reported in Ref. [197].

We finally note that a family of Bessel-Gauss pulses can be obtained as exact solutions of the homogenous scalar wave equation (that is, without having to make the slowly-varying envelope approximation), provided the ansatz, given here for the azimuthally symmetric zero-order solution, has the form

$$E(\rho, z, t) = \exp[ik_-(z + ct)]\, G[\rho, k_+(z - ct)]\,. \tag{3.49}$$

The amplitude Eq. (3.49) thus consists of a plane wave travelling in $-z$ direction and a general wave travelling in $+z$ direction. This type of solution can describe the propagation of electromagnetic energy localized both in space and time. The amplitudes for the Bessel-Gauss beam of section 3.3 can be recovered by taking the appropriate limits.

Chapter 4

The Propagation Equations

4.1 Introduction

In the present chapter we will derive in some detail the expression for the harmonic fields as they emerge from the medium in which they have been created and travelled through. As starting point, we take the macroscopic Maxwell equations,

$$\nabla \cdot \boldsymbol{D}(\mathbf{x},t) = \rho_{\text{free}}(\mathbf{x},t) \tag{4.1}$$

$$\nabla \cdot \boldsymbol{B}(\mathbf{x},t) = 0 \tag{4.2}$$

$$\nabla \times \boldsymbol{E}(\mathbf{x},t) = -\frac{\partial \boldsymbol{B}(\mathbf{x},t)}{\partial t} \tag{4.3}$$

$$\frac{1}{\mu_0} \nabla \times \boldsymbol{B}(\mathbf{x},t) = \boldsymbol{J}_{\text{free}}(\mathbf{x},t) + \frac{\partial \boldsymbol{D}(\mathbf{x},t)}{\partial t} \tag{4.4}$$

The relationship between the electromagnetic displacement vector $\boldsymbol{D}$ and the electromagnetic field strength $\boldsymbol{E}$ is written in the usual way (see, e.g., Ref. [33]) as

$$\boldsymbol{D} = \epsilon_0 \boldsymbol{E} + \boldsymbol{P}\,, \tag{4.5}$$

where we have introduced the macroscopic polarization $\boldsymbol{P}$. A straightforward calculation leads to the propagation equations in the form

$$\nabla^2 \boldsymbol{E} - \nabla(\nabla \cdot \boldsymbol{E}) - \frac{1}{c^2}\frac{\partial^2 \boldsymbol{E}}{\partial t^2} = \mu_0 \frac{\partial^2 \boldsymbol{P}}{\partial t^2} + \mu_0 \frac{\partial \boldsymbol{J}_{\text{free}}}{\partial t} \tag{4.6}$$

$$\epsilon_0 \nabla \cdot \boldsymbol{E} = -\nabla \cdot \boldsymbol{P} + \rho_{\text{free}}\,. \tag{4.7}$$

Unlike in section 3.5, the divergence condition (4.7) is not automatically included in the vector equation (4.6). Indeed, taking the divergence of the latter equation and requiring on physical grounds the continuity equation to hold for the free charges,

$$\nabla \cdot \boldsymbol{J}_{\text{free}} + \frac{\partial \rho_{\text{free}}}{\partial t} = 0\,, \tag{4.8}$$

we obtain

$$\frac{\partial^2}{\partial t^2}\left\{\epsilon_0 \nabla \cdot \boldsymbol{E} + \nabla \cdot \boldsymbol{P} - \rho_{\text{free}}\right\} = 0\,, \tag{4.9}$$

and thus

$$\epsilon_0\, \nabla \cdot \boldsymbol{E} + \nabla \cdot \boldsymbol{P} - \rho_{\text{free}} = H\, t + G\,, \tag{4.10}$$

where H and G are two arbitrary space-dependent functions. $\boldsymbol{E}$ includes both the fundamental and the harmonic fields. In the present case, we will impose as boundary condition an incident laser pulse, whose amplitude vanishes at every point in space for $t \to -\infty$. As a consequence, the macroscopic polarization $\boldsymbol{P}$ driven by the incident field, the harmonic fields generated by the nonlinear part of the polarization, and the build-up of free charges ρ_{free} due to ionization mechanims, necessarily obey the same boundary condition. Accordingly, H and G have to vanish because the right hand side of Eq. (4.10) vanishes at every point of space for $t \to -\infty$.

Having seen in section 3.5 that it reasonable to make use of the divergence condition for the Bessel-Gauss family of field amplitudes (keeping in mind the restriction on the Bessel angle) we shall proceed in the same way here by inserting Eq. (4.7) into Eq. (4.6) and neglecting the divergence condition Eq. (4.7) in all further calculations. The basic propagation equation now reads

$$\nabla^2 \boldsymbol{E} - \frac{1}{c^2}\frac{\partial^2 \boldsymbol{E}}{\partial t^2} = \mu_0 \frac{\partial^2 \boldsymbol{P}}{\partial t^2} + \mu_0 \frac{\partial \boldsymbol{J}_{\text{free}}}{\partial t} + \frac{1}{\epsilon_0}\nabla[-\nabla \cdot \boldsymbol{P} + \rho_{\text{free}}]\,. \tag{4.11}$$

Initially, for a neutral atomic gas, there are neither free charges (ρ_{free}) nor free currents ($\boldsymbol{J}_{\text{free}}$). At high intensities, though, the onset of strong ionization will result in a rapidly growing population of ions and electrons. One can neglect the effect of the ions as the electrons are by far the lightest of the charged particles involved,

thus showing a much stronger response than the ions to the fields inside the medium. Further, the contribution of the ions to harmonic generation is generally thought to be less than those of the corresponding neutral atoms, essentially because of their lower polarizability. As already mentioned in section 1.2.3, the ionic contribution to the harmonic spectrum shows only up in those cases, where their higher saturation intensity prevents them from getting ionized as quickly as the corresponding neutral atoms. This is essentially the case for the highest harmonics generated at very high intensities in helium and neon with a short fundamental wavelength ($\lesssim$ 500 nm) [227]. If hydrogen is considered in applications, the ionic contribution can of course be omitted altogether. In the following we neglect therefore all ionic contributions.

The contribution of the free electrons can be treated in the following approximate way: assuming the electrons to behave classically, we may write

$$\rho_{\text{free}}(\mathbf{x},t) = -e\mathcal{N}_{\text{el}}(\mathbf{x},t) \tag{4.12}$$

$$\boldsymbol{J}_{\text{free}}(\mathbf{x},t) = -e\mathcal{N}_{\text{el}}(\mathbf{x},t)\,\boldsymbol{v}_{\text{el}}(\mathbf{x},t)\,, \tag{4.13}$$

where $\mathcal{N}_{\text{el}}$ and $\boldsymbol{v}_{\text{el}}$ are the density and the velocity field of the electron gas, respectively. Using the simplest possible classical equation of motion,

$$\frac{\partial \boldsymbol{v}_{\text{el}}(\mathbf{x},t)}{\partial t} + \nu_{\text{coll}}\boldsymbol{v}_{\text{el}}(\mathbf{x},t) = -\frac{e}{m}\boldsymbol{E}(\mathbf{x},t), \tag{4.14}$$

where the damping term involving ν_{coll} includes phenomenologically electron-ion scattering [187], we arrive at

$$\frac{\partial \boldsymbol{J}_{\text{free}}(\mathbf{x},t)}{\partial t} = \mathcal{N}_{\text{el}}(\mathbf{x},t)\frac{e^2}{m}\boldsymbol{E}(\mathbf{x},t) + e\left[\nu_{\text{coll}}\mathcal{N}_{\text{el}}(\mathbf{x},t) - \frac{\partial \mathcal{N}_{\text{el}}(\mathbf{x},t)}{\partial t}\right]\boldsymbol{v}_{\text{el}}(\mathbf{x},t)\,, \tag{4.15}$$

and finally get, for the full wave equation,

$$\begin{aligned} \nabla^2\boldsymbol{E} - \frac{1}{c^2}\frac{\partial^2\boldsymbol{E}}{\partial t^2} - \mu_0\mathcal{N}_{\text{el}}(\mathbf{x},t)\frac{e^2}{m}\boldsymbol{E} &= \mu_0\frac{\partial^2\boldsymbol{P}}{\partial t^2} \\ -\frac{1}{\epsilon_0}\nabla\left(\nabla\cdot\boldsymbol{P} + e\mathcal{N}_{\text{el}}\right) &+ e\mu_0\left[\nu_{\text{coll}}\mathcal{N}_{\text{el}} - \frac{\partial\mathcal{N}_{\text{el}}}{\partial t}\right]\boldsymbol{v}_{\text{el}}\,. \end{aligned} \tag{4.16}$$

Eq. (4.16) has to be solved simultaneously together with Eq. (4.14), while the relation between the velocity and the density of the free electrons (the latter being determined by the ionization rate) is further restricted by virtue of the continuity equation (4.8).

The last question that remains to be addressed is the form of the constitutive relation between the polarization $\boldsymbol{P}$ and the driving field amplitude $\boldsymbol{E}$. We note first that it is convenient and customary to separate the linear contribution from the nonlinear contribution,

$$\boldsymbol{P} = \boldsymbol{P}_L + \boldsymbol{P}_{NL} \,. \tag{4.17}$$

In what follows, we will consider only the linear part for simplicity, though the conclusions we are going to draw from the following considerations are independent of the order of nonlinearity. The relationship is local in Fourier space,

$$P_{L,i}(\boldsymbol{k},\omega) = \epsilon_0 \sum_j \chi_{ij}(\boldsymbol{k},\omega) E_j(\boldsymbol{k},\omega) \,, \tag{4.18}$$

where χ_{ij} is the susceptibility tensor and $i,j = 1,2,3$ are cartesian indices. The reason for this is the general assumption in physics of a *local* exchange of energy and momentum between particles. The susceptibility in Eq. (4.18) can (in principle) be evaluated by diagrammatic techniques (Feynman diagrams) from the field theory of the electromagnetic force [63]. As a consequence, the relationship between $\boldsymbol{P}_L(\mathbf{x},t)$ and $\boldsymbol{E}(\mathbf{x},t)$ is generally nonlocal,

$$P_{L,i}(\mathbf{x},t) = \epsilon_0 \sum_j \int_0^{+\infty} \mathrm{d}\tau \int \mathrm{d}\mathbf{x}' \, \chi_{ij}(\mathbf{x},\mathbf{x}',\tau) \, E_j(\mathbf{x}',t-\tau) \,. \tag{4.19}$$

Neglecting the spatial nonlocality is easily justified in our case, because it is tantamount to the validity of the dipole approximation which we have asserted in section 1.2.1: neglecting the photon's momentum simply means, that Eq. (4.18) is effectively independent of the wavevector $\boldsymbol{k}$. In coordinate space this amounts to a spatially constant field amplitude with respect to the dimensions of the atomic system considered. We thus have to transform Eq. (4.16) into Fourier space only with respect to time, keeping the relationship between spatial coordinates local. Before doing this we suitably tailor the general equation (4.16) to our needs. We shall consider linear polarized fields throughout, as we have seen in section 1.2.2 that the harmonic yield decreases with increasing ellipticity of the incident field. Therefore, we let

$$\boldsymbol{E}(\mathbf{x},t) = \hat{\boldsymbol{e}}\, E(\mathbf{x},t) \,, \qquad \boldsymbol{P}(\mathbf{x},t) = \hat{\boldsymbol{e}}\, P(\mathbf{x},t) \,, \tag{4.20}$$

$\hat{\boldsymbol{e}}$ being a spatially fixed unit vector, and project Eq. (4.16) onto this direction. This leads to

$$\begin{aligned} \nabla^2 E - \frac{1}{c^2}\frac{\partial^2 E}{\partial t^2} - \mu_0 \mathcal{N}_{\rm el}(\mathbf{x},t)\frac{e^2}{m}E &= \mu_0 \frac{\partial^2 P}{\partial t^2} \\ -\frac{1}{\epsilon_0}(\hat{\boldsymbol{e}}\cdot\nabla)^2 P - \frac{e}{\epsilon_0}(\hat{\boldsymbol{e}}\cdot\nabla)\mathcal{N}_{\rm el} &+ e\left[\nu_{\rm coll}\mathcal{N}_{\rm el} - \frac{\partial \mathcal{N}_{\rm el}}{\partial t}\right](\hat{\boldsymbol{e}}\cdot\boldsymbol{v}_{\rm el})\,. \end{aligned} \tag{4.21}$$

Little work has been done to study the influence of the terms appearing in the second line of Eq. (4.21) on the generation and propagation of harmonics in gases and they are usually omitted in the literature. This happens essentially because of two reasons: first, the term proportional to the gradient of the polarization vanishes in the plane wave limit, $P \propto \exp(i\boldsymbol{k}\cdot\mathbf{x})$, because of $\hat{\boldsymbol{e}}\cdot\boldsymbol{k} = 0$. Second, the effect of the free electrons is generally assumed to be essentially confined to a mere change of the refractive index, the contribution to which is given by the term proportional to $\mathcal{N}_{\rm el}E$ in Eq. (4.21). Therefore, it is the equation given by the first line of (4.21) which is taken in most cases as starting point for propagation calculations [5, 7, 130, 131, 171, 188, 189, 201, 206] or expressions derived from this equation [158, 160]. We shall follow this approach here.

The transformation into Fourier space with respect to time is carried out in a way appropriate to quasi-monochromatic fields whose frequency spectrum is confined to a narrow bandwith around a given carrier frequency. The real fields are thereby expanded as

$$f(\mathbf{x},t) = \sum_q f_q(\mathbf{x},t)\,\exp(-iq\omega t) = f_0(\mathbf{x},t) + \sum_{q>0} \mathrm{Re}[2 f_q(\mathbf{x},t)\exp(-iq\omega t)]\,, \tag{4.22}$$

and we obtain the propagation equation in Fourier space in the form

$$\nabla^2 E_q + \left(\frac{q\omega}{c}\right)^2 n_q^2 E_q = -\frac{1}{\epsilon_0}\left(\frac{q\omega}{c}\right)^2 P_{{\rm NL},q}\,, \tag{4.23}$$

neglecting all time derivatives with respect to the Fourier components $f_q(\mathbf{x},t)$ [130, 131]. The refractive index n_q in Eq. (4.23) is given by

$$n_q = [1 + \mathcal{N}_{\rm at}(\mathbf{x},t)\chi_{\rm at}(q\omega) + \mathcal{N}_{\rm el}(\mathbf{x},t)\chi_{\rm el}(q\omega)]^{1/2}\,, \tag{4.24}$$

where we have made use of

$$P_{L,q}(\mathbf{x},t) = \epsilon_0 \chi E_q(\mathbf{x},t) = \epsilon_0 \mathcal{N}_{\rm at}(\mathbf{x},t)\chi_{\rm at}[q\omega, I_1(\mathbf{x},t)]E_q(\mathbf{x},t)\,, \tag{4.25}$$

and defined the electronic susceptibility,

$$\chi_{\rm el}(q\omega) = -\frac{e^2}{m\epsilon_0 q^2\omega^2} = -8.970\times 10^{-34}\frac{\lambda^2[\rm nm]}{q^2}\ \rm m^3\,. \tag{4.26}$$

In Eq. (4.25) we have made use of the macroscopical isotropy of the atomic gas and assumed a scalar relationship between the polarization and the driving field amplitude[1]. We have also replaced the linear macroscopic susceptibility by the product of the atomic density $\mathcal{N}_{\rm at}$ and the linear atomic susceptibility, which we have introduced in chapter 2. $I(\mathbf{x},t)$ is the intensity at a given point in space and time in the medium and will be specified at a later stage. All quantities entering Eqs. (4.23),(4.24) and (4.25) are understood to be slowly time-varying on the scale of the fundamental period of the incident laser field but this (remaining) time-dependence is now entirely local.

Going beyond the quasi-monochromatic approach leading to Eq. (4.23), the slowly-varying envelope approximation (in the time domain) takes additionally the first time-derivatives of the fields into account, leading to

$$\nabla^2 E_q + \frac{q^2\omega^2}{c^2}[1+\mathcal{N}_{\rm el}\chi_{\rm el}(q\omega)]E_q + \frac{2iq\omega}{c^2}\frac{\partial E_q}{\partial t} = -\mu_0\left(\omega^2 q^2 P_q + 2iq\omega\frac{\partial P_q}{\partial t}\right)\,. \tag{4.27}$$

This approach has been used recently by the authors of Ref. [5]. However, several approximations have to be made. Firstly, the time-derivative of the polarization is dropped, except for the linear term given by Eq. (4.25), where only the time-derivative of the electric field amplitude is taken into account. By further assuming the slowly-varying envelope approximation in the space domain (for the propagation direction z) to hold, Eq. (4.23) can be recovered by a transformation into the co-moving frame [5, 191],

$$z = z'\,, \qquad t' = t - z/v_{g,q}\,, \tag{4.28}$$

provided the group velocity $v_{g,q}$, which depends on the refractive index Eq. (4.24), is assumed to be constant. A more recent approach [7] consisted of solving Eq.

[1]The harmonic index q is thus not related in any way to the tensorial indices i, j in expressions (4.18) and (4.19).

(4.23) for a continous range of frequencies and obtaining the time-dependence of the electrical field by a Fourier transform back to the time-domain. This is possibly the most accurate method to date, although it is an approximation with respect to the electronic contribution too, because as a product of two time-dependent functions, the term $\mathcal{N}_{\rm el}E$ in Eq. (4.21) is, strictly speaking, a convolution in Fourier space.

We shall adopt a different approach here but one which is essentially equivalent to the slowly-varying envelope approximation outlined above. We replace expansion (4.22) by

$$f(\mathbf{x},t) = f_0(\mathbf{x},t) + \sum_{q>0} \mathrm{Re}[2f_q(\mathbf{x},t)]\,, \tag{4.29}$$

and we assume that we can solve the propagation equation for each harmonic component q,

$$\nabla^2 E_q(\mathbf{x},t) - \frac{1}{q^2\omega^2}\frac{\partial^2 k_q^2 E_q(\mathbf{x},t)}{\partial t^2} = \mu_0 \frac{\partial^2 P_{\mathrm{NL},q}(\mathbf{x},t)}{\partial t^2}\,, \tag{4.30}$$

separately, provided the smallest time-scale is still given by $T_q = 2\pi/q\omega$. In writing down Eq. (4.30) we have already made use of an assumption introduced above, namely that the effect of free electrons is entirely described by an appropriate change of the refractive index, such that $k_q = k_{0,q}n_q$, where $k_{0,q}$ is the free-space wave number and n_q the refractive index as given in Eq. (4.24). Clearly, Eq. (4.30) reduces immediately to Eq. (4.23) if we go back to the quasi-monochromatic limit. Some advantages are associated with proceeding in our way. Firstly, as will be shown in detail in the next section, we can make use of the retarded Green's function to get a compact expression for the harmonic far-field, secondly, we shall be able to derive the slowly-varying envelope approximation in a simple way and thirdly, the correction beyond the slowly-varying envelope approximation can be obtained in principle, as long as its variation is still small on the time-scale set by T_q.

4.2 Solution of the propagation equation

Various approaches exist for solving Maxwell's equations or propagation equations in general. L'Huillier *et al.* [130] first used an integral method to solve Eq. (4.23)

and later a space-marching Crank-Nicholson scheme for solving the same equation numerically on a large grid [131]. Different schemes for the first-order Maxwell equations are discussed by Hile and Kath [97], and a beam propagation method based on Padé approximants has been presented by Chiou and Chang [47]. In this thesis, we will use an upgraded version of the integral method of Ref. [130]. Though it is not possible in this way to determine the fields inside the medium or the near-field outside the medium, this approach allows, however, for a semi-analytical treatment of the propagation aspects. This, besides speeding up the calculations and reducing the risk of spurious numerical effects, makes it possible to search more effectively the huge parameter space which is generated by the many tunable parameters involved. As we are also more interested in making a general comparison between Gaussian and Bessel-Gauss beams rather than trying to explain every 'wiggle' in the far-field profiles, this straightforward and robust method is all the more convenient.

For the expression of the refractive index Eq. (4.24) we will take more specifically

$$n_q = [1 + \mathcal{N}_{\rm at}(\mathbf{x})\chi_q(\mathbf{x},t)]^{1/2} \tag{4.31}$$

$$\chi_q(\mathbf{x},t) = [1 - f_{\rm ion}(\mathbf{x},t)]\,\chi_{\rm at}[q\omega, I(\mathbf{x},t)] + f_{\rm ion}(\mathbf{x},t)\,\chi_{\rm el}(q\omega)\,, \tag{4.32}$$

where $f_{\rm ion}(\mathbf{x},t)$ is the photoionization probability[2]. Expression (4.32) thus assumes, that the interatomic distances are much larger than the distance the free electrons travel after ionization, which is a valid approach for dilute atomic gases and short pulses we are going to consider in applications. The photoionization probability $f_{\rm ion}(\mathbf{x},t)$ is defined by generalizing Eq. (2.26) to the time-dependent expression

$$f_{\rm ion}(\mathbf{x},t) = 1 - \exp\left\{-\int_{-\infty}^{t} \Gamma[I(\mathbf{x},t')]\,{\rm d}t'\right\}. \tag{4.33}$$

We proceed now to solve the propagation equation (4.30): following the approach outlined in Ref. [130], we assume $n_q = 1$ in a first step[3], which allows for an integral solution of the wave equation (4.30), namely [103]

$$E_q(\mathbf{x}',t') = \left(-\frac{\mu_0}{4\pi}\right)\int_{\rm medium} {\rm d}\mathbf{x}\,|\mathbf{x}'-\mathbf{x}|^{-1}\left[\frac{\partial^2 P_{{\rm NL},q}(\mathbf{x},t)}{\partial t^2}\right]_{t=t'-(k_q/q\omega)|\mathbf{x}'-\mathbf{x}|}, \tag{4.34}$$

[2]More precisely, $f_{\rm ion}(\mathbf{x},t)$ is the probability that the atom, located at position $\mathbf{x}$, is photoionized at or before time t. For simplicity, we shall continue using the expression (photo-)ionization probability.

[3]This is analogous to the assumption of a constant group velocity made in connection with transformation Eq. (4.28).

where we do not have to add a solution of the homogenous equation as no fields are present at $t \to -\infty$ before the interaction is switched on. This is achieved by imposing an adequate time dependence on $P_{\mathrm{NL},q}$, namely by considering an incident laser pulse of finite duration. We reintroduce in a second step the spatio-temporal dependence of n_q, proceeding as shown in detail later. The basic assumption underlying this two-step approach requires the medium to be dilute. We shall therefore require

$$\mathcal{N}_{\mathrm{at}}(\mathbf{x})\chi_1(\mathbf{x},t)\,,\mathcal{N}_{\mathrm{at}}(\mathbf{x})\,\chi_q(\mathbf{x},t) \ll 1 \tag{4.35}$$

to hold. It is ultimately the electronic contribution at the fundamental frequency which determines the limit of the validity of assumption (4.35). For example, using Eq. (4.26) for $\lambda = 355$ nm, we need $\mathcal{N}_{\mathrm{at}}(\mathbf{x}) \lesssim 10^{20}$ atoms/cm^3 in order to achieve $\mathcal{N}_{\mathrm{at}}\chi_{\mathrm{el}}(\omega) \lesssim 10^{-2}$. However, other considerations might independently put an upper limit on the atomic density that can be used. Indeed, we have neglected previously the distances the free electrons travel compared to interatomic distances, an approximation which permits us also to neglect electron-ion or electron-atom scattering. A crude, but order-of-magnitude estimate of the validity of this approximation can be gained by considering the quiver amplitude of a free electron in the driving laser field, which we need to be much smaller than the average distance between two neighbouring atoms [2]. The quiver amplitude for linear polarization being given by[4] [83]

$$\mathrm{a}_0 = E_0/\omega^2 \qquad \text{(in a.u.)} \tag{4.36}$$

$$= 1.36 \times 10^{-13} \sqrt{I_L[\mathrm{W/cm^2}]}\,\lambda^2[\mathrm{nm}] \qquad \text{(in nm)}\,, \tag{4.37}$$

we can write this condition as $\mathrm{a}_0 \ll \mathcal{N}_{\mathrm{at}}^{-1/3}$. For $I_L = 10^{14}$ W/cm^2 and $\lambda = 355$ nm one obtains $\mathrm{a}_0 = 0.17$ nm and therefore the requirement $\mathcal{N}_{\mathrm{at}} \ll 2 \times 10^{23}$ atoms/cm^3. Thus, this does not present any additional constraint in our case. Yet another constraint is imposed by the possible defocalization of the fundamental due to the free electrons. This was found to be of marginal importance by L'Huillier *et al.* [131] for $\mathcal{N}_{\mathrm{at}} \approx 5 \times 10^{17}$ atoms/cm^3 , but quite relevant at higher densities by Altucci *et al.* [2]. In our case we will use similar intensities as in Ref. [131], but an

[4]The same notation as in Eq. (1.3) is used.

electronic susceptibility which is one order of magnitude smaller, due to our short fundamental wavelength. If we additionally take the length L of the medium, over which defocalization can happen, into account, we can get a conservative estimate of the electronic density which should not be exceeded, namely $\mathcal{N}_{\rm el} < \lambda/L\chi_{\rm el}(\omega)$, with $\chi_{\rm el}(\omega)$ from Eq. (4.26). For $L = 0.5$ mm, this leads to $\mathcal{N}_{\rm el} < 6.3\times10^{18}$ electrons/cm^3. If we go above the 1s-2p resonance in hydrogen, described in chapter 2, we have to make sure that the initial atomic density is less than this value, as the medium will be ionized to a large degree. In all other situations the restrictions on $\mathcal{N}_{\rm at}$ and on the medium length L can be relaxed.

Provided we keep the restrictions made above in mind, we find that it is sufficient to use the free-space wavenumber $k_{0,1}$, when calculating the intensity of the fundamental on which the atomic response and the medium properties depend. Thus, we shall use

$$E(\rho,z,t) = E_{\rm BG}(\rho,z,t)\exp\left\{-2\ln 2\left[\frac{t-(k_1/\omega)z\cos\alpha}{\tau}\right]^2\right\}\exp(-i\omega t), \qquad (4.38)$$

where the time-dependence of $E_{\rm BG}$ comes from the time-dependent refractive index [that is, $k_1(\mathbf{x},t) = k_{0,1}(1+\chi_1)$], for describing the field amplitude of a Bessel-Gauss beam with a Gaussian temporal profile as introduced in Eq. (3.47), and

$$I(\rho,z,t) = I(\rho,z)\exp\left\{-4\ln 2\left[\frac{t-(z/c)\cos\alpha}{\tau}\right]^2\right\} \qquad (4.39)$$

$$I(\rho,z) = \frac{I_{\rm f}}{1+(2z/b)^2}\left|J_0\left(\frac{k_{0,1}\rho\sin\alpha}{1+i\,(2z/b)}\right)\right|^2 \times \exp\left\{-\left[\frac{2k_{0,1}(\rho^2+z^2\sin^2\alpha)/b}{1+(2z/b)^2}\right]\right\}. \qquad (4.40)$$

for calculating the intensity of the fundamental within the medium. Only phase and intensity of the incident beam, as given by expressions (4.38) and (4.39), will enter the calculation of the atomic quantities determining the generation and propagation of a given harmonic in the medium. We neglect in this way all possible effects of harmonic coupling[5], and, in particular, the effect of multi-colour ionization (see section 2.3).

[5]We shall give an example for the breakdown of this assumption in section 6.3.1.

If the amplitude Eq. (4.38) is written in the form

$$E(\rho,z,t) = |E(\rho,z,t)| \exp\{i \arg[E_{\rm BG}(\rho,z,t)]\} \exp(-i\omega t)\,, \tag{4.41}$$

we can identify the phase $\omega t + \varphi$ in Eq. (2.15) with the phase of the field in Eq. (4.41), thus getting $\varphi = -\arg[E_{\rm BG}(\rho,z,t)]$. Therefore, the atomic dipole moment $d_q(E)$ from Eq. (2.20), oscillating at the harmonic frequency $q\omega$, is given by

$$d_q(\rho,z,t) = |d_q[I(\rho,z,t)]| \exp\{i\Phi_{\rm at}[I(\rho,z,t)]\} \exp\{iq \arg[E_{\rm BG}(\rho,z,t)]\} \exp(-iq\omega t), \tag{4.42}$$

where we have already appended the harmonic time-dependence from expression (2.18). We have also written $d_q(I)$ in terms of modulus and phase and $\Phi_{\rm at}$ is known as the (intensity-dependent) atomic dipole phase. For the macroscopic nonlinear polarization, which is the source term of the harmonic field in Eq. (4.34), we thus get

$$P_{{\rm NL},q}(\mathbf{x},t) = \mathcal{N}_{\rm at}(\mathbf{x})[1 - f_{\rm ion}(\rho,z,t)]d_q(\rho,z,t)\,, \tag{4.43}$$

with target depletion included in this way. Calculating the second time derivative of this expression, one can classify the resulting terms according to inverse powers of $q\omega\tau$. We quote only the result up to first order in $1/q\omega\tau$,

$$\frac{\partial^2 P_{{\rm NL},q}}{\partial t^2} = -q^2\omega^2 \mathcal{N}_{\rm at}(\mathbf{x})\,[1 - f_{\rm ion}(\rho,z,t)]\,d_q(\rho,z,t)\,\mathcal{F}(\rho,z,t) \tag{4.44}$$

$$\mathcal{F}(\rho,z,t) = 1 - \frac{2}{q\omega}\left\{ i\Gamma[I(\rho,z,t)] - i\frac{1}{|d_q|}\frac{\partial |d_q|}{\partial I}\frac{\partial I}{\partial t} + \frac{\partial \Phi_{\rm at}}{\partial I}\frac{\partial I}{\partial t}\right\}, \tag{4.45}$$

where, in expression (4.45), we have omitted the term stemming from the time-derivative of $\arg[E_{\rm BG}(\rho,z,t)]$. Indeed, it would have introduced a term proportional to $(\partial\chi_1/\partial I)\,(\partial I/\partial t)$, which, because of assumption (4.35) makes it negligible compared to the other corrections of the same order in $1/q\omega\tau$. $\mathcal{F}(\rho,z,t)$ is the slowly-varying envelope approximation. It is possible, of course, to go beyond this limit and compute the remaining terms of order $1/(q\omega\tau)^2$. At this stage, however, we have to remember that the atomic quantities have been calculated using the quasi-monochromatic Floquet approach (chapter 2) and it would be therefore of little use going beyond the slowly-varying envelope approximation in the propagation calculation. For ultrashort pulses, where the intensity varies appreciably over one

cycle of the driving laser field, it is not possible any longer to compute the atomic quantities as a function of the intensity alone. Rather, it is necessary to evaluate the atomic response at every time-step during the propagation of the fields through the medium. This unified approach has been pioneered by Rae and Burnett [188] (and more recently by Christov *et al.* [49]) but the enormous computational effort restricts this method presently to one-dimensional model calculations.

4.3 Far-field limit

To obtain the far-field limit, we expand $|\mathbf{x}' - \mathbf{x}|$ in Eq. (4.34) as

$$|\mathbf{x}' - \mathbf{x}| \simeq |\mathbf{x}'| - \frac{1}{|\mathbf{x}'|}[z'z + \rho'\rho\cos(\phi' - \phi)] + O(1/|\mathbf{x}'|^3) \tag{4.46}$$

with $|\mathbf{x}'| = \sqrt{z'^2 + \rho'^2} \gg |\mathbf{x}|$. This expression agrees to order $(1/z')$ with the paraxial approximation given in Ref. [130],

$$|\mathbf{x}' - \mathbf{x}| \simeq z' - z + \frac{\rho'^2 + \rho^2 - 2\rho'\rho\cos(\phi' - \phi)}{2(z' - z)} + O(1/|z' - z|^3)\,, \tag{4.47}$$

but is better suited for additionally studying off-axis emission, which will be of significance for Bessel-Gauss beams. We take $|\mathbf{x}'|$ large enough for the terms in $(1/|\mathbf{x}'|^3)$ to be negligible in Eq. (4.46) and rewrite this expansion as

$$|\mathbf{x}' - \mathbf{x}| \simeq \sqrt{z'^2 + \rho'^2} - z\cos\beta - \rho\sin\beta\cos(\phi' - \phi) \tag{4.48}$$

$$= (z' - z)\cos\beta + \rho'\sin\beta - \rho\sin\beta\cos(\phi' - \phi) \tag{4.49}$$

in terms of the far-field angle β,

$$\beta = \tan^{-1}(\rho'/z'), \tag{4.50}$$

with

$$\sin\beta = \frac{\rho'}{\sqrt{z'^2 + \rho'^2}}\,, \qquad \cos\beta = \frac{z'}{\sqrt{z'^2 + \rho'^2}}\,. \tag{4.51}$$

as shown in Fig. 4.1.

According to Eq. (4.34) we have now to take the source term Eq. (4.44) at the retarded time $t \equiv t_{\rm ret} = t' - (k_q/\omega)|\mathbf{x}' - \mathbf{x}|$. Some care has to be taken, as both k_q and

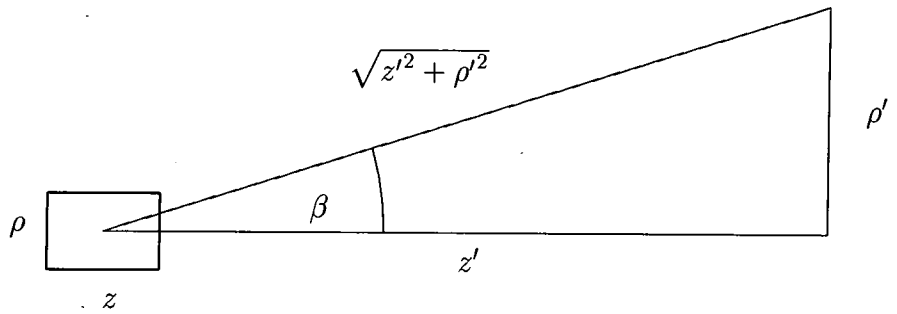

Figure 4.1: Definition of the far-field variables z', ρ' and β.

t_{ret} depend on each other due to the two-step approach in solving the propagation equation outlined above. For the sake of clarity, we rewrite the source term Eq. (4.44) in the form

$$\frac{\partial^2 P_{\mathrm{NL},q}}{\partial t^2} \propto [1 - f_{\mathrm{ion}}(I)]\, |d_q(I)| \mathcal{F}(I) \exp\{i\Phi_{\mathrm{at}}(I) + iq \arg[E_{\mathrm{BG}}(I)]\} \exp(-iq\omega t)\,, \tag{4.52}$$

where we have suppressed the dependence on the spatial coordinates and where the time dependence of the intensity I is understood. We first note that the source term depends on time only via the intensity, except for the fast oscillating harmonic time-dependence. In a first step, we thus replace in $\exp(-iq\omega t_{\mathrm{ret}})$ the retarded time t_{ret} by the full expression given above, $t' - (k_q/\omega)|\mathbf{x}' - \mathbf{x}|$, $k_q(I)$ being time- and space-dependent itself. This term, as we shall see, determines essentially the phase-matching properties. Now, for *all* remaining terms, the retarded time enters only indirectly via the intensity dependence and we can safely assume $k_q/\omega \approx 1/c$. Moreover, as appears clearly from Eq. (4.39), the intensity depends only on the combination $t_{\mathrm{ret}} - (z/c)\cos\alpha$ rather than on the retarded time alone, that is

$$ct_{\mathrm{ret}} - z\cos\alpha = ct' - \sqrt{z'^2+\rho'^2} + z(\cos\beta - \cos\alpha) + \rho \sin\beta \cos(\phi' - \phi)\,. \tag{4.53}$$

Recall from the discussion in section 3.5 that the term $(\rho/c\tau)\sin\beta\cos(\phi' - \phi)$ is negligible on an absolute scale for all cases of interest, while $(z/c\tau)(\cos\beta - \cos\alpha)$ will start to contribute with increasing medium length L and pulses becoming short $(L/c\tau \gg 1)$. The time-shift $(-\sqrt{z'^2+\rho'^2}/c\tau)$ affects far-field and time profiles but

not the overall conversion efficiency, as this shift is removed by a time integration over $t' \in (-\infty, +\infty)$[6]. In summary, we have to evaluate

$$\begin{aligned} \frac{\partial^2 P_{\mathrm{NL},q}}{\partial t^2}(t') &= -q^2\omega^2 \mathcal{N}_{\mathrm{at}}(\mathbf{x})[1 - f_{\mathrm{ion}}(I)]\,|d_q(I)|\mathcal{F}(I) \\ &\times \exp(i\{\Phi_{\mathrm{at}}(I) + q\arg[E_{\mathrm{BG}}(I)] + k_q(I)|\mathbf{x}' - \mathbf{x}| - q\omega t'\})\,, \end{aligned} \tag{4.54}$$

at the retarded time given by

$$ct_{\mathrm{ret}} - z\cos\alpha = ct' - \sqrt{z'^2 + \rho'^2} + z(\cos\beta - \cos\alpha)\,. \tag{4.55}$$

The two middle terms of the phase factor in Eq. (4.54) can be written, using Eqs. (4.38) and (4.49),

$$\begin{aligned} \Phi(I) &= q\left\{k_1(I)z\cos\alpha - \tan^{-1}(2z/b) + (2z/b)\left[\frac{k_1(I)(\rho^2 + z^2\sin^2\alpha)/b}{1 + (2z/b)^2}\right]\right\} \\ &+ k_q(I)[(z' - z)\cos\beta + \rho'\sin\beta - \rho\sin\beta\cos(\phi' - \phi)] \\ &+ q\arg\left[J_0\left(\frac{k_1(I)\rho\sin\alpha}{1 + i\,(2z/b)}\right)\right]. \end{aligned} \tag{4.56}$$

This phase is therefore the sum of the phases originating from the (beam) geometry and the dispersion of the medium. We can now correct partly for the initial approximation of taking the refractive index constant when deriving Eq. (4.34). For this, we replace the actual phase $\Phi(I)$ by the corresponding optical path integral along the main direction of propagation (see Ref. [130]), that is, the z-axis. The modification thus amounts to a replacement

$$k_q(z' - z) \to \int_z^{z'} k_q(\zeta)\mathrm{d}\zeta\,, \qquad k_1 z \to \int_{z_{\min}}^{z} k_1(\zeta)\mathrm{d}\zeta + k_{0,1}z_{\min}, \tag{4.57}$$

where we consider a medium stretching from $z_{\min}$ to $z_{\max}$. To preserve the azimutal symmetry in the calculations, we shall assume $\mathcal{N}_{\mathrm{at}}(\mathbf{x}) = \mathcal{N}_{\mathrm{at}}(\rho, z)$ in the following, which is not a restriction in applications. Combining now Eqs. (4.31) and (4.35) into

$$k_q(\rho, z, t) \simeq k_{0,q}\left[1 + \mathcal{N}_{\mathrm{at}}(\rho, z)\chi_q(\rho, z, t)/2\right], \tag{4.58}$$

the resulting expressions are given by

$$k_q(z' - z) \to k_{0,q}[z' - z - Z_q(\rho, z, t)] \tag{4.59}$$

$$Z_q(\rho, z, t) = \int_{z_{\max}}^{z} \mathcal{N}_{\mathrm{at}}(\rho, \zeta)\chi_q(\rho, \zeta, t)/2\;\mathrm{d}\zeta \tag{4.60}$$

[6]Without affecting the boundaries of other integration domains.

and

$$k_1 z \rightarrow k_{0,1}[z + Z_1(\rho, z, t)] \tag{4.61}$$

$$Z_1(\rho, z, t) = \int_{z_{\min}}^{z} \mathcal{N}_{\mathrm{at}}(\rho, \zeta)\chi_1(\rho, \zeta, t)/2 \, \mathrm{d}\zeta \, . \tag{4.62}$$

The careful treatment of the terms linked to axial propagation is very important because they are the largest terms appearing in Eq. (4.56) and possible cancellations (indicating axial phase-matching) have to be monitored accurately. The exact expression for the wavenumbers is much less of importance for the terms involving the radial coordinate ρ (and for the term containing $\sin^2\alpha$, owing to the small values of the Bessel angle α). In fact, for the remaining wave numbers in $\Phi(I)$ we can safely assume the corresponding free-space values - we shall come back to this point in section 4.5.2, when deriving the radial phase-matching condition.

4.4 Spatio-temporal profiles and conversion efficiency

We obtain the (slowly-varying) time-dependent harmonic intensity from the electric field amplitude by averaging over the fast oscillating component, which is the harmonic oscillation $\exp(-iq\omega t')$ in Eq. (4.54), thus getting

$$I_q(\rho', z', t') = 2c\epsilon_0 \, |E_q(\rho', z', t')|^2 \tag{4.63}$$

which will be used to compute the time profiles of the harmonic intensity at a given point ρ' in the far-field plane z'. From Eq. (4.63) the time profile of the harmonic power will be computed as

$$P_q(z', t') = 2\pi \int_0^{+\infty} I_q(\rho', z', t') \, \rho' \mathrm{d}\rho'. \tag{4.64}$$

Depending on the spatial resolution of the detector, either Eq. (4.63) or Eq. (4.64) will be more suited for characterizing the temporal shape of the generated harmonic pulse in the far-field region. The spatial far-field profile is defined as

$$\langle I_q(\rho', z') \rangle = \int_{-\infty}^{+\infty} I_q(\rho', z', t') \, \mathrm{d}t' \tag{4.65}$$

and, finally, the conversion efficiency as

$$\eta_q = (1/\mathcal{E}_1) \int_{-\infty}^{+\infty} P_q(z',t')\mathrm{d}t' = (1/\mathcal{E}_1)\, 2\pi \int_0^{+\infty} \langle I_q(\rho',z')\rangle \rho' \mathrm{d}\rho' \tag{4.66}$$

where $\mathcal{E}_1 = \int_{-\infty}^{+\infty} P_1(t')\mathrm{d}t'$ is the energy carried by the pulse of the fundamental beam, as given by Eq. (3.48). In fact, the conversion efficiency is independent of z' as will be shown in section E.3.

We conclude this section by giving a summary of all the expressions which enter the calculation of the harmonic field amplitude in Eq. (4.63). Defining, from Eq. (4.55), the dimensionless time-variable

$$\tilde{v}' = 2\sqrt{\ln 2}[t_{\mathrm{ret}} - (z/c)\cos\alpha]/\tau \tag{4.67}$$

$$= v' - 2\sqrt{\ln 2}\,[\sqrt{z'^2+\rho'^2} + z(\cos\alpha - \cos\beta)]/c\tau\,, \tag{4.68}$$

we may write the intensity of the incident beam Eq. (4.39) and the ionization probability Eq. (4.33) as

$$I(\rho,z,\tilde{v}') = I(\rho,z)\,\exp(-\tilde{v}'^2) \tag{4.69}$$

$$f_{\mathrm{ion}}[I(\rho,z),\tilde{v}'] = 1 - \exp\left\{-\frac{\tau}{2\sqrt{\ln 2}}\int_{-\infty}^{\tilde{v}'} \Gamma[I(\rho,z)\exp(-v^2)]\mathrm{d}v\right\} \tag{4.70}$$

The far-field envelope for the q^{th} harmonic is given by

$$\begin{aligned} E_q(\rho',z',\tilde{v}') = {} & \frac{1}{2\epsilon_0}\left(\frac{q\omega}{c}\right)^2 \frac{\exp(ik_{0,q}\sqrt{z'^2+\rho'^2})}{\sqrt{z'^2+\rho'^2}} \int_{z_{\min}}^{z_{\max}} \mathrm{d}z \int_0^{+\infty} \mathrm{d}\rho\,\rho \\ & \times \frac{\mathcal{N}_{\mathrm{at}}(\rho,z)\,[1 - f_{\mathrm{ion}}(\rho,z,\tilde{v}')]}{1 - (z/\sqrt{z'^2+\rho'^2})\cos\beta}\, J_0(k_{0,q}\rho\sin\beta)\,|d_q[I(\rho,z,\tilde{v}')]| \\ & \times \mathcal{F}(\rho,z,\tilde{v}')\,\exp\{i\Phi_{\mathrm{at}}[I(\rho,z,\tilde{v}')]\}\,\exp\{i\varphi(\rho,z,\tilde{v}')\}\,, \end{aligned} \tag{4.71}$$

this expression being valid for $z' \gg L$. Further,

$$\mathcal{F}(\rho,z,\tilde{v}') = 1 + \frac{8\sqrt{\ln 2}}{q\omega\tau}\left[\tilde{v}'\left(I\frac{\partial\Phi_{\mathrm{at}}}{\partial I}\right) - i\tilde{v}'\left(\frac{I}{|d_q|}\frac{\partial|d_q|}{\partial I}\right) - i\frac{\Gamma(I)\tau}{4\sqrt{\ln 2}}\right] \tag{4.72}$$

is the slowly-varying envelope approximation and

$$\begin{aligned} \varphi(\rho,z,\tilde{v}') = {} & k_{0,q}\,\{[z + Z_1(\rho,z,\tilde{v}')]\cos\alpha - [z + Z_q(\rho,z,\tilde{v}')]\cos\beta\} \\ & + q\left\{\arg\left[J_0\left(\frac{k_{0,1}\rho\sin\alpha}{1 + i\,(2z/b)}\right)\right]\right. \\ & \left. - \tan^{-1}(2z/b) + (2z/b)\,\frac{k_{0,1}(\rho^2 + z^2\sin^2\alpha)/b}{1 + (2z/b)^2}\right\}. \end{aligned} \tag{4.73}$$

The propagation of the harmonic field thus consists essentially of solving, for each time step, a two-dimensional integral over the nonlinear medium. For numerical convenience the shift entering the retarded time Eq. (4.67) is evaluated as,

$$\sqrt{z'^2+\rho'^2} = z' + \frac{\rho'^2}{z'+\sqrt{z'^2+\rho'^2}}, \tag{4.74}$$

and the term in z' is omitted. Therefore, the time reference at the detector plane at z' is given by $t'-z'/c$. We will give more details about the propagation code in Appendix E.

4.5 The Quasi-Stationary approach

4.5.1 Introduction

Though the time-dependent formalism developed in the previous sections is perfectly suited for our purposes it is worth investigating a much simpler approach, which will permit us to derive analytical expressions for phase-matching. In this way it will not only become possible to search more effectively the huge parameter space generated by the large number of parameters involved (which include essentially the atomic density $\mathcal{N}_0$, the medium length L, the confocal parameter b, the Bessel angle α and the harmonic order q), but will also enable us to make predictions about the efficiencies of the various Bessel-Gauss beams (including the Gaussian beam as limit case) in generating a given harmonic order. Moreover, we will show that in the regime where the approximations made in the following hold, the results are in very good agreement with the fully numerical and time-dependent calculations (see section 5.3).

In the present approach, we make use of the fact, that if the pulse duration is much longer than medium length L, $c\tau \gg L$, we can neglect all terms of the form $\xi/c\tau$, where ξ is any of the spatial coordinates. In fact, we shall neglect the pulse shape altogether and tabulate the harmonic generation rate as a function of the peak focal intensity I_f, this rate then being integrated over the intensities according to the temporal shape of the laser pulse. More precisely, in analogy to the defini-

tion of the conversion efficiency η_q given by Eq. (4.66) as the ratio of the emitted harmonic energy to the energy carried by the fundamental, we may write it for a time-independent calculation as the ratio of the emitted harmonic power to the power incident on target. As the latter is proportional to I_f, according to Eqs. (3.27) and (3.28), the functional form of the conversion efficiency is given by

$$\tilde{\eta}_q(I_f) = \frac{H_q(I_f)}{I_f}, \tag{4.75}$$

where H_q is proportional to the emitted harmonic power. Summing over the temporal distribution of the intensity we get

$$\begin{aligned} \eta_q(I_f) &= \frac{\int_{-\infty}^{+\infty} dt\, H_q\left(I_f \exp\left[-4\ln 2(t/\tau)^2\right]\right)}{\int_{-\infty}^{+\infty} dt\, I_f \exp\left[-4\ln 2(t/\tau)^2\right]} \\ &= \frac{2}{\sqrt{\pi}} \int_0^{+\infty} \mathrm{d}x\, \tilde{\eta}_q[I_f \exp(-x^2)], \end{aligned} \tag{4.76}$$

where we have introduced the normalized time $x = 2\sqrt{\ln 2}(t/\tau)$ and assumed a Gaussian temporal pulse shape as in Eq. (4.39). Note that, as expected in this limit, the conversion efficiency depends only on the shape of the pulse but not on the pulse duration τ. The spatial far-field profiles are averaged over the temporal pulse profile accordingly. In the weak field limit, where the power law $H_q(I_f) \propto I_f^q$, as a consequence of Eq. (2.21), holds, one simply has

$$\eta_q(I_f) = \frac{1}{\sqrt{q}}\, \tilde{\eta}_q(I_f). \tag{4.77}$$

We expect a good quantitative agreement with the full time-dependent calculations, with a possible exception in the case of strong ionization. Indeed, to model a time-independent ionization probability we use the end-of-pulse value defined in Eq. (2.26), namely

$$f_{\mathrm{ion}}(I_p) = 1 - \exp\left\{-\int_{-\infty}^{+\infty} \Gamma[I_p \exp(-4\ln 2(t/\tau)^2)]\mathrm{d}t\right\} \tag{4.78}$$

where I_p is evaluated from Eq. (4.40) for a given I_f and position within the medium[7]. Having set the upper boundary of the integral in Eq. (4.78) to infinity, we overestimate the ionization probability for a given I_p on the rising edge of the laser pulse.

[7]The ionization probability Eq. (4.78) is therefore the only quantity, where the pulselength τ enters explicitely.

However, considering the time-symmetric evaluation of the conversion efficiency Eq. (4.76), the ionization probability will at some stage be underestimated on the falling edge of the laser pulse. Indeed, introducing the normalized time $x = 2\sqrt{\ln 2}(t/\tau)$ as in Eq. (4.76), we find that the intensity has fallen from its peak value I_p down to I_p' after a time $x' = [\ln(I_p/I_p')]^{1/2}$. Consequently, the ionization rate will be underestimated in the calculation of the time-independent conversion efficiency for intensities lower than I_p satisfying

$$\int_{-\infty}^{+\infty} \Gamma[I_p' \exp(-x^2)]\mathrm{d}x = \int_{-\infty}^{x'} \Gamma[I_p \exp(-x^2)]\mathrm{d}x\,. \tag{4.79}$$

For guidance, assume a power law, $\Gamma \propto I^M$, and I_p' sufficiently close to I_p such that $x' \ll 1$. Then, to second order in x',

$$I_p' = (1 - x'^2)\, I_p\,, \qquad x' \approx \frac{0.49}{\sqrt{M}}\,. \tag{4.80}$$

We will not insist on the calculation of I_p' for various I_p in our case as it does not help gaining more insight about possible quantitative changes introduced in this way and we refer to chapter 5 where results comparing the time-dependent and time-independent methods are discussed. It follows from the considerations above, though, that the ionization rate is likely to be overestimated in the quasi-stationary approach. Actually, this will turn out to be very useful as we can get at the same time an idea of how the results (e.g., conversion efficiency versus peak focal intensity) would be affected, if two-colour ionization were to be of importance (see section 2.3).

4.5.2 Phase-matching conditions

We will profit from the quasi-stationary approach by deriving analytical expressions for phase-matching conditions in the case of sufficiently large confocal parameters, so that all terms z/b in the expression for the fields can be neglected (loose focusing limit). For this we require typically $b > 2L$ to hold[8], the expressions being exact in the limit $L/b \to 0$. In this case, we may write Eqs. (4.60) and (4.62) approximately

[8] We will discuss this in more detail in chapter 6.

as

$$Z_1(\rho,z) \approx (\mathcal{N}_0/2)\Sigma(\rho,z)\,\chi_1[I^{(0)}(\rho)] \tag{4.81}$$

$$Z_q(\rho,z) \approx (\mathcal{N}_0/2)[\Sigma(\rho,z)-\widehat{\sigma}(\rho)]\,\chi_q[I^{(0)}(\rho)]\,, \tag{4.82}$$

having introduced

$$\Sigma(\rho,z)=\int_{z_{\min}}^{z}\sigma(\rho,\zeta)\,\mathrm{d}\zeta\,, \tag{4.83}$$

with $\mathcal{N}_{\rm at}(\rho,z)=\mathcal{N}_0\sigma(\rho,z)$, $\mathcal{N}_0$ being the (initial) peak atomic density and $0\leq\sigma(\rho,z)\leq 1$. To make sure that the medium properties cease to affect the harmonic propagation for $z>z_{\max}$, we require further $\Sigma(\rho,z>z_{\max})=\Sigma(\rho,z_{\max})\equiv\widehat{\sigma}(\rho)$. We refer to Appendix B for a discussion of typical density profiles. We shall restrict to cases for which $\widehat{\sigma}(\rho)=g(\rho)L$, where L is the length of the medium entering the description of the density profiles. By requiring this form to hold for all density profiles under consideration, we make sure that the optical path through the medium is the same for all profiles, given a medium length L.

The intensity $I^{(0)}(\rho)$ is now only dependent on the radial coordinate and its profile is essentially a Bessel function damped by a Gaussian as can be seen from Eq. (4.40). We obtain in this way the following expression for the phase φ of Eq. (4.73),

$$\begin{aligned}\varphi^{(0)}(\rho,z) &\simeq k_{0,q}\sqrt{z'^2+\rho'^2}+k_{0,q}(\cos\alpha-\cos\beta)z+k_{0,q}\widehat{\sigma}\mathcal{N}_0\chi_q\cos\beta/2\\ &+ \mathcal{N}_0k_{0,q}(\chi_1\cos\alpha-\chi_q\cos\beta)\Sigma(\rho,z)/2\\ &+ q\,\arg\left[J_0\left(k_{0,1}\rho\sin\alpha\right)\right]\,,\end{aligned} \tag{4.84}$$

and, from there, for the harmonic far-field, using Eq. (4.71),

$$\begin{aligned}E_q^{(0)}(\rho',z') &= \frac{\mathcal{N}_0L}{2\epsilon_0}\frac{\exp\left\{ik_{0,q}\sqrt{z'^2+\rho'^2}\right\}}{\sqrt{z'^2+\rho'^2}}\left(\frac{q\omega}{c}\right)^2\int_0^\infty\rho\,\mathrm{d}\rho\,(1-f_{\rm ion})\\ &\times |d_q[I^{(0)}(\rho)]|\exp\{iq\arg\left[J_0\left(k_{0,1}\rho\sin\alpha\right)\right]\}\exp\{i\Phi_{\rm at}[I^{(0)}(\rho)]\}\\ &\times J_0\left(k_{0,q}\rho\sin\beta\right)\exp(iD)\;F_z(A,B,C)\exp(iAu_{\min})\,.\end{aligned} \tag{4.85}$$

We have introduced the dimensionless integral

$$F_z=\exp(-iAu_{\min})\int_{u_{\min}}^{u_{\max}}K'(u)\exp\{i[Au+BK(u)]\}\exp[-CK(u)]\,\mathrm{d}u\,, \tag{4.86}$$

where

$$K(u) = \Sigma(\rho, Lu)/g(\rho)L\,, \tag{4.87}$$

and $u_{\min,\max} = z_{\min,\max}/L$. The coefficients A, B, C and D, which do not depend on u, are given by

$$A = A(\rho,\rho',z') = 2(q\pi/\lambda)\widehat{\sigma}\,(\cos\alpha - \cos\beta) \tag{4.88}$$

$$B = B(\rho,\rho',z') = (q\pi/\lambda)\widehat{\sigma}\mathcal{N}_0\,\mathrm{Re}(\chi_1\cos\alpha - \chi_q\cos\beta) \tag{4.89}$$

$$C = C(\rho,\rho',z') = (q\pi/\lambda)\widehat{\sigma}\mathcal{N}_0\,\mathrm{Im}(\chi_1\cos\alpha - \chi_q\cos\beta) \tag{4.90}$$

$$D = D(\rho,\rho',z') = (q\pi/\lambda)\widehat{\sigma}\mathcal{N}_0\,\chi_q\cos\beta. \tag{4.91}$$

Note that while C may be negative [because of $\mathrm{Im}(\chi_1) > 0$ and $\mathrm{Im}(\chi_q) > 0$], one always has

$$\mathrm{Re}(iD) - CK(u) = -[\mathrm{Im}D + CK(u)] \leq 0\,, \tag{4.92}$$

for absorption, with

$$\mathrm{Im}D + CK(u) = (q\pi/\lambda)\widehat{\sigma}\mathcal{N}_0\,\mathrm{Im}\{K(u)\chi_1\cos\alpha + [1-K(u)]\chi_q\cos\beta\}\,. \tag{4.93}$$

The physical interpretation of Eq. (4.93) is an immediate consequence of the introduction of the optical path Eq. (4.57): Incident photons travel through an absorbing medium until they reach a point $u = z/L \in [u_{\min}, u_{\max}]$ after an effective optical path $K(u)\cos\alpha$. At u, the fundamental photons which have not been removed by absorption, create harmonic photons which in turn suffer absorption along their effective optical path $[1-K(u)]\cos\beta$ out of the medium[9].

We refer to Appendix B for a discussion of the integral F_z for various gas density profiles. Here we consider only the case of a rectangular profile, for which

$$F_z = \frac{(C+iS)[1-\cos S\,\exp(-C)] + (S-iC)\sin S\,\exp(-C)}{S^2+C^2}\,, \tag{4.94}$$

with $S = A+B$, as derived in Appendix B. $|F_z|$ is a maximum and F_z is purely real for $S = 0$, both independently of C. Therefore, $S = 0$ is the axial phase-matching

[9]The factors $\cos\alpha$ and $\cos\beta$ reflect the fact that only propagation properties along the main direction of propagation are taken into account in F_z.

condition. For $C = 0$, F_z takes the simple form

$$F_z(S, C = 0) = \frac{\sin(S/2)}{(S/2)} \exp(iS/2)\,, \tag{4.95}$$

which is the familiar $\sin(x)/x$ behaviour, typical for phase-matching in loose focusing geometries. The phase-matching condition $S = A + B = 0$ can be written, using Eqs. (4.88) and (4.89), as

$$\cos\beta = \frac{1 + \mathrm{Re}(\mathcal{N}_0\chi_1/2)}{1 + \mathrm{Re}(\mathcal{N}_0\chi_q/2)} \cos\alpha = \frac{n_1}{n_q} \cos\alpha\,, \tag{4.96}$$

in agreement with Eq. (3.14). Note that this expression is, as expected, independent of a possible transverse modulation $g(\rho)$ of the (initial) atomic density profile. Two limit cases of Eq. (4.96) can be distinguished: the medium being fully ionized ($f_{\mathrm{ion}} = 1$), in which case

$$\cos\beta = \frac{1 - \mathcal{N}_0|\chi_{\mathrm{el}}(\omega)|/2}{1 - \mathcal{N}_0|\chi_{\mathrm{el}}(q\omega)|/2} \cos\alpha, \tag{4.97}$$

or ionization being negligible, in which case

$$\cos\beta = \frac{1 + \mathrm{Re}[\mathcal{N}_0\chi_{\mathrm{at}}(\omega)/2]}{1 + \mathrm{Re}[\mathcal{N}_0\chi_{\mathrm{at}}(q\omega)/2]} \cos\alpha. \tag{4.98}$$

In a fully ionized medium the axial phase-matching condition can always be fulfilled for any angle α, with $\beta > \alpha$. The same conclusion applies as well to the case of a positively dispersive medium, $\chi_{\mathrm{at}}(q\omega) > \chi_{\mathrm{at}}(\omega)$, in the other limit. However, for a negatively dispersive medium, $\chi_{\mathrm{at}}(\omega) > \chi_{\mathrm{at}}(q\omega)$, Eq. (4.98) can be satisfied only for angles α satisfying

$$\cos\alpha < \frac{1 + \mathrm{Re}[\mathcal{N}_0\chi_{\mathrm{at}}(q\omega)/2]}{1 + \mathrm{Re}[\mathcal{N}_0\chi_{\mathrm{at}}(\omega)/2]} \tag{4.99}$$

thus giving preference to far-field angles $\beta < \alpha$.

It is unfortunately not possible to derive a similarly general formula for the radial phase-matching in a simple way, and we shall assume the low-intensity limit to hold, that is, no dependence of $\chi_{\mathrm{at}}(q\omega)$ on the intensity of the incident field, negligible photoionization and the dipole moment following the power law given by Eq. (2.21)[10]. We note first, that if $g(\rho) = 1$, axial and radial integration factorize, because the

[10]In particular, the atomic phase Φ_{at} is then independent of the intensity.

coefficients A, B, C and D become independent of the intensity, and hence of ρ, in this limit. The radial integral is then proportional to

$$\int_0^\infty \mathrm{d}\rho\, \rho\, J_0^q\left(k_{0,1}\rho \sin\alpha\right)\, J_0\left(k_{0,q}\rho \sin\beta\right)\, \exp(-qk_{0,1}\rho^2/b)\,, \tag{4.100}$$

which is a maximum when the arguments of the two Bessel functions coincide, since q is an odd integer. The radial phase-matching condition, valid in the perturbative limit, reads then

$$\sin\beta = \frac{k_{0,1}}{k_{0,q}} \sin\alpha = \frac{1}{q} \sin\alpha\,, \tag{4.101}$$

which implies $\beta < \alpha$. The same conclusion applies, if, for any $g(\rho)$, F_z takes the form of Eq. (4.95), and axial phase-matching is enforced, $S = 0$. In all other cases, $g(\rho)$ can in principle be used to influence the radial phase-matching condition. In the following, we shall, however, assume expression (4.101) to hold because of $g(\rho) = 1$. As noted at the end of section 4.3, it is not necessary here, in contrast to the case of axial phase-matching, Eq. (4.96), to use the full expression of the wavenumbers, because of the additional factor of $q \geq 3$ in Eq. (4.101) which sets the scale of the factor relating the two angles α and β.

The fact that both Eq. (4.96) and Eq. (4.101) contain the far-field variables (ρ', z') in the form of the angle β accounts for the *self-phase-matching* effect [85] we have already discussed in some detail in section 3.2: Rather than preventing phase-matching altogether, small changes in α, or in the refractive indices may simply result in changing the direction in which the harmonic is preferentially emitted. We have thus recovered the results previously obtained by Tewari *et al.* (see Refs. [217, 218] and also section 3.2) in the perturbative limit, for a pure Bessel beam, however with a few notable differences. Indeed, the use of a Bessel-Gauss beam prevents from having an infinite value in the radial integral as it is the case for a pure Bessel beam[11]. Further, the far-field angle β emerges naturally from the formalism and does not have to be introduced ad hoc as in their case. Perhaps most interesting of all, we stress that Eq. (4.96) is valid in *any* intensity regime as long as the assumption of a loose focusing geometry is valid. Note that this axial phase-matching condition

[11] This has also been pointed out recently in Ref. [166].

is thereby not a relationship between fixed parameters (for a given value of β) but depends on the intensity and thus on the radial coordinate ρ.

Comparing both phase-matching conditions, we recover the well known result that optimum phase-matching is only possible in a negatively dispersive medium, with $\beta < \alpha$ [217]. Eliminating the angle β in between Eqs. (4.96) and (4.101) gives an estimate of the angle α which, for a given medium, is expected to optimize phase-matching, namely

$$\sin \alpha_{\text{opt}} = \sqrt{\frac{n_1^2 - n_q^2}{n_1^2 - n_q^2/q^2}}, \tag{4.102}$$

which, for all practical purposes, can be written as[12]

$$\alpha_{\text{opt}} \approx [q^2/(q^2-1)]^{1/2} [2(n_1 - n_q)]^{1/2} \tag{4.103}$$

$$\alpha_{\text{opt}} \approx [q^2/(q^2-1)]^{1/2} [\mathcal{N}_0(\chi_1 - \chi_q)]^{1/2}. \tag{4.104}$$

This shows that α_{opt} can be expressed in a simple way as a function of the standard expression for the dispersive phase-mismatch in the paraxial limit,

$$\Delta k_{\text{disp}} = \frac{2\pi q}{\lambda} (n_q - n_1), \tag{4.105}$$

that is,

$$\alpha_{\text{opt}} \approx [q^2/(q^2-1)]^{1/2} [-(\lambda/q\pi)\, \Delta k_{\text{disp}}]^{1/2}. \tag{4.106}$$

This angle exists as long as $\text{Re}(\chi_1) \geq \text{Re}(\chi_q)$, a condition which depends both on the medium and on the intensity. The preferred emission angle β_q of the q^{th} harmonic is then approximately $\beta_q \simeq \alpha_{\text{opt}}/q$ (for small angles). Eqs. (4.103), (4.104) or (4.106) are useful in (roughly) predicting the cone angle of the incident beam for which the harmonic yield is expected to be maximal. It should be noted, however, that optimizing phase-matching for $\alpha > 0°$ cannot guarantee a higher conversion efficiency compared to the Gaussian limit, since increasing the angle α reduces the region where the atomic dipole moment is driven at high intensity, though this might be less important in a region of intensity where the atomic dipole moment is saturating. In the power law regime for the dipole moment, especially for a higher

[12]The first factor in the following equations can be neglected for $q > 3$.

order harmonic, only the central peak will contribute while the power contained in the secondary maxima will be lost (see Fig. 3.2). This obviously appears to be particularily severe if both the Bessel angle and the confocal parameter are large. Quite generally, the efficiency of the Bessel-Gauss beam depends on the balance between increased phase-matching and loss of driving power. These aspects are going to be developed in the following chapters. The phase-matching conditions derived in this section are valid in the loose focusing limit. In chapter 5 we report calculations which are based on this assumption. In chapter 6 we will relax this restriction and consider a broader range of focusing geometries. We will also investigate in more detail the relationship between the maximum of the conversion efficiency and the optimum angle α_{opt} for phase-matching.

Chapter 5

Results for Hydrogen at 355 nm

5.1 Introduction

We are going to apply the method of obtaining the harmonic far-field characteristics developed in the previous chapter to the study of third harmonic generation in a gas of atomic hydrogen. In fact, the present aim is twofold - not only beam geometries, namely the Gaussian and the Bessel-Gauss beam, will be compared with respect to their overall efficiency in generating harmonics, but also the influence of an ac-Stark-shifted resonance both on atomic and medium properties will be investigated.

In order to make the comparison between a Bessel-Gauss beam and a reference Gaussian beam meaningful, we will consider only incident beams of equal power and peak focal intensity I_f, unless stated otherwise. Thus, when increasing the Bessel angle α of the Bessel-Gauss beam, its confocal parameter has to be increased according to Eq. (3.29). We expect the differences between Bessel-Gauss beams and their Gaussian beam limit to become more pronounced with increasing Bessel angle α. Accordingly, our first task will be to find, with the help of Eq. (4.104), a suitably large α_{opt}. In the following, we will take the initial atomic density to be $\mathcal{N}_0 = 4 \times 10^{18}$ atoms/cm^3 and assume a rectangular gas profile, as given in Appendix B with $g(\rho) = 1$, and a medium length $L = z_{\max} - z_{\min} = 0.5$ mm.

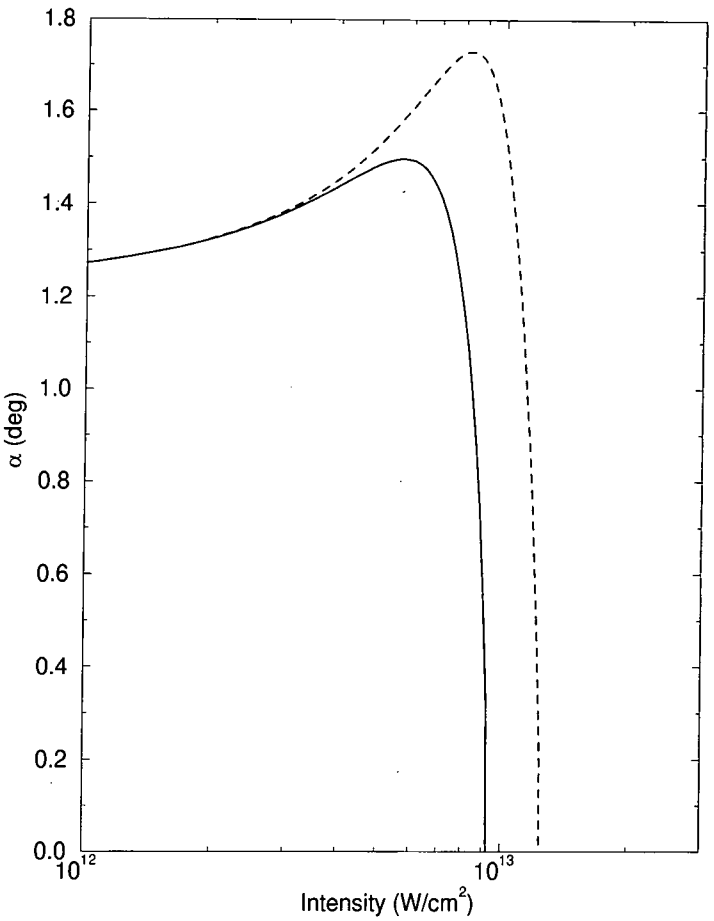

Figure 5.1: Optimum cone half-angle $\alpha_{\rm opt}$, defined by Eq. (4.104), as a function of the intensity. Solid line: The calculation includes photoionization (in the quasi-stationary approach), dashed line: photoionization is neglected.

5.2 The optimum Bessel angle

In a first step, we calculate the optimum value for the cone half-angle α as given by Eq. (4.104). For a given (initial) atomic density, this value will depend on the intensity-dependent generalized susceptibility as defined in Eq. (4.32). We take the intensity to be a simple parameter, and the ionization is taken into account in its time-independent version Eq. (4.78) according to the quasi-stationary approach outlined in section 4.5.1. The resulting curve $\alpha_{\rm opt} = \alpha_{\rm opt}(I)$ is shown in Fig. 5.1, both with and without photoionization being included in the calculation. The typical value found in the present case is $\alpha_{\rm opt} \approx 1.2^\circ - 1.4^\circ$ which is close to the value used by Glushko *et al.* [85] in the original experiment on self-phase-matching. To reach this value, we have to assume the fairly high value of the atomic density, as given

in the introduction. Though much higher densities have been used for rare gases in harmonic generation experiments [66], the present value has to be regarded as too high for an experiment to be carried out in atomic hydrogen as molecular hydrogen tends to form[1]. Lower densities could be used for a somewhat longer fundamental wavelength because of a larger negative susceptibility closer to the resonance (see Fig. 2.4). But also other atoms, such as the alkali metals, have large oscillator strengths and extensive regions of strongly negative dispersion requiring less dense media to achieve the same order of magnitude for $\alpha_{\rm opt}$. We keep the high density here, because, as pointed out in the introduction, if $\alpha_{\rm opt}$ is too close to zero one cannot expect a big difference between a Gaussian and a Bessel-Gauss beam.

Though Eq. (4.106) is only valid in the perturbative limit, we expect a fairly accurate prediction for $\alpha_{\rm opt}$ from the curve shown in Fig. 5.1 up to the resonance intensity. Indeed, the departure from the perturbative limit of the relevant atomic quantities with increasing intensity is very smooth (see Figs. 2.3 and 2.4). We expect further at least some qualitative insight into the behaviour of $\alpha_{\rm opt}$ at higher intensities. Considering first the curve neglecting photoionization in Fig. 5.1, one can see the optimum angle $\alpha_{\rm opt}$ to increase due to the corresponding variation of $\mathrm{Re}[\chi_{\rm at}(3\omega)]$. Indeed, the latter decreases until an intensity of about 8×10^{12} W/cm^2 is reached (Fig. 2.4). The medium then rapidly becomes positively dispersive and the value of $\alpha_{\rm opt}$ is purely imaginary, after having passed through zero. The role of the photoelectrons can be easily understood recalling the well known gas mixture technique for improving phase-matching [191]. Considering only the dispersive phase-mismatch [see Eq. (1.17)] for a two-component gas, of which one gas, $(\mathcal{N}_1, \chi_1)$, is negatively dispersive, the other one, $(\mathcal{N}_2, \chi_2)$, being positively dispersive, one obviously has

$$\Delta k_{\rm disp} \propto \mathcal{N}_1 \overbrace{[\chi_1(3\omega) - \chi_1(\omega)]}^{<0} + \mathcal{N}_2 \overbrace{[\chi_2(3\omega) - \chi_2(\omega)]}^{>0}, \tag{5.1}$$

and phase-matching can be achieved by adjusting the ratio of the two gas densities.

[1]The harmonic spectra of H_2 and H have been compared by Krause *et al.* [114]. Atomic and molecular hydrogen produce harmonics of comparable intensity and the spectra are very similar if the bond length of H_2 is stretched to match the ionization potential of atomic hydrogen [114]. Possibly in a regime where dissociation in a strong laser field is the dominant channel for H_2, an experiment using the hydrogen molecule would lead to results similar to those expected for atomic hydrogen.

In the present case, after a short glance at Eq. (4.32), the dispersive phase-mismatch can be written as

$$\Delta k_{\rm disp} \propto \mathcal{N}_0(1-f_{\rm ion})\{\overbrace{{\rm Re}[\chi_{\rm at}(3\omega)]-{\rm Re}[\chi_{\rm at}(\omega)]}^{<0}\}+\mathcal{N}_0 f_{\rm ion}\overbrace{[\chi_{\rm el}(3\omega)-\chi_{\rm el}(\omega)]}^{>0}, \tag{5.2}$$

and the two gas densities are replaced by the depletion of the atomic density and the built-up of a population of free electrons, respectively, due to increasing photoionization at higher intensities. Considering the orders of magnitude involved,

$$\begin{aligned} {\rm Re}[\chi_{\rm at}(3\omega, I\to 0)] &= -9.2\times 10^{-23}\,{\rm cm}^3 & \chi_{\rm el}(3\omega) &= -1.3\times 10^{-23}\,{\rm cm}^3 \\ {\rm Re}[\chi_{\rm at}(\omega, I\to 0)] &= 9.3\times 10^{-24}\,{\rm cm}^3 & \chi_{\rm el}(\omega) &= -1.1\times 10^{-22}\,{\rm cm}^3, \end{aligned}$$

it is easy to see that the dispersive phase-mismatch will be dominated by the atomic susceptibility at the third harmonic frequency and the electronic susceptibility at the fundamental frequency, both of which are of the same order of magnitude. The transition regime is in the range $8\times 10^{12}-1.2\times 10^{13}$ W/cm^2 approximately, where ionization is rapidly increasing (Fig. 2.5) and the sign of ${\rm Re}[\chi_{\rm at}(3\omega)]$ changing (Fig. 2.4). Thus, as can be seen from Fig. 5.1, the electronic contribution on one hand accelerates the change of sign of the overall dispersion, leading to an imaginary value of $\alpha_{\rm opt}$ even before the resonance is reached. On the other hand the electronic contribution balances the decrease of ${\rm Re}[\chi_{\rm at}(3\omega)]$ towards the resonance thus restricting the variation of $\alpha_{\rm opt}$ with the intensity. A control of phase-matching is therefore achieved to some extent. A similar use of the electronic contribution had already been suggested by Miyazaki and Kashiwagi [146] who considered third harmonic generation in sodium at intensities high enough to ionize the sodium atoms significantly. The large negative dispersion of the metal vapor[2] was compensated by adding xenon gas but a phase-mismatch was introduced at high intensities by the contribution of the free electrons to the index of refraction. This could in principle be compensated by taking the initial value of $\Delta k_{\rm disp}$ to be smaller than the optimum value when no free electrons are present. In their case, using $\lambda = 1064$ nm

[2]In their case the wavelength of the fundamental was $\lambda = 1064$ nm and ${\rm Re}[\chi_{\rm at}(3\omega)-\chi_{\rm at}(\omega)]\approx -3\times 10^{-22}{\rm cm}^3$. This value was intensity-independent due to negligible Kerr nonlinearities.

Table 5.1: Harmonic yield for a fixed focal intensity I_f of an incident Bessel-Gauss beam of cone half-angle α and confocal parameter b_{BG}. The results are normalized to unity for $\alpha = 0$. The focal intensity is (a) 1.0×10^{11} W/cm^2; (b) 5.0×10^{12} W/cm^2; (c) 9.0×10^{12} W/cm^2; (d) 1.1×10^{13} W/cm^2; (e) 1.3×10^{13} W/cm^2; (f) 3.0×10^{13} W/cm^2. Bold figures indicate the local maxima.

α (deg)	b_{BG} (mm)	(a)	(b)	(c)	(d)	(e)	(f)
0.00	2.0	1.00	1.00	1.00	1.00	1.00	1.00
0.35	3.2	1.01	1.08	1.06	1.01	1.03	0.96
0.40	3.9	1.02	1.14	**1.11**	**1.02**	1.06	0.90
0.45	5.4	1.04	1.24	1.08	**1.02**	**1.08**	0.83
0.50	7.4	1.07	1.31	1.08	0.98	1.01	0.71
0.55	9.5	1.11	1.38	1.03	0.92	0.88	0.66
1.00	33.7	1.75	4.80	1.14	0.71	0.87	7.05
1.05	37.2	**1.77**	5.38	1.18	0.73	0.94	8.53
1.10	40.8	**1.77**	5.91	1.23	0.75	1.02	10.05
1.15	44.7	1.73	6.36	**1.25**	**0.76**	1.07	11.54
1.20	48.7	1.66	6.69	**1.25**	**0.76**	1.10	12.87
1.25	52.8	1.55	**6.87**	1.23	0.75	**1.11**	13.72
1.30	57.1	1.42	**6.87**	1.17	0.71	1.09	14.36
1.35	61.6	1.26	6.70	1.10	0.67	1.04	**14.49**
1.40	66.3	1.08	6.34	1.01	0.61	0.96	14.04

radiation, controlling the phase-mismatch with the help of free electrons would have been a more difficult task due to the much larger electronic susceptibility. In contrast, because we want to find an optimum Bessel-Gauss beam for phase-matching, we aim at keeping the negative dispersion *large and constant*, as it determines the magnitude of α_{opt} according to Eq. (4.106).

The next step is to calculate the conversion efficiencies for a sufficiently large range of Bessel angles in order to find the optimum angle and to compare it with the theoretical predictions discussed above. The corresponding values of α_{opt}, calculated within the quasi-stationary approach as defined in Eq. (4.75), are shown in Fig. 5.2. In order to help interpreting the curves, results for a selection of intensities are shown in more detail in Table 5.1. Up to the resonance, we find the calculated values to follow closely the behaviour of the solid curve albeit at somewhat lower values of α. We will come back to this point when dealing with more refined aspects of phase-matching in the next chapter. The sharp drop and subsequent steep rise in the resonance region are artefacts of the way the data is presented. In fact,

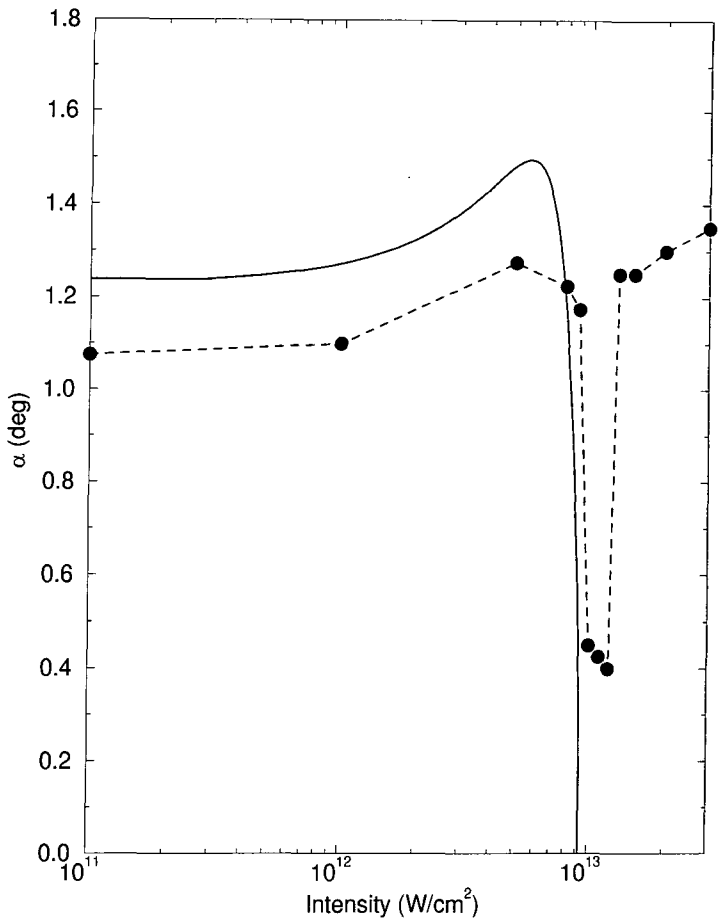

Figure 5.2: Optimum cone half-angle $\alpha_{\rm opt}$. The solid line is the same as in Fig. 5.1, the filled circles indicate the calculated values (see text). The dashed line is for guidance only.

as becomes clear from Table 5.1, a secondary maximum develops slowly around $\alpha \approx 0.45°$ as the intensity rises [column (c)] due to the sharp drop of $\alpha_{\rm opt}$ towards the resonance. This maximum takes gradually over the initial maximum around $\alpha = 1.2°$, and causes the dashed curve in Fig. 5.2 to jump discontinously as only the absolute maximum is shown. The jump back to the initial maximum can be easily explained considering the energy distribution in a Bessel-Gauss beam. Recalling from Fig. 3.2 that the bulk of the beam's power is in the secondary maxima, it is a straightforward matter to show that they are responsible for the renewed gain beyond the resonance. At less than 15 % of the intensity of the central peak (that is, at around 2 to 3×10^{12} W/cm^2), the secondary maxima are in a region of optimum phase-matching. Furthermore the medium in those regions is still undepleted in contrast to the central peak of the incident Bessel-Gauss beam which, at $I_{\rm f} = 2$ to 3×10^{13} W/cm^2 , ionizes rapidly the medium in a small cylindrical portion around

the axis of propagation. Indeed, masking the central peak reduces the conversion efficiency by about 90 % at $I_f = 5 \times 10^{12}$ W/cm^2, but by only 3 % at 3×10^{13} W/cm^2. The greater effective power available at these intensities manifests itself in a larger conversion efficiency as shown in column (f).

5.3 Conversion efficiency

Considering the intensity distribution in a real pulse, we expect some of the results of the previous section, valid at fixed I_f without temporal averaging, to be partly masked in a time-dependent calculation. The reason for this is the strong intensity dependence of the atomic data beyond the perturbative regime. The optimum angle α_{opt}, additionally to the spatial dependence which lead to the contribution of the secondary peaks of the incident beam as discussed in the previou section, will now rapidly change in time. We shall present calculations up to $I_f = 6 \times 10^{13}$ W/cm^2 , although atomic data are only available up to $I_f = 3 \times 10^{13}$ W/cm^2 (see section 2.2), based on the assumption that the regions of the atomic gas submitted to intensities above 3×10^{13} W/cm^2 are sufficiently depleted for atomic properties to be irrelevant. More quantitatively, consider the ionization probability at a given point in the medium. Recall that it can be written as

$$f_{ion}(I,u) = 1 - \exp\left\{-\frac{\tau}{2\sqrt{\ln 2}}\int_{-\infty}^{u}\Gamma[I\exp(-u'^2)]\,du'\right\}, \tag{5.3}$$

using the reduced time $u' = 2\sqrt{\ln 2}(t'/\tau)$. If I_0 is the maximum intensity at a given point in the medium, the probability that the atom is ionized before this intensity is reached is given by

$$f_0 = 1 - \exp\left\{-\frac{\tau}{2\sqrt{\ln 2}}\int_{-\infty}^{0.}\Gamma[I_0\exp(-u'^2)]\,du'\right\}. \tag{5.4}$$

If a higher peak intensity $I_1 > I_0$ is used, the rising pulse will reach the value of I_0 at an earlier time $u' = -u_1$, where $u_1 = \sqrt{\ln(I_1/I_0)} > 0$. The probability that the same atom has ionized when I_0 is reached is thus

$$f_1 = 1 - \exp\left\{-\frac{\tau}{2\sqrt{\ln 2}}\int_{-\infty}^{-u_1}\Gamma[I_1\exp(-u'^2)]\,du'\right\} \tag{5.5}$$

$$= 1 - \exp\left\{-\frac{\tau}{2\sqrt{\ln 2}}\int_{-\infty}^{0}\Gamma[I_0\exp(2u_1u')\exp(-u'^2)]\,du'\right\}. \tag{5.6}$$

Table 5.2: Ionization probability f_1 for a maximum pulse intensity I_1 when reaching the value $I_0 = 3 \times 10^{13}$ W/cm^2 . Data are for the dressed ground state of atomic hydrogen and $\tau = 15$ ps. Numbers in parenthesis indicate powers of ten.

I_1 [W/cm^2]	f_1 [%]
I_0	97.9
4 (13)	90.2
5 (13)	86.6
6 (13)	84.1
7 (13)	82.3
8 (13)	80.7
9 (13)	79.5
1 (14)	78.4

Comparing Eqs. (5.4) and (5.6) shows that always $f_1 < f_0$ for an ionization rate Γ which is an increasing function of the intensity. In our case $I_0 = 3 \times 10^{13}$ W/cm^2 , which is the maximum intensity for which the atomic data could be reliably computed. Table 5.2 gives the values for f_1 for intensities up to 10^{14} W/cm^2 . As can be seen from this table, about 16 % of the atoms survive the rising edge of a 15-ps laser pulse of peak focal intensity $I_f = 6 \times 10^{13}$ W/cm^2 until the intensity $I_0 = 3 \times 10^{13}$ W/cm^2 is reached. We assume that we can neglect the contribution of those remaining atoms in the calculations. To check the principle of such an approach within the range of available atomic data, we have performed a similar calculation for $I_0 = 2 \times 10^{13}$ W/cm^2 and $I_1 = 3 \times 10^{13}$ W/cm^2 successively including and neglecting all atomic data in the intensity range between I_0 and I_1. Despite a value of $f_1 = 78.1$ % in this particular case (that is, about 22 % of the atoms survive the pulse rise up to an intensity $I_0 = 2 \times 10^{13}$ W/cm^2), we have found only little difference in the results (conversion efficiency, spatio-temporal profiles) whether or not the atomic data in the intensity range 2 to 3×10^{13} W/cm^2 were included in the calculations at a peak focal intensity of $I_f = I_1 = 3 \times 10^{13}$ W/cm^2 .

In all of the following calculations we have fixed the Bessel angle to $\alpha = 1.2°$ as this value is close to α_{opt} for a large range of intensities as shown in the previous section. Hence we have to take $b_{BG} = 48.7$ mm for the value of the confocal parameter in order to match both the total power incident on target and the peak focal intensity

of a Gaussian reference beam with $\alpha = 0°$ and $b_G = 2$ mm (It is useful, at this point, to recall Fig. 3.2 before proceeding).

The full nonperturbative results for the Gaussian beam are reproduced in Fig. 5.3 for various cases as described in the figure caption. We first note that the quasi-stationary approach perfectly reproduces the fully time-dependent calculation when photoionization is neglected but underestimates the conversion efficiency when photoionization is taken into account, even though there is qualitative agreement between the two methods. Starting at $I_f = 10^{12}$ W/cm^2 , which is already somewhat beyond the perturbative regime for the Gaussian beam, an increasing phase-mismatch manifests in form of a shoulder in the curves as the medium becomes more and more negatively dispersive with increasing intensity. The phase-mismatch is beautifully illustrated by the data from the calculations where absorption has been neglected (open triangles): at around $I_f = 5 \times 10^{12}$ W/cm^2 the value for the conversion efficiency is even below the other curves, demonstrating that the harmonics generated in this regime start to interfere destructively within the medium if the harmonics created at intensities close to the peak focal intensity are not removed by absorption. As the intensity approaches the resonance region, however, α_{opt} tends quickly to zero (Fig. 5.1). As a consequence, the Gaussian beam becomes the optimum Bessel-Gauss beam and the conversion efficiency quickly raises. If it weren't for strong absorption at resonance, the conversion efficiency would even be larger than the corresponding perturbative value due to an enhanced atomic dipole moment (see Fig. 2.3). Beyond the resonance all curves including photoionization saturate and the conversion efficiency decreases slowly but steadily. If photoionization is neglected, an increasingly large fraction of the pulse contains intensities which favour a low α_{opt}, thus, together with missing target depletion, sustaining a continous raise in the conversion efficiency. Note that there is a small region close to resonance where the conversion efficiency including photoionization is actually larger than when photoionization is neglected. As target depletion affects the conversion efficiency just in the opposite way, this is clearly a phase-matching effect. This comes as no surprise, recalling that the medium changes from a negatively to a positively dispersive medium as the refractive index starts to be dominated by the

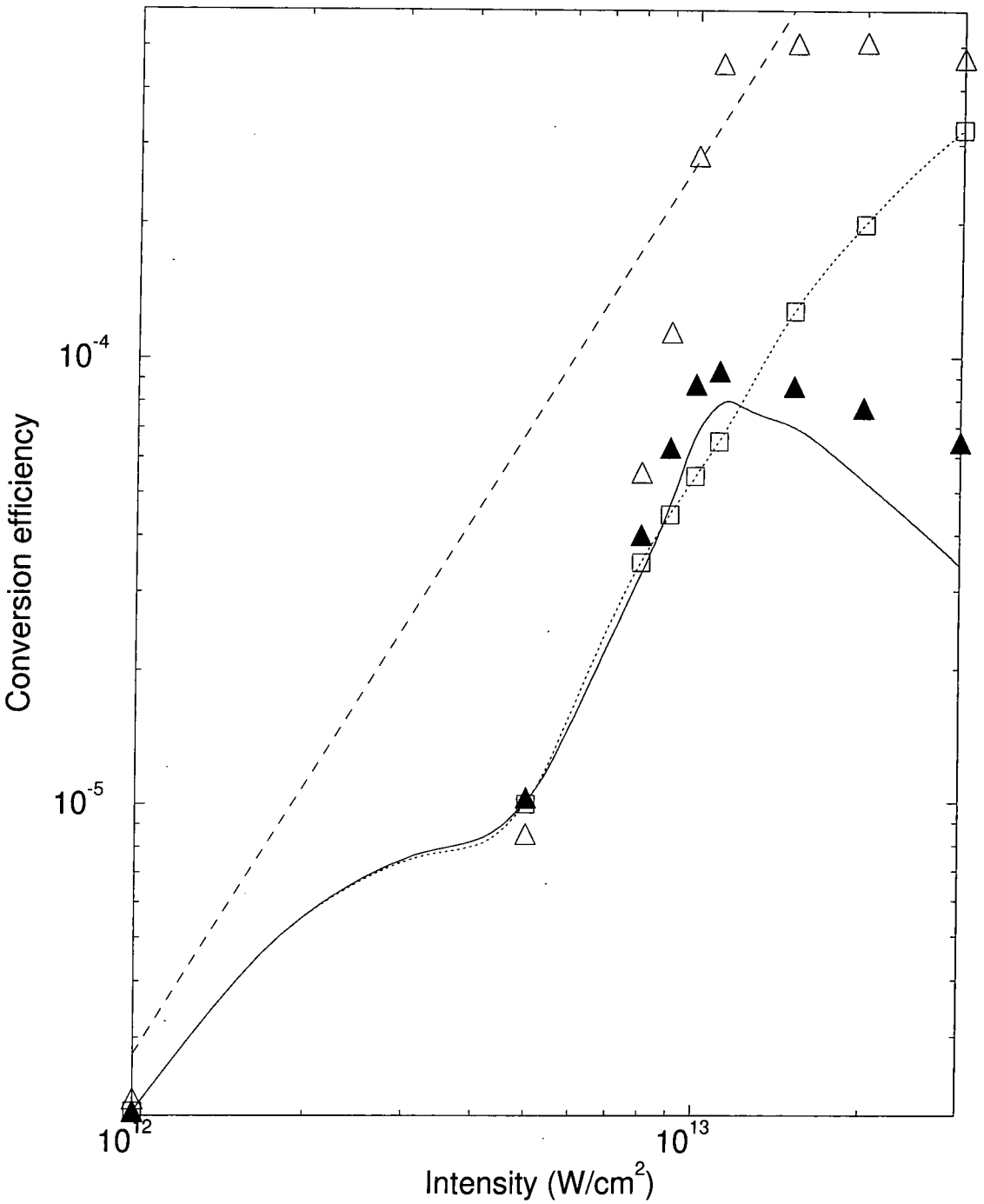

Figure 5.3: Conversion efficiency for a Gaussian beam ($\alpha = 0°$) versus the peak focal intensity I_f. The confocal parameter is $b_G = 2$ mm. The curves represent results of the quasi-stationary calculations. The markers represent results of the time-dependent calculations. Solid line and filled triangles: full results; dotted line and open squares: photoionization neglected; open triangles: same as filled triangles but with absorption neglected; dashed line: perturbation theory.

free-electron contribution[3].

The corresponding results are shown for the Bessel-Gauss beam in Fig. 5.4. They remain much closer to the perturbative limit compared to the Gaussian case, in fact, up to the resonance if absorption is neglected. The curve neglecting absorption does not cross the perturbative curve as in the Gaussian case, however, because the phase-mismatch has already become too important at this point (recall that the Gaussian beam is the optimum Bessel-Gauss beam in this region of intensities). A short transition period follows, where the contribution of the central maximum of the Bessel intensity profile quickly becomes negligible due to depletion (see end of section 5.2), resulting in a saturation of the conversion efficiency. Beyond the resonance, more and more secondary maxima reach a sufficiently high intensity to contribute appreciably to the harmonic generation process at optimum phase-matching. With photoionization being of less importance here than in the Gaussian case, the agreement of the quasi-stationary calculations with the full time-dependent calculations is much better than in Fig. 5.3.

Direct comparison of the conversion efficiencies for both beams up to $I_f = 6 \times 10^{13}$ W/cm^2 is illustrated in Fig. 5.5 for those curves which include photoionization. At the maximum intensity and for both absorption and photoionization taken into account, the conversion efficiency for the Bessel-Gauss beam is about five times higher than for the Gaussian beam. The saturation shown by the conversion efficiency of the Bessel-Gauss beam at the highest intensities is likely to come from the onset of absorption. This can be inferred both from the corresponding curve neglecting absorption (open triangles) which continues rising steeply and the similar saturation due to absorption below resonance, which affects the harmonic yield generated by the central peak of the Bessel-Gauss beam. As the conversion efficiency clearly exceeds 10^{-4} we have to remember the limitations set on the validity of one-colour ionization rate. We recall from section 2.3 (Fig. 2.5) that the one-colour ionization rate is likely to underestimate the true rate which can be significantly enhanced

[3]In fact, as neither the geometric nor the atomic dipole phase play a significant role in this case, the phase-mismatch for the Gaussian beam is roughly equally important far below and far above the resonance due the same order of magnitude of the relevant susceptibilities (see previous section).

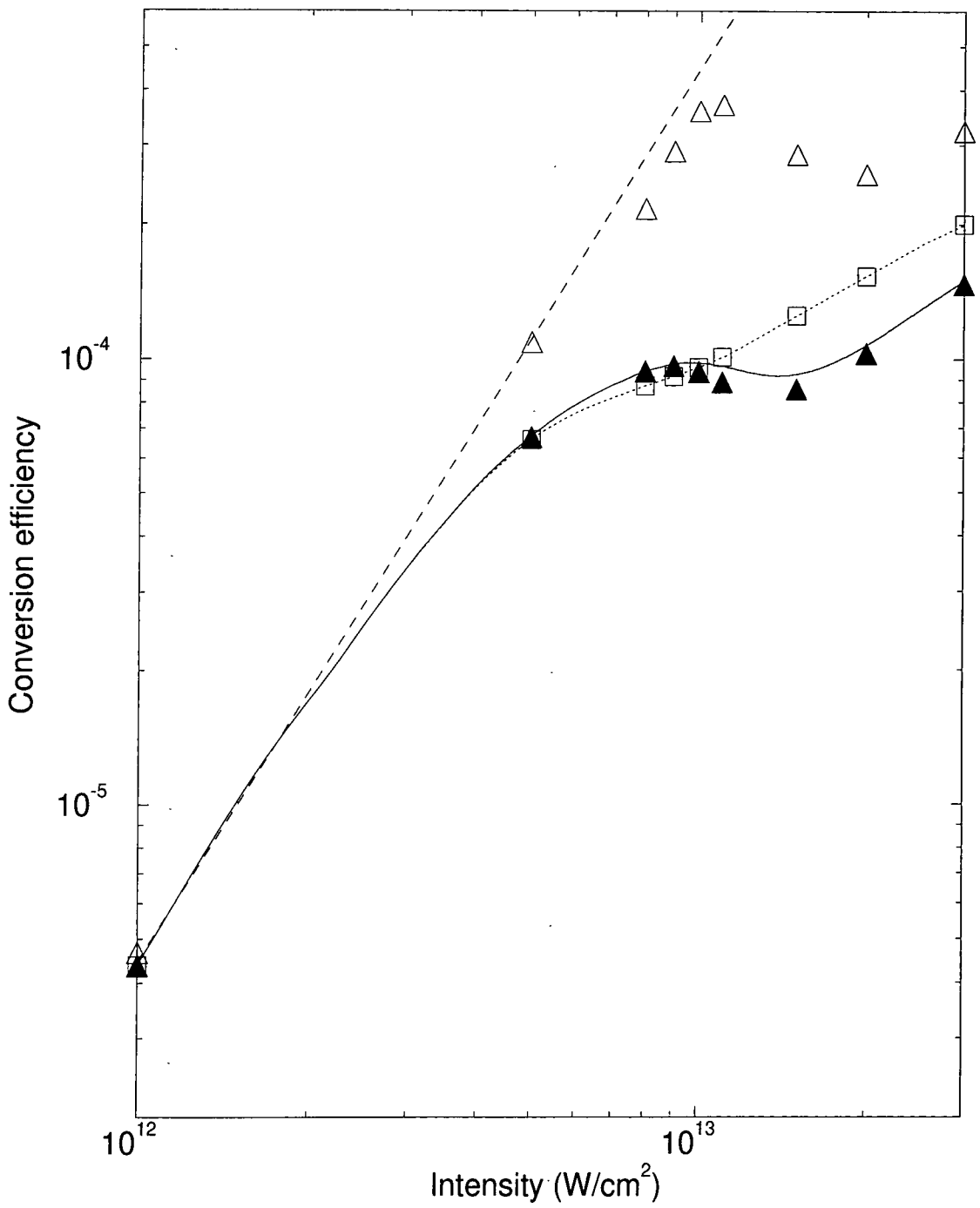

Figure 5.4: Same as Fig. 5.3 but for a Bessel-Gauss beam ($\alpha = 1.2°$). The confocal parameter is $b_{\mathrm{BG}} = 48.7$ mm.

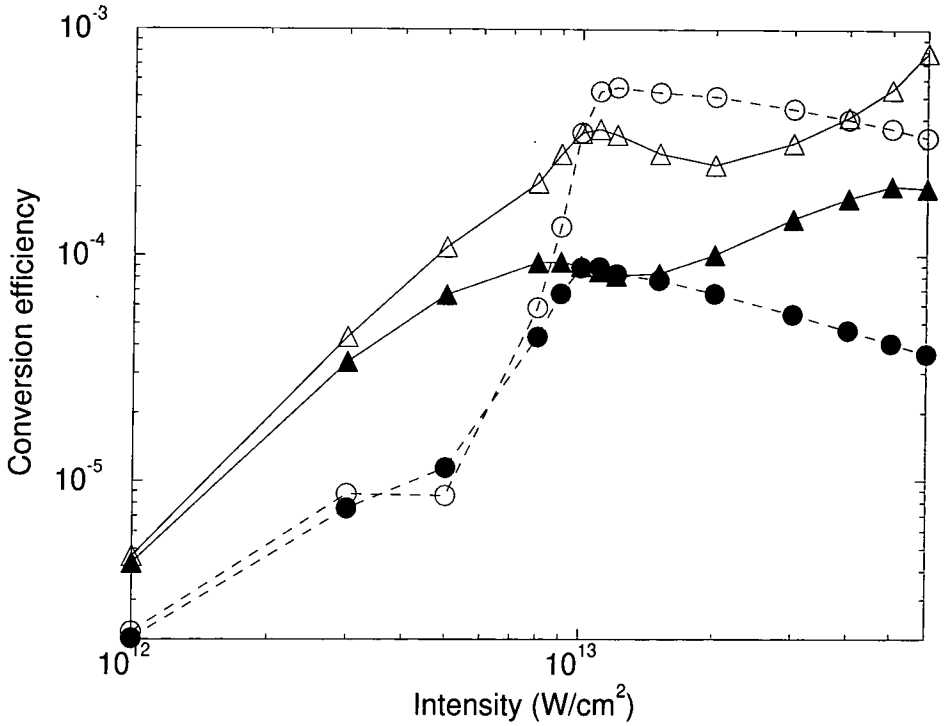

Figure 5.5: Comparison of conversion efficiencies up to $I_f = 6 \times 10^{13}$ W/cm^2 between the Gaussian (dashed lines) and the Bessel-Gauss beam (solid lines). The triangles are the same as in Fig. 5.4 (Bessel-Gauss beam), the circles are the same as the triangles in Fig. 5.3 (Gaussian beam).

by the presence of the strong third harmonic. However, as we have overestimated the ionization probability in the quasi-stationary calculations (Figs. 5.3 and 5.4), we may expect similar results for a calculation which would take two-colour ionization into account and the Bessel-Gauss beam would prove to be even more efficient because of the rapid target depletion in the case of an incident Gaussian beam.

How do the conversion efficiencies reported in the previous figures compare to values cited in the literature? For Gaussian beams, third harmonic generation using 355-nm radiation has been carried out by several workers in the past. For intensities typically in the range $10^{11} - 10^{13}$ W/cm^2 , Zych and Young [237] reported conversion efficiencies of nearly up to 1 % in a phase-matched xenon-argon mixture while Kung [118] used a pulsed supersonic xenon jet, achieving conversion efficiencies up to 10^{-4}, comparable to those obtained in the present study. Third harmonic generation in hydrogen was investigated by Liu *et al.* [126] using 1053-nm radiation, mainly for intensities much larger than the saturation intensity. In this plasma regime

the authors found only very low conversion efficiencies. More recently, Glushko *et al.* [85] (see section 3.2) measured a conversion efficiency of 1.5 % in frequency tripling of 1064-nm radiation focusing an annular beam in rubidium vapor. Peet and Tsubin [166] (see section 3.2) compared the efficiency of third harmonic generation in xenon close to the $6s$ resonance for Gaussian, annular ($\alpha \approx 3°$) and Bessel ($\alpha = 17°$) beams, however they could not directly measure the conversion efficiency of the latter due to the strong absorption of the harmonics within the medium. Indeed, for $\alpha = 17°$ to be an optimum phase-matching angle, a large dispersion is required. Such an order of magnitude can only be found very close to the resonance as is shown in Appendix C. Recently, Peatross *et al.* [163] obtained around 0.1 % conversion efficiency into the third harmonic by focusing 800-nm, 25-fs pulses in a gas cell backfilled with air or argon.

An interesting question at this point is, what happens to the conversion efficiency of the Gaussian beam when, at constant power, its peak focal intensity is varied. Results of the corresponding calculation are shown in Fig. 5.6. Each curve in this figure represents the conversion efficiency for a Bessel-Gauss beam with $\alpha = 1.2°$ and confocal parameter $b_{\mathrm{BG}} = 48.7$ mm, relative to that of a pure Gaussian beam of same power, versus the confocal parameter of the latter. Thus the peak focal intensity of the Gaussian beam varies along each curve, according to Eq. (3.28). The two beams have same peak focal intensity I_{f} for $b_{\mathrm{G}} = 2$ mm, which was the value adopted for drawing Fig. 5.3. Along each curve, I_{f} is higher (lower) for the Gaussian beam than for the Bessel-Gauss beam for $b_{\mathrm{G}} < (>)$ 2 mm. In relatively weak fields, a comparable or better conversion efficiency can be achieved with a focused Gaussian beam, as it drives the atomic dipole at higher intensity. However, in intense fields the Bessel-Gauss beam is always more efficient than a Gaussian beam of same power (the ratio always exceeds 1). As seen above, the conversion efficiency decreases rapidly above 1.1×10^{13} W/cm^2 in the Gaussian case, when photoionization becomes significant. The minimum of each curve in Fig. 5.6 occurs roughly at that intensity, and therefore moves to larger confocal parameters as the power increases[4].

[4]This figure differs slightly from the figure published in Ref. [43]. There, for both the quasi-

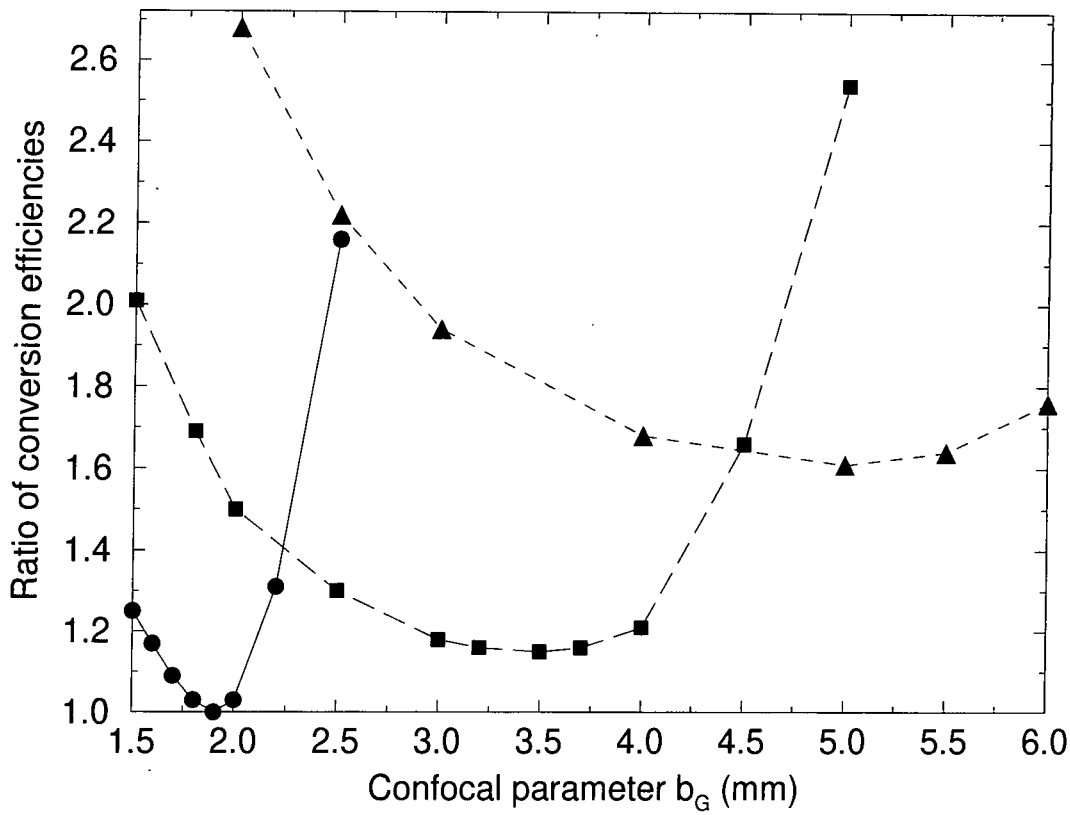

Figure 5.6: Conversion efficiency for an incident Bessel-Gauss beam ($\alpha = 1.2°, b_{BG} = 48.7$ mm) relative to that for an incident Gaussian beam of same power, versus the confocal parameter of the latter, b_G. The conversion efficiency is larger for the Bessel-Gauss beam when the ratio is larger than unity. The peak focal intensity I_f of the Bessel-Gauss beam is: circles: 1×10^{13} W/cm^2; squares: 2×10^{13} W/cm^2; triangles: 3×10^{13} W/cm^2. Each curve corresponds to a given total power incident on target. E.g. for $I_f = 10^{13}$ W/cm^2 , we obtain from from Eqs. (3.28) and (3.48) a total power of about 1.78×10^{10} mW, or, for $\tau = 15$ ps, a total energy of about 0.28 mJ on target.

As already mentioned in chapter 2, we have limited our calculations to the third harmonic of $\lambda = 355$ nm radiation because of lower atomic susceptibilities at higher harmonic frequencies,

$$\begin{aligned} \chi_{at}(5\omega) &\approx -5.4 \times 10^{-24}\,\mathrm{cm}^3 \\ \chi_{at}(7\omega) &\approx -2.8 \times 10^{-24}\,\mathrm{cm}^3 \\ \chi_{at}(9\omega) &\approx -1.7 \times 10^{-24}\,\mathrm{cm}^3 \end{aligned} \tag{5.7}$$

and, consequently, the low values which result for the optimum phase-matching angle α_{opt} for any reasonable value of the atomic density. Also, the propagation of the weaker 5^{th} - 9^{th} harmonics is likely to be influenced, at least in our case, by the strong

stationary approach and the time-dependent calculation, the approximation $b > 2L$ leading to the simplified expressions for the optical path integrals Eqs. (4.81) and (4.82) has been used.

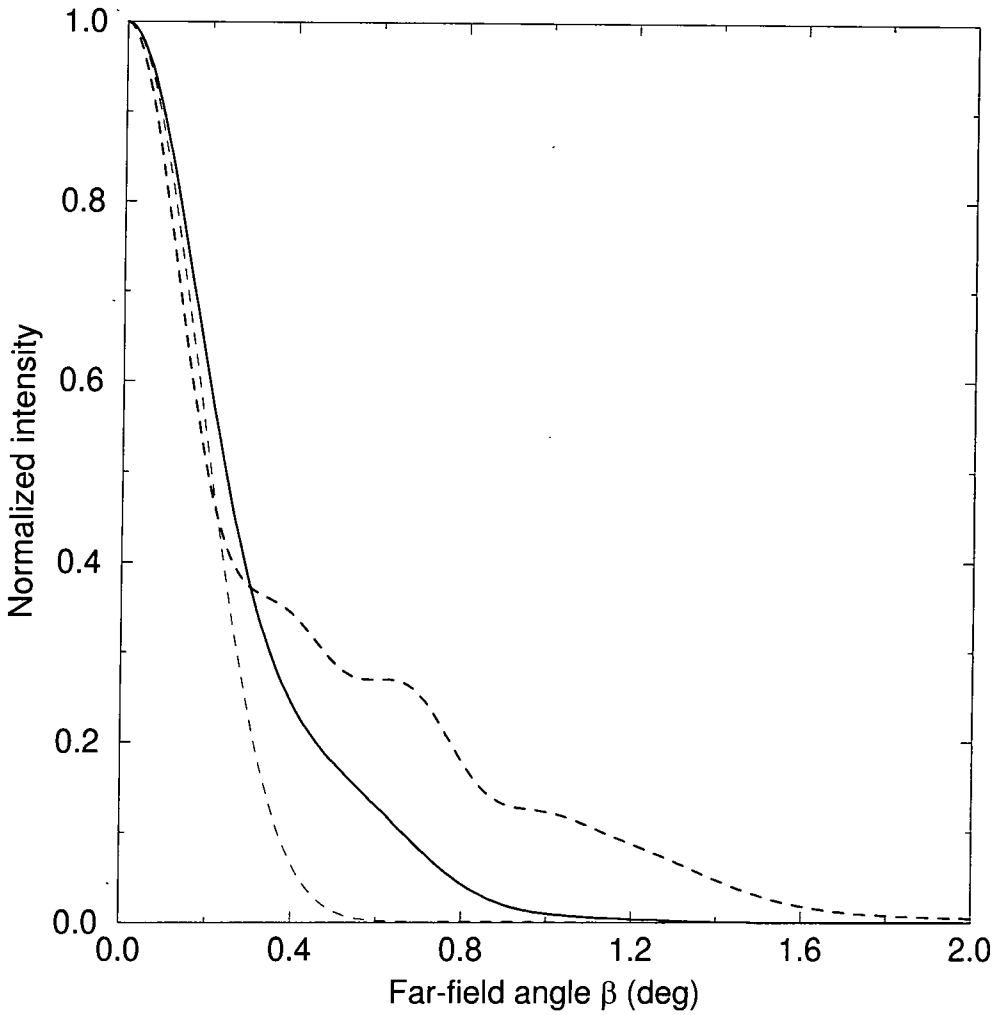

Figure 5.7: Far-field profile for a Gaussian beam ($\alpha = 0°, b_G = 2$ mm) as a function of the far-field angle β for various peak focal intensities I_f, obtained within the time-dependent approach. Thick dashed line: full calculation for $I_f = 3 \times 10^{13}$ W/cm^2 , thick solid line: same but for $I_f = 1 \times 10^{13}$ W/cm^2 , thin dashed line: same as thick dashed line but with photoionization neglected.

third harmonic and effects of harmonic coupling would have to be investigated. Though this is commonly neglected in most of the propagation calculations in the literature, the possibility of this to happen has been pointed out in a simplified case study by Pons and Plaja [171].

5.4 Spatial far-field profiles

The spatial far-field profiles, integrated over time as defined in Eq. (4.65) are shown and discussed in this section. For the Gaussian beam, they are shown in Fig. 5.7.

The harmonic profile is defocused for higher intensities due to the influence of the free electrons on the phase-matching conditions. Indeed, recall from Eq. (4.97) and the discussion thereafter, that strong ionization favours far-field angles $\beta > \alpha$. More precisely, an estimate from Eq. (4.97) using the data of section 5.2 yields $\beta \approx 1.1°$, consistent with the thick dashed curve shown in Fig. 5.7. We shall see in the next section, however, that the atomic phase contributes appreciably to the defocusing for the Gaussian beam. The radial phase-matching condition Eq. (4.101) favors $\beta = \alpha = 0°$ for the Gaussian beam, thus harmonics are emitted mainly along the propagation axis of the incident beam[5].

In contrast, the harmonic tends to be emitted along a cone in the Bessel-Gauss case (Fig. 5.8), with a preferred emission angle $\beta \approx \alpha/3 = 0.4°$ consistent with Eq. (4.101). Self-phase-matching manifests by slight variations of the preferred emission angle for a given α_{opt}. The broad maximum developing on axis for higher intensities arises from constructive interference between emissions from the secondary peaks of the incident beam. Its importance is less if photoionization is neglected (see Fig. 5.9) because the harmonic yield is then dominated by emission from the central peak of the incident beam. The far-field profile for a Bessel-Gauss beam calculated with photoionization included but absorption of the emitted harmonic neglected is also shown in Fig. 5.9. This profile was obtained for a peak focal intensity at which the susceptibility χ_3 is rapidly varying in the spatial region that contributes most to harmonic generation when absorption is turned off. That axial phase-matching favors smaller far-field angles β for lower values of $\text{Re}[\chi_3]$ manifests by the disappearance of the maximum at $\beta = 0.4°$. This effect is normally masked by the absorption of the harmonic photons at pump intensities close to the resonance.

Most interesting for applications is obviously the possibility of spatially separating the (strong) fundamental from the (weak) harmonic, peaking at different angles in the far-field. This had already been investigated experimentally by Peatross *et al.* [158] using annular beams. The high-order harmonics essentially peak on axis because β_{opt} tends to zero if the harmonic order q is large.

[5]In fact, the latter is a consequence of the pulse shape as the quasi-stationary calculation at fixed focal intensity I_f shows, that above the resonance off-axis emission can sometimes be larger than on-axis emission in the Gaussian case.

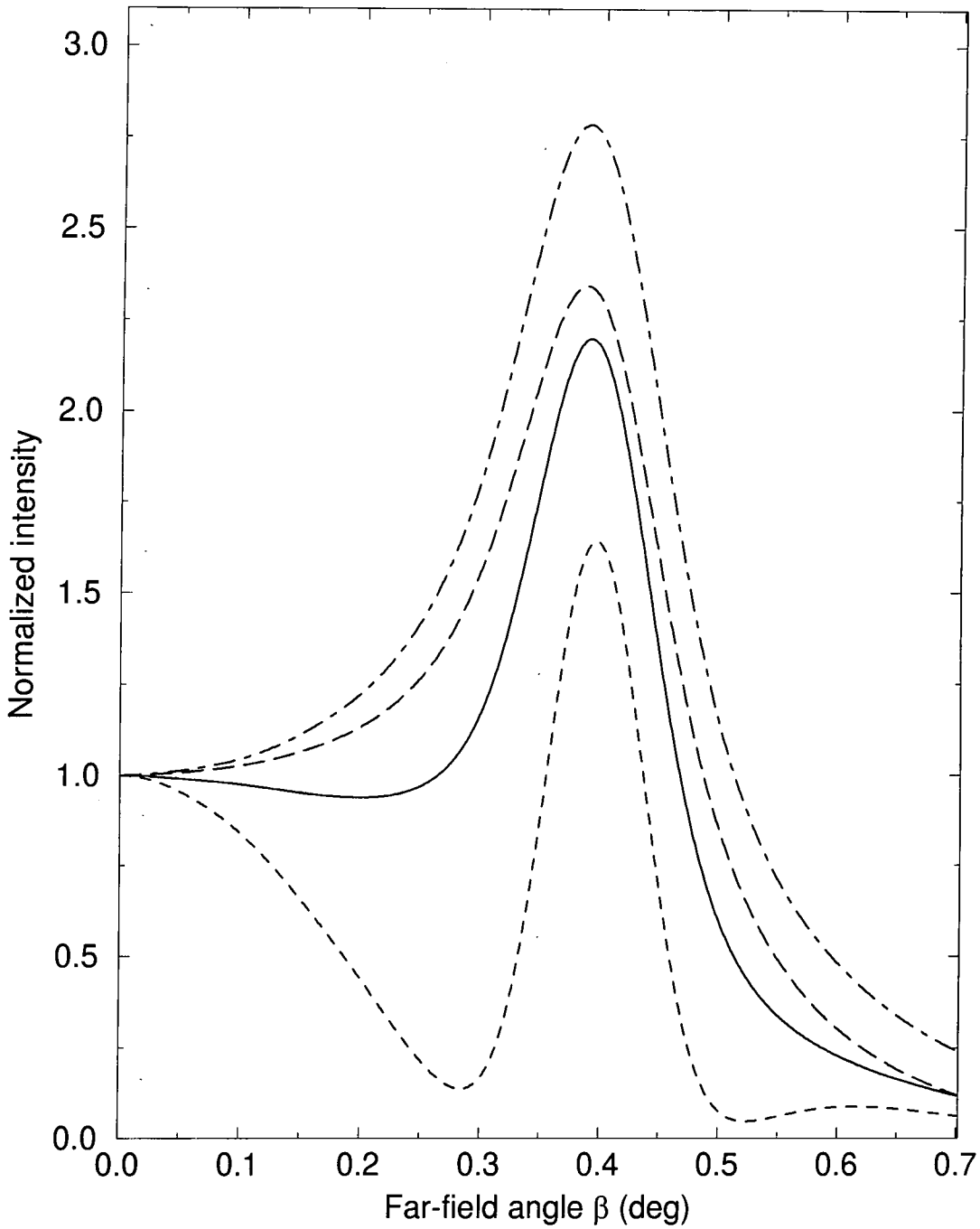

Figure 5.8: Far-field profile for a Bessel-Gauss beam ($\alpha = 1.2°, b_G = 48.7$ mm) as a function of the far-field angle β for various peak focal intensities I_f, obtained within the time-dependent approach (full calculation). Dashed line: $I_f = 3 \times 10^{13}$ W/cm^2 , solid line: $I_f = 1 \times 10^{13}$ W/cm^2 , long-dashed line: $I_f = 5 \times 10^{12}$ W/cm^2 , dot-dashed line: $I_f = 1 \times 10^{12}$ W/cm^2 .

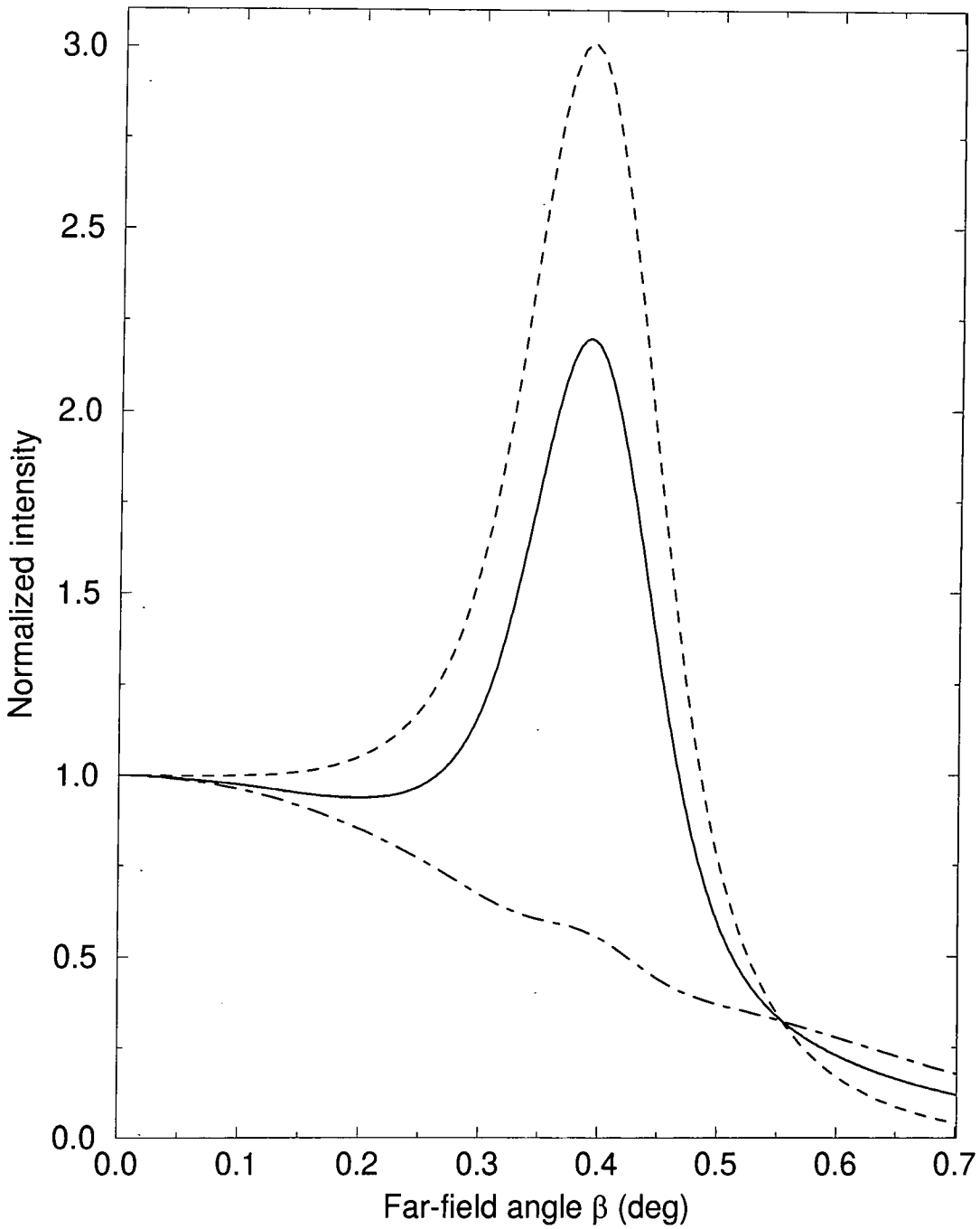

Figure 5.9: Far-field profile for a Bessel-Gauss beam ($\alpha = 1.2°, b_G = 48.7$ mm) as a function of the far-field angle β for various peak focal intensities I_f, obtained within the time-dependent approach for $I_f = 1 \times 10^{13}$ W/cm^2 . Solid line: full calculation (same as in Fig. 5.8), dashed line: photoionization neglected, dot-dashed line: absorption neglected.

5.5 The influence of the atomic dipole phase

As we have seen already in chapter 2, we expect the atomic dipole phase to be of secondary importance in the present calculations, essentially because of its slow overall variation and the fact that we are both in the loose focusing and long pulse regimes, thus limiting rapid spatio-temporal variations of the intensity within the medium. Indeed, computing the conversion efficiency for both the Gaussian and the Bessel-Gauss beam discussed in the previous sections, we find typically less than 10 % difference, if the atomic phase is neglected in the calculations. This was tested in the intensity range $I_f = 1$ to 3×10^{13} W/cm^2 , both for the full calculation and for the calculation neglecting photoionization, and has to be compared to changes in the conversion efficiency of nearly up to one order of magnitude that result from the successive inclusion and omission of photoionization and absorption in the calculations.

The impact of the atomic phase is more pronounced if the spatial far-field profiles are considered, as can be seen from Fig. 5.10. There, it appears clearly that part of the defocusing of the Gaussian beam, which we had attributed to the influence of the free electrons in the previous section, is actually due to the atomic phase, in agreement with the experimental findings of Peatross and Meyerhofer [159, 160]. As expected, the influence of the atomic phase is of lesser importance for the Bessel-Gauss beam at high intensities where the secondary maxima of the incident beam are responsible for harmonic generation. This corresponds to an intensity regime, where the atomic phase varies only little.

5.6 Temporal far-field profiles

The time profiles of the harmonic intensity, as defined in Eq. (4.63), further illustrate the striking differences between the two beams considered in the last section. As can be seen from Fig. 5.11, the time profile at the peak ($\beta \approx 0.4°$) of the harmonic generated by the Bessel-Gauss beam essentially retains the Gaussian profile of the

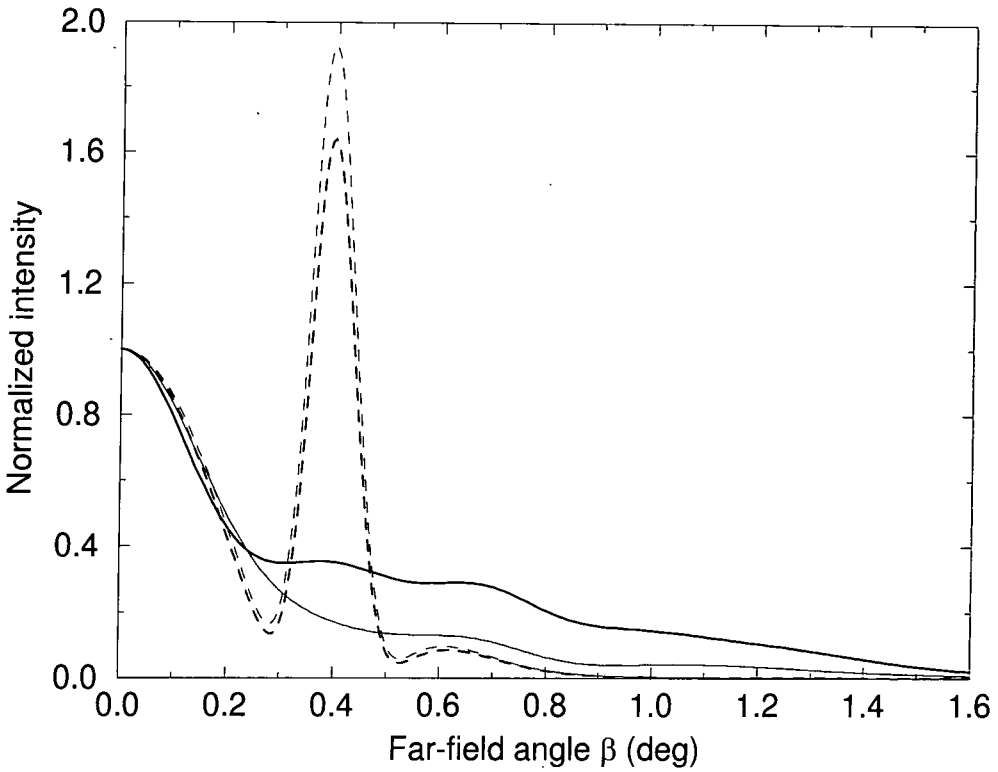

Figure 5.10: Influence of the atomic dipole phase on the spatial far-field profiles. Thick solid line: same as in Fig. 5.7, thick dashed line: same as in Fig. 5.8, thin lines: same as thick lines with the atomic dipole phase neglected in the calculations.

fundamental's temporal pulse shape, except for distorsions around the resonance. On the other hand, for the Gaussian beam at $\beta = 0°$ in Fig. 5.12, the pulse is cut into two distinct pulses at resonance, the two parts drifting apart in time as the intensity increases. The analysis of the corresponding time-profiles neglecting photoionization and/or absorption suggests that there are essentially two reasons for this: Firstly, the Gaussian beam is better phase-matched towards the end of the pulse than on the rising edge because, as noted earlier, the population of free electrons built-up by photoionization compensate for the negatively dispersive atomic susceptibility. As a consequence Δk_{disp} vanishes in Eq. (5.2) and so does α_{opt} in Eq. (4.106). Hence, the Gaussian beam becomes optimally phase-matched. Secondly, absorption, following the time profile of target depletion, affects only the main part of the harmonic pulse created at the rising edge of the fundamental, whereas the second part of the harmonic pulse travels in an absorption-free medium.

Note also that in the perturbative regime, the pulselength of the harmonic is given

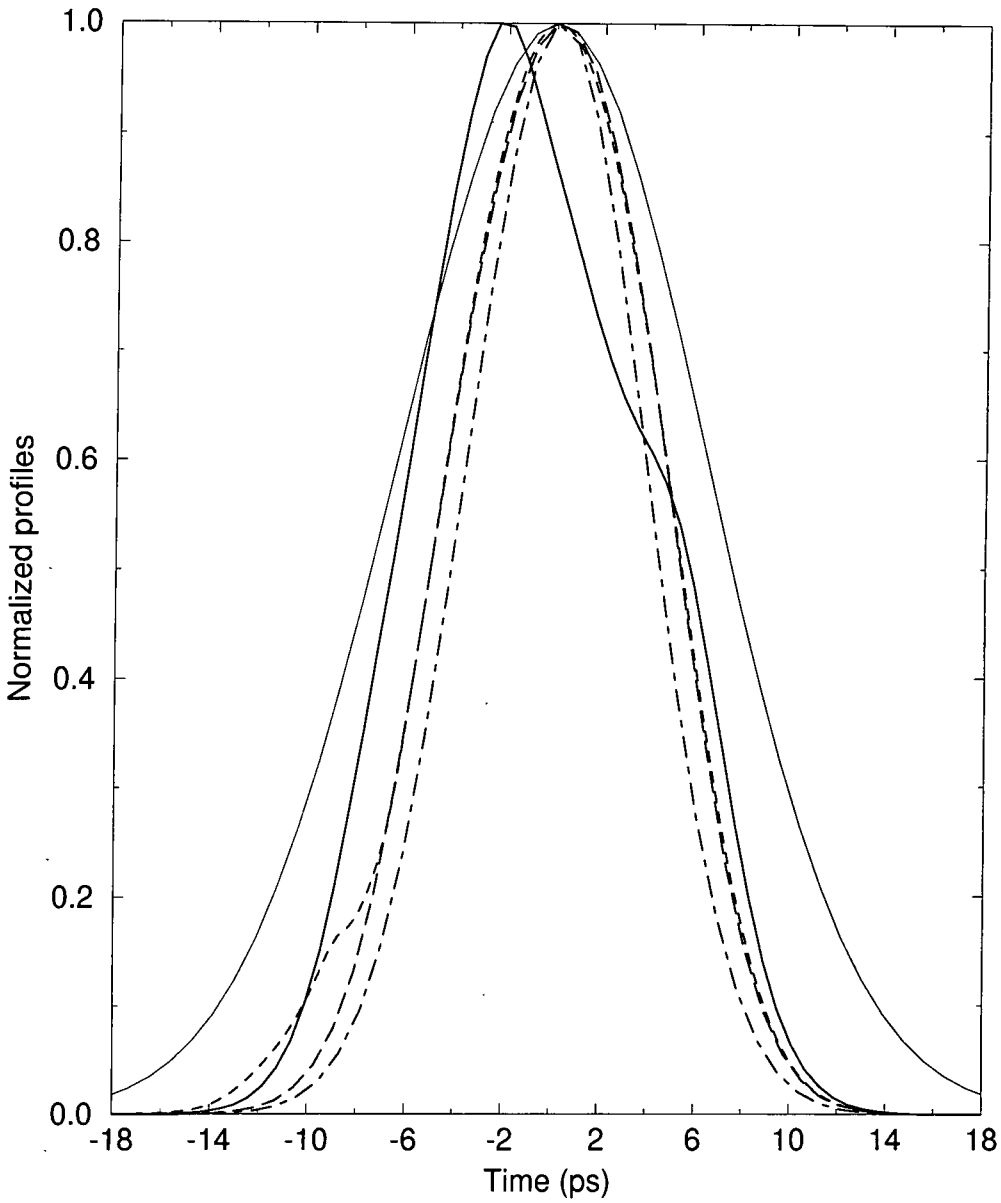

Figure 5.11: Time profiles for the Bessel-Gauss beam for various peak focal intensities (full calculation). The thin solid line shows the Gaussian time profile of the incident beam. The thick lines are, dot-dashed: $I_f = 1 \times 10^{12}$ W/cm^2 , long-dashed: $I_f = 5 \times 10^{12}$ W/cm^2 , solid: $I_f = 1 \times 10^{13}$ W/cm^2 , and dashed: $I_f = 3 \times 10^{13}$ W/cm^2 , respectively.

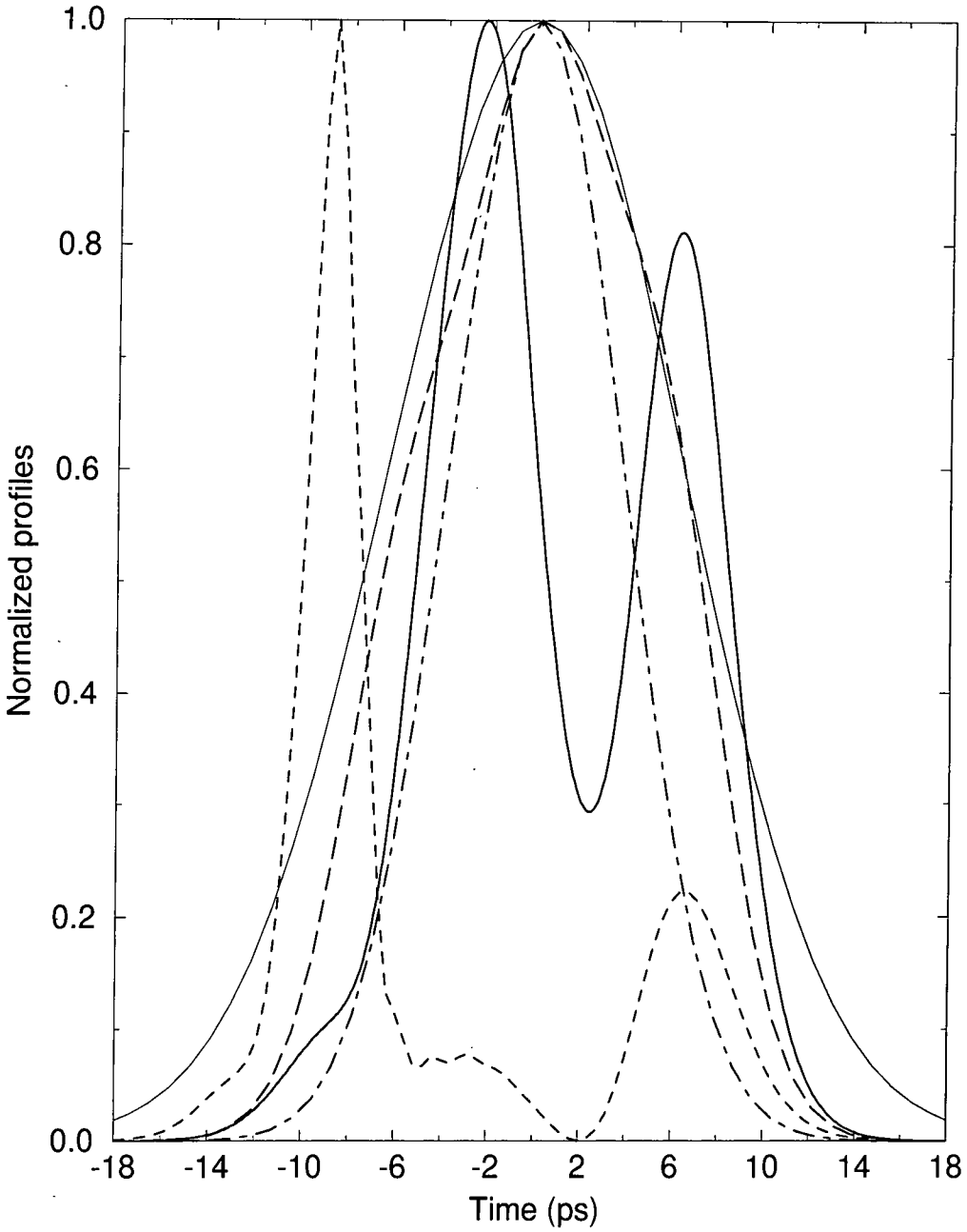

Figure 5.12: Time profiles for the Gaussian beam for various peak focal intensities (full calculation). The thin solid line shows the Gaussian time profile of the incident beam. The thick lines are, dot-dashed: $I_f = 5 \times 10^{11}$ W/cm^2 , long-dashed: $I_f = 5 \times 10^{12}$ W/cm^2 , solid: $I_f = 1 \times 10^{13}$ W/cm^2 , and dashed: $I_f = 3 \times 10^{13}$ W/cm^2 , respectively.

by[6] $\tau_q = \tau/\sqrt{q}$. For $q = 3$ and $\tau = 15$ ps this yield $\tau_3 \approx 8.7$ ps, in very good agreement with the pulselength of the harmonic at low-intensity shown in Figs. 5.11 and 5.12.

[6]This is an immediate consequence of the power law Eq. (2.21) of the dipole moment in the perturbative limit.

Chapter 6

Phase-matching Revisited

6.1 Introduction

In the present chapter we are going to investigate in much more detail the phase-matching conditions we have derived in a simplified form in section 4.5.2. Recall from there that expression Eq. (4.102) for the optimum Bessel angle $\alpha_{\rm opt}$ had been derived in the loose focussing limit $L/b \ll 1$, a reasonable criterion for validity being given by the requirement $b > 2L$. Though of secondary importance in connection with the calculations of chapter 5, the geometric phases, represented by the terms in z/b in Eq. (4.73) might otherwise contribute significantly to the determination of the optimum angle $\alpha_{\rm opt}$. We shall answer this question by giving a more general expression for the optimum Bessel angle, and we will subsequently test the new formula with the help of extensive numerical calculations, similar to those in section 5.2 but here using the full time-dependent code. At the same time, we will have a closer look at the approximations involved in deriving the expression for the optimum Bessel angle. Concerning the conversion efficiency for Bessel-Gauss beams we will draw conclusions which are, in fact, largely independent of the atomic gas considered, and we will support those conclusions by comparing corresponding results from calculations for both atomic hydrogen and xenon. We will report cases where the conversion efficiency significantly exceeds the corresponding values in the Gaussian beam limit. Very much as in section 4.5.2, the formulas derived in the following

will be, strictly speaking, only valid in the perturbative limit. We have seen in chapter 5 under which circumstances they can remain valid when the non-perturbative regime is entered. In this chapter we will consider only low-order harmonics in the perturbative regime for the sake of illustrating the effects of phase-matching. For high-order harmonic generation at high intensities we refer to our calculation in argon, reported in chapter 7.

6.2 Phase-matching and conversion efficiency

6.2.1 Preliminary remarks

In section 4.5.2 we had obtained the optimum Bessel angle by eliminating the far-field angle β between the two phase-matching conditions, the radial phase-matching condition Eq. (4.101) and the axial phase-matching condition Eq. (4.96). It is clear, that though we define unambigiously an angle $\alpha = \alpha_{\text{opt}}$ in this way, where the two maxima of the phase-matching conditions coincide for the same far-field angle β, we cannot make any definite statement about the resulting conversion efficiency as a function of α. Indeed, we had only assumed on these grounds the angle α_{opt} to be a good estimate for the Bessel angle which maximizes the conversion efficiency. However there is no reason, a priori, why optimum phase-matching should be tantamount to maximum conversion efficiency for $\alpha > 0°$. Firstly, it could be possible to achieve higher conversion efficiencies for angles $\alpha \neq \alpha_{\text{opt}}$ for which the two phase-matching conditions are fulfilled *separately*, that is for two different values of the far-field angle (over which we will have to integrate to get the harmonic yield), secondly, the *values* of the maxima of the phase-matching conditions might also depend on the Bessel angle α. In the following we shall therefore refer to α_{opt} as the optimum Bessel angle for phase-matching and to α_{max} as the Bessel angle for which the conversion efficiency has its absolute maximum[1]. The dependence of the conversion efficiency on the Bessel angle α can be obtained as follows: The far-field amplitude

[1]We continue to call α_{opt} the optimum Bessel angle because other potential applications for Bessel(-Gauss) beams might require optimum phase-matching without aiming primarily at maximum conversion efficiencies.

Eq. (4.85), as a function of the far-field variables (ρ', z'), can be written as

$$|E_q^{(0)}(\rho', z')|^2 \propto \frac{1}{z'^2 + \rho'^2} |F_z|^2 |G_\rho|^2 . \tag{6.1}$$

Here, F_z is the axial integral Eq. (4.86) and G_ρ is the radial integral Eq. (4.100) which we rewrite here as

$$G_\rho = \int_0^{+\infty} \mathrm{d}\rho\, \rho J_0(A\rho) J_0^q(B\rho) \exp(-\sigma^2\rho^2) , \tag{6.2}$$

where

$$A = qk_{0,1} \sin\beta , \qquad B = k_{0,1} \sin\alpha , \qquad \sigma^2 = qk_{0,1}/b . \tag{6.3}$$

The conversion efficiency, from Eq. (4.66), is then given by

$$\eta_q \propto \int_0^{+\infty} \frac{\rho' \,\mathrm{d}\rho'}{z'^2 + \rho'^2} |F_z|^2 |G_\rho|^2 . \tag{6.4}$$

Recalling $\tan\beta = \rho'/z'$ we finally obtain

$$\eta_q(\alpha) \propto \int_0^{\pi/2} \mathrm{d}\beta \, \tan\beta \, |F_z(\alpha, \beta)|^2 |G_\rho(\alpha, \beta)|^2 . \tag{6.5}$$

For large confocal parameters, σ^2 vanishes and G_ρ is sharply peaked for $A = B$ (see Refs. [217,218] and Eq. (3.7)), therefore selecting a precise value of the far-field $\beta = \alpha/q$. The optimum Bessel angle is then obtained by solving for the absolute maximum of $F_z(\alpha_{\mathrm{opt}}, \alpha_{\mathrm{opt}}/q)$. Though this corresponds to optimum phase-matching for the same value of β, even in this limit it *does not guarantee* $\alpha_{\mathrm{max}} = \alpha_{\mathrm{opt}}$. Indeed, though we take F_z at its absolute maximum and G_ρ at a relative maximum, the latter is not the largest value the radial integral can take on. The absolute maximum of the radial integral is always

$$G_\rho(\alpha = 0°, \beta = 0°) = 1/2\sigma^2 , \tag{6.6}$$

thus favouring $\alpha = 0°$. The relative maxima of G_ρ obtained for $\alpha > 0°$ are decreasing with the Bessel angle. This feature accounts for the potential loss of driving power as the central peak of the incident Bessel-Gauss beam becomes narrower with increasing Bessel angle α, a feature we had already pointed out in the concluding remarks of chapter 4. The impact of this effect on the conversion efficiency can obviously not be predicted from phase-matching considerations alone.

It is of course possible to investigate Eq. (6.5) numerically to obtain the precise nature of the function $\eta_q(\alpha)$. As this, however, amounts essentially to solving the propagation problem, except for the time integration, we try in the following to justify in more detail the simple approach of section 4.5.2. It led to expression Eq. (4.104) for the optimum Bessel angle α_{opt} which, in chapter 5, was found - after all - to be a reliable prediction for the angle α_{max}, corresponding to the maximum conversion efficiency. In a first step, we note from the radial and axial phase-matching conditions of section 4.5.2 that the influence of the radial phase-matching condition on the determination of the optimum Bessel angle is rather limited. If we assume $\beta_{\mathrm{opt}} \leq \alpha_{\mathrm{opt}}/q$, the contribution of the radial phase-matching condition amounts to the factor $[q^2/(q^2-1)]^{1/2}$ in Eq. (4.104), which is of importance for $q = 3$ at most. In the limit $\beta = 0°$ this factor disappears alltogether. It is thus reasonable to start our investigation by taking the axial integral F_z out of the integrand at some value β_0 to be determined later,

$$\eta_q(\alpha) \propto |F_z(\alpha, \beta_0)|^2 \int_0^{\pi/2} \mathrm{d}\beta \, \tan\beta \, |G_\rho(\alpha, \beta)|^2. \tag{6.7}$$

We can see that if the remaining integral Eq. (6.7) (not $G_\rho(\alpha, \beta)$ alone) is weakly dependent on α with respect to F_z, we can indeed expect the maximum of $\eta_q(\alpha)$ to be determined by the axial integral alone, hence $\alpha_{\mathrm{max}} \approx \alpha_{\mathrm{opt}}$. This is likely to be the case if F_z is strongly peaked itself while the loss of driving power associated with the radial integral is not too important. Thus we need to know the behaviour of $G_\rho(\alpha, \beta)$ in more detail. This is the subject of the following section.

6.2.2 Radial phase-matching

We recall first the derivation of the radial phase-matching condition, Eq. (4.101), by inspection of the integral Eq. (6.2). For odd harmonic orders q the integrand of Eq. (6.2) is positively definite if $A = B$. Lacking an analytical expression for this integral, we concluded that this maximizes the integral, therefore $A = B$ being the radial phase-matching condition. This conclusion was assumed to be independent of the harmonic order as long as q is an odd integer. We will show now that $A = B$ is the maximum only for large confocal parameters (Bessel beam limit), such as those

considered in section 4.5, and investigate the changes occuring for smaller confocal parameters. For this we determine the maxima of the integral Eq. (6.2) for a given B. Before considering an arbitrary (odd) q, we investigate the case $q = 1$. Indeed, the solution of Eq. (6.2) is known for $q = 1$ and given by Eq. (3.26) as

$$\int_0^{+\infty} \mathrm{d}\rho\, \rho \exp(-\sigma^2\rho^2) J_0(A\rho) J_0(B\rho) = \frac{1}{2\sigma^2} \exp\left(-\frac{A^2+B^2}{4\sigma^2}\right) I_0\left(\frac{AB}{2\sigma^2}\right). \quad (6.8)$$

Letting

$$x = A/\sqrt{2}\sigma = \sqrt{\pi b/\lambda}\,\sqrt{q}\sin\beta\,, \qquad \xi = B/\sqrt{2}\sigma = \sqrt{\pi b/\lambda}(1/\sqrt{q})\,\sin\alpha\,, \quad (6.9)$$

we find for $q = 1$ that the zeroes of the derivative with respect to x of the function

$$f_\xi(x) = \exp[-(x^2+\xi^2)/2] I_0(x\xi) \quad (6.10)$$

are given by

$$f'_\xi(x) = \exp[-(x^2+\xi^2)/2][\xi I_1(x\xi) - x I_0(x\xi)] = 0\,. \quad (6.11)$$

For small arguments of the modified Bessel functions in Eq. (6.11) we have $[\xi I_1(x\xi) - xI_0(x\xi)] \approx x(\xi^2/2 - 1)$, thus $x = 0$ is a maximum independently of ξ up to $\xi = \sqrt{2}$. For large arguments of the Bessel functions we have $[\xi I_1(x\xi) - xI_0(x\xi)] \approx \xi - x$ and $x = \xi$ is the maximum of $f_\xi(x)$ in this limit. The full plot of the function $x = x(\xi)$ for which there is a maximum is shown in Fig. 6.1. We see that the maximum condition $A = B$ (that is $x = \xi$) holds both asymptotically and for $x = \xi = 0$. In Fig. 6.1 we can distinguish three regions, approximately defined as

$$0 \le \xi \le \xi^{(0)} \quad , \qquad \xi^{(0)} = \sqrt{2} \quad (6.12)$$

$$\xi^{(0)} \le \xi \le \xi^{(1)} \quad , \qquad \xi^{(1)} \approx 3 \quad (6.13)$$

$$\xi^{(1)} \le \xi < +\infty \quad , \quad (6.14)$$

which correspond to $x = 0$ ($\beta = 0°$), a transitory region where x increases rapidly with ξ, and the asymptotic region $x = \xi$ ($\beta = \alpha/q$), respectively. This translates, according to Eq. (6.9), into the following bounds for the corresponding angles α,

$$0 \le \alpha \le \alpha^{(0)}\,, \qquad \alpha^{(0)} = \xi^{(0)}\sqrt{\lambda/b\pi}\,, \qquad \beta = 0° \quad (6.15)$$

$$\alpha^{(0)} \le \alpha \le \alpha^{(1)}\,, \qquad \alpha^{(1)} = \xi^{(1)}\sqrt{\lambda/b\pi}\,, \qquad 0° \le \beta \le \alpha/q \quad (6.16)$$

$$\alpha^{(1)} \le \alpha < +\infty\,, \qquad \beta = \alpha/q \quad (6.17)$$

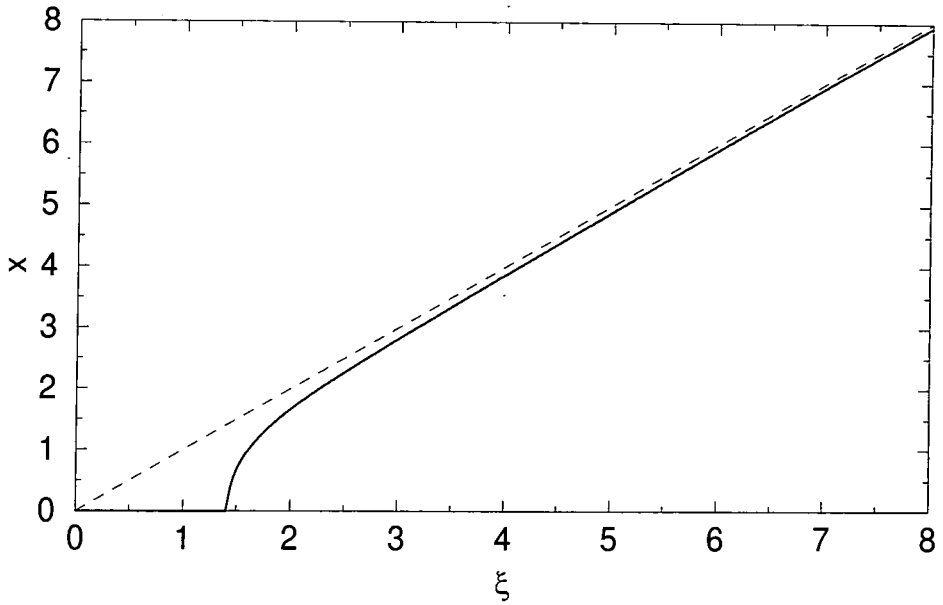

Figure 6.1: Thick solid line: plot of the function $x = x(\xi)$ maximizing the integral Eq. (6.8), x and ξ being defined by Eq. (6.9). The dashed line is $x = \xi$.

where $q = 1$. Obviously $\alpha^{(0)} = \alpha^{(1)} = 0°$ in the limit $b \to +\infty$ and the maximum condition is then always $A = B$ for any given B.

How are these features changing when we consider harmonic orders $q > 1$? Because of the similarity of the Bessel and the trigonometric functions, we can model these cases by replacing Eq. (6.2) with

$$\tilde{G}_\rho = \int_0^{+\infty} \mathrm{d}\rho \cos(A\rho) \cos^q(B\rho) \exp(-\sigma^2\rho^2) . \tag{6.18}$$

Using integral 3.898.2 of Ref. [88] we obtain for $q = 1$, following the same steps as above, a function $f_\xi^{(q=1)}$ and its derivative with respect to x given by

$$f_\xi^{(q=1)}(x) = \exp[-(x^2 + \xi^2)/2] \cosh(x\xi) , \tag{6.19}$$

and

$$f_\xi^{(q=1)'}(x) = \exp[-(x^2 + \xi^2)/2][\xi \sinh(x\xi) - x \cosh(x\xi)] , \tag{6.20}$$

respectively. The difference between expression (6.10) and (6.19) is that we have $\exp(-x)I_0(x) \sim 0.4/\sqrt{x}$ for large x while $\exp(-x)\cosh(x)$ converges towards 0.5 in the same limit. As can be easily seen, this does not affect the maximum condition in the limits $\xi \ll 1$ and $\xi \gg 1$, in which we are particularly interested in. Indeed,

we have both $\cosh(x) \sim \mathrm{d}\cosh(x)/\mathrm{d}x = \sinh(x)$ and $I_0(x) \sim \mathrm{d}I_0(x)/\mathrm{d}x = I_1(x)$ for large x, as well as $\cosh(0) = I(0) = 1$ and $\sinh(0) = I_1(0) = 0$. More precisely, for $x \ll 1$ we find $\sinh(x) \sim x$ while $I_1(x) \sim x/2$. This is the reason why we obtain $\xi^{(0)} = 1$ using Eq. (6.20) compared to $\xi^{(0)} = \sqrt{2}$ using Eq. (6.11). Thus, to make the modelling more adequate, we replace $\sinh(x)$ by $x/2$ in the limit $x \ll 1$.

After these preliminaries we are now ready to tackle the case of an arbitrary harmonic order. The corresponding power of q in Eq. (6.18) can be easily linearized using

$$\cos^q(B\rho) = \frac{1}{2^{q-1}} \sum_{k=0}^{(q-1)/2} \binom{q}{k} \cos[(q-2k)B\rho]\,, \tag{6.21}$$

which is valid for odd integers q. Straightforward algebra leads to the function

$$\begin{aligned} f_\xi^{(q)}(x) &= \exp[-(x^2+\xi^2)/2] \\ &\times \sum_{k=0}^{(q-1)/2} \binom{q}{k} \exp\{-[(q-2k)^2-1]\xi^2/2\} \cosh[(q-2k)x\xi]\,, \end{aligned} \tag{6.22}$$

which reduces to Eq. (6.19) for $q = 1$. Differentiating $f_\xi^{(q)}(x)$ with respect to x, we find that the expression determining the zeroes x is now given by

$$\begin{aligned} &\textstyle\sum_{k=0}^{(q-1)/2} \binom{q}{k} \exp\{-[(q-2k)^2-1]\xi^2/2\} \\ &\times\{\xi(q-2k)\sinh[(q-2k)x\xi] - x\cosh[(q-2k)x\xi]\} = 0 \quad . \end{aligned} \tag{6.23}$$

The asymptotic limit $x, \xi \gg 1$ is determined by the only term in Eq. (6.23) which is not exponentially decaying, that is for $k = (q-1)/2$. Because $q - 2k = 1$ and $\sinh(x\xi) \sim \cosh(x\xi)$ in this limit we find again $x = \xi$ as being the (asymptotic) maximum condition, hence $\beta = \alpha/q$ from Eq. (6.9). We have verified this numerically from Eq. (6.23) up to harmonic order $q = 9$. The limit $x, \xi \ll 1$ has to be investigated numerically because of the exponential function appearing in Eq. (6.23) which leads to a transcendental equation for $\xi^{(0)}$ when searching for the range of values ξ for which $x = 0$. From Eq. (6.23) we obtain that $\xi^{(0)}$ decreases slowly from $\xi_{q=1}^{(0)} = 1$ down to $\xi_{q=9}^{(0)} \approx 0.92$. On the other hand, if we replace $\sinh[(q-2k)x\xi]$ by $\sinh[(q-2k)x\xi]/2$ to model the behaviour of the modified Bessel function I_1 for small arguments as explained above, we find a value $\xi_q^{(0)}$ very close to $\sqrt{2}$ for all harmonic orders considered (up to $q = 9$). We therefore conclude that Eqs. (6.12)-(6.17) hold

for any harmonic order though we cannot assign a precise value to $\xi^{(1)}$ and $\alpha^{(1)}$. How quickly do the maxima of the radial integral decrease with growing Bessel angle? To get a rough idea, we consider the case $q = 1$ for simplicity and letting $x = 0$ in Eq. (6.9), we find $f_\xi(0) = \exp(-\xi^2)$. On the other hand, for the asymptotic limit, we let $x = \xi$ and we find this time $f_\xi(x = \xi) = \exp(-\xi^2) I_0(\xi^2)$ which decreases only as $0.4/\xi$ for $\xi \gg 1$. The important difference between these two limits is that the first one corresponds to Bessel angles α which all favour the value $\beta = 0°$ and, therefore, does not yield any significant contribution to the integral Eq. (6.7) due to the factor $\tan\beta$ appearing in the integrand. On the other hand, once values of β are reached which contribute to the integral, the dependence of the maxima on the Bessel angle α has become very weak.

We can now give a qualitative explanation why (or rather when) the optimum Bessel angle α_{opt}, as determined from the axial phase-matching condition, is a good estimate for the Bessel angle α_{max}, where maximum conversion efficiency occurs. For large confocal parameters, $\alpha^{(0)} \to 0$ and the loss of driving power favours $\alpha = 0°$. Physically this corresponds to the Bessel beam limit, where the energy contained in the beam is spreading out over many Bessel nodes (see Fig. 3.2). Provided the axial integral is sufficiently peaked, we will still find the maximum conversion efficiency for $\alpha_{\text{max}} \approx \alpha_{\text{opt}}$ but the gain with respect to the Gaussian limit $\alpha = 0°$ cannot expected to be very high (if gain there is). This case is essentially described in chapter 5, below the resonance. Above resonance, or more generally when the dipole moment is saturating, the situation may reverse, because the power law determining the behaviour of the radial integral in the perturbative regime does not hold any longer. The energy contained in the secondary maxima can then contribute efficiently to the harmonic generation process as seen in chapter 5. For small confocal parameters, a large range of Bessel angles, starting from $\alpha = 0°$, are strongly defavoured. Provided $\alpha_{\text{opt}} > \alpha^{(0)}$, we expect not only the maximum of the conversion efficiency to occur at $\alpha_{\text{max}} \approx \alpha_{\text{opt}}$ but also a significant gain in conversion efficiency with respect to the Gaussian limit $\alpha = 0°$. This situation corresponds to a Bessel-Gauss beam with a large Bessel angle and a small confocal parameter. Its characteristics are very different from both the Gaussian and the Bessel beam limit.

Table 6.1: Values of $\alpha^{(0)}$ and $\alpha^{(1)}$, defined in Eqs. (6.15) and (6.16), for various confocal parameters b and $\lambda = 355$ nm. All angles are given in deg.

b [mm]	$\alpha^{(0)}$	$\alpha^{(1)}$
1.0	0.86	1.82
2.0	0.61	1.29
5.0	0.39	0.82
48.7	0.12	0.26

Very much as for the Gaussian beam the power is concentrated close to axis but the phase-matching conditions are more those of a Bessel beam. The drawback in this case is the comparatively low power which can be upconverted for a given peak focal intensity. Moreover, it is more difficult to predict how this picture changes when going beyond the perturbative limit.

We can summarize as follows: in a large number of cases, the Bessel angle predicting a maximum conversion efficiency can be obtained as the optimum phase-matching angle from the axial phase-matching condition. The recommended value for β_0 in Eq. (6.7) is $\beta_0 = \alpha/q$. If $\alpha_{\rm opt} \leq \alpha^{(0)}$ then $\alpha_{\rm opt}$ should be recalculated letting $\beta_0 = 0°$. Normally, this will affect only the case $q = 3$. Note that in principle the curve $\eta_q(\alpha)$ might, a priori, have several relative maxima and minima before reaching the absolute maximum $\alpha_{\rm max} \approx \alpha_{\rm opt}$. If F_z is not strongly peaked at $\alpha_{\rm opt}$ (e.g. too low atomic densities) and/or the confocal parameter is too large (in the perturbative limit), then $0 \leq \alpha_{\rm max} < \alpha_{\rm opt}$ should be expected. In Table 6.1 we have given the values of $\alpha^{(0)}$ and $\alpha^{(1)}$ for $\lambda = 355$ nm and a few confocal parameters of interest. The value $b = 48.7$ mm was used in chapter 5, where we had worked with an optimum Bessel angle $\alpha_{\rm opt} \approx 1.2°$, much higher than the bounds given in Table 6.1. Accordingly, we had found the far-field maximum given by Eq. (6.17), namely $\beta \approx 1.2°/3 = 0.4°$. The remaining values given in this table will be considered in later sections.

We have seen so far how the radial phase-matching condition is affected when we decrease the confocal parameter b. However, to complete this picture we have to study the influence of the z/b-dependent terms entering the harmonic far-field amplitude

Eq. (4.71) and which we had neglected in our earlier phase-matching considerations in section 4.5.2. The radial phase-matching integral has still the form of Eq. (6.2) but now with

$$A = k_{0,q} \sin\beta\,, \qquad B = \frac{k_{0,1}\sin\alpha}{1+2iz/b}\,, \qquad \sigma^2 = \frac{qk_{0,1}/b}{1+2iz/b}\,. \tag{6.24}$$

The integral is therefore both complex and $z-$dependent. As a consequence, radial and axial integration do not separate and the integral Eq. (6.2) yields $z-$dependent phases which contribute to axial phase-matching. It is artificial to distinguish radial and axial phase-matching in this case and, in fact, more appropriate to talk about optimizing both modulus and phase of the integrand of the harmonic far-field integral. We shall be content to derive the first correction including the confocal parameter to the expression for the optimum Bessel angle of section 4.5.2 and to discuss qualitatively the modifications of the asymptotic maximum condition $A = B$ due to focusing. For this we rewrite the solution of the integral Eq. (6.8) as

$$\exp\left(-\frac{A^2+B^2}{4\sigma^2}\right) I_0\left(\frac{AB}{2\sigma^2}\right) = \exp\left[-\frac{(A-B)^2}{4\sigma^2}\right] \exp\left(-\frac{AB}{2\sigma^2}\right) I_0\left(\frac{AB}{2\sigma^2}\right)\,. \tag{6.25}$$

This makes the maximum condition $A = B$ apparent and we can reformulate the problem of finding this condition by requiring the exponents of all exponentially decaying functions to be minimal[2]. The first of these exponents is therefore $-\mathrm{Re}[(A-B)^2/4\sigma^2]$. Going back to the full expression of the harmonic far-field amplitude, Eq. (4.71), we have to replace $d_q(I)\exp[i\Phi_{\mathrm{at}}(I)]$ by the corresponding power law (Eq. (2.21)). Taking the full Bessel-Gauss amplitude Eq. (3.22) to the q^{th} power, we see that, besides the ρ-dependent terms already taken into account, we also have to take the exponentially decaying z/b-dependent term $\exp\{-qk_{0,1}z^2\sin^2\alpha/b[1+(2z/b)^2]\}$ into account. It is a straightforward matter to evaluate the sum of these two contributions and the resulting exponent is given (except for an overall minus sign) by

$$\begin{aligned}\mathrm{Re}\left[\frac{(A-B)^2}{4\sigma^2}\right] + \frac{qk_{0,1}z^2\sin^2\alpha}{b[1+(2z/b)^2]} &= k_{0,q}^2\sin\beta^2 - 2k_{0,1}k_{0,q}\sin\alpha\sin\beta \\ +k_{0,q}^2\sin^2\alpha\left[1-\frac{1}{1+(2z/b)^2}\right] &+ \frac{k_{0,1}^2\sin^2\alpha}{1+(2z/b)^2}\,.\end{aligned} \tag{6.26}$$

[2]Recall that $\exp(-x)I_0(x) \sim 0.4/\sqrt{x}$ for large x.

We replace $1/[1+(2z/b)^2]$ by an average value F, between 0 (for $L/b \to +\infty$, where L is the medium length) and 1 (for L/b=0). Trying to make the exponent vanish alltogether does not lead to real valued angles for $F < 1$. If we look for the minimum by deriving Eq. (6.26) with respect to α, we find the angles α and β to be related by

$$\beta = \alpha\,[F/q + q(1-F)]\,, \tag{6.27}$$

where we have assumed $\sin\alpha \approx \alpha$ and $\sin\beta \approx \beta$. Thus, we recover $\beta = \alpha/q$ in the limit $F \to 1$. On the other hand, we obtain $\beta = q\alpha > \alpha$ in the limit $F \to 0$.

Before turning to axial phase-matching, we briefly recall our findings so far: axial and radial phase-matching condition are, in most cases, largely independent of each other. While axial phase-matching determines essentially the optimum Bessel angle for maximum conversion efficiency, radial phase-matching influences the spatial far-field profile. For a given focusing geometry (L, b) we find that there is no far-field peak at all for Bessel angles α below a certain value $\alpha^{(0)}$. The far-field peak subsequently emerges and reaches a value $\beta = \alpha/q$ but may take on larger values if α is further increased and $F < 1$.

6.2.3 Axial phase-matching

In this section we shall derive an expression for the optimum Bessel angle which contains the first correction due to focusing and which will be valid for any of the gas density profiles given in Appendix B. Indeed recall that Eq. (4.104) is only valid for a rectangular gas profile. The leading order correction is given by the term proportional to $\tan^{-1}(2z/b)$ in Eq. (4.73) as we shall see later. We have pointed out in the last section that the radial integral, being complex and z-dependent will yield terms which contribute to the axial phase factors. One of these is

$$\frac{1}{2\sigma^2} = \frac{1+2zi/b}{2k_{0,q}/b} = \frac{\sqrt{1+(2z/b)^2}}{2k_{0,q}/b}\exp[i\tan^{-1}(2z/b)]\,, \tag{6.28}$$

which is the prefactor of Eq. (6.2) depending only on the exponential appearing in this integral. This term changes $q\tan^{-1}(2z/b)$ in Eq. (4.73) into $(q-1)\tan^{-1}(2z/b)$.

All remaining phases are similar to the corresponding term proportional to $z^2 \sin^2 \alpha$ in Eq. (4.73) and we will ignore these terms in the following. Therefore, we take as starting point the axial phase to be given by

$$\tilde{\phi}(z) = k_{0,q} \{[z + Z_1(z)] \cos \alpha - [z + Z_q(z)] \cos \beta\} - (q-1) \tan^{-1}(2z/b) \,, \quad (6.29)$$

where, from Eqs. (4.62) and (4.60),

$$Z_1(z) = \mathcal{N}_0 \Sigma(z) \chi_1(I)/2 \,, \qquad Z_q(z) = \mathcal{N}_0 [\Sigma(z) - L] \chi_q(I)/2 \,, \quad (6.30)$$

and the gas density profiles are assumed to be z-dependent only,

$$\Sigma(z) = \int_{z_{\min}}^{z} \sigma(z) \mathrm{d}z \,. \quad (6.31)$$

In the expressions (6.30) we have kept the intensity I as a fixed parameter, as the previous derivations remain valid, if the linear atomic susceptibilities are weakly dependent on the intensity. Unlike in section 4.5.2, where we obtained the axial phase-matching condition from the complete expression of the axial integral F_z, Eq. (4.86), we will proceed here simply by requiring the variation of the phases over the axial medium dimensions to be minimal. In fact, the full expression for F_z is only of use if one needs an analytical expression for the axial integral for computational purposes, but it is not required for determining the optimum Bessel angle α_{opt}. The great advantage of the method outlined below is that we will obtain α_{opt} for all gas density profiles given in Appendix B, the disadvantage (from the computational point of view) being that the actual propagation calculations have to be carried out fully numerically despite being in the perturbative regime due to the lack of a closed expression for F_z. An analytical expression for F_z would have been especially helpful in the tight focusing limit, where the proper convergence of the fully numerical calculations can be a particularly awkward task.

Ideally, the derivative of $\tilde{\phi}$, $\tilde{\phi}'(z) \equiv \mathrm{d}\tilde{\phi}/\mathrm{d}z$, should vanish so as to have no phase variations over the medium dimensions. As, in practice, $\tilde{\phi}'(z)$ will assume both positive and negative values, we will require the angle α to be chosen in such a way as to minimise the total area enclosed by the square of this function and the z-axis. More precisely, we look for the minimum with respect to the Bessel angle α of the

function

$$S(\alpha) = \frac{1}{k_{0,q}^2 L} \int_{z_{\min}}^{z_{\max}} \left(\frac{\mathrm{d}\tilde{\phi}}{\mathrm{d}z} \right)^2 \mathrm{d}z \,, \tag{6.32}$$

where we consider the square of the derivative in order to avoid cancellation of the areas above and below the z-axis, thereby forcing the points of the curve $\tilde{\phi}'(z)$ to be as close as possible to zero. Writing the derivative of $\tilde{\phi}(z)$ as

$$\frac{1}{k_{0,q}} \tilde{\phi}'(z) = P(z) \cos\alpha - Q(z) \cos\beta - \frac{\lambda}{\pi b} \left(1 - \frac{1}{q} \right) R(z) \,, \tag{6.33}$$

where

$$P(z) = 1 + \mathcal{N}_0 \sigma(z) \chi_1 / 2 \tag{6.34}$$

$$Q(z) = 1 + \mathcal{N}_0 \sigma(z) \chi_q / 2 \tag{6.35}$$

$$R(z) = 1/[1 + (2z/b)^2] \,, \tag{6.36}$$

we find after some elementary calculations the following expression for the derivative of $S(\alpha)$,

$$S'(\alpha) = 2 \sin\alpha \left[-\cos\alpha F_1 + \cos\beta F_2 + \lambda(1 - 1/q)/\pi b F_3 \right] . \tag{6.37}$$

The functions F_j appearing in Eq. (6.37) are defined by

$$F_1 = \frac{1}{L} \int_{z_{\min}}^{z_{\max}} P^2(z) \, \mathrm{d}z \tag{6.38}$$

$$F_2 = \frac{1}{L} \int_{z_{\min}}^{z_{\max}} P(z) Q(z) \, \mathrm{d}z \tag{6.39}$$

$$F_3 = \frac{1}{L} \int_{z_{\min}}^{z_{\max}} P(z) R(z) \, \mathrm{d}z \,. \tag{6.40}$$

6.2.4 A formula for the optimum Bessel angle

We can now combine the results from the two previous sections: requiring the square brackets to vanish in Eq. (6.37), expanding the cosines up to second order in α and β, respectively, and using $\beta \approx \alpha/q$ as the radial phase-matching condition, we obtain

$$\alpha_{\mathrm{opt}} = \left[\frac{2(F_1 - F_2) - 2\lambda(1 - 1/q)/\pi b F_3}{F_1 - F_2/q^2} \right]^{1/2} . \tag{6.41}$$

Now,

$$\begin{aligned} 2(F_1 - F_2) &= (2/L)\int_{z_{\min}}^{z_{\max}} P(z)[P(z) - Q(z)]\mathrm{d}z \\ &= [\mathcal{N}_0(\chi_1 - \chi_q)/L]\int_{z_{\min}}^{z_{\max}} P(z)\sigma(z)\mathrm{d}z \\ &\approx [\mathcal{N}_0(\chi_1 - \chi_q)/L]\int_{z_{\min}}^{z_{\max}} \sigma(z)\mathrm{d}z \\ &= \mathcal{N}_0(\chi_1 - \chi_q)\Sigma(z_{\max})/L \\ &= \mathcal{N}_0(\chi_1 - \chi_q) \end{aligned}$$

and for the denominator,

$$F_1 = F_2 \approx \frac{z_{\max} - z_{\min}}{L},$$

while for F_3 we may use

$$F_3 \approx \frac{1}{L}\int_{z_{\min}}^{z_{\max}} R(z)\mathrm{d}z = \frac{b}{2L}\left[\tan^{-1}\left(\frac{2z_{\max}}{b}\right) - \tan^{-1}\left(\frac{2z_{\min}}{b}\right)\right].$$

Recalling $z_{\min} = -z_{\max}$, for the gas profiles under consideration, we finally obtain in this way,

$$\alpha_{\mathrm{opt}} = \left(\frac{L}{2z_{\max}}\frac{q^2}{q^2-1}\right)^{1/2}\left\{\mathcal{N}_0(\chi_1 - \chi_q) - \frac{2\lambda}{\pi b}\left(1 - \frac{1}{q}\right)\left[\frac{b}{L}\tan^{-1}\left(\frac{2z_{\max}}{b}\right)\right]\right\}^{1/2}. \tag{6.42}$$

We stress again, that the radial phase-matching condition enters this expression only in form of the prefactor $[q^2/(q^2-1)]^{1/2}$. This factor has to be omitted if a first calculation of the optimum Bessel angle using Eq. (6.42) yields a value $\alpha_{\mathrm{opt}} \lesssim \alpha^{(0)}$, where $\alpha^{(0)}$ is defined in Eq. (6.15).

Recall, from Appendix B, $z_{\max} = 0.5L$ for a rectangular gas profile, $z_{\max} \approx 0.78L$ for a truncated Lorentz gas profile and $z_{\max} = L$ for a cosine-square gas profile. In order to make the connection with the expressions derived previously for the optimum Bessel angle, Eqs. (4.103)-(4.106), we consider a rectangular gas profile. While up to now we had not to distinguish clearly between plane wave limit and loose focusing limit, we will henceforth define more specifically the plane wave limit by $L/b \to 0$ and $\lambda/b \to 0$, and the loose focusing limit by $L/b \to 0$ at λ/b fixed. We obviously recover Eq. (4.104) in the plane wave limit, but we remain with an

additional contribution, lowering the value of the optimum Bessel angle, in the loose focusing limit. Hence, this is the leading correction to the plane wave limit as all other phases vanish in the limit $L/b = 0$. Very much as in Eq. (4.106), we can write the optimum Bessel angle again as a function of the well known phase-mismatch for the Gaussian beam in the loose focusing limit, namely

$$\alpha_{\text{opt}} \approx [q^2/(q^2-1)]^{1/2}[-(\lambda/q\pi)\Delta k_{\text{lf}}]^{1/2}\,, \tag{6.43}$$

with [130, 191],

$$\Delta k_{\text{lf}} = \Delta k_{\text{disp}} + 2(q-1)/b\,. \tag{6.44}$$

In the tight focusing limit we have $L/b \gg 1$ and consequently $F_3 \to 0$. In this case, Eq. (6.42) suggests that we recover the value of α_{opt} of the plane wave limit. This would imply the Gaussian beam to be optimally phase-matched in a dispersionless medium in the tight focusing limit, which is known not to be the case [130, 191]. On these grounds and because we have neglected phases which contribute to higher orders in L/b, we expect the breakdown of our derivation to occur typically for confocal focusing geometries ($L \approx b$).

From Eqs. (6.42) and (6.44), finally, we recover the well known fact that the Gaussian beam is the optimum Bessel-Gauss beam in the plane wave limit for a dispersionless medium (e.g. an appropriate gas mixture), that is for $\Delta k_{\text{disp}} = 0$, and for a moderately negatively dispersive medium in the loose focusing limit, provided $\Delta k_{\text{lf}} = 0$. It is easy to see how the flexibility of Bessel-Gauss beams comes into play in these cases. Consider e.g. the condition $\Delta k_{\text{lf}} = 0$. For a given macroscopic dispersion and harmonic order q, this condition fixes automatically the confocal parameter b. For a given peak focal intensity I_{f}, phase-matching with a Gaussian beam can thus be obtained only for one single value of the input power, this value being given by Eq. (3.28). On the other hand, we may achieve phase-matching, for a fixed peak focal intensity, for a large range of confocal parameters (thereby varying the input power continously) by simply choosing a Bessel-Gauss beam with a conical half-angle given by Eq. (6.43).

6.3 Results and discussion

6.3.1 Introduction

The following calculations will be carried out in the weak-field limit, for which the expressions derived in the previous sections are valid. In order to check the accuracy of Eq. (6.42), we have to fix the confocal parameter while tuning the Bessel angle α. As a consequence, at least one of the two parameters, total incident power or peak focal intensity, will have to vary with the Bessel angle α. Note that we could keep both the peak focal intensity and the total energy on target, Eq. (3.48), fixed, provided we increase the pulse duration τ such as to compensate the loss in incident power, the latter being a decreasing function of the Bessel angle at fixed peak focal intensity I_{f} according to Eqs. (3.27) and (3.28). However, an increasing pulse duration affects the photoionization probability and thereby both phase-matching and target depletion. As the conversion efficiency itself already relates the energy of the harmonic to the energy of the incident beam, the best choice is to keep all parameters fixed, except for the total power (and therefore the total energy for a given pulselength), which will now depend on the Bessel angle α.

It is important to stress at this point that, because we work within the perturbative regime, we can compute conversion efficiency curves which are, under certain circumstances, completely independent of the atomic gas considered. Indeed, the atomic properties enter the calculation only via the linear atomic susceptibilities and the prefactor in the power law Eq. (2.21)[3]. Therefore, if we compute the ratio $R(\alpha)$ of the conversion efficiency of the Bessel-Gauss beam to the conversion efficiency of the Gaussian beam limit ($\alpha = 0°$), this prefactor will drop out, and so will the gas density $\mathcal{N}_0$ appearing in the overall prefactor and the peak focal intensity I_{f}^q. As a consequence, for a given focusing geometry (L, b) and a given wavelength λ of the incident beam, the ratio $R(\alpha)$ will be essentially independent of the atomic gas provided that the value of the dispersion, proportional to $\mathcal{N}_0 \mathrm{Re}(\chi_1 - \chi_q) > 0$, is the same and absorption is negligible. $R(\alpha)$ will also be independent of the peak focal inten-

[3]That is, the q^{th} -order nonlinear susceptibility describing the generation of the q^{th} harmonic for the atom under consideration.

sity I_f. We expect this universality of the curve $R(\alpha)$ to hold typically to the same extent as Eq. (6.42) correctly predicts the optimum Bessel angle. The advantage of having only to require the macroscopic dispersion to be equal is obviously that the dispersion per atom, $\mathrm{Re}(\chi_1 - \chi_q)$, does not have to be the same for every atomic system under consideration in order to obtain the same curve $R(\alpha)$. On the other hand, $\mathrm{Re}(\chi_1 - \chi_q)$ must be evaluated at the same wavelength of the fundamental because the ratios λ/b and λ/L enter the propagation calculations. This restriction can be removed if both L and b are changed accordingly with the wavelength, as the ratio L/b remains then unaffected too. We have, however, made no attempt to demonstrate the latter assertion and we will restrict to the same wavelength of the fundamental for all atomic systems considered, $\lambda \approx 355$ nm. The ideal candidate for a comparison with atomic hydrogen is xenon. The third harmonic of $\lambda = 354.7$ nm (the wavelength used in Refs. [118, 237]) lies just below the $5d[\frac{3}{2}]$ resonance. This resonance has the largest oscillator strength in xenon (see section C.3). Moreover, both xenon and atomic hydrogen are ionized by four photons at this wavelength and we are therefore essentially avoiding problems due to resonances involving the harmonic generated in the medium. This is different e.g. for a wavelength $\lambda \approx 440$ nm of the fundamental, where the third harmonic lies below the $6s$ resonance in xenon. Here, we have the possibility of a reabsorption of the third harmonic via resonant two-photon ionization $3\hbar\omega + \hbar\omega$ from the $4f$ state [73]. Of course our propagation code cannot cope with this type of problem, as we have neglected all harmonic couplings from the outset. Luckily, this type of process has usually a clear signature in experiments, both due to the missing (third) harmonic and the strong ionization signal from the resonant state [166] and problems related to this effect in treating harmonic generation in our approximation can, in general, be anticipated. Another, though somewhat less optimal, candidate for comparison is krypton. Two possibilities appear: for $\lambda \approx 369$ nm, the third harmonic lies just below the $5s$ resonance, for $\lambda \approx 348$ nm, the third harmonic lies just below the $5s'$ resonance, both of which have the largest oscillator strengths in krypton [44]. These two options differ by the number of photons required for ionizing the atom: four photons are needed for $\lambda = 348$ nm, five for $\lambda = 369$ nm, the ionization potential of krypton

being $I_p = 14.0$ eV. At $\lambda = 369$ nm, we would have, a priori, to expect resonant two-photon processes close to the ionization threshold. The remaining noble gases are unsuitable at these wavelengths[4].

In the following we shall restrict to a comparison between atomic hydrogen and xenon at $\lambda = 355$ nm. The linear atomic susceptibilities for xenon are evaluated with the help of the Sellmeir formula (see Appendix C), the third-order nonlinear susceptibility entering the power law Eq. (2.21) is taken to be $\chi^{(3)} = 5.6 \times 10^{-35}$ esu [118]. The conversion into the dipole moment in atomic units is described in detail in section E.3.2.

In all of the subsequent calculations, we have fixed the values of some of the parameters, unless stated otherwise, as follows: the pulselength is $\tau = 15$ ps, the peak focal intensities are $I_f = 10^{12}$ W/cm^2 for atomic hydrogen and $I_f = 5.7 \times 10^{11}$ W/cm^2 for xenon. These two intensities correspond approximately to the maximum value for which the power law Eq. (2.21) holds[5]. Moreover, the two different values will enable us to check, whether the curves $R(\alpha)$ are indeed independent of I_f. The wavelength of the incident laser field is $\lambda = 355.0$ nm for atomic hydrogen and $\lambda = 354.7$ nm for xenon. We present our calculations in the following in form of case studies:

No.1: Compares atomic hydrogen and xenon for third harmonic generation of 355-nm radiation for a focusing geometry $(L, b) = (0.5, 5)$ mm. The peak gas density is $\mathcal{N}_0 = 4\times10^{18}$ atoms/cm^3 for atomic hydrogen and $\mathcal{N}_0 = 1.95\times10^{18}$ atoms/cm^3 for xenon.

No.2: Compares atomic hydrogen and xenon for third harmonic generation of 355-nm radiation for a focusing geometry $(L, b) = (0.5, 2)$ mm. The peak gas density is $\mathcal{N}_0 = 4\times10^{18}$ atoms/cm^3 for atomic hydrogen and $\mathcal{N}_0 = 1.95\times10^{18}$ atoms/cm^3 for xenon.

No.3: Compares atomic hydrogen and xenon for third harmonic generation of 355-nm radiation for a focusing geometry $(L, b) = (1, 1)$ mm. The peak gas

[4]We recall from Table 5 of Ref. [191] that the wavelengths for which the rare gases first exhibit a negative real part of the linear atomic polarizability are: helium: 58.4 nm, neon: 74.4 nm, argon: 106.6 nm, krypton: 123.5 nm, and xenon: 147 nm.

[5]For hydrogen, see Fig. 2.3, for xenon see Ref. [118,237].

density is $\mathcal{N}_0 = 1 \times 10^{19}$ atoms/cm^3 for atomic hydrogen and $\mathcal{N}_0 = 4.8 \times 10^{18}$ atoms/cm^3 for xenon.

No.4: Investigates fifth harmonic generation of 355-nm radiation in atomic hydrogen for the two focusing geometries $(L, b) = (1, 5)$ mm, with $\mathcal{N}_0 = 6 \times 10^{18}$ atoms/cm^3 and $(L, b) = (1, 1)$ mm, with $\mathcal{N}_0 = 1 \times 10^{19}$ atoms/cm^3 .

No.5: Investigates third harmonic generation of 355-nm radiation in xenon with reference to the experiment by Kung [118] for various confocal parameters. In particular we investigate the dependence of the conversion efficiency as a function of the medium length L. (The pulse duration is $\tau = 2.9$ nsec in this case)

6.3.2 Case study No.1

We consider here a case rather similar to the one discussed in chapter 5 but with a fixed confocal parameter while the total input power is varying. We take L =0.5 mm and b =5 mm. The peak atomic density for atomic hydrogen is $\mathcal{N}_0 = 4 \times 10^{18}$ atoms/cm^3 . In order to obtain the same macroscopic dispersion we need a peak atomic density of $\mathcal{N}_0 = 1.95 \times 10^{18}$ atoms/cm^3 for xenon. Table 6.2 gives the optimum Bessel angles for hydrogen and xenon as calculated from Eq. (6.42). A range of angles is given for hydrogen as the linear atomic polarizability at the third harmonic frequency is already weakly intensity-dependent (see Fig. 2.4). For this reason we will compare the conversion efficiency curves with respect to the gas density profiles only for xenon, having assumed the linear atomic polarizabilities to be intensity-independent throughout. The resulting curves for the conversion

Table 6.2: Calculated values for α_{opt}, as given by Eq. (6.42) for atomic hydrogen (H) and xenon (Xe) and $(L, b) = (0.5, 5)$ mm. For xenon, both the rectangular gas profile (RP) and the truncated Lorentz gas profile (TLP) have been considered.

α_{opt} (deg.)	H	Xe
RP	1.18-1.23	1.22
TLP	-	0.96

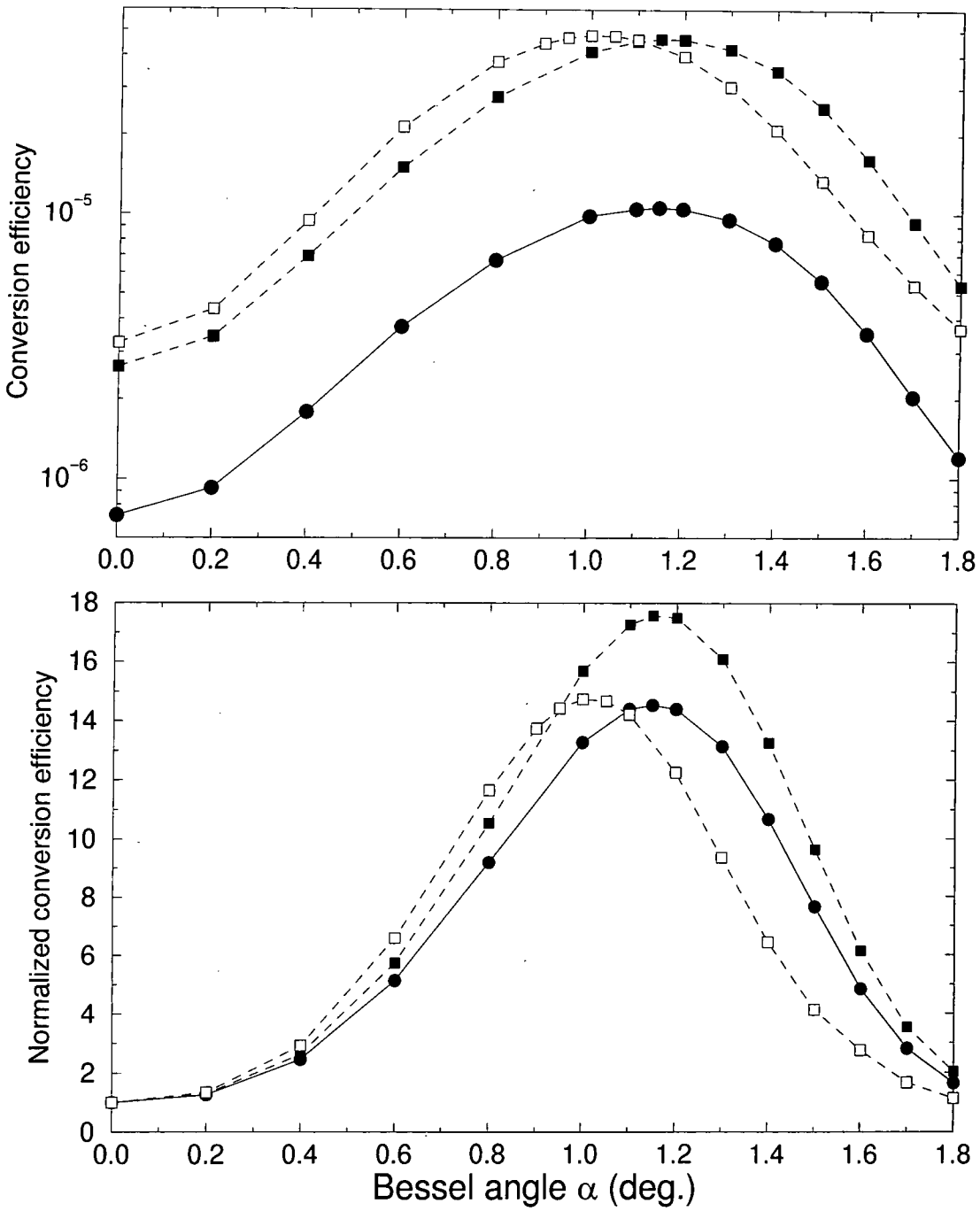

Figure 6.2: Top: Absolute conversion efficiencies for atomic hydrogen (circles and solid lines) and xenon (squares and dashed lines) versus the Bessel angle α for the following focusing parameters: $(L, b) = (0.5, 5)$ mm. Filled symbols are for a rectangular gas profile, open symbols for a truncated Lorentzian gas profile. Bottom: Normalized conversion efficiencies $R(\alpha)$ with respect to the value in the Gaussian limit ($\alpha = 0°$). The total energy on target drops from 7.1×10^{-2} mJ ($\alpha = 0°$) to 6.1×10^{-3} mJ ($\alpha = 1.80°$) for hydrogen, and from 4.0×10^{-2} mJ to 3.5×10^{-3} mJ for xenon.

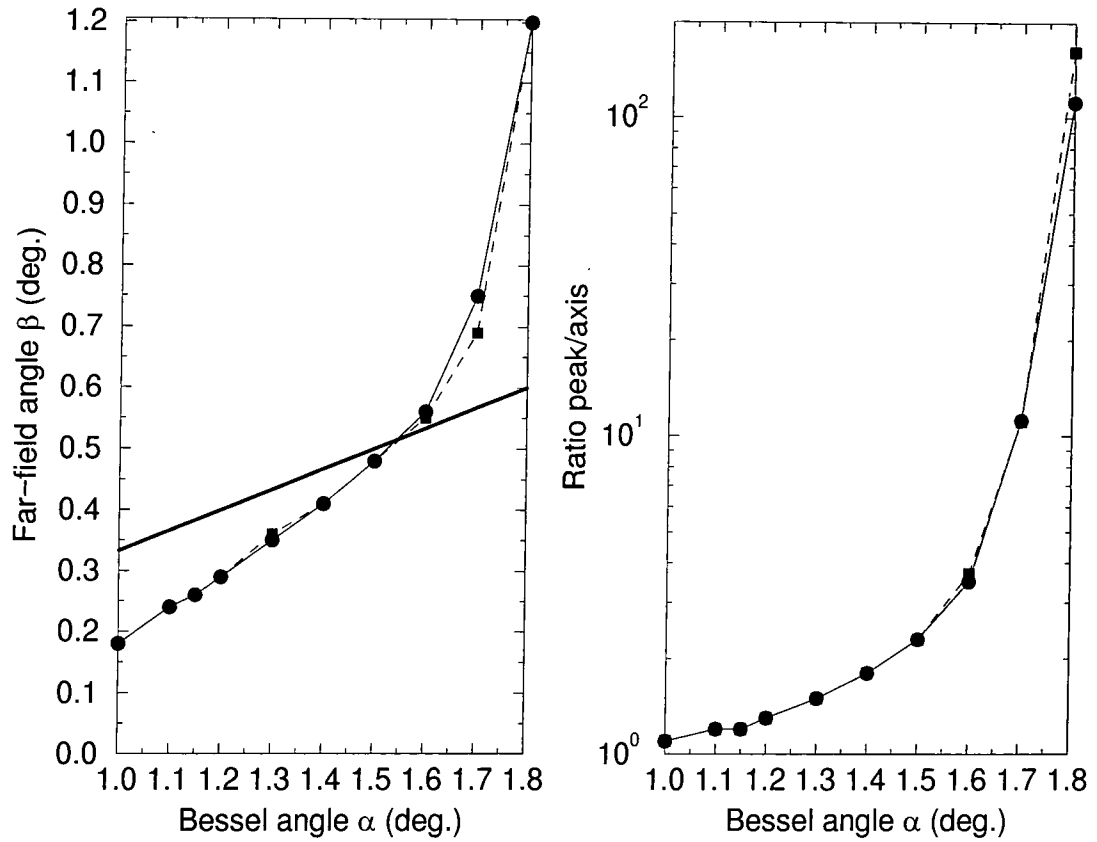

Figure 6.3: Symbols as in Fig. 6.2. Left: Position of the absolute maximum (off-axis) of the spatial far-field profile in terms of the far-field angle β, versus the Bessel angle α. For guidance, the curve $\beta = \alpha/3$ is also shown (thick line). Right: Ratio of the maximum off-axis to the value on axis versus the Bessel angle α.

efficiencies are shown in Fig. 6.2. In the top figure the absolute conversion efficiencies are given. They are larger in the case of xenon compared to atomic hydrogen, as expected, due to xenon being more polarizable. Rectangular gas profile and truncated Lorentz gas profile lead to approximately the same maximum conversion efficiency, which is about $\eta \approx 5 \times 10^{-5}$ in this case for xenon. If a rectangular gas profile is used, the maxima of the curves occur in the range $\alpha = 1.15 - 1.20°$, in good agreement with the figures given in Table 6.2. For the truncated Lorentz profile, the corresponding curve peaks around $\alpha = 1.00 - 1.05°$ compared to $\alpha_{\text{opt}} = 0.96°$. The bottom figure of Fig. 6.2 shows the normalized conversion efficiency curves $R(\alpha)$ corresponding to the curves in the top figure and illustrates the universality of the quantity $R(\alpha)$ with respect to the atomic species considered, provided the criteria listed above are satisfied. Fig. 6.3 shows the evolution of the far-field angle

β, at those points of the spatial far-field profile where the largest peak exceeds the maximum on axis, the corresponding ratio of the heights being given in the right hand side figure. The far-field peak emerges in between $\alpha = 0.8 - 1.0°$[6]. This value is actually fairly close to the value of $\alpha^{(1)}$ given in Table 6.1 for $b = 5$ mm. Though this must be taken with some caution, we point it out at this stage because of similar findings in the following case studies. The curve approaches slowly the value $\alpha/3$ well beyond the value $\alpha = \alpha_{\rm opt}$ and increases rapidly afterwards. The peak height is similarly enhanced.

6.3.3 Case study No.2

In this study we move somewhat closer to the confocal focusing geometry ($L = b$) and monitor the changes in the curves with respect to those shown in the previous case. Table 6.3 gives the values of the optimum Bessel angle for $L = 0.5$ mm and $b = 2$ mm. The peak atomic densities for hydrogen and xenon are unchanged. The corresponding curves are shown in Fig. 6.4. For the rectangular gas profile, the maxima have moved to $\alpha \approx 1.10°$, for the truncated Lorentz gas profile, the maximum can now be found at $\alpha \approx 0.95°$. Both values are still in good agreement with the values of $\alpha_{\rm opt}$ given in Table 6.3. Note again, from the bottom figure of Fig. 6.4, the very good agreement between the curves $R(\alpha)$ for atomic hydrogen and xenon. As in the previous section, it can be seen, that, though the maximum conversion efficiency is roughly equal for both gas density profiles, the relative gain

[6]The stepsize for the Bessel angle α was dictated by the variations of the conversion efficiency curves. As a consequence, the onset of the off-axis maximum is not always determined to a high precision. In the present case we have redone the calculation and found the far-field peak to emerge within the range $\alpha = 0.85 - 0.90°$.

Table 6.3: Calculated values for $\alpha_{\rm opt}$, as given by Eq. (6.42) for atomic hydrogen (H) and xenon (Xe) and $(L, b) = (0.5, 2)$ mm. For xenon, both the rectangular gas profile (RP) and the truncated Lorentz gas profile (TLP) have been considered.

$\alpha_{\rm opt}$ (deg.)	H	Xe
RP	1.11-1.16	1.15
TLP	-	0.87

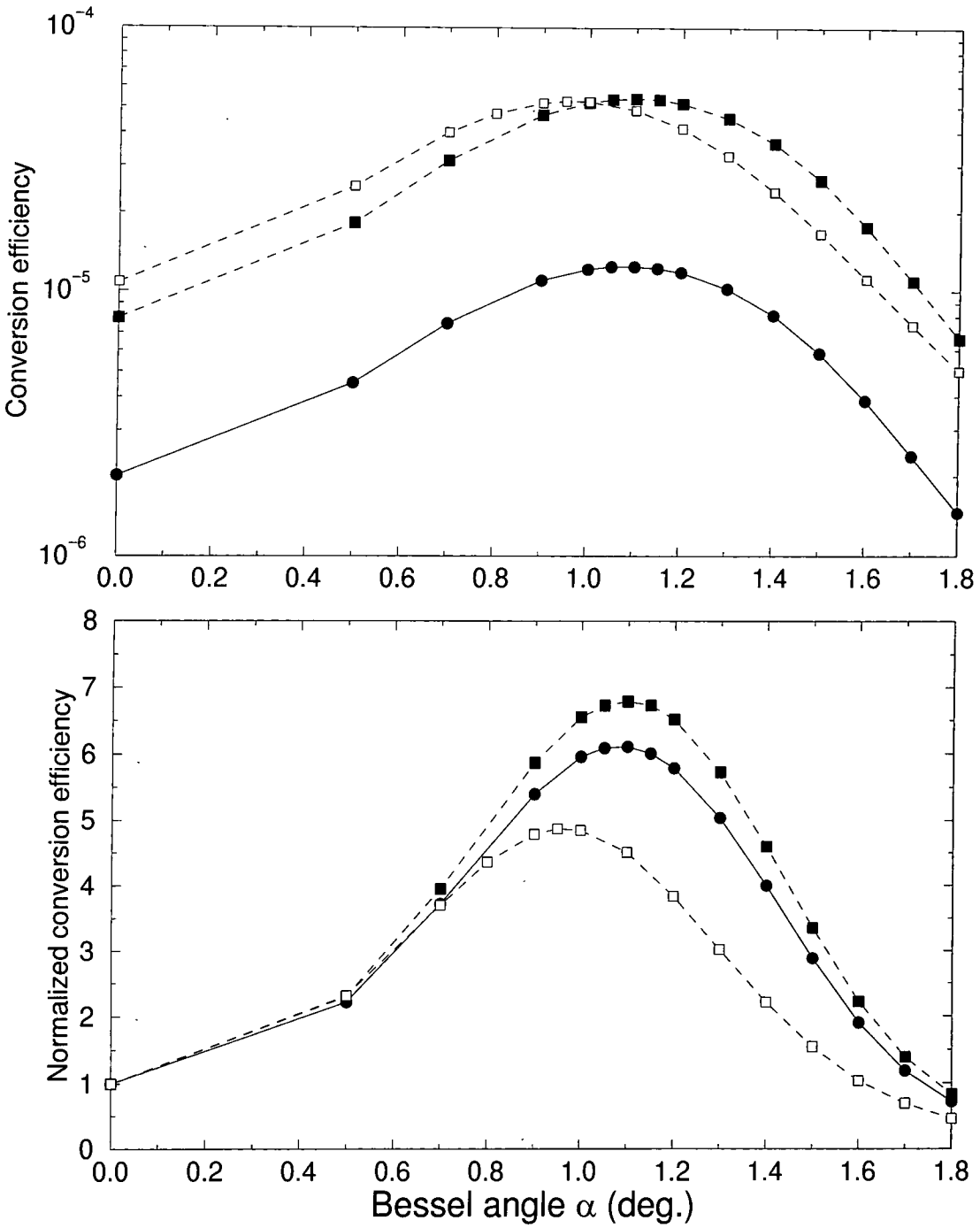

Figure 6.4: Same as Fig. 6.2 but for $b = 2$ mm. Top: Absolute conversion efficiencies for atomic hydrogen (circles and solid lines) and xenon (squares and dashed lines) versus the Bessel angle α for the following focusing parameters: $(L, b) = (0.5, 2)$ mm. Filled symbols are for a rectangular gas profile, open symbols for a truncated Lorentzian gas profile. Bottom: Normalized conversion efficiencies $R(\alpha)$ with respect to the value in the Gaussian limit ($\alpha = 0°$). The total energies on target are obtained from those given in Fig. 6.2 after multiplying by 2/5=0.4.

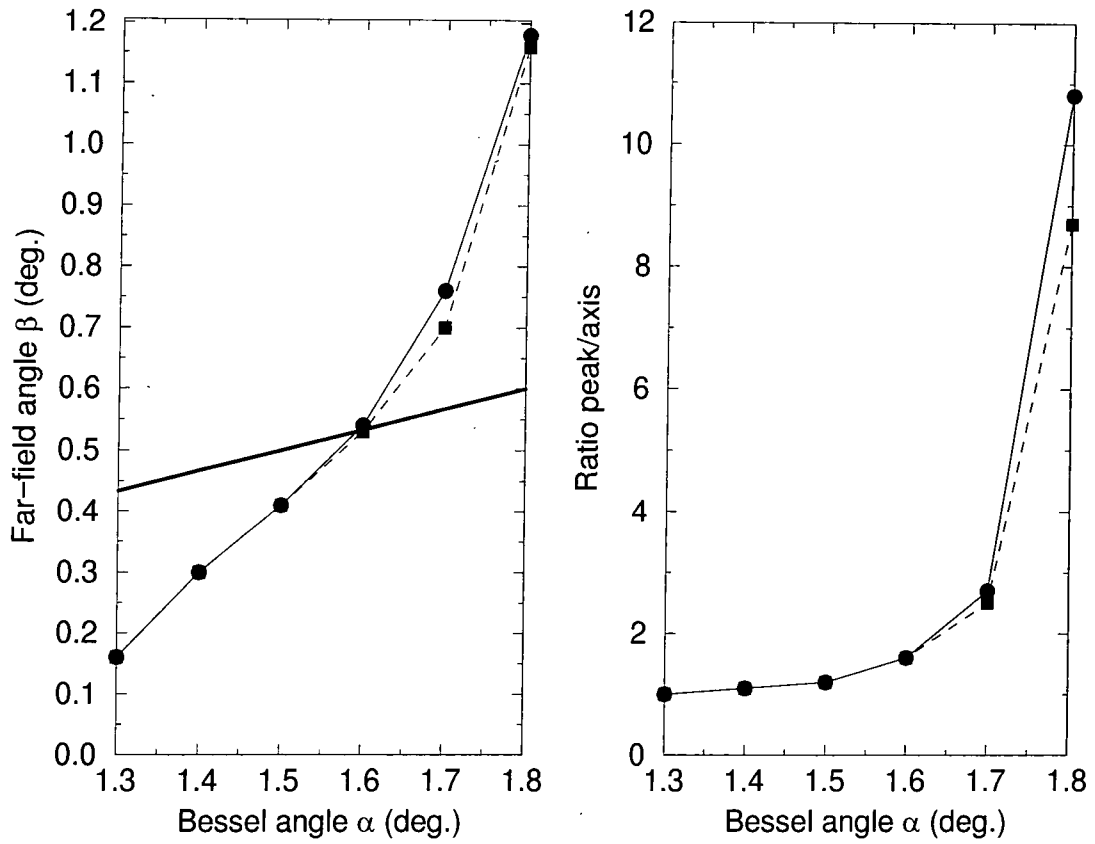

Figure 6.5: Symbols as in Fig. 6.4. Left: Position of the absolute maximum (off-axis) of the spatial far-field profile in terms of the far-field angle β, versus the Bessel angle α. For guidance, the curve $\beta = \alpha/3$ is also shown (thick line). Right: Ratio of the maximum off-axis to the value on axis versus the Bessel angle α.

is less in the case of a truncated Lorentz profile. From Fig. 6.5 we can see the onset of an absolute maximum off-axis in the spatial far-field profile occurring for even larger values of α than those reported in Fig. 6.3. The harmonic emission is preferentially along the propagation direction for Bessel angles $\alpha \lesssim 1.30°$. Note again the agreement between this value and the value of $\alpha^{(1)}$ in Table 6.1 for $b = 2$ mm. As the range $\alpha < \alpha^{(1)}$ now also includes the optimum angles $\alpha_{\rm opt}$ given in Table 6.3 we recalculate these values omitting the term $[q^2/(q^2-1)]^{1/2}$ in Eq. (6.42) (that is we assume $\beta = 0°$). We find in this way $\alpha_{\rm opt} = 1.08°$ for a rectangular gas profile and $\alpha_{\rm opt} = 0.82°$ for a truncated Lorentz profile for xenon. The agreement with the maximum of the curve for the rectangular gas profile is now excellent, while still being fair in the case of a truncated Lorentz profile. The peak height relative to the local maximum on axis is lower when compared to the previous case.

6.3.4 Case study No.3

Compared to the two previous studies, we have now moved to a confocal focusing geometry, $L = b = 1$ mm. At the same time, we have increased the gas density, so as to obtain large optimum Bessel angles: $\mathcal{N}_0 = 1 \times 10^{19}$ atoms/cm^3 for atomic hydrogen and $\mathcal{N}_0 = 4.8 \times 10^{18}$ atoms/cm^3 for xenon. Theses angles are listed in Table 6.4. Fig. 6.6 shows the absolute and normalized conversion efficiencies for both atomic hydrogen and xenon. Unlike in the previous cases, the conversion efficiency curves pass through a pronounced minimum around $\alpha = 0.9°$ before reaching the absolute maximum at higher values of the angle α. We attribute this minimum to the delicate balance between a loss of driving power when increasing the angle α and the continously improving phase-matching. In fact, one can show, that this minimum disappears again, if the power law for the dipole moment is replaced by a flat dipole moment[7]. We had pointed out the possibility of a departure from the single-maximum curves $R(\alpha)$, such as those in Figs. 6.2 and 6.4, when discussing radial phase-matching in section 6.2.2. We note in particular the large increase in conversion efficiency in agreement with the predictions made in that section. This gain is even large in terms of absolute output energy, considering that the energy on target in the Gaussian limit is only 5.4 times larger than for the Bessel-Gauss beam with $\alpha = \alpha_{\text{opt}}$. Note however that a low confocal parameter limits the overall input power that can be upconverted for a given peak focal intensity.

While the maxima shown in Fig. 6.6 agree well with the values given in Table 6.4 for a rectangular gas profile, the behaviour of the corresponding results for a truncated

[7]For this calculation, we had taken $d_q(I)$ to be constant for intensities in the range $I = I_f$ down to $I = 10^{-2}\, I_f$, followed by rapid cut-off.

Table 6.4: Calculated values for α_{opt}, as given by Eq. (6.42) for atomic hydrogen (H) and xenon (Xe) and $(L, b) = (1, 1)$ mm. For xenon, both the rectangular gas profile (RP) and the truncated Lorentz gas profile (TLP) have been considered.

α_{opt} (deg.)	H	Xe
RP	1.82-1.90	1.87
TLP	-	1.47

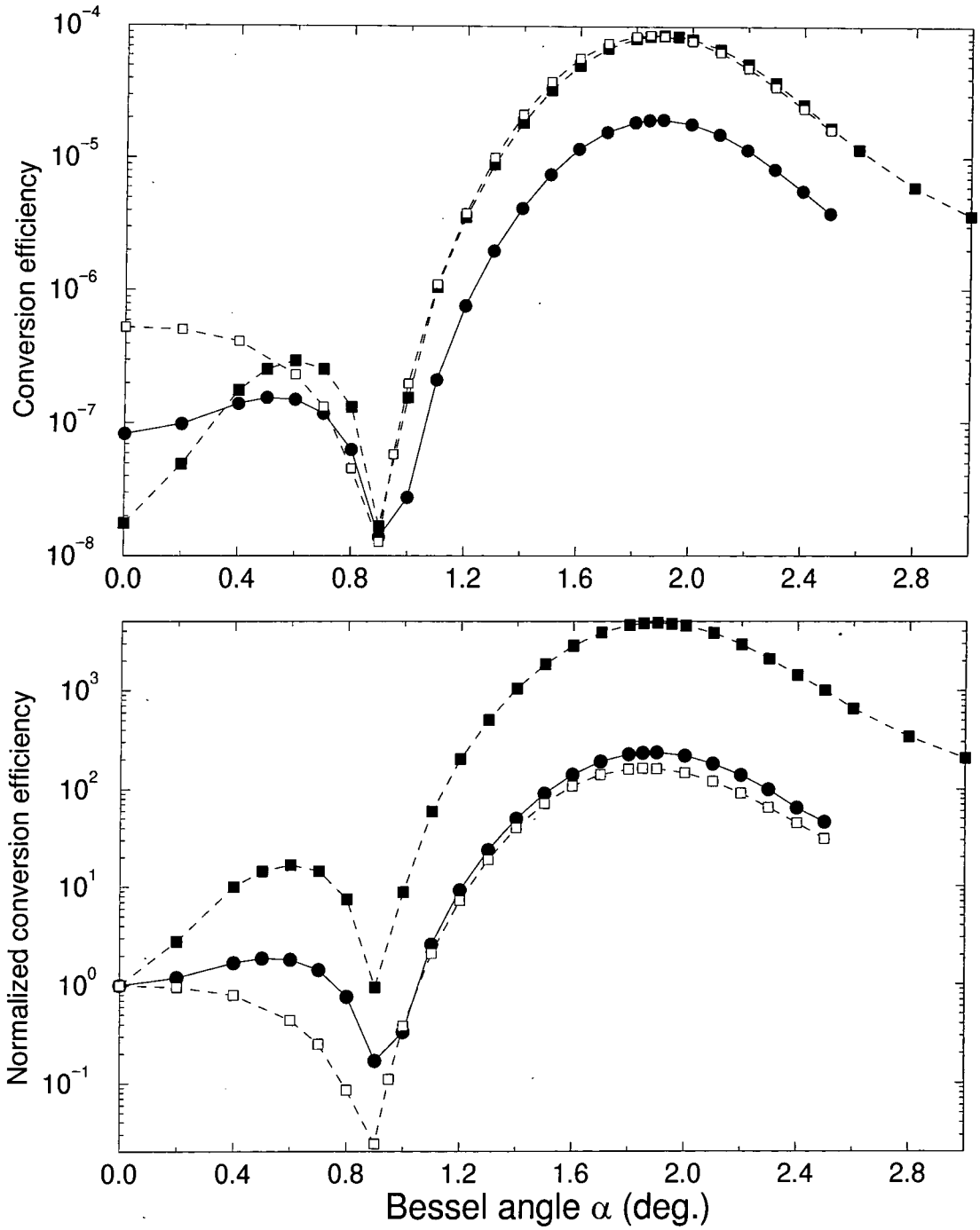

Figure 6.6: Same as Fig. 6.2 but for $(L, b) = (1, 1)$ mm. Top: Absolute conversion efficiencies for atomic hydrogen (circles and solid lines) and xenon (squares and dashed lines) versus the Bessel angle α. Filled symbols are for a rectangular gas profile, open symbols for a truncated Lorentzian gas profile. Bottom: Normalized conversion efficiencies $R(\alpha)$ with respect to the value in the Gaussian limit ($\alpha = 0°$). The total energies on target are obtained from those given in Fig. 6.2 after multiplying by 1/5=0.2.

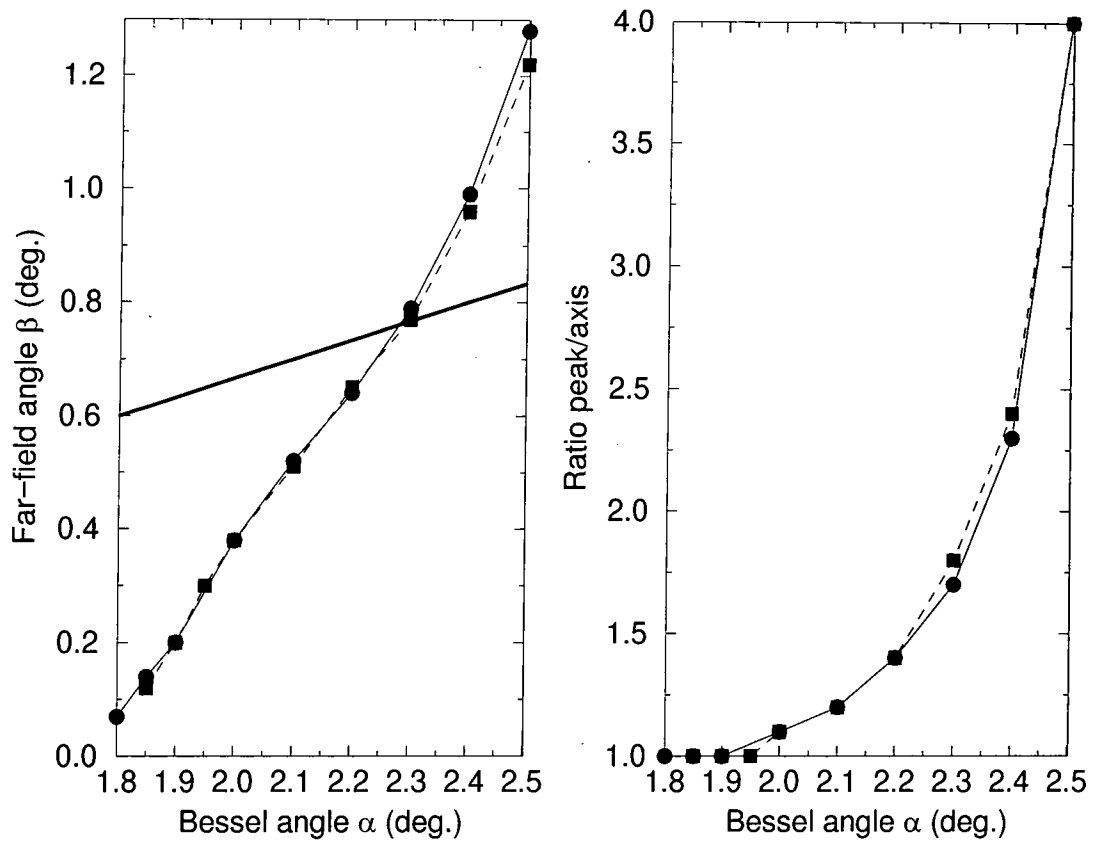

Figure 6.7: Symbols as in Fig. 6.6. Left: Position of the absolute maximum (off-axis) of the spatial far-field profile in terms of the far-field angle β, versus the Bessel angle α. For guidance, the curve $\beta = \alpha/3$ is also shown (thick line). Right: Ratio of the maximum off-axis to the value on axis versus the Bessel angle α.

Lorentz profile is strikingly different: Beyond the minimum at $\alpha = 0.9°$ the curves for xenon are virtually identical for the two gas profiles in terms of absolute conversion efficiency, while for the normalized conversion efficiency, the curves for xenon and for atomic hydrogen corresponding to two different gas profiles are very close. In fact, the same pattern can be observed in Figs. 6.2 and 6.4 provided the curves for the truncated Lorentz profile are shifted to the right so as to overlap the curves for the rectangular gas profile. We therefore expressedly note the breakdown of Eq. (6.42) for the truncated Lorentz profile in the confocal focusing region.

The behaviour of the absolute maximum of the spatial far-field profile, for which the position and the ratio peak/axis are shown in Fig. 6.7, are similar to those of the previous case studies: the slope of the (roughly) linear function $\beta = \beta(\alpha)$ increases with the focusing. It seems that the ratios peak/axis diminish accordingly

but this may be due to the limited maximum value of the Bessel angle α for which the calculation has been carried out. We note finally that while the normalized conversion efficiency curves $R(\alpha)$ for xenon and atomic hydrogen in the case of the same (rectangular) gas density profile have become dissimilar, the position and height of the absolute maximum off-axis are still in close agreement. Again, the appearence of the far-field peak is well described by the corresponding value of $\alpha^{(1)}$ given in Table 6.1.

6.3.5 Case study No.4

In this case study we report briefly on the generation of the fifth harmonic of 355-nm radiation in atomic hydrogen. Due to the low atomic susceptibility at the corresponding harmonic frequency (see section 2.4), this (and the higher order) harmonic(s) are of limited interest for this particular value of the wavelength of the fundamental (in atomic hydrogen). Nevertheless, it is useful to check, whether the concepts developed so far regarding the phase-matching conditions do also hold for $q > 3$ as they should. The conversion efficiency curve for a loose focusing geometry $(L, b) = (1, 5)$ mm and peak atomic density $\mathcal{N}_0 = 6 \times 10^{18}$ atoms/cm^3 (a rectangular gas profile was assumed) is shown in the top figure of Fig. 6.8. The optimum Bessel angle, evaluated from Eq. (6.42), is $\alpha_{\text{opt}} = 0.43°$, in excellent agreement with the (small) maximum of the corresponding curve. The absolute conversion efficiency in the Gaussian limit is $\eta = 5.1 \times 10^{-11}$. The bottom figure in Fig. 6.8 is for a confocal focusing geometry, $(L, b) = (1, 1)$ mm, and a peak atomic density of $\mathcal{N}_0 = 1 \times 10^{19}$ atoms/cm^3 . Despite this high value of the atomic density, the optimum Bessel angle is only $\alpha_{\text{opt}} = 0.14°$, in 'good' agreement with the fact, that no maximum could be found in the calculations. The spatial far-field profiles did not exhibit any peaks, in qualitative agreement with the values of $\alpha^{(1)}$ given in Table 6.1.

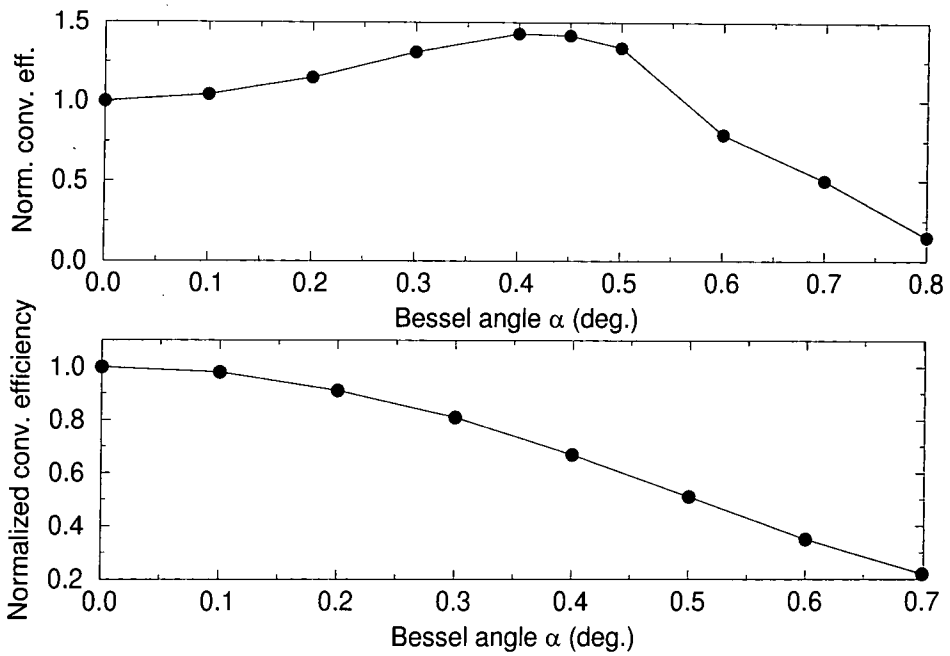

Figure 6.8: Top: Normalized conversion efficiency $R(\alpha)$ for atomic hydrogen at the fifth harmonic versus the Bessel angle α. The parameters are $L = 1$ mm, $b = 5$ mm and $\mathcal{N}_0 = 6 \times 10^{18}$ atoms/cm^3 (rectangular gas profile). Bottom: Same as above but with $b = 1$ mm and $\mathcal{N}_0 = 1 \times 10^{19}$ atoms/cm^3 .

6.3.6 Case study No.5

The aim of this last study is to make a calculation similar to the one of chapter 5 but for a case where experiments have already been carried out for the Gaussian limit. We refer here in particular to the experiment by Kung [118] on third harmonic generation in xenon at 354.7 nm wavelength. We have used the data provided by Kung about this experiment to test the overall accuracy of our propagation code and the atomic data for xenon. We refer to section E.3.2 for a detailed report on both the experiment and our test calculation. In the present section we will revert to the mode of comparison with respect to the type of the incident beam used in chapter 5, namely keeping the total power and peak focal intensity constant while the confocal parameter is varied with the Bessel angle thereby involving large confocal parameters. Thus the phase-matching conditions for the optimum Bessel-Gauss beam are well defined and independent of L. Therefore, for the optimum Bessel-Gauss beam we can also test the dependence of the conversion efficiency

on the medium length L. In case of exact phase-matching, this should be simply a L^2 power law. The xenon gas density has a rectangular profile with a FWHM of $L = 1$ mm, the (peak) gas density being $\mathcal{N}_0 = 1.75 \times 10^{18}$ atoms/cm^3 which corresponds approximately to the end of the third coherence length maximum in the Gaussian limit (Fig. E.2). The gas density corresponding to the end of the first coherence length, $\mathcal{N}_0 = 6.4 \times 10^{17}$ atoms/cm^3 , is too low (for the present values of the linear atomic polarizabilities) to allow for a sufficiently large optimum angle $\alpha_{\rm opt}$.[8] Fig. 6.9 shows how the results depend on the Bessel angle α: the conversion efficiency, after having passed a minimum around $\alpha = 0.70 - 0.80°$, peaks around $\alpha = 1.15 - 1.20°$ in excellent agreement with $\alpha_{\rm opt} = 1.20°$ from Eq. (6.42)[9]. The normalization at $\alpha = 0°$ corresponds to an absolute value for the conversion efficiency of $\eta = 1.2 \times 10^{-5}$. The gain is rather moderate as expected, very much of the same order of magnitude than found in the calculations of chapter 5 at low intensities for atomic hydrogen (see e.g. Table 5.1). The absolute maximum of the far-field profile appears, after some fluctuations in a region of very low conversion efficiencies, at the 'correct' position given by $\beta = \alpha_{\rm opt}/3$ over a rather large interval of Bessel angles, centered approximately at $\alpha = \alpha_{\rm opt}$. The confocal parameter required to keep the incident beam's energy constant increases rapidly with the Bessel angle. Despite its large value for $\alpha > \alpha_{\rm opt}$, we find that β takes on larger values than predicted by the asymptotic radial phase-matching condition $\beta = \alpha/3$. We could not find any simple explanation for this behaviour.

To test how well phase-matching is realized for Bessel angles around $\alpha_{\rm opt}$, we have set $\alpha = 1.17°$ and calculated the conversion efficiency as a function of the medium length L. The corresponding curve, shown in Fig. 6.10 is seen to saturate rapidly, reaching a maximum of $\eta = 3.2 \times 10^{-4}$ for $L = 9 - 10$ mm. Considering the large value of the confocal parameter, $b = 185.5$ mm, one would have expected to be in a situation where expression (4.95) for the axial integral holds, therefore defining a coherence length $L_{\rm coh} = \pi/S$. In principle, we should be able, by fine-tuning α and/or $\mathcal{N}_0$, to obtain an arbitrarily large value of $L_{\rm coh}$. It turns out that this is

[8] In this case one finds $0 \lesssim \alpha_{\rm max} < \alpha_{\rm opt}$.

[9] Calculated in the plane wave limit, independent of the value of the confocal parameter b.

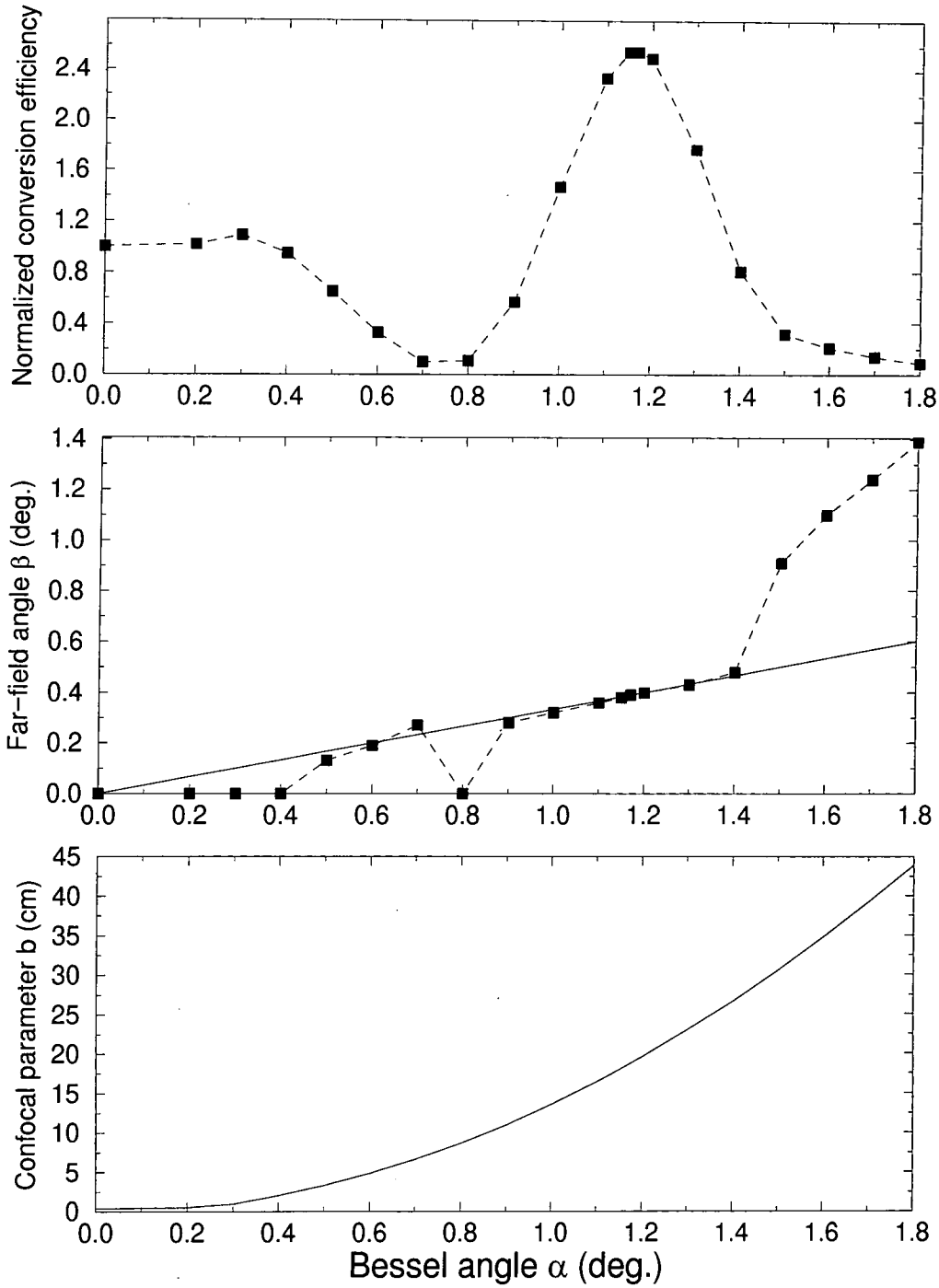

Figure 6.9: Top: Normalized conversion efficiency for xenon versus the Bessel angle α for $L = 1$ mm, $\mathcal{N}_0 = 1.75 \times 10^{18}$ atoms/cm^3 and a constant energy on target of 6.24 mJ. Middle: Far-field angle β of the absolute maximum of the spatial far-field profile versus the Bessel angle α. Bottom: Confocal parameter of the Bessel-Gauss beam at constant peak focal intensity $I_f = 5.7 \times 10^{11}$ W/cm^2 and constant energy 6.24 mJ [corresponding to a peak power of 2 MW and a pulse duration of 2.9 nsec (FWHM of the intensity)] versus the Bessel angle α.

not possible because, despite the small ratios L/b, the Bessel-Gauss beam is *not* diffraction-free for values $L \gtrsim 1$ mm. This can be seen from Eq. (4.40) where the exponentially decaying term along the $z-$direction has an order of magnitude given by

$$O = 4\pi \frac{L}{\lambda} \frac{L}{b} \sin^2 \alpha \,. \tag{6.45}$$

For $L = 1$ mm one obtains $O = 0.06$, for $L = 4$ mm already $O = 1.03$. Consequently, Eq. (4.95) does not hold and the curve shown in Fig. (6.10) departs almost immediately from the L^2-power law for exact phase-matching. The bottom figure of Fig. 6.10, finally, shows the far-field profile of the third harmonic for a medium length $L = 10$ mm. The position of maximum has dropped (with increasing L) to a value $\beta = 0.36°$. Most of the harmonic energy is contained in the off-axis peak,

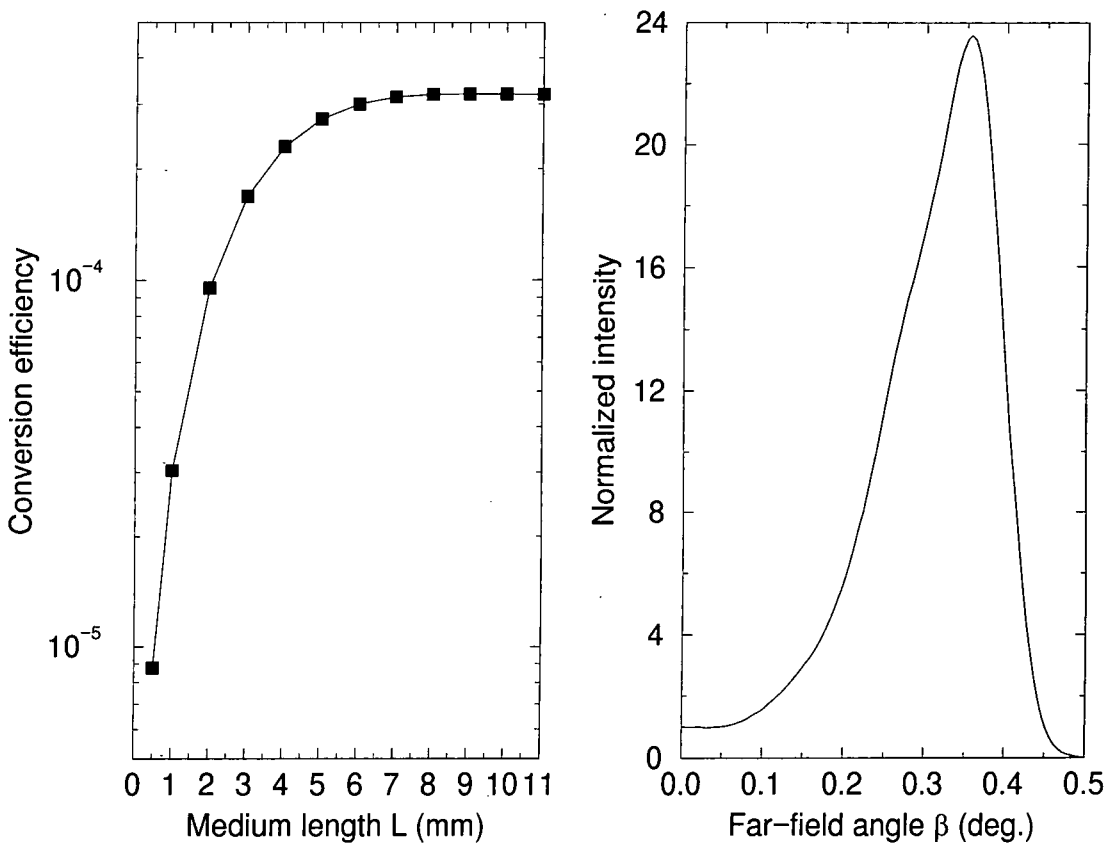

Figure 6.10: Left: Conversion efficiency for xenon at $\alpha = 1.17°$ versus the medium length L. For $L = 1$ mm, the value is the same than in Fig. 6.9. Right: Far-field profile of the third harmonic for $\alpha = 1.17°$ and $L = 10$ mm versus the far-field angle β.

especially emission in forward direction is strongly suppressed.

6.4 Summary

In this chapter we have given a fairly comprehensive account on phase-matching with Bessel-Gauss beams in the perturbative limit. We have argued that the optimum value for the Bessel angle which is likely to maximize the conversion efficiency is determined by the axial phase-matching condition while the radial phase-matching condition governs the spatial far-field profile. Numerical calculations reported in this chapter support these findings which are based on a simplified semi-analytical investigation of the harmonic far-field amplitude. The main result of this chapter is expression (6.42) which predicts the optimum Bessel angle beyond the loose-focusing limit for any gas density profile (provided it satisfies the general criteria given in Appendix B). Expression (6.42) can usually be considered reasonably accurate down close to the confocal focusing limit, where it breaks down. A closed expression for the optimum Bessel angle in the tight focusing limit, if it exists, could not be obtained.

In the case studies 1,2,3 and 4 we have kept the focusing geometry fixed in order to assess the accuracy of expression (6.42) for the optimum Bessel angle. The comparison between different Bessel-Gauss beams, the Gaussian beam limit included, is therefore somewhat hampered by the fact that the energy on target necessarily decreases with the Bessel angle. Even when this decrease is taken into account, a significant gain compared to the Gaussian limit can be achieved considering the conversion efficiencies reported in these studies (except for study No.4 which did only serve the purpose of checking the formula for the optimum Bessel angle). A particularly interesting feature confirmed in studies 1,2 and 3 is the independence of the normalized conversion efficiency curves of the atomic gas, provided a certain number of (not too stringent) conditions are met.

In study No.5, very much as in chapter 5, a rapidly growing confocal parameter was required to keep the total energy and peak focal intensity on target fixed while increasing the Bessel angle. As expected, we find the increase in conversion efficiency

to be low for very large confocal parameters. Indeed, the energy on target is spread over a large number of Bessel nodes. This energy is lost in the perturbative regime where the secondary maxima of the incident beam cannot contribute efficiently to the harmonic generation process. In fact, based on the experience gained in chapter 5, we could carry out the same calculation as in study No.5 for a peak focal intensity in the range $I_f = 5 - 6 \times 10^{13}$ W/cm^2 , where all the contributions to harmonic generation come from the secondary maxima just below saturation. As seen in chapter 5, the intensity-dependent atomic quantities are of negligible importance in this case as the central peak of the Bessel profile can be omitted in the corresponding calculations. Although we have not done this calculation we expect, in analogy to the case for atomic hydrogen, significantly higher conversion efficiencies at high energies on target compared to those reported in Figs. 6.9 and 6.10. The low increase in conversion efficiency is in stark contrast to the findings of case study No.3, where a low confocal parameter (but also a larger dispersion) was used. For similar values of α_{opt} the Bessel-Gauss beam with the lower confocal parameter is thus more effective (in the perturbative regime) as the power is concentrated closer to the axis. On the other hand, a lower confocal parameter limits the power on target which can be converted into harmonic radiation.

Chapter 7

Results for Argon at 810 nm

7.1 Introduction

In this chapter we will investigate a completely different regime than previously studied in hydrogen and xenon. The present calculation was motivated by the projected use of the large-scale laser facility at the Laboratoire d'Optique Appliquée (LOA, Palaiseau, France) for an experiment on higher-order harmonic generation by focusing an annular laser beam, similar in many respects to a Bessel beam, in an argon gas jet. The powerful 'yellow room' 30-fs, 810-nm terawatt Ti:Sapphire laser is capable of delivering up to 300 mJ on target, though only a fraction of this energy may be usefully employed in high-order harmonic generation experiments because of the otherwise quasi instantaneous formation of a plasma which drastically reduces harmonic emission. We have already carried out an experimental realization of the Bessel type beam to be used in this context at the LOA laser facility. We refer to appendix D for a detailed account of this experiment.

7.2 Atomic properties of argon

A problem is posed in the present application by the very short pulse duration. Indeed, a 30-fs pulse of 810-nm radiation contains only about eleven cycles within the

FWHM of the intensity profile. This is relevant for both the atomic response to the driving laser field and the treatment of the pulse envelope of the propagating harmonic. While the theory developed in chapter 4 allows for the propagation of short pulses, it assumes, however, the atomic data to depend on time only via the intensity. This is a consequence of the Floquet approach (see chapter 2), which provides the atomic data as a function of intensity only, assuming a negligible variation of the intensity over one optical cycle. We have nevertheless adopted the same approach for the present calculation in argon: the data for the atomic dipole moment can been obtained by applying the Floquet method to the 3D-delta-potential model (see section 1.3.1). In particular, for the calculations in argon reported in this chapter, the atomic dipole moments have been obtained from Ref. [67]. Within the framework of the 3D-delta-potential model, the ionization potential I_p of the atom under consideration is replaced by an effective ionization potential $\tilde{I}_p$, which corresponds to the energy difference between the ground state and the first excited state of opposite parity [26]. For the case of argon, with an ionization potential of $I_p = 15.8$ eV and a ground state configuration $^1S_0(3s^2 3p^6)$, the two first excited states of opposite parity are the $^2P_{3/2}(4s)$ and the $^2P_{1/2}(4s')$ states. This corresponds to an effective ionization potential of $\tilde{I}_p = 11.6$ eV and $\tilde{I}_p = 11.8$ eV, respectively. The $^2P_{1/2}(4s')$ state lies somewhat higher than the $^2P_{3/2}(4s)$ state but has an oscillator strength about four times larger than the latter [44]. Considering the overall accuracy of the following calculation, the small energy difference between these two states is neglected and we have used $\tilde{I}_p = 11.6$ eV. Note that we also neglect the possible contribution of all other excited states to the dipole moment in this way. Wave mixing processes are also neglected in this calculation.

To determine up to which intensities the atomic data are required, we have estimated in a first step the ionization rate and the saturation intensity for argon using the ADK tunnelling ionization formula [3], as given by Ilkov *et al.* in Ref. [100]. We have taken the general formula (8) stated in Ref. [100], which includes the dependence of the tunneling formula on the Keldysh parameter γ, Eq. (1.6). Applied to the case of argon, where we average the tunneling formula over the magnetic quantum number m_l of the filled $3p^6$ shell - see Ref. [169], Eq. (61) - we obtain for a linearly polarized

incident field the ionisation rate $w(F)$ as a function of the field-strength F,[1]

$$w(F) = I_p\sqrt{\frac{6}{\pi}}|C_{n^*,l^*}|^2\left(\frac{2F_0}{F\sqrt{1+\gamma^2}}\right)^{2n^*-3/2} A_0(\gamma)\exp\left[-\frac{2F_0}{3F}g(\gamma)\right], \qquad (7.1)$$

where we have defined

$$\begin{aligned}
|C_{n^*,l^*}|^2 &= \frac{1}{2\pi n^*}\left(\frac{4e^2}{n^{*2}-l^{*2}}\right)^{n^*}\left(\frac{n^*-l^*}{n^*+l^*}\right)^{l^*+1/2} \\
A_0(\gamma) &= \frac{4}{\sqrt{3\pi}}\frac{\gamma^2}{1+\gamma^2}\sum_{k\geq\max(\langle\nu\rangle,k_0)}^{+\infty}\exp[-a(\gamma)(k-\nu)]p[\sqrt{b(\gamma)(k-\nu)}] \\
p(x) &= \exp(-x^2)\int_0^x \exp(y^2)\,\mathrm{d}y
\end{aligned}$$

with

$$\begin{aligned}
a(\gamma) &= 2\left(\sinh^{-1}\gamma - \frac{\gamma}{\sqrt{1+\gamma^2}}\right) \\
b(\gamma) &= \frac{2\gamma}{\sqrt{1+\gamma^2}} \\
g(\gamma) &= \frac{3}{2\gamma}\left[\left(1+\frac{1}{2\gamma^2}\right)\sinh^{-1}\gamma - \frac{\sqrt{1+\gamma^2}}{2\gamma}\right] \\
\nu &= \frac{I_p}{\omega}\left(1+\frac{1}{2\gamma^2}\right) \\
k_0 &= \left\langle\frac{I_p}{\omega}+1\right\rangle
\end{aligned}$$

where $\langle\rangle$ indicates the integer part of the real number in brackets, $F_0 = (2I_p)^{3/2}, n^* = Z(2I_p)^{-1/2}, l^* = n^* - 1$, and Z is the charge of the resulting ion. We have only considered single ionization, that is $Z = 1$. The resulting (end-of-pulse) ionization probability, defined by Eq. (4.78), versus the intensity is shown in Fig. 7.1. The saturation intensity is approximately $I_S = 4 - 5 \times 10^{14}$ W/cm^2 for a pulse duration of $\tau = 30$ fs.[2] We will consider in the following a range of intensities $I_1 = 1 - 3 \times 10^{14}$ W/cm^2 in order to limit the ionization of the medium. Thus we do not have

[1]The ionization rate $w(F)$ is given in atomic units. Electric field strengths and intensity are related by $I = cF^2/8\pi$ in atomic units.

[2]For $\tau = 250$ fs we find a saturation intensity of approximately $I_S = 2.5 \times 10^{14}$ W/cm^2 in good agreement with the value cited in Ref. [226] for $\lambda = 794$ nm.

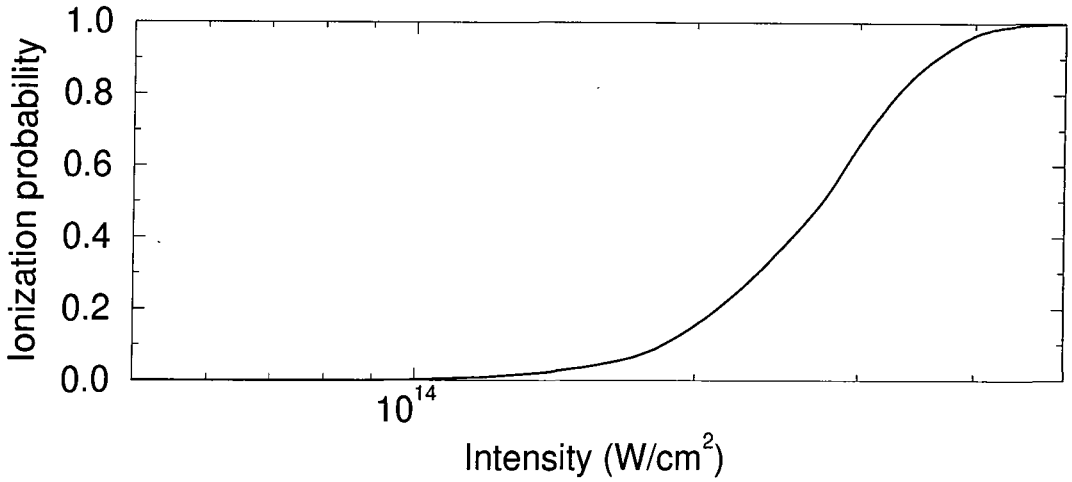

Figure 7.1: Ionization probability versus the intensity of a 810-nm, 30-fs pulse for argon, as defined in Eq. (4.78).

any restrictions on the medium density or the medium length which are necessary otherwise in order to avoid a defocusing of the incident beam due to free electrons, as this feature is not included in our calculations. We neglect the contribution of the other harmonic fields present in the medium to the overall photoionization rate. Indeed, none of the low-order harmonics q=3, 5 and 7, which normally are the strongest harmonics present in the medium, are resonantly enhanced, and it is assumed that the conversion efficiency for higher-order harmonics is sufficiently low for them not to affect significantly the ionization process.

For the range of intensities given above, we find from the cut-off rule (1.2),

$$N_{\max} \approx \frac{15.8 + 19.4\, I_1\,[10^{14}\mathrm{W/cm^2}]}{1.5}, \tag{7.2}$$

the following values for the maximum harmonic order emitted[3]: $N_{\max} \approx 23$ for $I_1 = 1 \times 10^{14}$ W/cm^2 and $N_{\max} \approx 49$ for $I_1 = 3 \times 10^{14}$ W/cm^2 . We therefore restrict the present study to harmonic orders lower than $q = 23$, all of which are then plateau harmonics[4]. Otherwise, the precision of the experimental comparison between Bessel-Gauss and Gaussian beams might be affected by the low conversion efficiencies for harmonics situated beyond the cut-off of the plateau. At the same

[3]We have ignored the possible effect of propagation on the cut-off law [which reduces the prefactor of I_1 in Eq. (7.2), see section 1.4.2] for this simple estimate.

[4]Recall from section 1.2.2 that plateau harmonics are generated at approximately equal strength.

time we want to investigate higher harmonic orders and we also have to find a suitable region of negative dispersion. For this, we have taken the values for the linear atomic polarizabilities for argon from Ref. [128]. It emerges from there that the harmonic orders $q = 17$ and $q = 19$, corresponding to a wavelength of the harmonic of 47.6 nm and 42.6 nm, respectively, are particularly suitable for our purposes. Their linear atomic susceptibilities are roughly given as

$$\chi_{\rm at}(\omega) = 4\pi\alpha_{\rm pol}(\omega) \approx 2.0 \times 10^{-23}\ {\rm cm}^3 \tag{7.3}$$

$$\chi_{\rm at}(q\omega) = 4\pi\alpha_{\rm pol}(q\omega) \approx (-1.5 + i\,2.5) \times 10^{-23}\ {\rm cm}^3\,. \tag{7.4}$$

We have ignored any possible intensity dependence of the linear atomic susceptibilities, though we note that the 17^{th} harmonic (corresponding to a photon energy of 26.0 eV) is fairly close to the $^1P_1(3s3p^64p)$ state at 26.6 eV and the 19^{th} harmonic (29.1 eV) is very close to the $^1P_1(3s3p^611p)$ state of about the same energy. A priori, ac-Stark shift induced resonances could modify the behaviour of the linear atomic susceptibilities.

The dipole moments for the harmonic orders q =17, 19, and 21 are shown in Fig. 7.2. While the moduli follow a power law $|d_q|^2 \propto I_1^q$, in agreement with Eq. (2.21), up to about $I_1 = 10^{14}$ W/cm^2 , the atomic dipole phases depart from constant values at already much lower values of the intensity. Beyond $I_1 \approx 10^{14}$ W/cm^2 , the dipole moments rapidly saturate. The dipole moments are given in arbitrary units and we will therefore only present conversion efficiencies (as a function of the angle α) normalized with respect to the Gaussian limit $\alpha = 0°$.

7.3 Phase-matching and the atomic phase

Expression (6.42) for the optimum Bessel angle, derived in the perturbative limit, does not take the influence of the atomic dipole phase into account. Recall from section 1.4.1 that the atomic phase can be modelled for harmonics in the plateau or in the cut-off regions as a (piecewise) linear function of the intensity,

$$\Phi_{\rm at}(I) = -C\,U_p(I)/\hbar\omega + \Phi_{\rm at}(0)\,. \tag{7.5}$$

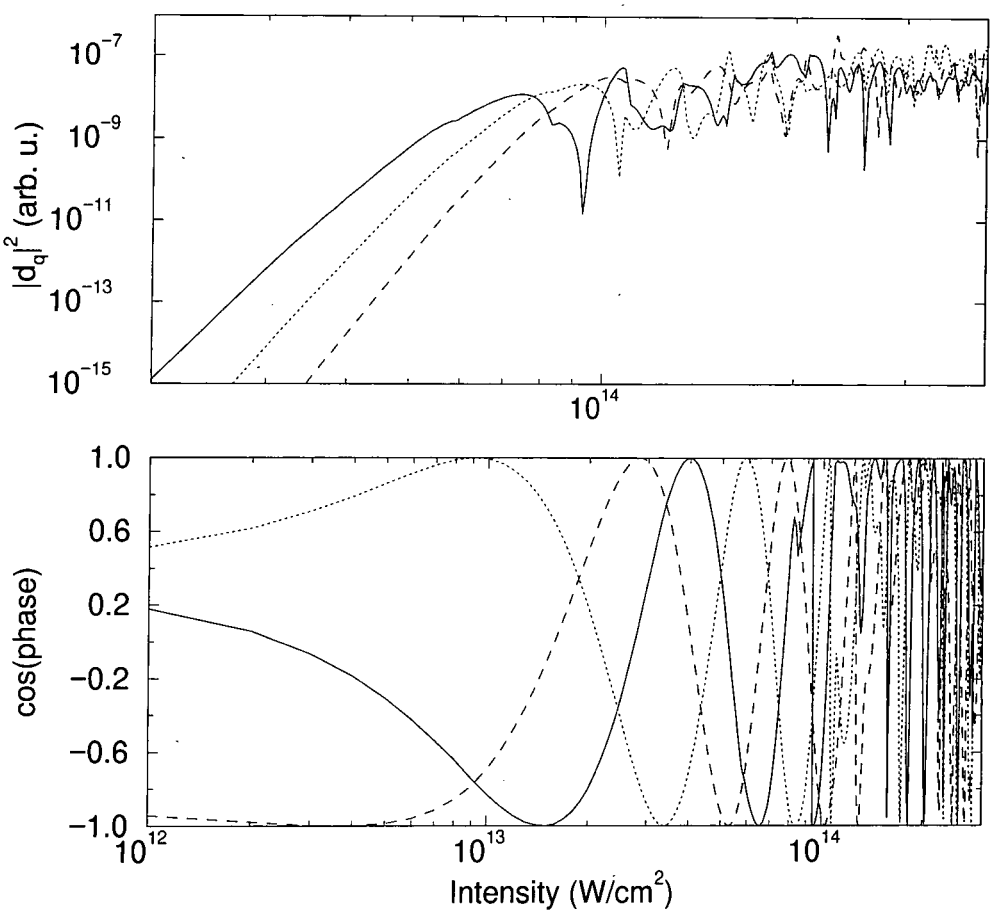

Figure 7.2: Modulus square (top) and phase (bottom) of the atomic dipole moment of argon versus intensity for the harmonics $q = 17$ (solid line), $q = 19$ (dotted line), and $q = 21$ (dashed line). The wavelength of the fundamental is $\lambda = 810$ nm. For the sake of clarity, the cosine of the phases has been plotted. Note also the different range of intensities of the two figures.

Here, U_p is the ponderomotive potential defined in Eq. (1.3) and depending linearly on the intensity, and $C \approx 3.2$ for a harmonic of order q for which the intensity is such that $q > N_{\max}$ in Eq. (7.2), $C \approx 5.8$ otherwise. As an example, we consider the 19^{th} harmonic of argon from Fig. 7.2. We find Eq. (7.5) to be a good fit in this case for $C = 3.2$ and $\Phi_{\rm at}(0) = 1.15$ rad for intensities up to $I_1 = 1 \times 10^{14}$ W/cm^2 , as shown in Fig. 7.3.[5] Provided we assume

$$\frac{L}{b} \ll 1\,, \qquad 4\pi \frac{L^2}{\lambda b} \sin^2\alpha \ll 1\,, \tag{7.6}$$

[5]In fact, C changes nominally from the value 3.2 to 5.8 above 6.5×10^{13} W/cm^2 for $q = 19$ as can be calculated from Eq. (7.2).

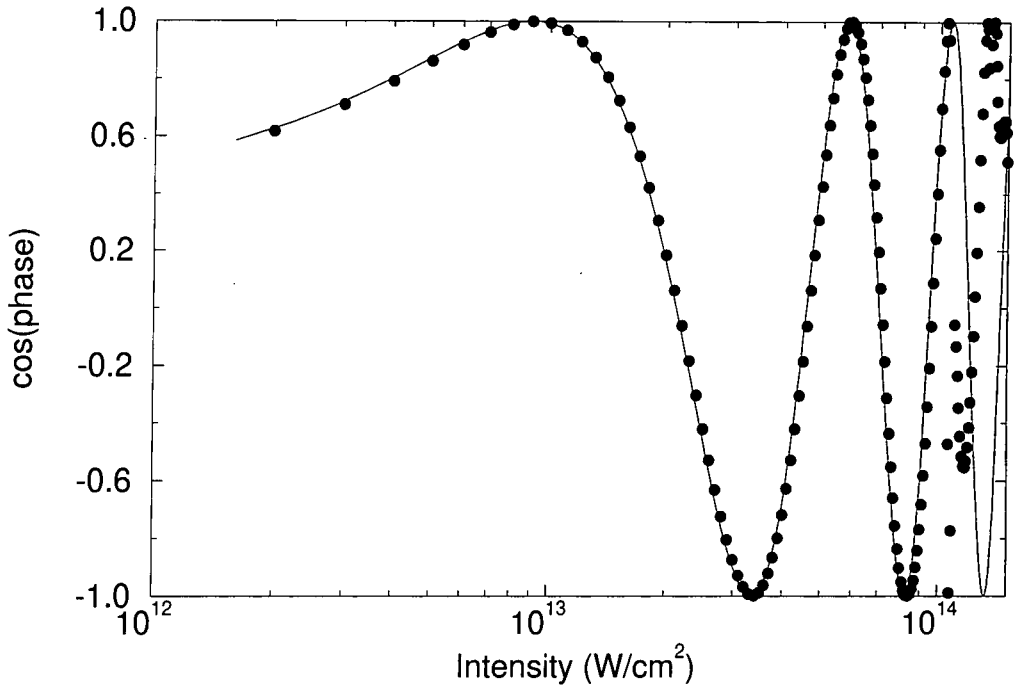

Figure 7.3: Phase of the 19^{th} harmonic (filled circles), same as the dotted line in Fig. 7.2. Solid line is the fit given by Eq. (7.5).

we can approximate the expression for the intensity, Eq. (4.40), by

$$I(\rho = 0, z) \approx I_{\rm f} g(z) \qquad g(z) = 1 - \frac{4\pi z^2 \sin^2 \alpha}{\lambda b}. \tag{7.7}$$

Letting further

$$\tilde{C} = C\, U_p(I_{\rm f})/\hbar\omega\,, \tag{7.8}$$

we find

$$\Phi_{\rm at}(z) = -\tilde{C} g(z)\,, \tag{7.9}$$

which is added to the axial phase variation Eq. (6.29). We follow now the steps outlined in section 6.2.2 with this additional contribution. When evaluating $S(\alpha)$, Eq. (6.32), it is immediately obvious that all mixed terms drop out because of the functions P, Q and R being odd with respect to z, while $\Phi_{\rm at}$ is even[6]. We end up, therefore, with a single contribution to the derivative of $S(\alpha)$, Eq. (6.37),

$$S'(\alpha) = 2 \sin\alpha \left[F_4 \sin^2\alpha \cos\alpha / 2q^2\right], \qquad F_4 = \frac{128}{3} \tilde{C}^2 \frac{z_{\rm max}}{Lb^2}. \tag{7.10}$$

[6]These parity considerations hold only if the medium is centered at the focus of the beam.

In short, we have to replace $F_1 - F_2/q^2$ in the denominator of Eq. (6.41) by $F_1 - (F_2 - F_4)/q^2$. We notice $F_4 > 0$ and consequently the atomic dipole phase reduces the optimum Bessel angle in this approximation. This is irrespective of the sign of the phase but related to the even parity of the phase with respect to z. Further, the contribution of the atomic phase decreases with harmonic order q. This is an immediate consequence of the universality of Eq. (7.5): the constant C depends only very weakly on the harmonic order (and on the atomic system) [124], while both the dispersion and the geometric phases increase linearly with q. To assess the order of magnitude of F_4, we assume a rectangular gas profile with $z_{\max} = 0.5L$ for which we recall $F_1 = F_2 \approx 1$. We find, using $\tilde{C} = 12.8$ for $I_f = 1 \times 10^{14}$ W/cm^2 , a value $F_4 \approx 1.8$. For $q \geq 17$, $(F_2 - F_4)/q^2$ is much smaller than F_1. Hence, the effect of the atomic phase on the optimum Bessel angle should be negligible for all calculations presented in this chapter.

7.4 Conversion efficiencies

For the present calculation, we have used parameters which could be realized experimentally [20], while still likely to produce results which are qualitatively similar to those obtained in previous chapters. We took the (initial) atomic density to be $\mathcal{N}_0 = 3 \times 10^{18}$ atoms/cm^3 (which is about the maximum value that can be achieved with the pulsed argon gas jet used) in order to maximise the optimum Bessel angle α_{opt}. A truncated Lorentzian of FWHM= $L = 1$ mm (see Appendix B) describes accurately the gas density profile and working in the loose focusing limit, we will assume a confocal parameter of $b = 9.1$ mm [20]. This yields, using Eq. (6.42), a value of $\alpha_{\text{opt}} \approx 0.22°$. The experimental conditions in the present case are best simulated by keeping both the confocal parameter and the total energy on target constant. Hence, the peak focal intensity of the Bessel-Gauss beam increases with the angle α according to Eq. (3.29). The gain in conversion efficiency through better phase-matching may therefore be masked by the larger atomic dipole moment at higher intensities. To assess the effect of increasing the peak focal intensity while searching for the optimum Bessel angle, we have computed the conversion efficiency for the

Table 7.1: Harmonic yield for Bessel-Gauss and Gaussian beams of same power for various cases. The confocal parameter of the Bessel-Gauss beam is $b_{\mathrm{BG}} = 9.10$ mm and its peak focal intensity I_{f} increases with the angle α according to Eq. (3.29). The confocal parameter of the Gaussian beam decreases with increasing I_{f} according to Eq. (3.28). The results are normalized to unity at $\alpha = 0°$ and $I_{\mathrm{f}} = 10^{14}$ W/cm^2 for the full calculation. The columns display the following parameters and results: (a) Bessel angle α (in deg.), (b) Peak focal intensity I_{f} ($\times 10^{14}$ W/cm^2), (c) Bessel-Gauss beam: full calculation, (d) as in (c) but without photoionization, (e) as in (c) but without atomic phase, (f) confocal parameter b_{G} (in mm) of the Gaussian beam, (g) Gaussian beam: full calculation, (h) as in (g) but without photoionization, (i) as in (g) but without atomic phase.

α	I_{f}	(c)	(d)	(e)	b_{G}	(g)	(h)	(i)
0.00	1.00	1.0	1.0	1.3	9.10	1.0	1.0	1.3
0.20	1.22	1.5	1.5	2.2	7.46	1.5	1.5	2.2
0.30	1.53	1.6	1.7	2.6	5.95	1.6	1.6	2.5
0.40	1.98	1.7	2.0	3.0	4.60	1.5	1.8	2.7
0.50	2.55	1.2	1.8	2.6	3.57	1.1	1.7	2.5
0.60	3.18	0.8	1.1	1.6	2.87	0.8	1.4	1.8

corresponding Gaussian beam at the same power and peak intensity (but necessarily different confocal parameter). Table 7.1 provides a summary of the results obtained from the calculations for the harmonic order $q = 17$. Though the variations in the conversion efficiencies reported in Table 7.1 are small, we can clearly distinguish the features already encountered in previous chapters: the conversion efficiency for the full calculation for the Bessel-Gauss beam peaks at a given value of the Bessel angle, of about $\alpha = 0.3° - 0.4°$ [column (c)] in the present case, which is larger than the predicted value of $\alpha_{\mathrm{opt}} \approx 0.22°$. This is also the case if photoionization is neglected, while achieving only a somewhat higher harmonic yield [column (d)]. It clearly appears from the data above, however, that the conversion efficiency is mostly dependent on the variation of the peak focal intensity, as the same pattern can be found in the yields of the corresponding Gaussian beam [columns (g) and (h)]. Neglecting the atomic dipole phase in the calculations does not visibly affect the value of the intensity at which the maximum conversion efficiencies occur, though it enhances the harmonic yields [columns (e) and (i)]. However, the fit Eq. (7.5) of the atomic phase holds only up to $I_{\mathrm{f}} = 1 \times 10^{14}$ W/cm^2 and we have to postpone the discussion about the atomic phase until later parts of this section. We have also performed the full calculation for the Bessel-Gauss beam including the slowly-varying envelope approximation Eq. (4.72) in the calculations (not shown in the table). Though small

changes were noticeable, the overall impact on the conversion efficiency was below the accuracy of the figures given in Table 7.1. This is likely to be a consequence of the fairly high harmonic order under consideration. Indeed, recall that the contribution stemming from the slowly-varying envelope approximation is proportional to $1/q$, the value of the prefactor entering Eq. (4.72) being approximately 5×10^{-3} despite the short pulse duration[7]. A similar argument has been put forward by the authors of Ref. [5] in their treatment of the slowly-varying envelope approximation. The weak dependence of the (normalized) conversion efficiency, as a function of the Bessel angle α, with respect to gas density profiles, the atomic dipole phase and ionization, has (at least) the merit of making measurements rather immune to fluctuations in the parameters of the calculations.

In order to get a better understanding of the various mechanisms which might influence phase-matching in the present short pulse generation of higher-order harmonics, we have carried out some calculations for the same atomic system, but for parameters simulating experimental conditions different from those considered previously. To disentangle the effects of both the phase-matching and the atomic dipole strength, we keep the peak focal intensity constant in the following and we fix its value to $I_{\rm f} = 1 \times 10^{14}$ W/cm^2 in all further calculations. It this way we also make sure that the atomic dipole phase is properly modelled by Eq. (7.5).

We keep first the total power incident on target constant, thus varying the confocal parameter, which we have set to $b = 4.0$ mm at $\alpha = 0°$. Furthermore, we have raised the atomic density to a value of $\mathcal{N}_0 = 6 \times 10^{18}$ atoms/cm^3 in an attempt to obtain larger optimum Bessel angles[8]. Table 7.2 shows the various parameters used in the calculations together with the normalized conversion efficiencies. The optimum angle $\alpha_{\rm opt}$, calculated according to Eq. (6.42), is varying with the confocal parameter before reaching the plane wave limit values of $\alpha_{\rm opt} = 0.83°$ for a rectangular gas profile and $\alpha_{\rm opt} = 0.67°$ for a truncated Lorentz gas profile. The maxima of the conversion efficiency curves occur around $\alpha = 0.50-0.55°$, in much better agreement with the predicted optimum angles than in the previous study. Very much as seen

[7]For comparison, the prefactor would be the same for the third harmonic of a 170-fs pulse.

[8]Note that photoionization is negligible for the intensity considered in this calculation, thus the value of $\mathcal{N}_0$ (or L) is not limited by a possible defocalization of the incident beam.

Table 7.2: Conversion efficiencies for various Bessel-Gauss beams at fixed total power and peak intensity $I_1 = 10^{14}$ W/cm^2 for the harmonic orders $q = 17$ and $q = 19$. The Bessel-Gauss beam has a conical half-angle α (in deg.) and a confocal parameter $b_{\rm BG}$ (in mm). The optimum Bessel angle $\alpha_{\rm opt}$ is determined from Eq. (6.42), where (RP) stands for a rectangular gas profile and (LP) for truncated Lorentz profile. The optimum Bessel angle is the same for $q = 17$ and $q = 19$ to the precision of the numbers given in this table ($\pm 0.01°$). The results are normalized to the value at $\alpha = 0°$ (Gaussian beam limit): (a) $q = 17$ and a truncated Lorentz gas profile, (b) as in (a) but for a rectangular gas profile, (c) as in (a) but for $q = 19$ and (d) as in (c) but without the atomic dipole phase.

α	$b_{\rm BG}$	$\alpha_{\rm opt}^{(RP)}$	$\alpha_{\rm opt}^{(LP)}$	(a)	(b)	(c)	(d)
0.00	4.0	0.55	0.26	1.00	1.00	1.00	1.00
0.20	4.4	0.58	0.31	1.01	1.00	1.01	1.01
0.30	5.2	0.63	0.38	1.02	1.02	1.06	1.04
0.40	7.0	0.67	0.47	1.08	1.05	1.18	1.14
0.50	12.1	0.75	0.56	1.19	1.12	1.44	1.31
0.60	20.0	0.78	0.61	1.13	1.10	1.39	1.13
0.70	28.2	0.80	0.62	0.90	0.98	1.01	0.65
0.80	37.3	0.81	0.64	0.50	0.83	0.48	0.19

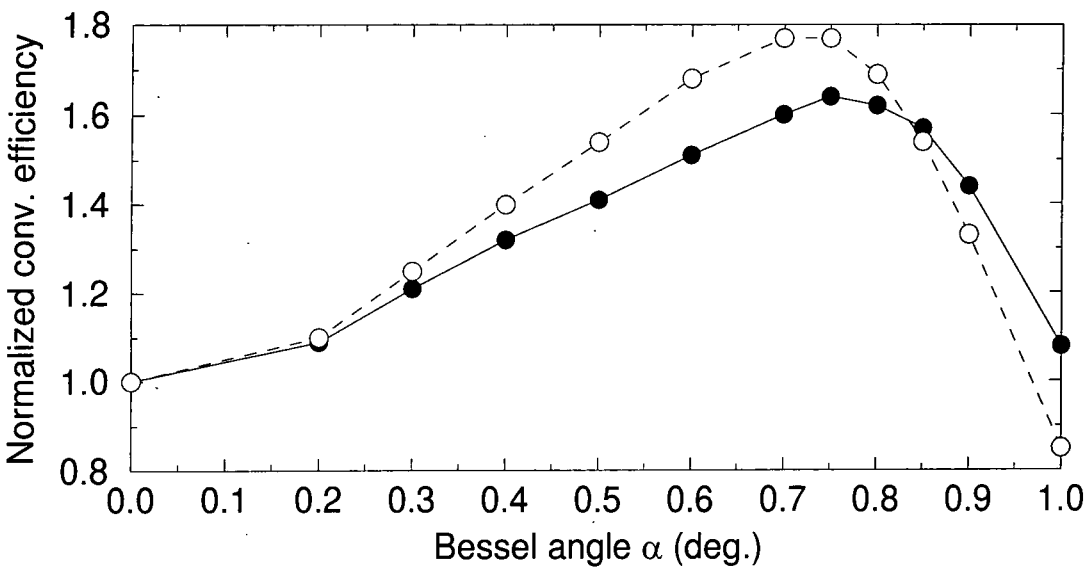

Figure 7.4: Conversion efficiencies for the 19^{th} harmonic of 810-nm radiation in argon versus the Bessel angle. A rectangular gas profile, with $L = 1$ mm, and a confocal parameter of $b = 22$ mm were assumed. Filled circles (solid line) are for the full calculation, open circles (dashed line) are for the calculation where the atomic dipole phase has been neglected.

already before in Table 7.1, we find the position of these maxima to depend only weakly on the gas density profiles or on the atomic dipole phase. The absolute yields differ only very little for all conversion efficiencies given in Table 7.2.

In a second calculation we have kept the focusing geometry fixed, taking the confocal parameter to be $b = 22$ mm. For a rectangular gas profile ($L = 1$ mm), this rises the value of the optimum Bessel angle to $\alpha_{\text{opt}} = 0.79°$. Peak focal intensity and atomic density are as before and the energy on target is decreasing with increasing Bessel angle. We have assumed a pulse duration (FWHM of the intensity) of $\tau = 150$ fs in this last calculation[9]. We have calculated here the normalized conversion efficiencies for the harmonic order $q = 19$, first including then neglecting the atomic dipole phase in the calculations. The resulting curves are shown in Fig. 7.4. The position of the maxima are now in very good agreement with the predicted value of α_{opt}. As before, we find little difference in the normalized conversion efficiencies for both cases (this applies also to the absolute conversion efficiencies). Though the curves are in very good qualitative agreement with theory predicting a negligible influence of the atomic dipole phase on the optimum Bessel angle, a trend towards larger optimum Bessel angles is discernible if the atomic dipole phase is taken into account. We tentatively attribute this quantitative discrepancy to the neglect of the variation of the intensity with the radial coordinate in Eq. (7.7).

7.5 Far-field profiles

We do not attempt to discuss results for the spatio-temporal far-field profiles in much detail, as they are more difficult to converge than the overall conversion efficiency (see also section E.2). The latter is a fairly 'robust' quantity in the sense that it is a single number obtained by an integration over time and space and as such converges much faster (to the degree of precision given in the tables) than the shape of the various individual time- and space-dependent profiles which enter its calculation.

The spatial far-field profiles of the harmonics essentially peak on axis, both for the Bessel-Gauss and the Gaussian beam. This comes as no surprise, as we already expect a low value of the far-field angle $\beta_{\text{opt}} \approx \alpha_{\text{opt}}/q$ due to the fairly high harmonic orders considered. This is also in qualitative agreement with the experimental find-

[9]The reason for this lies essentially in an improved convergence for calculations for large Bessel angles. Ionization is still negligible for a peak focal intensity of $I_f = 1 \times 10^{14}$ W/cm^2 .

ings of Peatross *et al.* [157] who generated higher order harmonics (from the 11^{th} harmonic of 1054 nm radiation onwards) using an annular beam (corresponding to a range of Bessel angles $\alpha \approx 0.2° - 0.3°$) focused into a xenon gas jet and found the harmonic radiation to be emitted essentially along the axis of propagation. In this way, the authors were able to separate the incident beam from the harmonic beam simply by placing an annular aperture behind the medium, blocking the emerging fundamental beam off-axis[10].

7.6 Discussion and summary

In this chapter we have extended the application of the theory of harmonic generation using Bessel-Gauss beams to higher harmonic orders. These calculations are rather exploratory in nature: the various atomic properties (dipole moments, linear atomic polarizabilities and ionization rate) have been obtained from different sources and are subject to rather crude approximations. This does not matter if the model atom is taken as being defined by these data but application to argon is to be made cum granum salis. The use of Floquet data for pulse durations as short as 30 fs is at least questionable. We stress again that this is not affected by the fact that we did not find any significant difference in the results whether or not the slowly-varying envelope correction was included in the propagation calculations.

With regard to the results we note that our reported gains in conversion efficiency through the use of Bessel-Gauss beams are too small to be relevant from an experimental point of view. From a theoretical point of view, we find the dependence of the conversion efficiency on the Bessel angle to be in fair agreement with the theory and similar findings in the previous chapters. This agreement (and the gain in conversion efficiency) significantly increases with increasing optimum Bessel angle. In particular, we could show in the present case, both theoretically and through numerical calculations, the optimum Bessel angle not to be affected by the atomic dipole

[10]Unfortunately, no study of the conversion efficiencies was reported in Ref. [157]. Note also, that the loss of intensity when creating the annular beam by blocking the central part of a Gaussian beam was approximately 50 % .

phase. Altogether, this study suggests that the use of Bessel-Gauss beams may lead to substantial improvements for the conversion efficiencies under experimental conditions which favor large Bessel angles for optimum phase-matching. However, because of the rather small negative dispersion of the system studied in this chapter, high gas densities are required to achieve a suitably large value for α_{opt}. In view of the results of chapters 5, it would be very useful to study the conversion efficiency for large Bessel angles and large confocal parameters, at peak focal intensities around $I_{\mathrm{f}} \approx 10^{15}$ W/cm^2 - indeed, ionization occurs only in a narrow central region of the medium while all secondary peaks of the Bessel profile contribute to the generation of harmonic radiation just below saturation.

Finally, we stress that even for negligible gains in conversion efficiency, the Bessel-Gauss beam still retains the advantage of facilitating the spatial separation of the harmonic from the fundamental in the far-field region. The harmonics are preferentially emitted along the propagation direction, while the fundamental has a conical shape in the far-field region, the conical half-angle being the Bessel angle α.

Conclusions

This thesis reports the first theoretical and numerical investigation of harmonic generation in gases using the most general form of a (zero-order) Bessel-Gauss beam. Previous work has been limited to beam geometries which are special cases of Bessel-Gauss beams, namely Gaussian beams, Bessel beams and plane waves. Harmonic generation using Bessel beams has only been considered for low-order harmonics in the perturbative regime, both theoretically [217, 218] and experimentally [85, 165, 166, 231]. In the present work, we have extended the theoretical investigations to the nonperturbative regime. In addition to work on low-order harmonics, we have studied applications to higher-order harmonic generation. In contrast to previous work on Bessel beams, the propagation aspect is fully time-dependent and allows for the simulation of realistic laser pulses. To the best of our knowledge, it is also the first time that the effect of an ac-Stark-shifted resonance on the phase-matching properties has been investigated in such detail for any type of incident beam.

What conclusions can be drawn from the calculations presented in chapters 5 to 7, considering that the overall aim of introducing the Bessel-Gauss beam was to improve the conversion efficiency in harmonic generation processes through better phase-matching? To put things into perspective, it is worth stressing again that both the Gaussian beam and the plane wave are nothing but two special cases of the large family of Bessel-Gauss beams. As discussed in the connection with the derivation of Eq. (6.42) for the optimum Bessel angle, both the Gaussian beam and the plane wave can provide optimum phase-matching for a number of cases and are, by definition, the corresponding optimum Bessel-Gauss beams. Hence, the search for a more general Bessel-Gauss beam providing optimum conditions relies more on situations where, due to externally imposed conditions on some of the focusing parameters (medium length, confocal parameter) and/or medium properties (gas density and profile, dispersion due to atoms or possibly to ions and electrons), the more 'traditional' beams are known to fail in achieving phase-matching. A simple example is the phase-matching of a negatively dispersive atomic gas in the plane

wave limit: instead of mixing the pure gas with some other, positively dispersive, component, phase-matching can be achieved by use of a suitable Bessel-Gauss beam in the pure gas.

The question about the potential usefulness of Bessel-Gauss beams[11] contains two different aspects of which we have treated only one in the present work. Indeed, we have always assumed, in our models and calculations, a Bessel-Gauss beam of total energy and peak focal intensity on target comparable to the reference Gaussian beam. Therefore, we do not take power losses in the Bessel beam generator into account. This might hamper the conversion efficiency comparison, if, in fact, a much higher input power is required, in order to obtain the same power on target than for the reference Gaussian beam. Another problem might arise from the possible lack of a sufficient beam quality. Additional optical elements, e.g., such as to apodize the intensity fluctuations of the Bessel-Gauss beam along the propagation direction, might render the experimental set-up complicated and the power loss in the Bessel beam generator even more severe. Conical lenses do not exhibit any significant power losses but the Bessel angle cannot be tuned. Moreover, these lenses are difficult to manufacture and barely available commercially. From a conceptual point of view, the most satisfactory approach is the one by Jabczynski [102], who used a resonator with an annular active medium to generate a Bessel type beam. More generally speaking, the development of a laser system generating a Bessel-Gauss beam mode is desirable. Overall, the prerequisite for the successful application of Bessel-Gauss beams in nonlinear optics is an energy-efficient Bessel beam generator, delivering beams of (up to) high power densities, tunable in its characteristics (Bessel angle) and providing a spatial beam quality comparable to what can be achieved for Gaussian beams.

The second aspect, which we have treated in detail in the present study, can be loosely formulated as follows: for which conditions is the gain in conversion efficiency through improved phase-matching significantly higher than potential losses in driving power, when increasing the Bessel angle α which defines the Bessel-Gauss beam (the Gaussian beam limit being given by $\alpha = 0°$)? Losses in driving power

[11] It is always understood that this refers to harmonic generation processes only.

occur when, with increasing Bessel angle, the energy of the incident Bessel-Gauss beam spreads out radially into regions of lower intensities. Less power is therefore available in the central region driving the atomic dipole at high intensities. There is no answer which can be given a priori and only a numerical calculation of the conversion efficiency as a function of the Bessel angle α will tell. However, we have developed qualitative and partly quantitative criteria, which predict fairly accurately which Bessel-Gauss beam to choose in order to obtain larger conversion efficiencies than for a comparable Gaussian beam. These findings can be summarized as follows: as a rather elementary condition, we find that the Bessel angle which corresponds to a maximum conversion efficiency must be large enough in order for the Bessel-Gauss beam to be sufficiently distinct from the Gaussian reference beam. In this case, a good estimate for this angle is the optimum phase-matching angle α_{opt}, determined by Eq. (6.42). For large confocal parameters (the Bessel beam limit) the energy of the beam will spread out over a large number of nodes of the Bessel profile, which are of lower peak intensity compared to the central maximum. There is a strong competition between phase-matching and the loss of power driving the atomic dipole at high intensities. The gain in conversion efficiency will be moderate and a high atomic density (more precisely, a large macroscopic negative dispersion) is required to make this gain through phase-matching prevailing over the loss of driving power. This situation may change completely in the high-intensity limit as we found in chapter 5. There, the dipole moment saturates and the secondary peaks reach an intensity where they can contribute efficiently to harmonic generation. The Bessel-Gauss beam then offers in principle all the advantages of a plane wave geometry (smaller variations of the intensity within the medium limiting, e.g., the influence of the atomic dipole phase, at least along the propagation direction) together with improved phase-matching. With respect to high-order harmonic generation, the results of chapter 7, though less conclusive than the results for low-order harmonics reported in chapters 5 and 6, should therefore be greeted with cautious optimism. Smaller confocal parameters restrict the power carried by the beam closer to axis, even for larger Bessel angles. This was found to be suitable for working in the perturbative limit, where large gains in conversion efficiency where obtained. However,

for a fixed focal intensity, smaller confocal parameters limit the power on target which can be converted into harmonic radiation.

Last but not least, we stress again the necessity of a negatively dispersive medium in order to achieve optimum phase-matching with a Bessel-Gauss beam. Alkali vapors are probably the best candidates due to their extended regions of negative dispersion coupled with large oscillator strengths. Their low ionization potential, however, limits their usefulness to low-order harmonic generation at moderate intensities. Rare gases are likely to be the best 'all round' components: it is reasonably easy to find regions of negative dispersion and they are suitable for high-order harmonic generation. We recall from the introduction that many more atomic and molecular systems have been tested as target gases in harmonic generation experiments. Depending on their dispersion properties they might also be suitable for harmonic generation using Bessel-Gauss beams.

No definite conclusions can be drawn for positively dispersive media from the present work. Furthermore, we have not studied tight focusing in sufficient detail to be able to draw conclusions with respect to this particular focusing limit. Irrespective of the gain in conversion efficiency, the spatial separation of the harmonic from the fundamental is facilitated in the case of a Bessel-Gauss beam. The fundamental has a conically shaped far-field profile, the conical half-angle is given by the Bessel angle α. The harmonic is typically emitted much closer along the axis of propagation. For a Bessel beam, the preferred emission angle is simply α/q, where q is the harmonic order. For Bessel-Gauss beams of moderate and small confocal parameters the determination of the preferred emission angle is more complicated.

In summary, Bessel-Gauss beams introduce an additional degree of freedom into the otherwise well known phase-matching conditions for Gaussian beams. The possibility of a substantial gain in conversion efficiency is given, provided the nonlinear medium is negatively dispersive. The application of Bessel-Gauss beams on a larger scale in harmonic generation experiments (or even in industrial devices) is likely to be dependent to the development of a Bessel-Gauss beam source of a quality comparable to existing sources for Gaussian beams.

Appendix A

Conversion Factors

In this appendix we discuss briefly the units of some of the most relevant physical quantities appearing in this thesis and also how to convert the pressure of an atomic gas, given in some experimental papers on the subject, into atomic densities.

A.1 Conversion between SI and atomic units

All atomic data obtained with the Floquet code [181] are given in atomic units (a.u.). They have to be converted into SI units which are used in treating the propagation of the harmonic fields.

The *linear atomic polarizability* $\alpha_{\rm pol}$ is computed as $d_{\rm L} = \alpha_{\rm pol}\, E$ in a.u. and defined as $d_{\rm L} = \epsilon_0 \chi\, E$ in SI units [see Eq. (2.20)]. As $4\pi\epsilon_0 = 1$ in atomic units, dividing by ϵ_0 is equivalent to multiplying by 4π. Further, the physical dimension of the polarizability being a volume, we have to multiply by a_0^3, the Bohr radius being the atomic unit of length, $a_0 = 5.292 \times 10^{-9}$ cm. Thus:

$$\chi_{\rm at}\ [{\rm cm}^3] = 4\pi a_0^3\ \alpha_{\rm pol}\ [{\rm a.u.}]\,. \tag{A.1}$$

In the literature, the electromagnetic displacement vector is often defined as $\boldsymbol{D} = \boldsymbol{E} + 4\pi\,\boldsymbol{P}$ instead of Eq. (4.5), see, e.g., Ref. [33]. In that case both the linear atomic polarizability and the linear atomic susceptibility are the same quantity[1], and the

[1] As long as local-field corrections are negligible.

factor of 4π appearing in Eq. (A.1) has to be omitted.

The *dipole moment* is defined in the same way in both unit systems, hence only the physical dimension has to be added, which is electronic charge times length:

$$d_q \text{ [SI]} = e a_0 \, d_q \text{ [a.u.]}. \tag{A.2}$$

A.2 Pressure and atomic gas density

In many experimental papers on harmonic generation in gases the pressure (in Torr or mbar) is quoted rather than the (peak) atomic density $\mathcal{N}_0$ in atoms/cm^3 . For gases in a gas cell, thermodynamic equilibrium can be assumed, and the ideal gas law holds,

$$\mathcal{N}_0 \text{ [atoms/cm}^3 \text{]} = 10^{-4}/(kT)\, p \text{ [mbar]}, \tag{A.3}$$

where k is Boltzmann's constant, $k = 1.381 \times 10^{-23}$ J/K. For a gas jet this is, strictly speaking, not valid. The pressure (and temperature) distribution determining the local gas density in the interaction chamber has to be calculated using hydrodynamics in order to model the flow of the gas from the gas container (at a given backing pressure) down to the gas nozzle and into the vacuum chamber. For all practical purposes, it is generally assumed that the ideal gas law still holds up to high pressures (in the vacuum chamber) though it is difficult to give an upper bound for the validity of this assumption.

Recalling 1 Torr = 1.333 mbar and assuming that all laboratories are kept at an

Table A.1: Comparison between cited and calculated values of the atomic density in the literature. The density $\mathcal{N}_0$ is in atoms/cm^3 (the numbers in parenthesis indicate powers of ten), the temperature T in $°C$, the unit of the pressure p is given in the corresponding column.

Ref.	p (cit.)	T (cit.)	$\mathcal{N}_0$ (cit.)	$\mathcal{N}_0$ (calc.)
[130]	15 Torr	-	5 (17)	5.0 (17)
[2]	80 mbar	-	2 (18)	2.0 (18)
[163]	1000 Torr	-	3.2 (19)	3.3 (19)
[85]	4.4 Torr	355	7 (16)	6.8 (16)

average temperature of about $T \approx 20°C$, we arrive at

$$\mathcal{N}_0\,[\text{atoms/cm}^3\,] \approx 2.5 \times 10^{16}\,p\,[\text{mbar}] = 3.3 \times 10^{16}\,p\,[\text{Torr}]\,. \qquad \text{(A.4)}$$

This is generally in good agreement with the figures given in the literature. The following Table A.1 gives an overview of the comparison between the cited values and those obtained from Eqs. (A.3) and (A.4).

Appendix B

Atomic Gas Densities

B.1 Gas density profiles

We discuss here several gas density profiles $\sigma(\rho, z)$, having the general features assumed in section 4.5.2, namely

$$0 \leq \sigma(\rho, z) \leq 1 \tag{B.1}$$

$$\Sigma(\rho, z_{\max}) \equiv \widehat{\sigma}(\rho) = g(\rho)L\,, \tag{B.2}$$

where $\Sigma(\rho, z)$ is defined by Eq. (4.83) and L is the length of the medium to be introduced in the following. Condition Eq. (B.1) has two purposes; firstly, to make sure the density profile is defined as being positive definite, secondly, to allow for the interpretation of $\mathcal{N}_0$ as the peak atomic density by normalizing the largest value of the profile to unity.

The first gas density profile we consider has a Lorentian shape given by

$$\sigma(\rho, z) = \frac{g(\rho)}{1 + (2z/L)^2}\,, \tag{B.3}$$

with $g(\rho) \leq 1$, but otherwise arbitrary. Because of $\sigma(\rho, z = \pm L/2) = \sigma(\rho, z = 0)/2$, L is the FWHM, which we take to be the definition of the medium length[1]. The

[1]It is easy to describe profiles which are not centered at the focal plane $z = 0$ by making the replacement $z \to z - z_0$.

optical path integral Eq. (4.83) yields

$$\Sigma(\rho,z) = g(\rho)\frac{L}{2}\left[\tan^{-1}\left(\frac{2z}{L}\right) - \tan^{-1}\left(\frac{2z_{\min}}{L}\right)\right], \tag{B.4}$$

and in order to satisfy condition Eq. (B.2), we truncate the Lorentz profile such that $z_{\min} = -(L\tan 1)/2 \approx -0.78L$ and $z_{\max} = -z_{\min}$. A truncated Lorentzian profile for the description of the atomic density in a gas jet has been used e.g. in Ref. [5].

Another gas density profile is described by

$$\sigma(\rho,z) = g(\rho)\cos^2(\pi z/2L) \tag{B.5}$$

$$\Sigma(\rho,z) = g(\rho)\frac{L}{2}\left[\frac{z}{L} + \frac{1}{\pi}\sin\left(\frac{\pi z}{L}\right) - \frac{z_{\min}}{L} - \frac{1}{\pi}\sin\left(\frac{\pi z_{\min}}{L}\right)\right], \tag{B.6}$$

where L is again the FWHM and $z_{\max} = -z_{\min} = L$. This cosine-square profile has the advantage of fitting experimental gas jet profiles as accurately as the truncated Lorentz profile while decreasing smoothly to zero. Fig. B.1 shows a comparison between the Lorentz and the cosine-square profile. The experimental data points have been taken from Ref. [125]. Both curves fit these points reasonably well.

The last density profile to be considered is the rectangular gas profile. It is suitable for gas cells or gas jets with sharp boundaries. The rectangular gas profile is described by

$$\sigma(\rho,z) = g(\rho) \tag{B.7}$$

$$\Sigma(\rho,z) = g(\rho)\frac{L}{2}\left[\frac{2z}{L} - \frac{2z_{\min}}{L}\right], \tag{B.8}$$

with $z_{\max} = -z_{\min} = L/2$.

B.2 The axial integral

We turn now to the axial integral Eq. (4.86). Recalling the definition of $K(u)$ from Eq. (4.87), we note first $K(u \le u_{\min}) = 0$ and $K(u \ge u_{\max}) = 1$. Since $K(u)$ is a monotonically increasing function of u, we can bring the integral Eq. (4.86) into the form

$$F_z(A,B,C) = \exp(-iAu_{\min})\int_0^1 \exp\{i[AK^{-1}(w) + Bw]\}\exp(-Cw)\,\mathrm{d}w \tag{B.9}$$

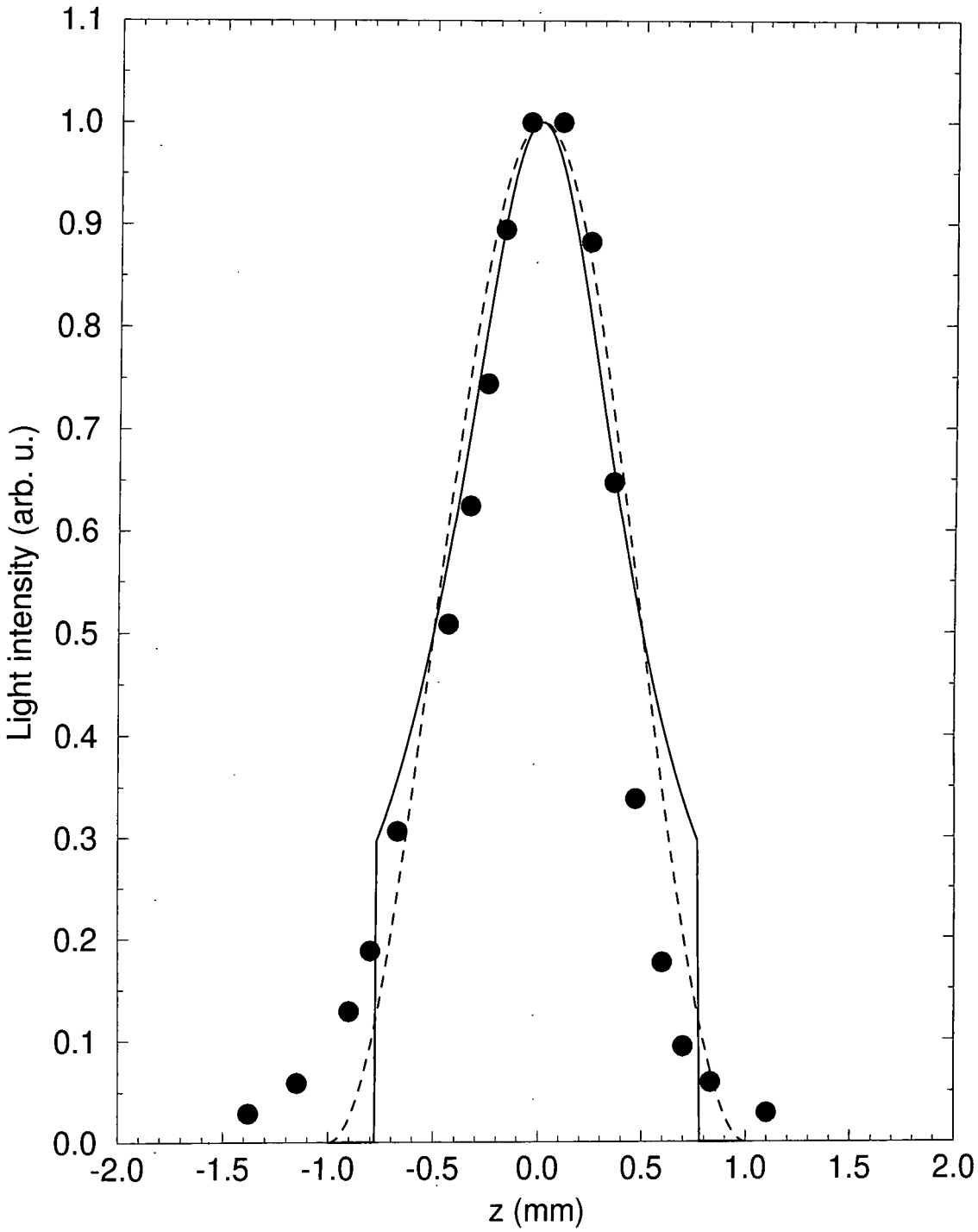

Figure B.1: Comparison between the truncated Lorentz profile (solid line) and the cosine-square profile (dashed line) for fitting experimental data points of a typical gas jet profile (filled circles). The experimental data points have been taken from Li [125] and show the intensity of laser induced fluorescence light (in arb.u.) versus the position (in mm) of the detector. The gas density is taken proportional to the detector signal. The FWHM of this gas jet profile is approximately 1 mm and this value of L has been taken for the fitting profiles.

where $K^{-1}(w) = u$ is the inverse function of $w = K(u)$. Since

$$\int_{w_a}^{w_b} f(w)\mathrm{d}w \leq \int_{w_a}^{w_b} |f(w)|\mathrm{d}w\,,$$

we find immediately that

$$|F_z| \leq \frac{1-\exp(-C)}{C} \stackrel{C\to 0}{\longrightarrow} 1\,, \tag{B.10}$$

irrespective of the values of A and B.

For the truncated Lorentz profile we obtain

$$K(u) = (1/2)[\tan^{-1}(2u)+1] \tag{B.11}$$

$$K'(u) = 1/(1+4u^2) \tag{B.12}$$

$$K^{-1}(w) = \tan[2(w-1/2)]/2\,, \tag{B.13}$$

whith $u_{\min} = -(1/2)\tan 1$ and $u_{\max} = +(1/2)\tan 1$, however the axial integral cannot be obtained analytically in this case. This is different for the cosine-square profile,

$$K(u) = 1/2\,[u + (1/\pi)\,\sin(\pi u) + 1] \tag{B.14}$$

$$K'(u) = \cos^2(\pi u/2) \tag{B.15}$$

with $u_{\min} = -1$ and $u_{\max} = +1$. Inserting these expressions into the integral Eq. (4.86), we obtain after a straightforward calculation

$$\begin{aligned} F_z &= \frac{i\pi^2}{2}\left(e^{2iz}-1\right)\sum_{N=-\infty}^{+\infty} J_N\left(\frac{B+iC}{2\pi}\right) \\ &\times \left[\frac{1}{(z-(N-1)\pi)(z-N\pi)(z-(N+1)\pi)}\right], \end{aligned} \tag{B.16}$$

where $z = A + B/2 + iC/2$. For the rectangular gas profile we simply have

$$K(u) = u + 1/2 \tag{B.17}$$

$$K'(u) = 1 \tag{B.18}$$

$$K^{-1}(w) = w - 1/2 \tag{B.19}$$

with $u_{\min} = -1/2$ and $u_{\min} = +1/2$. This leads to

$$\begin{aligned} F_z &= \frac{[C+i\,(A+B)][1-\cos(A+B)\,\exp(-C)]}{(A+B)^2+C^2} \\ &+ \frac{[(A+B)-i\,C]\sin(A+B)\,\exp(-C)}{(A+B)^2+C^2}. \end{aligned} \tag{B.20}$$

Appendix C

The Sellmeir Formula

C.1 Introduction

In this appendix we calculate linear atomic polarizabilities with the help of the well known Sellmeir formula [33, 191]. This formula can be obtained from perturbation theory within the density matrix formalism (to account for relaxation terms) and is valid in the low-intensity limit. In this way we can check the Floquet results from chapter 2 in the vicinity of resonances, at least for the low-intensity limit. Moreover, the Floquet method does not take spontaneous emission into account, and for atoms in a gas other line-broadening mechanisms become important, which we can also treat approximately with the Sellmeir formula. By comparing the imaginary part of the linear atomic polarizability obtained in both ways, we will be able to infer the minimum intensity to be reached for the intensity-induced width to be larger than the natural width due to spontaneous emission for the isolated hydrogen atom at rest and, more importantly, the corresponding minimum intensity to be reached for the light-induced width to be larger than the line broadening for the atomic hydrogen gas. We will also use the Sellmeir formula to calculate the frequency dependence of the linear atomic polarizabilities for xenon, as required for the calculations in chapter 6 and in Appendix E. The Sellmeir formula is given by

$$\alpha_{\mathrm{pol}}(\lambda)[\mathrm{cm}^3] = \frac{r_e}{(2\pi)^2} \sum_i \frac{f_i}{\lambda_i^{-2} - \lambda^{-2} + \left(\frac{\Gamma_i}{4\pi c}\right)^2 - i\frac{\Gamma_i}{2\pi c\lambda}}, \tag{C.1}$$

where we have expressed the frequency dependence in terms of the wavelength[1]. In this equation, $r_e = 2.818 \times 10^{13}$ cm is the classical radius of the electron and f_i is the optical oscillator strength for the i-th transition at wavelength λ_i (in cm) and of width $\hbar\Gamma_i$ (Γ_i in 1/s). Eq. (C.1) assumes a Lorentzian shape for the resonances. This is valid for the two cases considered, an isolated atom at rest, where $\Gamma_i = \Gamma_i^{(n)}$ is the natural linewidth, and for an atom in a gas for gas densities where pressure broadening exceeds Doppler broadening, which is the case in the present work [79]. Thus, $\Gamma_i = \Gamma_i^{(p)}$ in this limit, with

$$\Gamma_i^{(p)}[1/\mathrm{s}] \approx 1.1 \times 10^{-2}\, \lambda_i[\mathrm{cm}]\, \mathcal{N}_0[\mathrm{at./cm^3}]\, f_i\,. \tag{C.2}$$

Expression (C.2) is valid for self-broadening in a pure gas with a typical accuracy of $< 10\%$ [79, 156][2]. To assess the importance of absorption, we will compute the absorption coefficient for a plane wave travelling a distance L through a linear medium [33],

$$I(L) = I(0)\, \exp(-KL)\,, \qquad KL = 8\pi^2 q (L/\lambda) \mathcal{N}_0\, \mathrm{Im}(\alpha_{\mathrm{pol}})\,. \tag{C.3}$$

For $\lambda = 355$ nm and $q = 3$, we obtain

$$KL \approx 6.7 \times 10^5\, L[\mathrm{mm}]\, \mathcal{N}_0[\mathrm{at./cm^3}]\, \mathrm{Im}(\alpha_{\mathrm{pol}})[\mathrm{cm^3}]\,. \tag{C.4}$$

The medium is increasingly opaque for $KL \geq 1$ and transparent for $KL \ll 1$.

C.2 Application to hydrogen

We are specializing in the following to atomic hydrogen. The values of both the oscillator strengths f_i and the transition rates $\Gamma_i^{(n)}$ for E1-transitions to the ground state are well known [28], and the oscillator strength for the contribution of the continuum, f_c, can be inferred from the oscillator strength sum rules, yielding $f_c = 0.4350$. We can therefore treat the continuum to a good approximation as a single discrete level with oscillator strength f_c. The wavelength corresponding to this

[1] Recall from Appendix A, Eq. (A.1), that in this work there is a factor of 4π difference between the atomic polarizability and the atomic susceptibility.

[2] The shift due to self-broadening is considered to be negligible.

transition, λ_c, can be determined as follows: for $\lambda \to +\infty$ (static limit) we know the value of the polarizability of hydrogen, namely $\alpha_{\text{stat}} = 4.5$ a.u. Thus, taking a finite number of bound and one continuum transitions, we require

$$\alpha_{\text{stat}} \equiv \frac{r_e}{(2\pi)^2} \left(\sum_i^{i_m} f_i \lambda_i^2 + f_c \lambda_c^2 \right) \tag{C.5}$$

to hold. We have neglected the widths here, as they are only of importance close to resonances. In Eq. (C.5), i_m is the maximum number of bound states taken into account. Only a few bound states are needed to converge the results considering the range of wavelengths of interest (> 100 nm). λ_c can be determined from from Eq. (C.5) and be used to compute the polarizability from Eq. (C.1). Depending on i_m, λ_c is typically in the range 65-68 nm in the present calculations. Fig. C.1 shows the comparison between the Sellmeir formula and the Floquet data for the real part of the linear atomic polarizability in a range of wavelengths which includes both the $1s$-$2p$ and the $1s$-$3p$ resonances. Considering the simplifying assumption of a single-state discrete continuum in applying the Sellmeir formula, the agreement between both calculations is very good. In fact, the Floquet method is by far more accurate than our simplified Eq. (C.1) away from resonances, but we want to make sure that the Floquet approach gives the correct result even in the vicinity of the latter. We have therefore given in Table C.1 the corresponding values for the wavelength of interest in chapter 2. The agreement between the two calculations regarding the real part of the atomic polarizability is good and the intensities we will consider will always be larger than the minimum intensities shown in the last column of Table C.1. The intensity-induced width will thus always be larger than the natural width even in the vicinity of the resonance considered. In fact, only the values of the intensity given for the third harmonic wavelengths are of any relevance because absorption at the fundamental frequencies is entirely negligible for any reasonable value of the atomic density, as can be seen from Eq. (C.4). If we now include pressure broadening, the widths increase typically by three orders of magnitude for $\mathcal{N}_0 = 1 \times 10^{19}$ atoms/cm^3 (which is the highest gas density we have considered for atomic hydrogen in this work). This yields, e.g., $\text{Im}[\alpha_{\text{pol}}(\lambda = 355/3)] \approx 5.4 \times 10^{-27}$ cm^3, and therefore, with $L = 1$ mm, a value of $KL = 3.8 \times 10^{-2}$. The intensity-induced width leads to larger values of the imaginary part of the polarizability for intensities of the order of

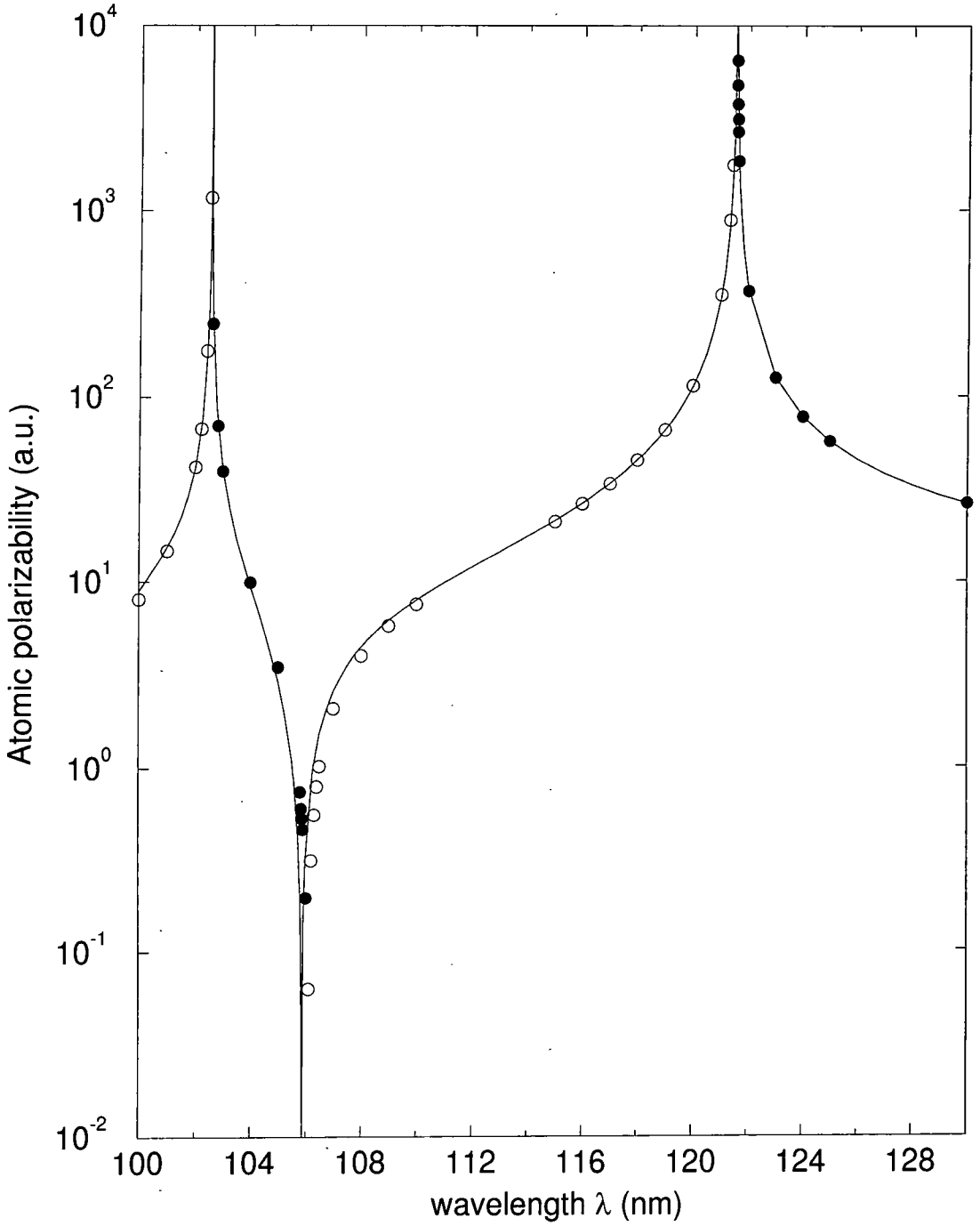

Figure C.1: Linear atomic polarizability (in a.u.) for hydrogen versus wavelength. The curve (solid line) has been obtained from the Sellmeir formula Eq. (C.1), the data represented by the circles have been obtained from a Floquet calculation (see chapter 2). Open circles correspond to a range of wavelengths for which the polarizability is actually negative but shown positive for convenience.

Table C.1: Comparison between the linear atomic polarizabilities as obtained from the Floquet approach (chapter 2) and the Sellmeir formula Eq. (C.1) in the zero-intensity limit. The imaginary part of the intensity-induced width is practically zero (ϵ). The third column gives the order of magnitude for the intensity to be reached for the imaginary part of the polarizability to be dominated by the intensity-induced width, compared to the natural line broadening due to spontaneous emission. Numbers in parenthesis indicate powers of ten.

λ [nm]	Floquet data $\alpha_{\rm pol}$ [cm^3]	Sellmeir data $\alpha_{\rm pol}$ [cm^3]	min. intensity [W/cm^2]
real part			
350	7.43(-25)	7.40(-25)	-
355	7.41(-25)	7.38(-25)	-
364	7.37(-25)	7.34(-25)	-
350/3	-4.50(-24)	-4.61(-24)	-
355/3	-7.35(-24)	-7.52(-24)	-
364/3	-1.13(-22)	-1.45(-22)	-
imaginary part			
350	ϵ	8.21(-33)	$\sim$ 1(11)
355	ϵ	8.03(-33)	$\sim$ 7(10)
364	ϵ	7.74(-33)	$\sim$ 5(10)
350/3	ϵ	2.57(-30)	$\sim$ 1(8)
355/3	ϵ	6.12(-30)	$\sim$ 1(8)
364/3	ϵ	1.94(-27)	$\sim$ 1(8)

10^{10} W/cm^2 . Thus, even with pressure broadening included, the intensity-induced width will dominate the linear atomic polarizability in our applications. One should not conclude from these figures that, e.g., $\lambda = 364$ nm is not a suitable wavelength because of a large value $\mathrm{Im}[\alpha_{\rm pol}(\lambda = 364/3)] \approx 2 \times 10^{-24}\,\mathrm{cm}^3$. Indeed, firstly, the minimum intensity to reach is roughly independent of the wavelength, very much as in the case of the natural linewidth shown in Table C.1, secondly and independently, because of the larger real part of the polarizability, the value of the atomic density necessary to achieve a given Bessel angle, according to Eq. (6.42), is lower. We shall come back to this point in more detail in the next section.

C.3 Application to xenon

We proceed in this section by relating similar results for xenon, as required for the calculations in section 6.2.1, following the steps outlined by Peet and Tsubin [166]

Table C.2: Data for xenon entering the Sellmeir formula Eq. (C.1). The oscillator strengths f_i are from Refs. [44, 168]. The first column gives the state with $J = 1$ under consideration. E_i are the energy levels in eV, λ_i the corresponding wavelength of the transition to the ground state in nm, and $\Gamma_i^{(n)}$ are the transition rates as evaluated from Eq. (C.6), in 10^8/s. $\Gamma_i^{(n),\mathrm{ref}}$ are the corresponding rates from Ref. [134], where available.

state	λ_i	E_i	f_i	$\Gamma_i^{(n)}$	$\Gamma_i^{(n),\mathrm{ref}}$
$^2P_{3/2}6s[\frac{3}{2}]$	146.95	8.437	0.273	2.81	2.8
$^2P_{1/2}6s'[\frac{1}{2}]$	129.56	9.570	0.186	2.46	2.5
$^2P_{3/2}5d[\frac{1}{2}]$	125.02	9.917	0.011	0.15	-
$^2P_{3/2}5d[\frac{3}{2}]$	119.20	10.401	0.379	5.93	6.2
$^2P_{3/2}7s[\frac{3}{2}]$	117.04	10.593	0.086	1.39	-
$^2P_{3/2}6d[\frac{1}{2}]$	112.93	10.979	~ 0.001	0.02	-
$^2P_{3/2}6d[\frac{3}{2}]$	110.07	11.163	0.084	1.50	-
$^2P_{3/2}8s[\frac{3}{2}]$	109.97	11.274	0.022	0.41	-
$^2P_{3/2}7d[\frac{1}{2}]$	108.54	11.423	0.023	0.43	-
$^2P_{3/2}7d[\frac{3}{2}]$	107.86	11.495	~ 0.001	0.02	-
$^2P_{3/2}9s[\frac{3}{2}]$	107.04	11.583	~ 0.001	0.02	-
$^2P_{1/2}5d'[\frac{3}{2}]$	106.82	11.607	0.191	3.72	-
$^2P_{3/2}8d[\frac{1}{2}]$	106.12	11.683	0.009	0.17	-
$^2P_{3/2}8d[\frac{3}{2}]$	105.61	11.740	0.097	1.93	-
$^2P_{3/2}10s[\frac{3}{2}]$	105.50	11.752	0.029	0.58	-
-	96.11	12.9	0.9	-	-
-	65.26	19	3.8	-	-
-	12.40	100	8	-	-

for the computation of the linear atomic polarizability. The relevant data are listed in Table C.2, where the transition rates to the ground state $^1S_0$ have been obtained from the oscillator strengths using the formula

$$\Gamma_i^{(n)}\,[1/\mathrm{s}] = \frac{6.6702 \times 10^{13}}{\lambda^2\,[\mathrm{nm}]}\,\frac{f_i}{g_i} = 4.3391 \times 10^7\,E_i^2\,[\mathrm{eV}]\,\frac{f_i}{g_i}\,, \tag{C.6}$$

where E_i is the energy level corresponding to the wavelength of the transition, λ_i, and g_i are the statistical weights, $g_i = 3$ for all transitions in the present case[3] [134].

Fifteen bound states have been taken into account and the continuum, above the first ionization threshold at $E = 12.13$ eV, has been modelled as a set of three discrete levels [168]. The real part of the linear atomic polarizability is shown in Fig. C.2. The static limit obtained in this way, $\alpha_{\mathrm{pol}}(\infty) \approx 22.6$ a.u., is below both the theoretical and experimental value cited in Ref. [128], $\alpha_{\mathrm{stat}} \approx 27.1$ a.u. On the

[3]We are considering $J = 1 \to J = 0$ transitions in xenon.

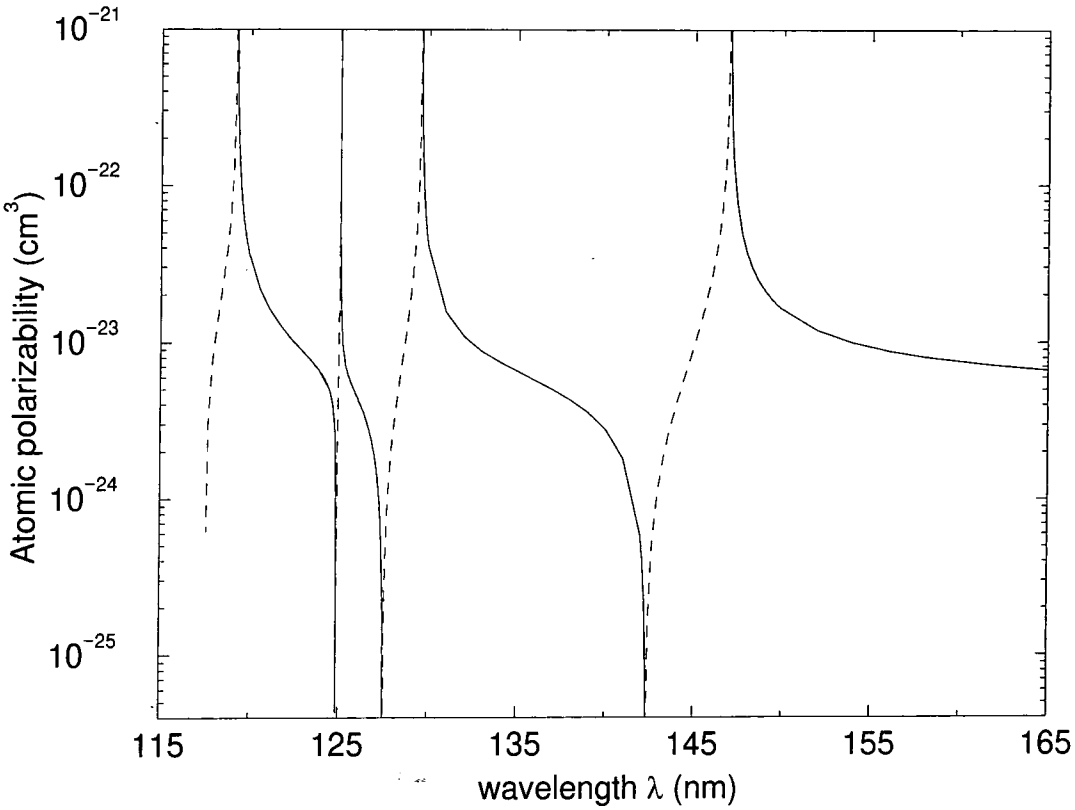

Figure C.2: Real part of the linear atomic polarizability for xenon versus wavelength. The regions where the curve is dashed correspond to regions, where this susceptibility is actually negative but shown positive for convenience. The resonances correspond to the first four energy levels given in Table C.2.

other hand, we find for $\lambda_1 = 354.7$ nm and $\lambda_3 = \lambda/3$ the values

$$\mathrm{Re}[\alpha_{\mathrm{pol}}(\lambda_1)] \approx 3.7 \times 10^{-24}\,\mathrm{cm}^3 \tag{C.7}$$

$$\mathrm{Re}[\alpha_{\mathrm{pol}}(\lambda_3)] \approx -1.4 \times 10^{-23}\,\mathrm{cm}^3\,, \tag{C.8}$$

leading to an atomic phase-mismatch in very good agreement with the value cited by Kung [118] (see section E.3.2). If we include pressure broadening, we find for $\mathcal{N}_0 = 4.8 \times 10^{18}$ atoms/cm^3 (which is the highest gas density we have considered for xenon in this work) a value of $\mathrm{Im}[\alpha_{\mathrm{pol}}(\lambda = 355/3)] \approx 2.2 \times 10^{-26}\,\mathrm{cm}^3$, and therefore, with $L = 1$ mm, a value of $KL = 7.1 \times 10^{-2}$. No information about the intensity-induced widths for xenon was available[4] and considering that for intensities $\leq 10^{12}$

[4]The intensity-dependence of the real part of the linear atomic polarizability starts to affect the conversion efficiency for third-order harmonic generation in xenon around 5×10^{12} W/cm^2 at this wavelength [237].

W/cm^2 absorption is negligible for hydrogen (even when the larger light-induced shift is taken into account, see Figs. 5.3 and 5.4), we have simply assumed absorption to be negligible for xenon for this range of intensities in all calculations reported in this thesis.

Consider now the experiment by Peet and Tsubin [166], which we had discussed in connection with the conversion efficiency in section 5.3. The authors had considered, amongst others, third harmonic generation in xenon using a Bessel beam with $\alpha = 17°$. We will show, that in order for $\alpha = 17°$ to be the optimum Bessel angle according to Eq. (4.104), one has to be too close to resonance, all harmonic radiation being absorbed within the medium as predicted by the authors. The real part of the linear atomic polarizability is evaluated fromi Eq. (4.104) as

$$\mathrm{Re}[\alpha_{\mathrm{pol}}(\lambda/3)] \approx -(1 - 1/q^2)[\alpha_{\mathrm{opt}} = 17°]^2/4\pi\mathcal{N}_0\,, \tag{C.9}$$

and the corresponding imaginary part is determined from the Sellmeir equation. From there, the absorption coefficient KL is evaluated for $\lambda = 440$ nm and a medium length $L = 2$ mm [168]. It is obvious from the figures shown in Table C.3 that the medium is completely opaque for the whole range of gas densities used in the experiment of Ref. [166]. Interestingly, the value of KL is essentially constant over this range which illustrates a point already mentioned at the end of section C.2: The closer the resonance, the higher is absorption but the lower is also the density required for obtaining a given Bessel angle.

Table C.3: Absorption of harmonic radiation in the experiment of Peet and Tsubin [166] as a function of the atomic density $\mathcal{N}_0$ (in atoms/cm^3), determined from the pressure p in mbar, see Appendix A). The linear atomic polarizability is in cm^3: (a) real part, (b) imaginary part, at the harmonic wavelength, respectively. Numbers in parenthesis indicate powers of ten.

p	$\mathcal{N}_0$	(a)	(b)	KL
100	2.5(18)	-2.8(-21)	2(-22)	5(2)
200	5.0(18)	-1.4(-21)	8(-23)	4(2)
400	1.0(19)	-7.0(-22)	4(-23)	4(2)
1000	2.5(19)	-2.8(-22)	2(-23)	5(2)
1500	3.8(19)	-1.8(-22)	1(-23)	4(2)

Appendix D

Experimental Realization of a Bessel Beam

D.1 Introduction

In chapter 3 we had shortly discussed various ways of experimentally realizing Bessel beams. The present appendix describes an experimental realization of a Bessel type beam we have carried out in collaboration with Philippe Balcou and co-workers at the Laboratoire d'Optique Appliquée (LOA) in Palaiseau, France. The design of the Bessel beam generator and the subsequent measurements reported here were realized within the framework of the experiment on high-order harmonic generation in an argon gas reported in chapter 7.

The Bessel type beam will be obtained essentially by illuminating an annular aperture. In the first section we investigate theoretically how the Bessel beam amplitude is going to be obtained. Section D.3 is devoted to the description of the experimental set-up. Both the measurements and the results are discussed in section D.4. Section D.5 provides a short conclusion, section D.6 contains the figures.

D.2 Theoretical considerations

Before embarking on the description of the experimental set-up, we first give a brief theoretical description of how a Bessel beam amplitude can be obtained by illuminating an annular slit. To this aim, we start from the (scalar) Kirchhoff-Fresnel integral for the diffraction by a plane aperture A, which is given by [23]

$$E(\mathbf{x}) = -\frac{ik}{2\pi}\int_A \mathrm{d}S' E_A(x',y')\,\frac{1+z/R}{2}\,\frac{\exp(ikR)}{R}\,, \tag{D.1}$$

where $R=[(x-x')^2+(y-y')^2+z^2]^{1/2}$ is the distance between the point of observation $P(x,y,z)$ and the points $A(x',y',0)$ of the aperture, and E_A is the field amplitude incident on the aperture. We assume to be far away from the aperture, that is $\sqrt{z^2+\rho^2} \gg \rho'^2$, where we have introduced cylindrical coordinates $P(\rho,z,\phi)$ and $A(\rho',0,\phi')$. We may thus expand R as

$$R \approx \sqrt{z^2+\rho^2}\left[1-\frac{\rho\rho'\cos(\phi-\phi')}{z^2+\rho^2}+\frac{1}{2}\,\frac{\rho'^2}{z^2+\rho^2}\right]\,, \tag{D.2}$$

and Eq. (D.1) can then be approximated by

$$\begin{aligned} E(\rho,z,\phi) &= -\frac{ik}{2\pi}\,\frac{\exp(ik\sqrt{z^2+\rho^2})}{\sqrt{z^2+\rho^2}}\int_A \mathrm{d}S' E_A(\rho',\phi')\,\frac{1+z/\sqrt{z^2+\rho^2}}{2} \\ &\times \exp\left[-ik\frac{\rho\rho'\cos(\phi-\phi')}{\sqrt{z^2+\rho^2}}\right]\exp\left(ik\frac{\rho'^2}{\sqrt{z^2+\rho^2}}\right). \end{aligned} \tag{D.3}$$

If further both the aperture and the incident field are azimutally symmetric, one obtains

$$\begin{aligned} E(\rho,z) &= -ik\frac{\exp(ik\sqrt{z^2+\rho^2})}{\sqrt{z^2+\rho^2}}\int_{\delta_1}^{\delta_2}\mathrm{d}\rho'\,\rho'\,E_A(\rho')\,\frac{1+z/\sqrt{z^2+\rho^2}}{2} \\ &\times J_0\left(\frac{k\rho\rho'}{\sqrt{z^2+\rho^2}}\right)\exp\left(ik\frac{\rho'^2}{\sqrt{z^2+\rho^2}}\right). \end{aligned} \tag{D.4}$$

Moving to the paraxial limit, we write $z=z_0+\Delta z$ with $z_0 \gg \rho$ and $\Delta z/z_0 \ll 1$, thus approximating $\sqrt{z^2+\rho^2}$ by $z_0+\Delta z$ and $1/\sqrt{z^2+\rho^2}$ by $(1-\Delta z/z_0)/z_0$, respectively. At the same time we introduce the new variables

$$u=\frac{\rho'}{z_0}\,, \qquad \alpha_i=\frac{\delta_i}{z_0} \qquad i=1,2\,, \tag{D.5}$$

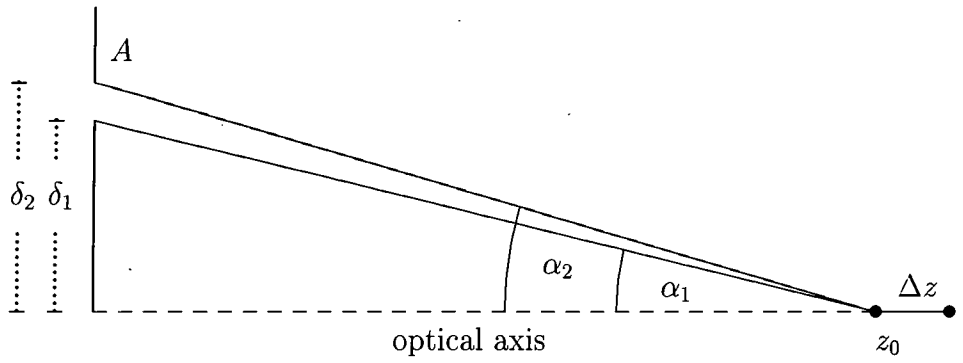

Figure D.1: Definition of the angles α_i and the far-field variable Δz.

(see Fig. D.1) and obtain the electric field amplitude in the form

$$E(\rho,\Delta z) = -ikz_0\exp(ikz_0)\exp(ik\Delta z)\,(1-\Delta z/z_0)\int_{\alpha_1}^{\alpha_2} du\,u\,E_A(uz_0) \times J_0\left[k\rho u\left(1-\frac{\Delta z}{z_0}\right)\right]\exp\left[i\frac{kz_0u^2}{2}\left(1-\frac{\Delta z}{z_0}\right)\right]. \quad \text{(D.6)}$$

We can neglect $\Delta z/z_0$ in the prefactor but also in the argument of the Bessel function with respect to the argument of the exponential, provided $\rho' \gg \rho$, which requires $\delta_2 > \delta_1 \gg \rho$. If we assume a plane wave illumination of the aperture, $E_A(uz_0) = E_0$, we arrive finally at

$$E(\rho,\Delta z) = -ikz_0E_0\exp(ikz_0)\int_{\alpha_1}^{\alpha_2} du\,u\,J_0\,(k\rho u) \times \exp[ik\Delta z(1-u^2/2)]\exp(ikz_0u^2/2)\,. \quad \text{(D.7)}$$

It is easy to see from this expression, how an annular beam emerges as a superposition of Bessel beam amplitudes with a range of Bessel angles $\alpha \in [\alpha_1, \alpha_2]$. Recalling the three approximations which have been made in deriving Eq. (D.7), namely $z_0 \gg \rho, \delta_1, \delta_2$, $\Delta z \ll z_0$, and $\delta_1, \delta_2 \gg \rho$, we find that they are well satisfied under experimental conditions, where we typically have

z_0	:	a few tens of centimeters
δ_1, δ_2	:	a few millimeters
Δz	:	a few millimeters
ρ	:	a few tens of microns

The paraxial version of the pure Bessel beam is easily recovered from expression (D.7) in the case where α_1 and α_2 are close enough for the integrand to be taken at

the intermediate value $\alpha = (\alpha_1 + \alpha_2)/2$, leading to

$$E(\rho, \Delta z) = \tilde{E}_0 J_0 (k\rho\alpha) \exp[ik\Delta z(1 - \alpha^2/2)] . \tag{D.8}$$

D.3 Experimental setup

A simplified illustration of the experimental set-up is shown in Fig. D.2. A Gaussian

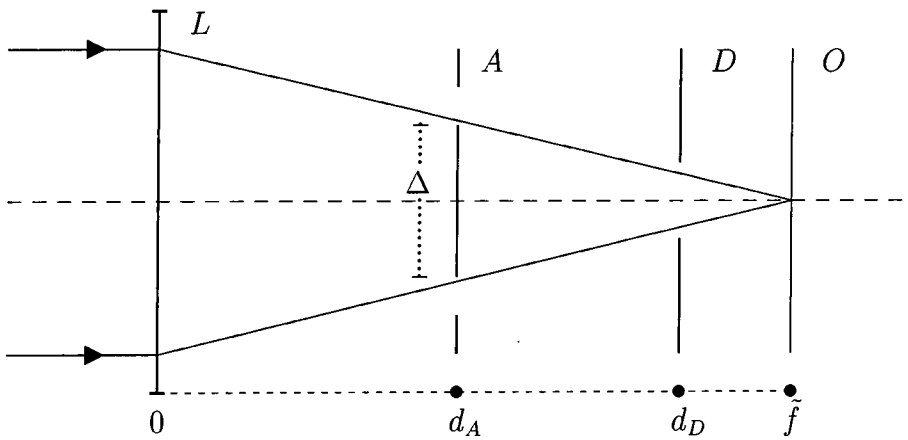

Figure D.2: Schematic illustration of the experimental set-up.

beam is generated by a 632-nm He-Ne laser and widened to about 3 cm of diameter. The well collimated beam illuminates a $f/500$ lens L which focuses the incident beam through the Bessel beam generator onto an object plane O, located at $\tilde{f} = 495$ mm from the lens L. Object plane and focal plane normally coincide, but the focal plane can be moved either way with respect to the object plane by moving the lens L. The object plane O is imaged with a $f/20$ lens onto a CCD camera, which records the intensity profile of the beam transmitted through the Bessel beam generator at the position of the object plane. The Bessel beam generator consists of an aperture A and a diaphragm D, located at d_A and $d_D = 370$ mm from the lens L, respectively. The inner diameter of the aperture being Δ, we have, using the notation from the previous section, $\delta_1 = \Delta/2$ and $z_0 = \tilde{f} - d_A$ to yield

$$\alpha_1 = \frac{\Delta}{2(\tilde{f} - d_A)} . \tag{D.9}$$

The value of δ_2 was significantly larger than δ_1 but we monitored the thickness of the annular beam with the help of a diaphragm D of maximum diameter 4 mm. This

adjustment was done online, that is, while displaying the output of the CCD camera on a video screen. In this way, the optimum opening of the diaphragm was regulated such as to obtain a maximum contrast on the screen up to a point where further reduction of the opening blurred the picture, thus indicating secondary diffraction of the beam due to the diaphragm. Note that Eq. (D.9) is therefore expected to be the lower bound for the measured range of Bessel angles. This lower bound could

Table D.1: Expected values for the Bessel angle α_1, as calculated from Eq. (D.9) for $\Delta = 12$ mm and various d_A. The fourth column refers to the figure showing the measured intensity profile from which the experimental value of the Bessel angle $\alpha_{\rm exp}$ has been determined. The values shown include already the statistical errors (see next section).

d_A [mm]	α_1 [mrad]	α_1 [deg]	Figure	$\alpha_{\rm exp}$ [mrad]	$\alpha_{\rm exp}$ [deg]
76	14.3±0.2	0.82±0.01	D.4	14.4-17.4	0.83-1.00
152	17.5±0.2	1.00±0.01	D.5	17.5-21.9	1.00-1.25
225	22.2±0.3	1.27±0.02	D.6	19-23 (?)	1.1-1.3 (?)
282	28.2±0.5	1.61±0.03	D.7	-	-

be modified by varying the distance d_A. Table D.1 shows the values of the angle α_1 as predicted by Eq. (D.9) for $\Delta = 12$ mm and for several values of the distance d_A between lens L and aperture A. The statistical error on α_1 has been calculated as

$$\Sigma(\alpha_1) = \left|\frac{\partial\alpha_1}{\partial\Delta}\right| \mathrm{d}\Delta + \left|\frac{\partial\alpha_1}{\partial\tilde{f}}\right| \mathrm{d}\tilde{f} + \left|\frac{\partial\alpha_1}{\partial d_A}\right| \mathrm{d}d_A\,, \tag{D.10}$$

where we have made the conservative estimates

$$\mathrm{d}\tilde{f} = \mathrm{d}d_A = 1 \text{ mm}\,, \qquad \mathrm{d}\Delta = 0.1 \text{ mm}\,,$$

for the abolute accuracy to which the various lengths could be measured. The range of values for d_A shown in this table was limited due to restrictions on the size of the set-up for later applications. To access different ranges of values for the Bessel-angle, different lenses or apertures have to be taken. Table D.1 also shows the measured values of the Bessel angles (where available), as discussed in the next section.

D.4 Measurements and results

In order to make absolute measurements of the spatial dimensions of the intensity profiles, we recorded the image of a finely graded scale, fixed in the object plane O. The recorded picture is shown in Fig. D.3. The gradings are nominally separated by a distance of 100 microns, thus the absolute scale for all subsequent pictures is

$$\text{Scaling factor:} \qquad 1 \text{ cm } \equiv 37.0 \text{ microns} .$$

We have tested that this scale does not change appreciably, when the $f/20$ lens (which governs the magnification of the imaging) is slightly displaced along the optical axis: the scaling factor was observed to decrease by approximately 0.4 microns, when the $f/20$ lens was moved up to 3.5 mm away from the CCD camera.

Figs. D.4-D.7 show the recorded intensity profiles for the Bessel beams of Table D.1. Each picture consists of 240 rows and 240 columns. To find the value of the Bessel angle (or rather the range of Bessel angles) we have analyzed the rows and columns separately to find the cut through the central maximum. A typical profile, corresponding to the vertical cuts at positions $x = 100$ and $x = 101$ of the profile of Fig. D.4, is shown in Fig. D.8. Only a fraction of the peak has been recorded because of the CCD camera being saturated in order to make the secondary peaks clearly visible. From Fig. D.8 it is clear that it is easier to measure the position of the maxima than the position of the minima. As $J_0'(z) = -J_1(z)$, the positions of the maxima of $J_0^2(z)$ are given by the zeros of $J_1(z)$. The argument of the Bessel function being $z = k\rho\alpha$, according to Eq. (D.7), we obtain for the value of the angle α, as determined from the j^{th} secondary peak,

$$\alpha_j = \frac{z_j}{\rho_j[\mu\text{m}]} \frac{\lambda[\mu\text{m}]}{2\pi} , \tag{D.11}$$

where $\lambda = 0.632\,\mu$m is the wavelength of the He-Ne laser, ρ_j is half the distance between the two maxima corresponding to the same ring and calculated as $\rho_j[\mu\text{m}] = \tilde{\rho}_j[\text{cm}] \times S$ $(S = 37.0)$, and the z_j are the zeros of the Bessel function $J_1(z)$ [1]. The statistical error on the angles α_j is evaluated as

$$\Sigma(\alpha_j) = \left|\frac{\partial \alpha_j}{\partial \tilde{\rho}_j}\right| \mathrm{d}\tilde{\rho}_j + \left|\frac{\partial \alpha_j}{\partial S}\right| \mathrm{d}S , \tag{D.12}$$

where we made the conservative estimates

$$\mathrm{d}\tilde{\rho}_j = 0.05 \text{ cm} , \qquad \mathrm{d}S = 0.4 ,$$

for the absolute accuracy to which these quantities could be determined. The results of this analysis for Figs. D.4-D.6 is given in Table D.1. They might be less reliable for the values given in the third row of this table, while they could not be obtained at all for the Bessel beam of Fig. D.7. It is also possible to test whether the recorded intensity profiles are suitably modelled by a J_0^2-profile by determining the ratios of the successive secondary maxima, the latter being given by $v_j = J_0^2(z_j)$. Taking again Fig. D.8 as an example, we see that the difficulty lies essentially in defining the zero-intensity baseline. Taking for the right hand side peaks $y = 40$ as baseline, we find $(v_2/v_3)_{\text{exp.}} \approx 1.34$ and $(v_2/v_4)_{\text{exp.}} \approx 1.81$ compared to the theoretical values 1.45 and 1.88 [1], respectively. Deviations from the theoretical values can be attributed to the form of the radial cut-off, as a result of a truncation due to the finite apertures (truncated Bessel beam) or due to the exponential radial decay (Bessel-Gauss beam) in the case where the apertures are large enough for the radial profile of the incident Gaussian beam to decay.

The most notable feature in the measured intensity profiles is the intensity pattern of the first ring with its threefold azimutal symmetry, which can also be found in the second ring to some extent. Several factors might be responsible for this pattern. First, the central part of the incident Gaussian beam being blocked by the aperture, the Bessel beam is formed by interference of the outer wings of the Gaussian beam which have not, in general, the same quality as the central part of the beam, thus possibly introducing an azimutal dependence as observed. Second, an azimutal dependence appears, if the aperture or the incident beam are not properly aligned along the optical axis. A third possibility is the deviation of the aperture from an annular shape.

D.5 Conclusions

The experimental realization of a Bessel type beam described in this Appendix shows that, with an otherwise unsophisticated experimental apparatus, it is possible to obtain intensity profiles, which are in fair agreement, both qualitatively and quantitatively, with predictions from scalar diffraction theory. Clearly, it is possible to improve both the quality of the Bessel beam's spatial intensity profile and the measurement of its characteristics without too much effort. First, the beam quality can be improved by monitoring the alignment more accurately and improving the quality of the aperture, second, the monitoring of the beam characteristics would benefit from measuring the profiles both in the saturated and unsaturated regimes, so as to be able to resolve both the central peak and a sizeable number of smaller secondary peaks. A better shielding of the experimental set-up, and especially of the CCD camera, from stray light fields should also help to supress the background and allow for an easier identification of the minima (the baseline for zero-intensity) in the recorded profiles. A greater magnification of the imaging apparatus would add to the overall accuracy of the measurements.

In subsequent measurements it would be desirable to study the dependence on the confocal parameter in order to determine the length of the diffraction-free zone.

D.6 Figures

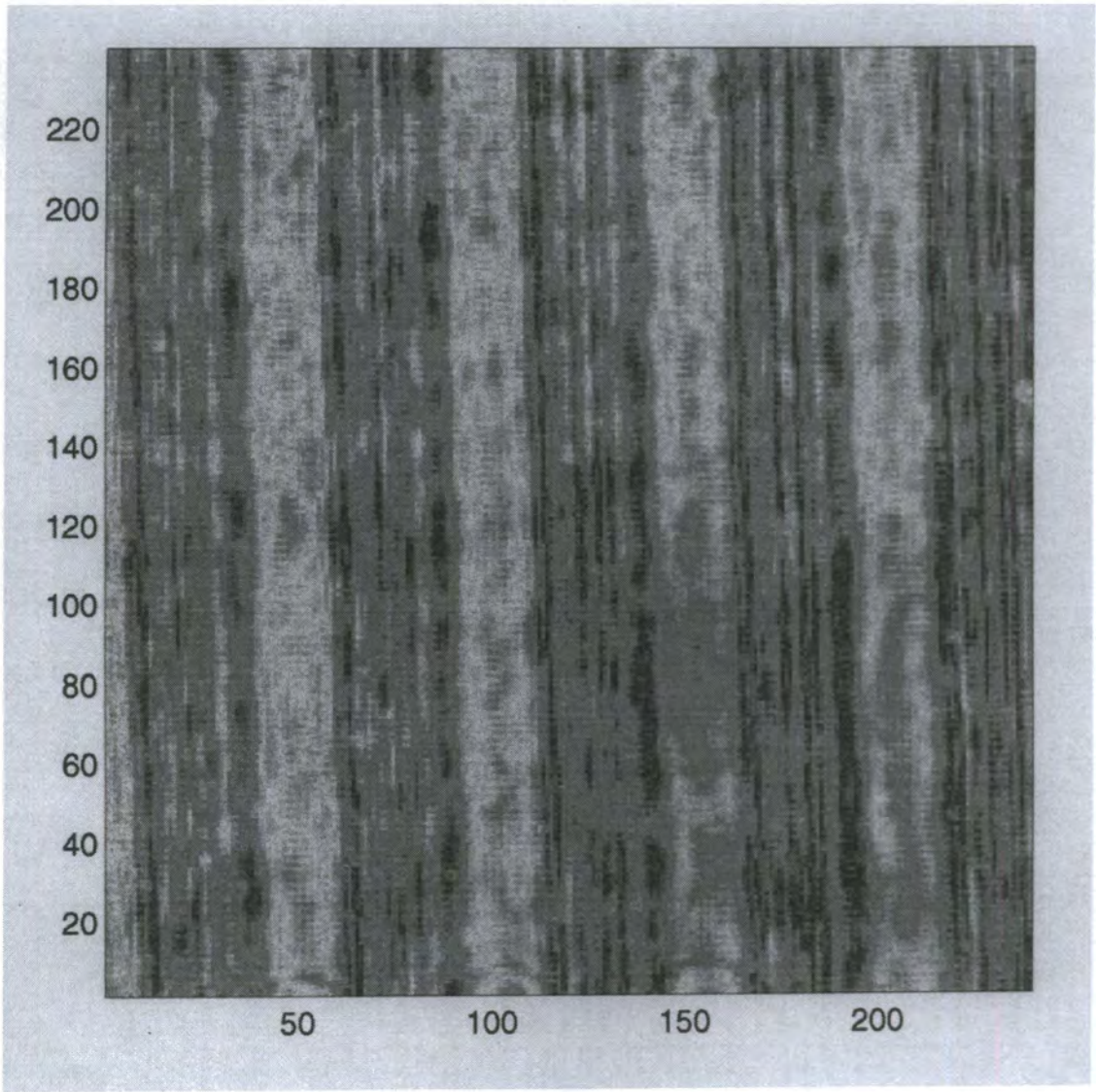

Figure D.3: Image of a finely graded scale. The gradings are nominally separated by 100 microns. The distance between the left (right) hand edges of the vertical bars at x=50 and x=200 is approximately 81 mm, corresponding to 300 microns.

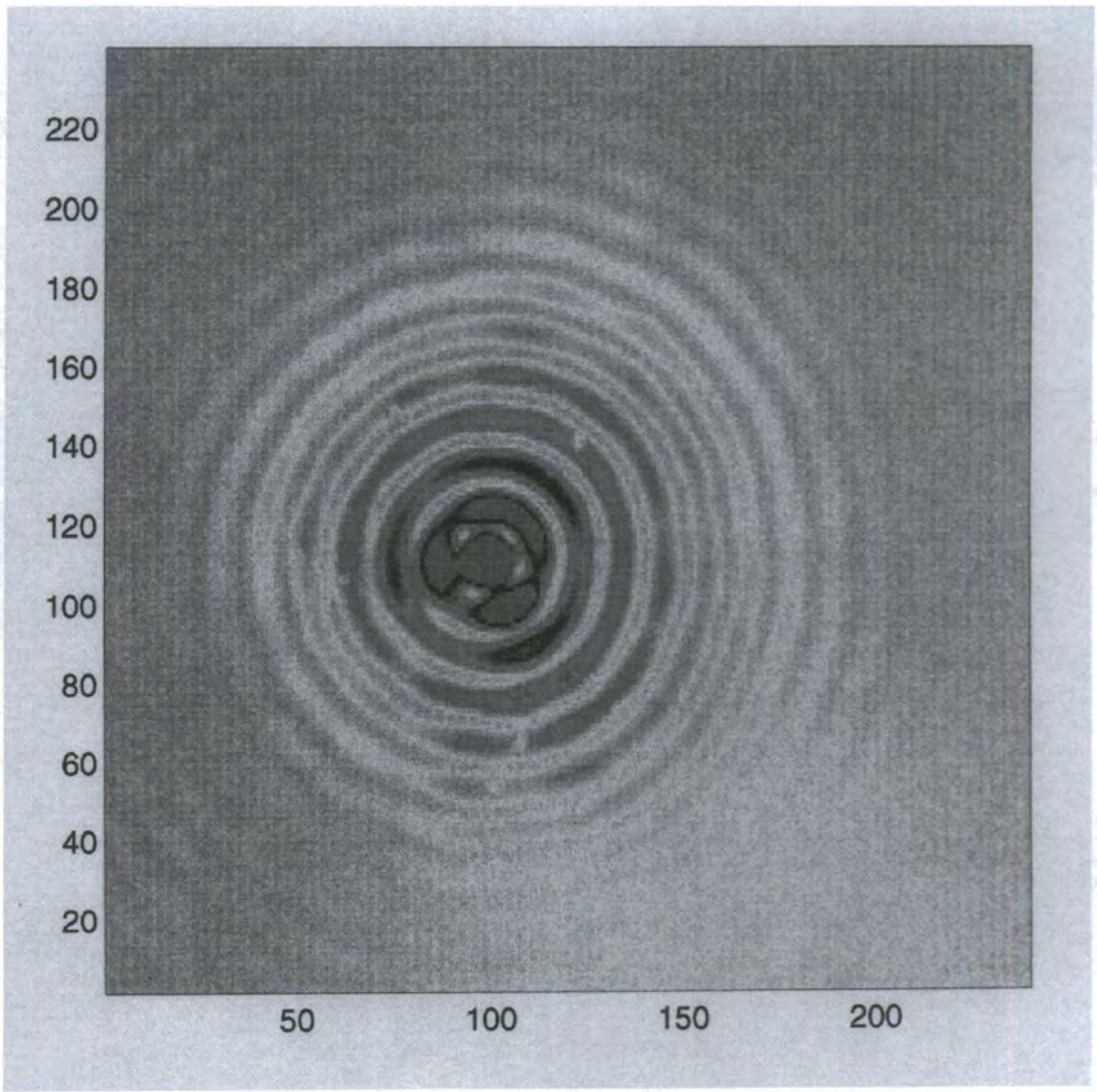

Figure D.4: Intensity profile of a Bessel type beam close to focus, corresponding to a (mean) value $\alpha \approx 15.9$ mrad $= 0.91°$ (see Table D.1). The central peak is saturated with respect to the surrounding rings.

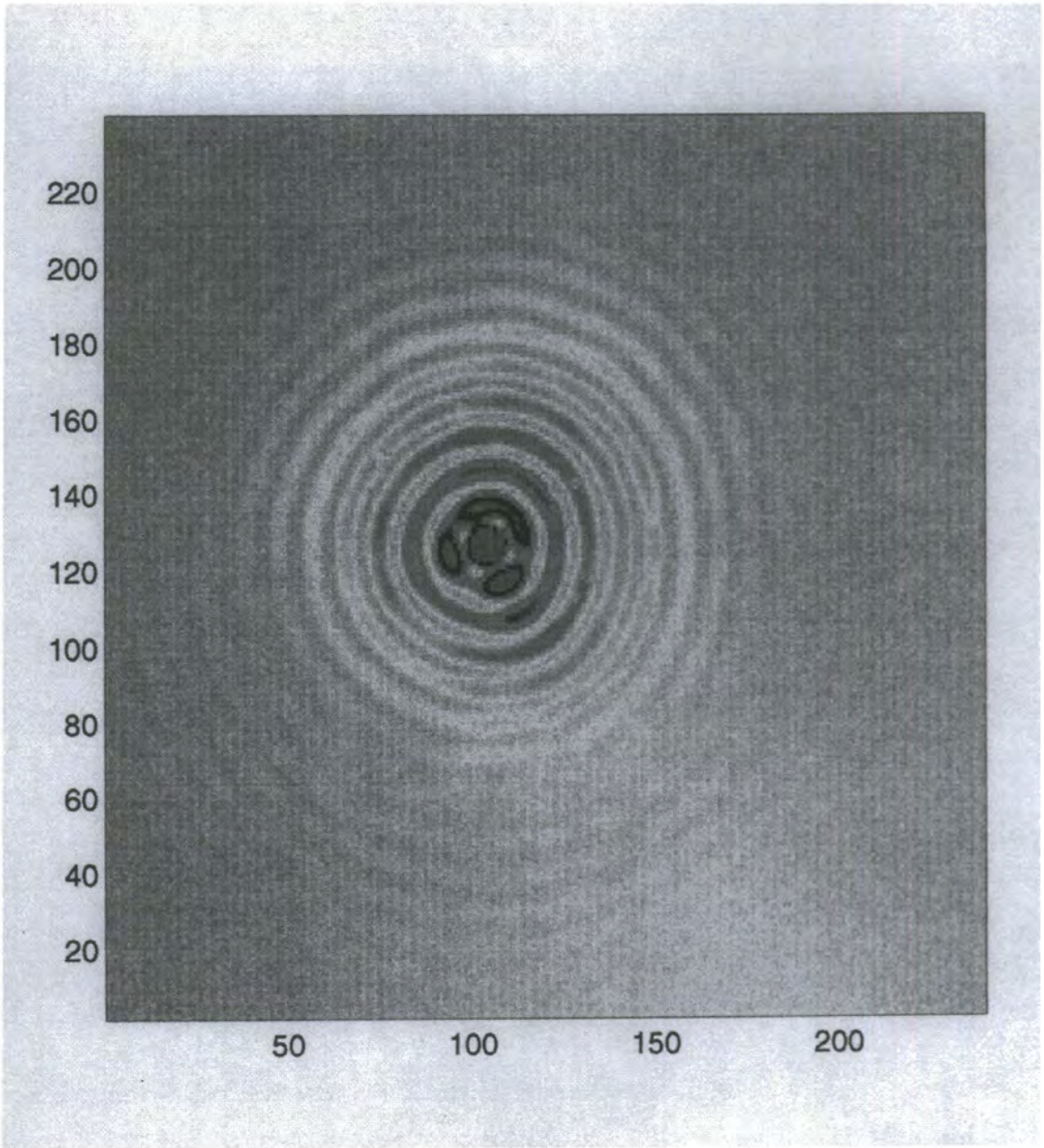

Figure D.5: Intensity profile of a Bessel type beam close to focus, corresponding to a (mean) value $\alpha \approx 19.7$ mrad $= 1.13°$ (see Table D.1). The central peak is saturated with respect to the surrounding rings.

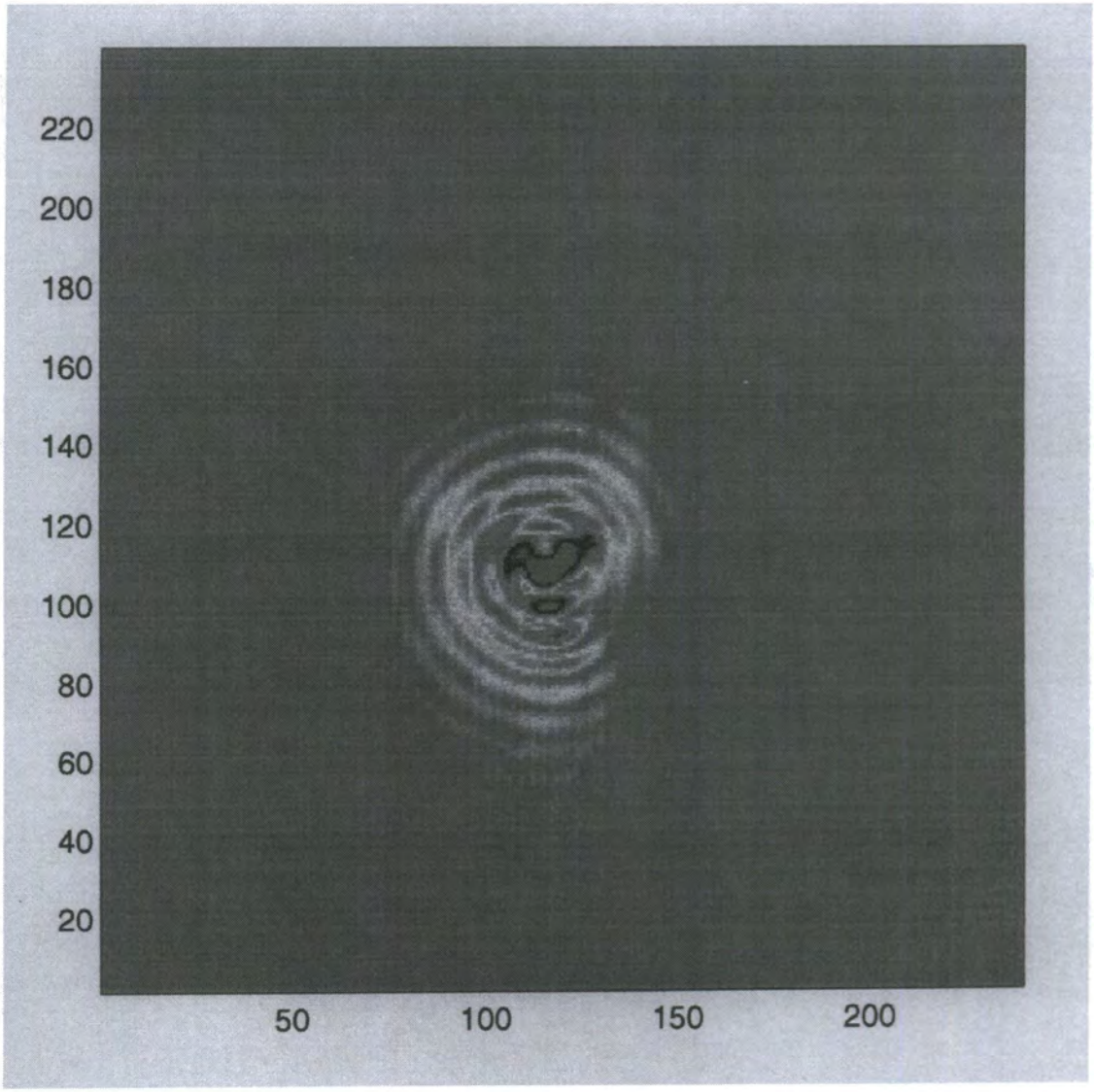

Figure D.6: Intensity profile of a Bessel type beam close to focus, corresponding to a theoretical (minimum) value $\alpha_1 \approx 22.2$ mrad $= 1.27°$ (see Table D.1). The central peak is saturated with respect to the surrounding rings.

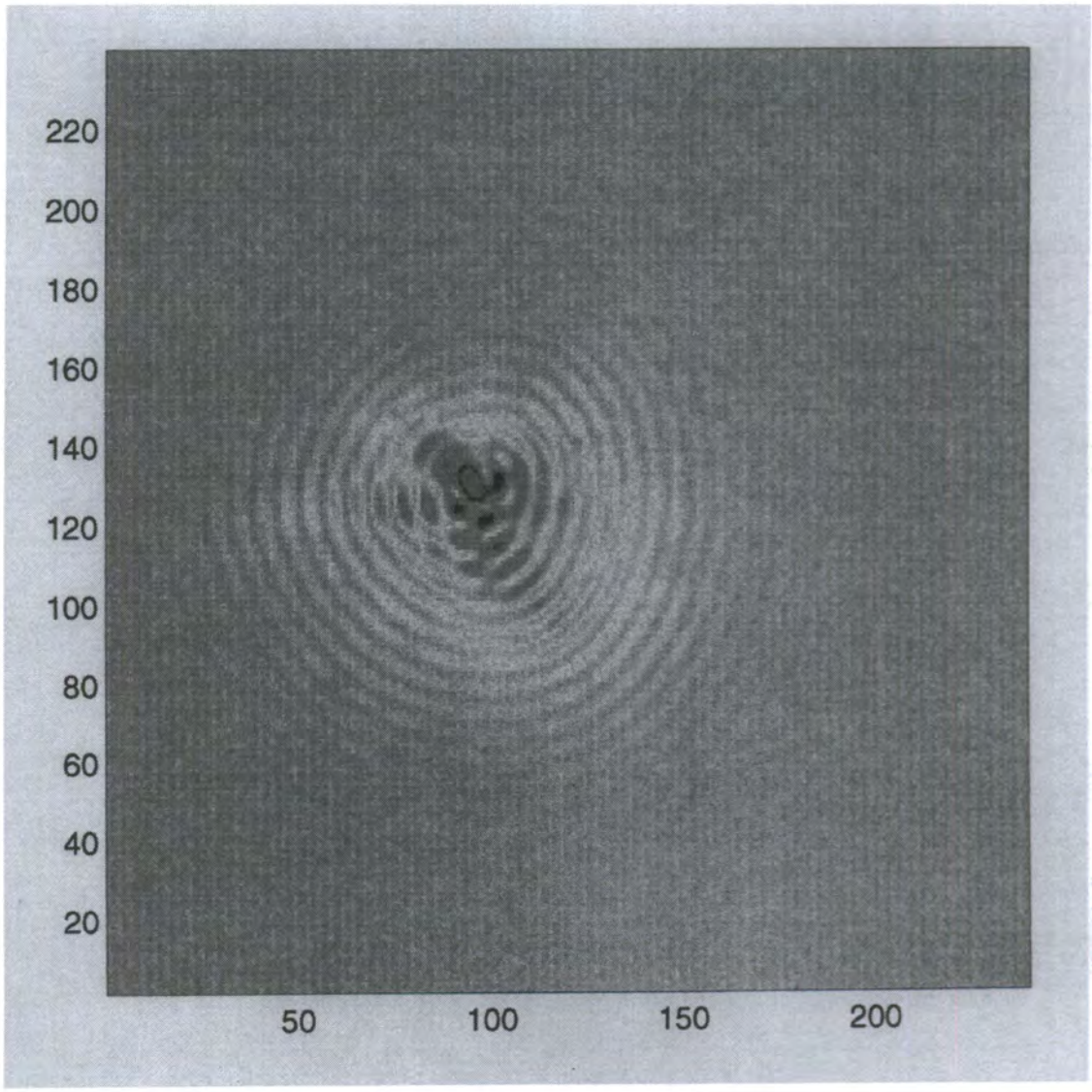

Figure D.7: Intensity profile of a Bessel type beam close to focus, corresponding to a theoretical (minimum) value $\alpha_1 \approx 28.2$ mrad $= 1.61°$ (see Table D.1). The central peak is saturated with respect to the surrounding rings.

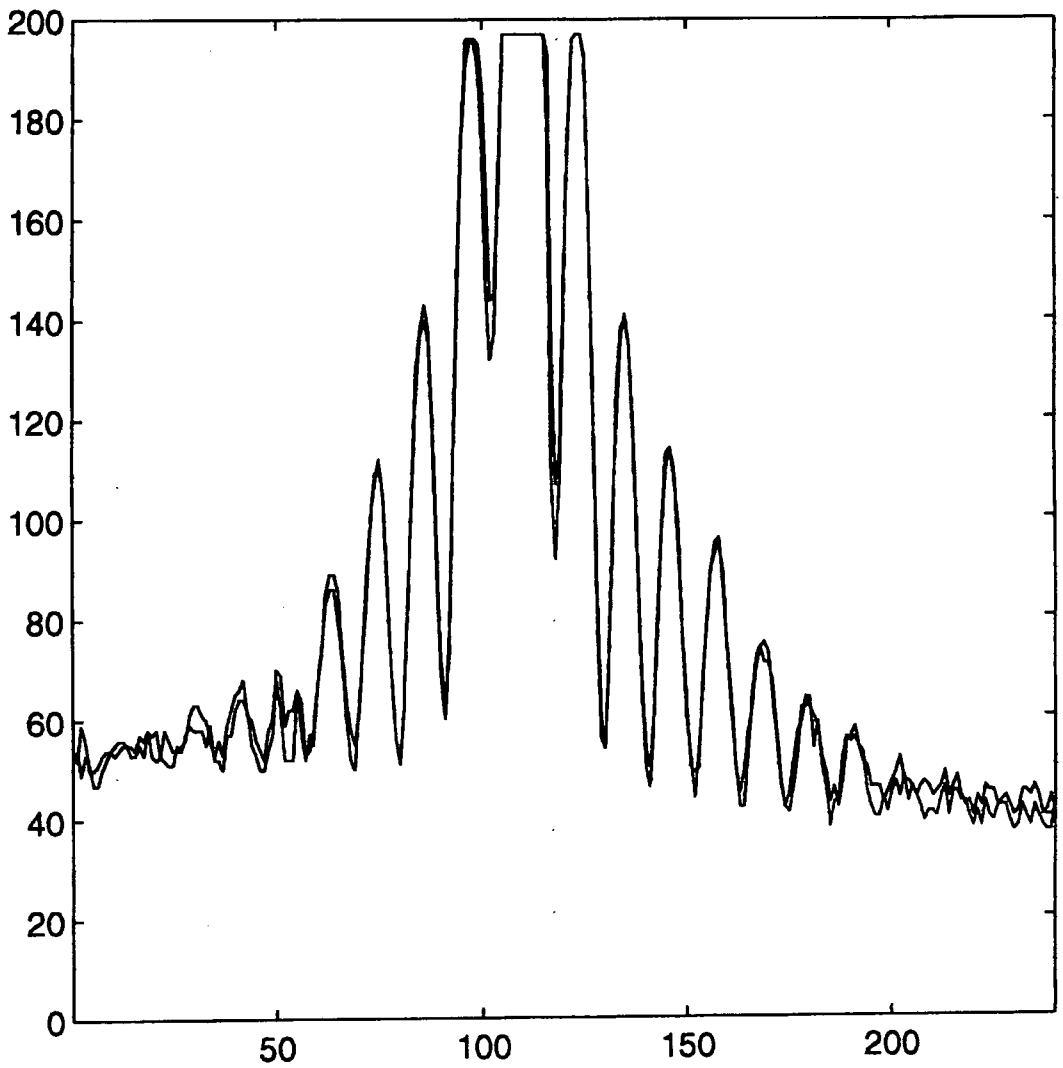

Figure D.8: Overlap of the vertical cuts at $x = 100$ and $x = 101$ of the profile shown in Fig. D.4 from which an estimate of the range of Bessel angles α can be obtained from Eq. D.9 by measuring the distance between the two maxima corresponding to the same secondary maximum (i.e. the same ring in the intensity profile). The horizontal cut in this figure at $y = 40$ is used as the reference baseline for measuring the height of the secondary peaks on the right hand side of central peak (see text).

Appendix E

The Propagation Code

E.1 Introduction

The propagation code has been conceived and developed on the basis of the expressions given in section 4.4 for the computation of the harmonic field envelope E_q, Eq. (4.71). The code is written in FORTRAN 77 and uses some of the NAG-library's quadrature routines. The main integral over the nonlinear medium, Eq. (4.71), is carried out employing a method described in Ref. [214]: in this approach, a multidimensional integral,

$$I = \int_{G_n} f(\mathbf{x})\,\mathrm{d}\mathbf{x}\,, \tag{E.1}$$

where G_n is the unit cube in n-space, $0 \leq x_i \leq 1$, is evaluated as

$$Q = \frac{1}{N}\sum_{k=0}^{N-1} f_p\left(\frac{k\boldsymbol{a}^{(N)}}{N}\right). \tag{E.2}$$

$\boldsymbol{a}^{(N)}$ is an n-tuple of integers which depend only on N and f_p indicates the 1-periodic extension of the function f over the whole n-space. The aim is to find the n-tuples $\boldsymbol{a}^{(N)}$ such that $|Q - I|$ vanishes as rapidly as possible with increasing N. Making use of periodicity of f_p, this function is expanded into a Fourier series

$$f_p(\mathbf{x}) = \sum_{\boldsymbol{m}} C(\boldsymbol{m})\,\exp(2\pi i\mathbf{x}\cdot\boldsymbol{m})\,, \tag{E.3}$$

where the $\boldsymbol{m}$ are n-tuples of integers. Noting that

$$C(\boldsymbol{m}) = \int_{G_n} f(\mathbf{x}) \exp(-2\pi i \mathbf{x} \cdot \boldsymbol{m}) \, \mathrm{d}\mathbf{x} \,, \tag{E.4}$$

and $C(\mathbf{0}) = I$, one finds

$$Q = I + \sum_{\boldsymbol{m} \neq \mathbf{0}} C(\boldsymbol{m}) \, \delta(\boldsymbol{m} \cdot \boldsymbol{a}^{(N)}) \,, \tag{E.5}$$

with

$$\delta(\boldsymbol{m} \cdot \boldsymbol{a}^{(N)}) = (1/N) \sum_{k=0}^{N-1} \exp\{2\pi i \, [\boldsymbol{m} \cdot \boldsymbol{a}^{(N)}] \, k/N\} \tag{E.6}$$

$$= 1 \quad \text{if} \quad \boldsymbol{m} \cdot \boldsymbol{a}^{(N)} = Nj, \; j = 0, \pm 1, \pm 2, ... \tag{E.7}$$

$$= 0 \quad \text{otherwise.} \tag{E.8}$$

Hence, in order to minimise the rest term in Eq. (E.5), one tries to find n-tuples $\boldsymbol{a}^{(N)}$ such that $\boldsymbol{m} \cdot \boldsymbol{a}^{(N)} \neq Nj, \; j = 0, \pm 1, \pm ; ...$ as often as possible. It can be shown (see Ref. [214] and references therein) that in two dimensions a possible solution is given by

$$N = F_j \longrightarrow \boldsymbol{a}^{(N)} = (1, F_{j-2}) \,, \tag{E.9}$$

where the F_j are the Fibonnaci numbers,

$$F_j = F_{j-1} + F_{j-2} \,, \qquad F_0 = 0, F_1 = 1, \; j = 2, 3, ... \tag{E.10}$$

Subroutines which perform the computation of (complex) Bessel functions and both linear and bicubic interpolation are based on methods and formulas given in Refs. [1, 183].

E.2 The input file

A typical input file has the form

ibeam	ichoice	I_G	b_G	I_{BG}	b_{BG}
1	1	5.00d12	4.0d0	5.00d12	4.d0
L	λ	$\mathcal{N}_0$	α	τ	t-steps
1.0d0	0.355d0	5.d18	1.20d0	15.d-12	50
nhar	ifar	imin	istep	imax	nloc
3	100	0	50	5000	5
igas	ie	iatnpert	iabsorb	ishort	
1	1	1	1	0	
Nfi	rhomax	ampli(t-)	ampli(t+)	nrout	
19	66	-1.6d0	1.6d0	4	
		atomic data files			
file1	file2	file3	file4	file5	

In the following we give a brief explanation of each of the parameters appearing in the input file.

ibeam: takes on the values 1 (Gaussian beam) and 2 (Bessel-Gauss beam). If *ibeam*=1, the code uses the values I_G, b_G, and $\alpha = 0$, otherwise I_{BG}, b_{BG} and the value of α given in the input file.

ichoice: takes on the values 1 to 4. One of the four values I_G, I_{BG}, b_G and b_{BG} is redundant and can be determined from the three others according to Eq. (3.29) for beams of equal power. The intensities are given in W/cm^2 , the confocal parameters in mm.

ichoice=1: $(I_G, I_{BG}, b_G) \longrightarrow b_{BG}$

ichoice=2: $(I_G, b_{BG}, b_G) \longrightarrow I_{BG}$

ichoice=3: $(I_G, I_{BG}, b_{BG}) \longrightarrow b_G$

ichoice=4: $(I_{BG}, b_{BG}, b_G) \longrightarrow I_G$

The value calculated supersedes the corresponding value given in

the input file.

L: length of the medium in mm.

λ: wavelength in μm.

$\mathcal{N}_0$: (initial) peak atomic density in atoms/cm^3 .

α: Bessel angle in deg.

τ: pulse duration (FWHM of intensity) in sec.

t-steps: number of steps in the time propagation.

nhar: harmonic order.

ifar: far-field variable z' in units of L (see Fig. 4.1).

imin: far-field variable ρ'_{min} in units of λ (see Fig. 4.1).

istep: step-size of $\Delta\rho'$ in units of λ (see Fig. 4.1).

imax: far-field variable ρ'_{max} in units of λ (see Fig. 4.1).

nloc: localizes the first *nloc* maxima in the spatial far-field profile.

igas: takes on the values 1 (rectangular gas profile) and 2 (truncated Lorentz profile).

ie: takes on the values 1 (photoionization included) and 2 (photoionization neglected).

iatsus: takes on the values 1 to 3 and determines the way, the real part of the dressed linear atomic susceptibility is included.
iatsus=0: all values set to zero
iatsus=1: values as loaded (intensity-dependent)
iatsus=2: all values set to the perturbative value ($I \to 0$).

iabsorb: same as for *iatsus* but for the imaginary part of the dressed linear atomic susceptibility (absorption).

ishort: takes on the values 0 and 1. If *ishort*=1, then the slowly- varying envelope approximation Eq. (4.45) is included in the computation.

Nfi: determines the Fibonacci number F_{Nfi} (see section E.1) for converging the integration over the medium dimensions

rhomax: maximum radial distance $\rho_{\max}$ (in units of λ) taken into account by the integration over the medium dimensions (see Fig. 4.1).

ampli(t−): lower bound of the reduced time $\tilde{v}'$ in Eq. (4.69).

ampli(t+): upper bound of the reduced time $\tilde{v}'$ in Eq. (4.69).

nrout: takes on the values 1,2,3,4,5,6,8,10,12,14,16,20,24,32,48,64. *nrout* controls the accuracy of the Gauss-Legendre quadrature (NAG-routine D01BAF) used for computing the integrals Eqs. (4.60) and (4.62).

file1: file containing the intensity-dependent atomic dipole moment (modulus, phase and their derivatives with respect to intensity).

file2: file containing the ionization probability as a function of time and intensity.

file3: file containing the complex linear atomic susceptibility at the fundamental frequency as a function of the intensity.

file4: file containing the complex linear atomic susceptibility at the harmonic frequency as a function of the intensity.

file5: file containing the ionization rate, only used, if *ishort=1.*

The parameters which affect the convergence of the results (spatio-temporal profiles, conversion efficiency) are *t-steps,istep,imax,Nfi,rhomax,nrout* and *amplit(±).*

E.3 Testing the code

E.3.1 General considerations

Multiple tests are performed by the code, in order to reduce as much as possible errors and inaccuracies. The input file is checked for its consistency and the accuracy of quadrature routines is monitored throughout the calculations. Results of those checks are written on status and info files, which can be consulted during the execution of the program. The conversion efficiency is cross-checked by interchanging the order of integration, as stated in Eq. (4.66).

In the following we report on an investigation which tests both the validity of the far-field approximation made in deriving the harmonic far-field amplitude Eq. (4.71) and its implementation by the code. We will concentrate on the most stringent test, which requires the harmonic yield (or equally the conversion efficiency) to be independent of the the position z' of the far-field plane. Moreover, the corresponding spatial far-field profiles are shown to be only dependent on the far-field angle β. For this calculation we have taken the input file as given in the previous section, and varied the parameter *ifar*. In order for the comparison to be meaningful, we have to work at constant maximum far-field angle β, that is we have to vary *istep* and *imax* in the same way than *ifar*, all other input data remaining unchanged. The results are displayed in Table E.1. We have monitored the variation of the conversion efficiency and the ratio of the first off-axis maximum to the maximum on axis. As the latter is about three orders of magnitude larger than the former in the present case, we expect this ratio to be much more sensitive to the variation of z' than the ratio of the conversion efficiencies. The relative errors have been calculated with respect to the results obtained for *ifar*=1000,

$$\mathrm{ERR} = \frac{|V_{1000} - V_{\mathrm{ifar}}|}{V_{1000}} \times 100\,\%. \tag{E.11}$$

Selected far-field profiles obtained from the calculations above are shown in Fig. E.1. The normalized far-field profiles can be seen to depend only on the far-field angle β. The far-field profiles converge with increasing parameter *ifar* rapidly to the same limit over the whole range of far-field angles β. The position of the first off-axis

Table E.1: Test of the independence of the calculations with respect of the far-field plane z'. The relative errors are determined with respect to the results for $z' = 1000L = 1000$ mm according to Eq. (E.11). ERR1 is the relative error on the conversion efficiency, ERR2 is the relative error on the ratio of the first off-axis maximum to the maximum on axis.

ifar	istep	imax	ERR1 (%)	ERR2 (%)
1000	500	50000	≈ 0.0	≈ 0.0
800	400	40000	≈ 0.0	≈ 0.0
500	250	25000	0.1	0.2
200	100	10000	0.4	0.9
100	50	5000	1.0	2.0
50	25	2500	2.1	4.6
40	20	2000	2.7	6.0
20	10	1000	5.6	14.2
10	5	500	12.2	40.0

maximum does not vary with z' to the precision given in Table E.1.

Similar checks carried out during the calculations reported in chapter 5, confirm the rule of thumb, that above $z' \approx 100L$, the relative error due to finite z' is generally less than the overall convergence accuracy of a given calculation with respect to the parameters listed at the end of the previous section. The z'-dependence of the temporal profiles is essentially removed by the transformation Eq. (4.74) which takes the time reference to be dependent on the far-field plane. We note that in the case of very short pulses the small remaining z'-dependence can sometimes lead to spurious numerical effects affecting the tails of the temporal profiles.

E.3.2 Comparison of results with existing data

We have tested the overall reliability of the code by reproducing data already published in the literature for Gaussian beams. Particularly suitable for such a calculation is the experiment by Kung [118] on third-order harmonic generation in xenon at the same fundamental wavelength, $\lambda = 354.7$ nm, than we have used for atomic hydrogen throughout the thesis. The calculations here are compared to the experimental data of Kung for a power of 2 MW on target, the latter consisting of a pulsed xenon gas jet. To describe the gas jet profile we have assumed a rectangular gas

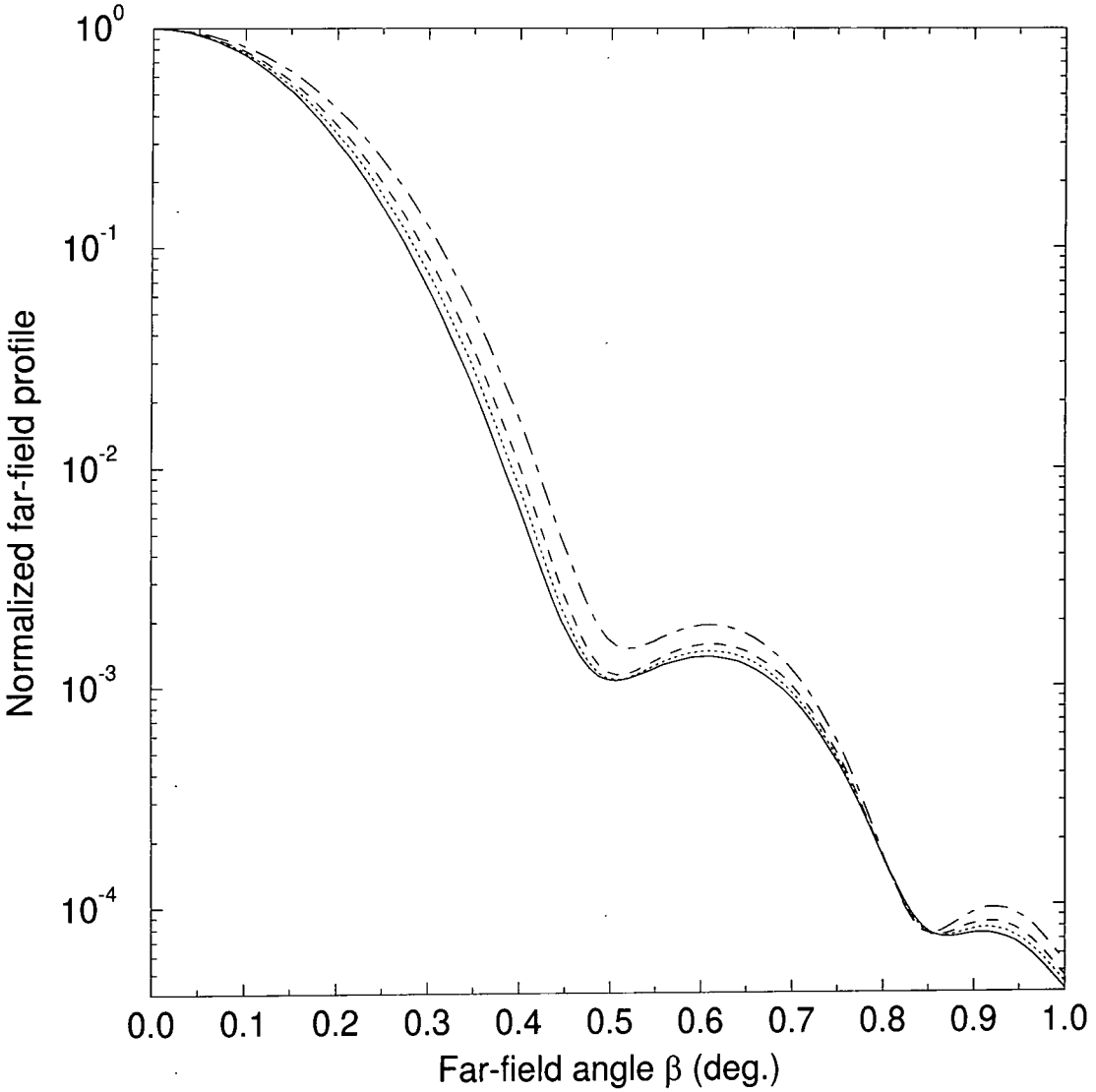

Figure E.1: Far-field profiles at various far-field planes z' as a function of the far-field angle β. The curves are for *ifar*=10 (dot-dashed line), *ifar*=20 (dashed line), *ifar*=40 (dotted line) and *ifar*=1000 (solid line).

profile of length L =1 mm for the reasons outlined below. The reported beam waist is $w_0 = \sqrt{b/k} = 30\,\mu$m, yielding a confocal parameter $b \approx 4$ mm. According to Eq. (3.28), the peak focal intensity is then about $I_f = 5.7 \times 10^{11}$ W/cm^2 in agreement with the value cited by Kung[1]. This value of the intensity approximately delimits the power law regime [see Eq. (2.21)] from the saturation regime in xenon at this

[1]Therefore, Kung assumes a Gaussian beam profile for the incident beam. He states this explicitely only when he refers to his calculated values for the conversion efficiency (footnote c in Table 1 of Ref. [118]), but notes at the same time that the actual incident beam has a doughnut-shaped profile, without giving any further precisions. We therefore assume the incident beam to be well described by a Gaussian beam profile which is consistently described by the parameters given by Kung and perfectly matches his experimental results.

wavelength [118, 237]. For the third-order polarizability of xenon, which enters the calculation of the dipole moment in Eq. (2.21), we have used the value cited by Kung, $\chi^{(3)} = 5.6 \times 10^{-35}$ esu. The conversion into the dipole moment in atomic units is carried out using both Table IV of Ref. [130] and the table in Ref. [174]. We obtain in this way

$$d(I)\,[\text{a.u.}] = 6.20 \times 10^{33}\,\chi^{(3)}[\text{esu}]\,(I/I_0)^{(q/2)}\,, \tag{E.12}$$

where $q = 3$ in the present case[2]. The prefactor in this equation corresponds to a normalizing value of the intensity of $I_0 = 3 \times 10^{13}$ W/cm^2 . Using these data, and the linear atomic susceptibilities determined as reported in Appendix C, we have calculated the conversion efficiency for a Gaussian beam as a function of the atomic density $\mathcal{N}_0$. Fig. E.2 shows the comparison between the data obtained from the propagation code and the curve obtained from the following equation,

$$\eta_q = C\,\mathcal{N}_0^2\,\frac{\sin^2\{[\Delta k_{\text{at}}\mathcal{N}_0 + 2(q-1)/b]L/2\}}{\{[\Delta k_{\text{at}}\mathcal{N}_0 + 2(q-1)/b]L/2\}^2}\,, \tag{E.13}$$

which gives the well known theoretical dependence of the conversion efficiency on the atomic density for a Gaussian beam in both the perturbative and the loose focusing limits [130, 191]. Δk_{at} is the phase-mismatch per atom, obtained from Eq. (4.105) as

$$\Delta k_{\text{at}} = \Delta k_{\text{disp}}/\mathcal{N}_0 = \frac{(2\pi)^2 q}{\lambda}[\alpha_{\text{pol}}(\lambda/3) - \alpha_{\text{pol}}(\lambda)]. \tag{E.14}$$

In the present case we find, using the values of the linear atomic polarizability given by Eqs. (C.7) and (C.8), $\Delta k_{\text{at}} = -5.9 \times 10^{-17}$ cm^2/atom, in very good agreement with the experimental value cited in Ref. [118], $\Delta k_{\text{at}} = -6.0 \times 10^{-17}$ cm^2/atom. The constant C in Eq. (E.13) has been normalized such as to make the first maxima in Fig. E.2 coincide. The agreement between the results from the propagation code and the theory predicted by Eq. (E.13) is excellent and they both fit the experimental curve obtained by Kung[3]. As absolute value of the peak conversion efficiency, corresponding to the first maximum in Fig. (E.2), Kung cites a measured

[2]Note that the conversion factor depends on the harmonic order. The prefactor in Eq. (E.12) is thus only valid for $q = 3$.

[3]Fig. 2 of Ref. [118], filled symbols. His data could not be reproduced in Fig. E.2 because of the lack of information about the vertical scale of his plot.

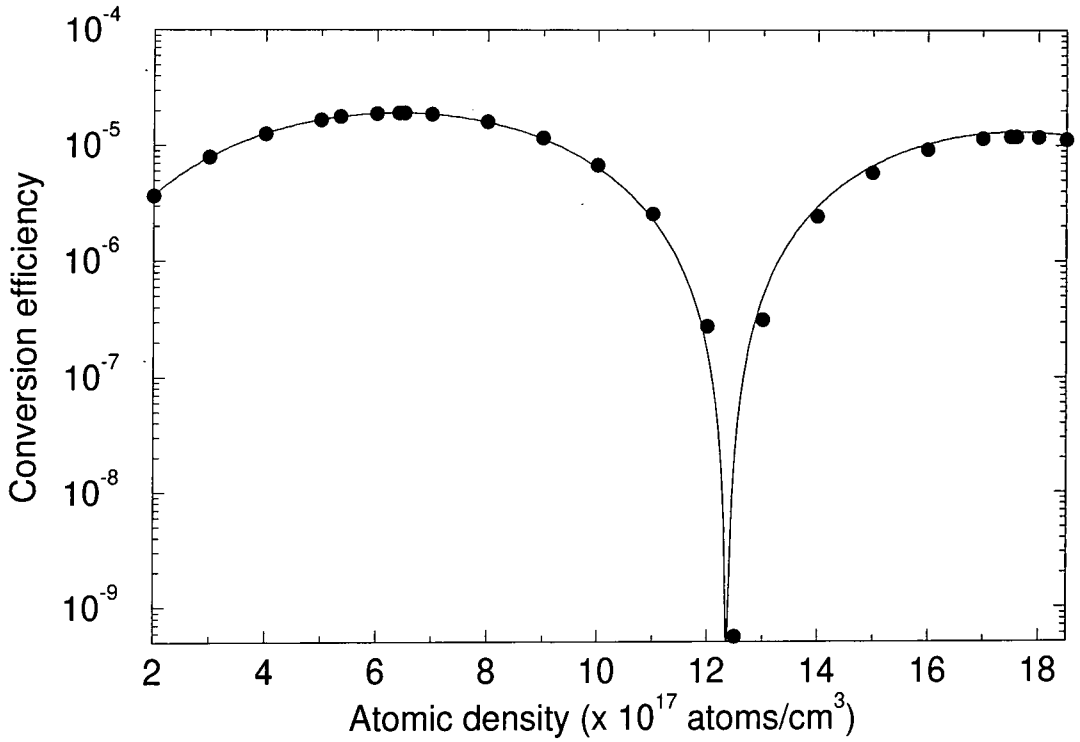

Figure E.2: Conversion efficiency versus atomic density for the Gaussian beam as described in the text. Filled circles: data points obtained from the propagation code, solid line: conversion efficiency obtained from Eq. (E.13) by fitting the curve to the first maximum at $\mathcal{N}_0 = 6.4\times10^{17}$ atoms/cm^3 . The second maximum occurs around $\mathcal{N}_0 = 1.75\times10^{18}$ atoms/cm^3 .

value of $\eta_q = 1.5 \times 10^{-5}$ which compares very well to $\eta_q = 1.9 \times 10^{-5}$ found in our calculation. The densities at which the two maxima occur are given by Kung as $\mathcal{N}_0^{(1)} \approx 5.3 \times 10^{17}$ atoms/cm^3 (p=16.2 Torr) and $\mathcal{N}_0^{(2)} \approx 1.6 \times 10^{18}$ atoms/cm^3 (p=48.6 Torr), respectively. These values are predicted by Eq. (E.13), provided one neglects the small shift due to the geometric phase. The absolute value of the atomic density can then be inferred from Eq. (E.13), as done by Kung, by identifying the two maxima with the first and third coherence lengths[4],

$$L_{\rm coh} = \frac{\pi}{\Delta k_{\rm at}\mathcal{N}_0^{(1)}}, \qquad 3L_{\rm coh} = \frac{\pi}{\Delta k_{\rm at}\mathcal{N}_0^{(2)}}, \tag{E.15}$$

respectively, where the author assumed an effective width of L=1 mm in Eq. (E.13), this expression being, in fact, only valid for a rectangular gas profile. It is for this reason that we also have assumed a rectangular profile for the gas jet in our calculation.

[4]The second coherence length corresponds, of course, to the minimum in Fig. E.2.

In summary, we have given a detailed presentation of a test calculation performed with our propagation code in the Gaussian beam limit and in the perturbative regime. The results obtained compare very well, both qualitatively and quantitatively, with well known theoretical models, as given by Eq. (E.13), and published experimental data for xenon [118].

Bibliography

[1] M. Abramowitz and I. A. Stegun, eds., *Handbook of Mathematical Functions*, (Dover, New York, 1964).

[2] C. Altucci, T. Starczewski, E. Mevel, C.-G. Wahlström, B. Carré, and A. L'Huillier *J. Opt. Soc. Am. B* **13,** 148-156 (1996).

[3] M. V. Ammosov, N. B. Delone, and V. P. Krainov *Sov. Phys. JETP* **64,** 1191-1194 (1986).

[4] N. E. Andreev, Y. A. Aristov, L. A. Polonskii, and L. N. Pyatnitskii *Sov. Phys. JETP* **73,** 969-975 (1991).

[5] P. Antoine, A. L'Huillier, M. Lewenstein, P. Salières, and Betrand Carré *Phys. Rev. A* **53,** 1725-1745 (1996).

[6] P. Antoine, A. L'Huillier, and M. Lewenstein *Phys. Rev. Lett.* **77,** 1234-1237 (1996).

[7] P. Antoine, D. B. Milošević, A. L'Huillier, M. B. Gaarde, P. Salières, and M. Lewenstein *Phys. Rev. A* **56,** 4960-4969 (1997).

[8] P. Antoine, B. Piraux, D. B. Milošević, and M. Gajda *Phys. Rev. A* **54,** R1761-R1764 (1996).

[9] P. Antoine, B. Piraux, and A. Maquet *Phys. Rev. A* **51,** R1750-R1753 (1995).

[10] G. B. Arfken and H. J. Weber, *Mathematical Methods for Physicists*, (Academic Press, London, 1995).

[11] S. Augst, D. Strickland, D. D. Meyerhofer, S. L. Chin, and J. H. Eberly *Phys. Rev. Lett.* **63,** 2212-2215 (1989).

[12] S. Backus, J. Peatross, Z. Zeek, A. Rundquist, G. Taft, M. M. Murnane, and H. C. Kapteyn *Opt. Lett.* **21,** 665-667 (1996).

[13] V. Bagini, R. Borghi, F. Gori, A. M. Pacileo, M. Santasiero, D. Ambrosini, and G. Schirripa Spagnolo *J. Opt. Soc. Am. A* **13,** 1385-1394 (1996).

[14] V. Bagini, F. Frezza, M. Santarsiero, G. Schettini, and G. Schirripa Spagnolo *J. Mod. Opt.* **43,** 1155-1166 (1996).

[15] P. Balcou, C. Cornaggia, A. S. L. Gomes, L. A. Lompré, and A. L'Huillier *J. Phys. B: At. Mol. Opt. Phys.* **25,** 4467-4485 (1992).

[16] P. Balcou and A. L'Huillier *Phys. Rev. A* **47,** 1447-1459 (1993).

[17] P. Balcou, P. Salières, K. S. Budil, T. Ditmire, M. D. Perry, and A. L'Huillier *Z. Phys. D* **34,** 107-110 (1995).

[18] P. Balcou, A. L'Huillier, and D. Escande *Phys. Rev. A* **53,** 3456-3468 (1996).

[19] P. Bàlcou, P. Salières, A. L'Huillier, and M. Lewenstein *Phys. Rev. A* **55,** 3204-3210 (1997).

[20] P. Balcou, private communication.

[21] A. D. Bandrauk, J. Ruel, T. Zuo, and H. Yu *Int. J. Quant. Chem.* **64,** 613-617 (1997).

[22] M. Bao and A. F. Starace *Phys. Rev. A* **53,** R3723-R3726 (1996).

[23] G. Barton, *Elements of Green's Functions and Propagation*, (Clarendon Press, Oxford, 1989).

[24] W. Becker, S. Long, and J. K. McIver *Phys. Rev. A* **41,** 4112-4115 (1990).

[25] W. Becker, S. Long, and J. K. McIver *Phys. Rev. A* **46,** R5334 (1992).

[26] W. Becker, S. Long, and J. K. McIver *Phys. Rev. A* **50,** 1540-1560 (1994).

[27] W. Becker, A. Lohr, M. Kleber, and M. Lewenstein *Phys. Rev. A* **56,** 645-656 (1997).

[28] H. A. Bethe and E. E. Salpeter, *Quantum Mechanics of One- and Two-Electron Atoms*, (Plenum Publishing, New York, 1977).

[29] N. Bleistein and R. A. Handelsmann, *Asymptotic Expansions of Integrals*, (Dover Publications, New York, 1975).

[30] R. Borghi and M. Santasiero *Opt. Lett.* **22,** 262-264 (1997).

[31] R. Borghi, M. Santarsiero and F. Gori *J. Opt. Soc. Am. A* **14,** 23-26 (1997).

[32] Z. Bouchal and M. Olivik *J. Mod. Opt.* **42,** 1555-1566 (1995).

[33] R. W. Boyd, *Nonlinear Optics*, (Academic Press, New York, 1992).

[34] L. Brown and T. W. B. Kibble *Phys. Rev.* **133,** A705 (1964).

[35] K. S. Budil, P. Salières, A. L'Huillier, T. Ditmire, and M. D. Perry *Phys. Rev. A* **48,** R3437-R3440 (1993).

[36] P. G. Burke, P. Francken, and C. J. Joachain *Europhys. Lett.* **13,** 617 (1990).

[37] R. Burlon, G. Ferrante, C. Leone, P. A. Oleinikov, and V. T. Platonenko *J. Opt. Soc. Am. B* **13,** 162-169 (1996).

[38] K. Burnett, V. C. Reed, J. Cooper, and P. L. Knight *Phys. Rev. A* **45,** 3347-3349 (1992).

[39] N. H. Burnett, C. Kan, and P. B. Corkum *Phys. Rev. A* **51,** R3418-R3421 (1995).

[40] P. N. Butcher and D. Cotter, *The Elements of Nonlinear Optics*, (Cambridge University Press, Cambridge, 1990).

[41] C. F. R. Caron, Diploma Thesis (unpublished), University of Karlsruhe (Germany), 1993.

[42] C. F. R. Caron (unpublished).

[43] C. F. R. Caron and R. M. Potvliege *J. Opt. Soc. Am. B* **15,** 1096-1106 (1998).

[44] W. F. Chan, G. Cooper, X. Guo, G. R. Burton, and C. E. Brion *Phys. Rev. A* **46,** 149-171 (1992).

[45] Z. Chang, A. Rundquist, H. Wang, M. M. Murnane, and H. C. Kapteyn *Phys. Rev. Lett.* **79,** 2967-2970 (1997).

[46] S. L. Chin and P. A. Golovinski *J. Phys. B: At. Mol. Opt. Phys.* **28,** 55-63 (1995).

[47] Y. Chiou and H. Chang *Opt. Lett.* **22,** 949-951 (1997).

[48] I. P. Christov, J. Zhou, J. Peatross, A. Rundquist, M. M. Murnane, and H. C. Kapteyn *Phys. Rev. Lett.* **77,** 1743-1746 (1996).

[49] I. P. Christov, M. M. Murnane, and H. C. Kapteyn *Phys. Rev. A* **57,** R2285-R2288 (1998).

[50] S. I. Chu and W. P. Reinhardt *Phys. Rev. Lett.* **39,** 1195-1198 (1977).

[51] G. Compagno, K. Dietz, and F. Persico *J. Phys. B: At. Mol. Opt. Phys.* **27,** 4779-4815 (1994).

[52] J. Connerade and C. H. Keitel *Phys. Rev. A* **53,** 2748-2751 (1996).

[53] E. Constant, V. D. Taranukhin, A. Stolow, and P. B. Corkum *Phys. Rev. A* **56,** 3870-3878 (1997).

[54] P. B. Corkum *Phys. Rev. Lett.* **71,** 1994-1997 (1993).

[55] E. Cormierand and P. Lambropoulos *J. Phys. B: At. Mol. Opt. Phys.* **30,** 3095-3106 (1997).

[56] J. Courtial, K. Dholakia, L. Allen, and M. J. Padgett *Phys. Rev. A* **56,** 4193-4196 (1997).

[57] A. J. Cox and D. C. Dibble *Appl. Opt.* **30,** 1330-1332 (1991).

[58] A. J. Cox and D. C. Dibble *J. Opt. Soc. Am. A* **9,** 282-286 (1992).

[59] A. J. Cox and J. D'Anna *Opt. Lett.* **17,** 232-234 (1992).

[60] J. K. Crane, M. D. Perry, D. Strickland, S. Herman, and R. W. Falcone *IEEE Trans. Plasma Sci.* **21,** 82-89 (1993).

[61] J. A. Davis, E. Carcole, and D. M. Cottrell *Appl. Opt.* **35,** 593-598 (1996).

[62] H. C. Day, *Floquet Calculations of Atomic Photo-Electron Spectra in Intense Laser Fields*, PhD Thesis (unpublished), University of Durham (UK), 1997.

[63] N. B. Delone and V. P. Krainov, *Atoms in Strong Light Fields*, (Springer, Berlin, 1985).

[64] N. B. Delone and V. P. Krainov, *Fundamentals of Nonlinear Optics of Atomic Gases*, (John Wiley, New York, 1988).

[65] T. Ditmire, E. T. Gumbrell, R. A. Smith, J. W. G. Tisch, D. D. Meyerhofer, and M. H. R. Hutchinson *Phys. Rev. Lett.* **77,** 4756-4759 (1996).

[66] T. Ditmire, J. K. Crane, H. Nguyen, L. B. DaSilva, and M. D. Perry *Phys. Rev. A* **51,** R902-R905 (1995).

[67] M. Dörr and W. Becker, private communication.

[68] J. Durnin *J. Opt. Soc. Am. A* **4,** 651-654 (1987).

[69] J. Durnin, J. J. Miceli, Jr., and J. H. Eberly *Phys. Rev. Lett.* **58,** 1499-1501 (1987).

[70] J. Durnin, J. J. Miceli, Jr., and J. H. Eberly *Opt. Lett.* **13,** 79-80 (1988).

[71] J. H. Eberly and M. Kalinski, in *Multiphoton Processes 1996*, ed. P. Lambropoulos and H. Walther, Proceedings of the 7th International Conference on Multiphoton Processes, (IOP Publishing, Bristol, 1997).

[72] H. Eichmann, S. Meyer, K. Riepl, C. Momma, and B. Wellegehausen *Phys. Rev. A* **50,** R2834-R3836 (1994).

[73] M. Elk, P. Lambropoulos, and X. Tang *Phys. Rev. A* **44,** R31-R34 (1991).

[74] T. J. Englert and E. A. Rinehart *Phys. Rev. A* **28,** 1539-1545 (1983).

[75] S. J. van Enk, J. Zhang, and P. Lambropoulos *J. Phys. B: At. Mol. Opt. Phys.* **29,** 4041-4051 (1996).

[76] S. Erhard and E. K. U. Gross, in *Multiphoton Processes 1996*, ed. P. Lambropoulos and H. Walther, Proceedings of the 7th International Conference on Multiphoton Processes, (IOP Publishing, Bristol, 1997).

[77] C. Figueira de Morrison Faria, M. Dörr, and W. Sandner *Phys. Rev. A* **55,** 3961-3963 (1997).

[78] M. Ferray, A. L'Huillier, X. F. Li, L. A. Lompré, G. Mainfray and C. Manus *J. Phys. B: At. Mol. Opt. Phys.* **21,** L31-L35 (1988).

[79] W. R. Ferrell, M. G. Payne, and W. R. Garrett *Phys. Rev. A* **36,** 81-89 (1987).

[80] P. Franken, A. Hill, C. Peters, and G. Weinreich *Phys. Rev. Lett.* **7,** 118 (1961).

[81] D. J. Fraser, M. H. R. Hutchinson, J. P. Marangos, Y. L. Shao, J. W. G. Tisch, and M. Castillejo *J. Phys. B: At. Mol. Opt. Phys.* **28,** L739-L745 (1995).

[82] F. I. Gauthey, C. H. Keitel, P. L. Knight, and A. Maquet *Phys. Rev. A* **52,** 525-540 (1995).

[83] M. Gavrila, in *Atoms in Intense Laser Fields*, ed. M. Gavrila, Advances in Atomic, Molecular and Optical Physics, Supplement 1, (Academic Press, New York, 1992).

[84] T. E. Glover, R. W. Schoenlein, A. H. Chin, and C. V. Shank *Phys. Rev. Lett.* **76,** 2468-2471 (1996).

[85] B. Glushko, B. Kryzhanovsky, and D. Sarkisyan *Phys. Rev. Lett.* **71,** 243-246 (1993).

[86] F. Gori, G. Guattari, and C. Padovani *Opt. Comm.* **64,** 491-495 (1987).

[87] F. Gori *Opt. Comm.* **107,** 335-341 (1994).

[88] I. S. Gradshteyn and I. M. Ryzhik, *Table of Integrals, Series and Products*, (Academic Press, London, 1992).

[89] R. Haight and D. R. Peale *Phys. Rev. Lett.* **70,** 3979-3982 (1993).

[90] P. L. Greene and D. G. Hall *J. Opt. Soc. Am. A* **13,** 962-966 (1996).

[91] D. G. Hall *Opt. Lett.* **21,** 9-11 (1996).

[92] D. C. Hanna, M. A. Yuratich, and D. Cotter, *Nonlinear Optics of Free Atoms and Molecules*, (Springer Verlag, New York, 1979).

[93] R. Hässner, W. Theobald, S. Niedermeier, H. Schillinger, and R. Sauerbrey *Opt. Lett.* **22,** 1491-1493 (1997).

[94] R. M. Herman and T. A. Wiggins *J. Opt. Soc. Am. A* **8,** 932-942 (1990).

[95] R. M. Herman and T. A. Wiggins *Appl. Opt.* **31,** 5913-5915 (1992).

[96] H. Heuser, *Gewöhnliche Differentialgleichungen*, (Teubner, Stuttgart, 1989)

[97] C. V. Hile and W. L. Kath *J. Opt. Soc. Am. B* **13,** 1135-1145 (1996).

[98] Z. L. Horváth, M. Erdélyi, G. Szabó, Z. Bor, F. K. Kittel,and J. R. Cavallaro *J. Opt. Soc. Am. A* **14,** 3009-3013 (1997).

[99] S. Hughes and J. M. Burzler *Phys. Rev. A* **56,** R1103-1106 (1997).

[100] F. A. Ilkov, J. E. Decker, and S. L. Chin *J. Phys. B: At. Mol. Opt. Phys.* **25,** 4005-4020 (1992).

[101] M. Ivanov, P. B. Corkum, T. Zuo, and A. Bandrauk *Phys. Rev. Lett.* **74,** 2933-2936 (1995).

[102] J. K. Jabczynski *Opt. Comm.* **77,** 292-294 (1990).

[103] J. D. Jackson, *Classical Electrodynamics*, (John Wiley, New York, 1975).

[104] Z. Jaroszewicz, J. F. Roman Dopazo, and C. Gomez-Reino *Appl. Opt.* **35,** 1025-1031 (1996).

[105] Z.-P. Jiang *Opt. Comm.* **125,** 207-210 (1996).

[106] C. J. Joachain, in *Multiphoton Processes 1996*, ed. P. Lambropoulos and H. Walther, Proceedings of the 7th International Conference on Multiphoton Processes, (IOP Publishing, Bristol, 1997).

[107] C. Kan, C. E. Capjack, R. Rankin, T. Brabec, and N. H. Burnett *Phys. Rev. A* **54,** R1026-R1029 (1996).

[108] C. Kan, N. H. Burnett, C. E. Capjack, and R. Rankin *Phys. Rev. Lett.* **79,** 2971-2974 (1997).

[109] C. H. Keitel, P. L. Knight, and K. Burnett *Europhys. Lett.* **24,** 539-544 (1993).

[110] L. V. Keldysh *Sov. Phys. JETP* **47,** 1945-1957 (1965).

[111] D. Kim, C. S. Mullin, and Y. R. Shen *J. Opt. Soc. Am. B* **14,** 2530-2542 (1997).

[112] V. P. Koronkevitch, I. A. Mikhaltsova, E. G. Churin, and Yu. I. Yurlov *Appl. Opt.* **34,** 5761-5771 (1995).

[113] J. L. Krause, K. J. Schafer, and K. C. Kulander *Phys. Rev. Lett.* **68,** 3535-3538 (1992).

[114] J. L. Krause, K. J. Schafer, and K. C. Kulander *Chem. Phys. Lett.* **178,** 573-578 (1991).

[115] K. C. Kulander and B. W. Shore *Phys. Rev. Lett.* **62,** 524-526 (1989).

[116] K. C. Kulander, K. J. Schafer, and J. L. Krause, in *Atoms in Intense Laser Fields*, ed. M. Gavrila, Advances in Atomic, Molecular and Optical Physics, Supplement 1, (Academic Press, New York, 1992).

[117] K. C. Kulander, K. J. Schafer, and J. L. Krause, in *Super-Intense Laser-Atom Physics*, ed. B. Piraux *et al.* , NATO ASI Series, Vol. 316, (Plenum Press, New-York 1993).

[118] A. H. Kung *Opt. Lett.* **8,** 24-26 (1983).

[119] N. J. Kylstra, A. M. Ermolaev, and C. J. Joachain *J. Phys. B: At. Mol. Opt. Phys.* **30,** L449-L460 (1997).

[120] D. G. Lappas, A. Sanpera, J. B. Watson, K. Burnett, P. L. Knight, R. Grobe, and J. H. Eberly *J. Phys. B: At. Mol. Opt. Phys.* **29,** L619-L627 (1996).

[121] J. Larsson, E. Mevel, R. Zerne, A. L'Huillier, C.-G. Wahlström, and S. Svanberg *J. Phys. B: At. Mol. Opt. Phys.* **28,** L53-L58 (1995).

[122] M. Lax, W. H. Louisell, and W. B. McKnight *Phys. Rev. A* **11,** 1365-1370 (1975).

[123] M. Lewenstein, P. Balcou, M. Y. Ivanov, A. L'Huillier, and P. B. Corkum *Phys. Rev. A* **49,** 2117-2132 (1994).

[124] M. Lewenstein, P. Salières, and Anne L'Huillier *Phys. Rev. A* **52,** 4747-4754 (1995).

[125] X. F. Li, *Etude de la génération d'harmoniques d'ordre élevé dans les gaz rares - influence de l'ionisation multiphotonique*, PhD Thesis (unpublished), Université Paris VI (France), 1989.

[126] X. Liu, D. Umstadter, E. Esarey, and A. Ting *IEEE Trans. Plasma Sci.* **21,** 90-93 (1993).

[127] C. Lynga, A. L'Huillier, and C.-G. Wahlström *J. Phys. B: At. Mol. Opt. Phys.* **29,** 3293-3302 (1996).

[128] A. L'Huillier, X. F. Li, and L. A. Lompré *J. Opt. Soc. Am. B* **7,** 527-536 (1990).

[129] A. L'Huillier, K. J. Schafer, and K. C. Kulander *J. Phys. B: At. Mol. Opt. Phys.* **24,** 3315-3341 (1991).

[130] A. L'Huillier, L. A. Lompré, G. Mainfray, and C. Manus, in *Atoms in Intense Laser Fields*, ed. M. Gavrila, Advances in Atomic, Molecular and Optical Physics, Supplement 1, (Academic Press, New York, 1992).

[131] A. L'Huillier, P. Balcou, S. Candel, K. J. Schafer, and K. C. Kulander *Phys. Rev. A* **46,** 2778-2790 (1992).

[132] A. L'Huillier, M. Lewenstein, P. Salières, P. Balcou, M. Y. Ivanov, J. Larsson, and C.-G. Wahlström *Phys. Rev. A* **48,** R3433-R3436 (1993).

[133] R. P. MacDonald, J. Chrostowski, S. A. Boothroyd, and B. A. Syrett *Appl. Opt.* **32,** 6470-6474 (1993).

[134] W. C. Martin and W. L. Wiese, in *Atomic, Molecular, & Optical Physics Handbook*, ed. G. W. F. Drake, (AIP Press, New York, 1996).

[135] I. Mercer, E. Mevel, R. Zerne, A. L'Huillier, P. Antoine, and C.-G. Wahlström *Phys. Rev. Lett.* **77,** 1731-1734 (1996).

[136] E. Meşe, *Floquet Calculations of Rates of Frequency Conversion and Multiphoton Ionisation in Intense Laser Fields*, PhD Thesis (unpublished), University of Durham (UK), 1997.

[137] E. Meşe and R. M. Potvliege, poster presented at the 7th International Conference on Multiphoton Processes (ICOMP VII), October 1996 (see book of abstracts).

[138] E. Meşe and R. M. Potvliege, poster presented at the 7th International Conference on Multiphoton Processes (ICOMP VII), October 1996 (see book of abstracts).

[139] E. Meşe and R. M. Potvliege, unpublished (1997).

[140] E. Meşe and R. M. Potvliege, private communication.

[141] D. L. Mills, *Nonlinear Optics*, (Springer, Heidelberg, 1991).

[142] P. W. Milonni and J. H. Eberly, *Lasers*, (John Wiley, New York 1988).

[143] D. B. Milošević and B. Piraux *Phys. Rev. A* **54,** 1522-1531 (1996).

[144] S. R. Mishra *Opt. Comm.* **85,** 159-161 (1991).

[145] D. M. Mittleman, D. C. Douglass, Z. Henis, O. R. Wood II, R. R. Freeman, and T. J. McIlrath *J. Opt. Soc. Am. B* **13,** 170-179 (1996).

[146] K. Miyazaki and H. Kashiwagi *Phys. Rev. A* **18,** 635-643 (1978).

[147] K. Miyazaki and H. Takada *Phys. Rev. A* **52,** 3007-3021 (1995).

[148] P. Moreno, L. Plaja, V. Malyshev, and L. Roso *Phys. Rev. A* **51,** 4746-4753 (1995).

[149] P. Moreno, L. Plaja, and L. Roso *Europhys. Lett.* **28,** 629 (1994).

[150] P. Moreno, L. Plaja, and L. Roso *J. Opt. Soc. Am. B* **13,** 430-435 (1996).

[151] H. G. Muller, P. Agostini, and G. Petite, in *Atoms in Intense Laser Fields*, ed. M. Gavrila, Advances in Atomic, Molecular and Optical Physics, Supplement 1, (Academic Press, New York, 1992).

[152] L. Niggl, T. Lanzl, and Max Maier *J. Opt. Soc. Am. A* **14,** 27-33 (1997).

[153] P. L. Overfelt *Phys. Rev. A* **44,** 3941-3947 (1991).

[154] P. L. Overfelt and C. S. Kenney *J. Opt. Soc. Am. A* **8,** 732-745 (1991).

[155] M. Padgett and L. Allen *Physics World* **10,** 35-38 (1997).

[156] G. Peach, in *Atomic, Molecular, & Optical Physics Handbook*, ed. G. W. F. Drake, (AIP Press, New York, 1996).

[157] J. Peatross, J. L. Chaloupka, and D. D. Meyerhofer *Opt. Lett.* **19,** 942-944 (1994).

[158] J. Peatross, M. V. Fedorov, and K. C. Kulander *J. Opt. Soc. Am. B* **12,** 863-869 (1995).

[159] J. Peatross and D. D. Meyerhofer *Phys. Rev. A* **51,** R906-R909 (1995).

[160] J. Peatross and D. D. Meyerhofer *Phys. Rev. A* **52,** 3976-3987 (1995).

[161] J. Peatross, M. V. Fedorov, and K. C. Kulander *J. Opt. Soc. Am. B* **12,** 863-870 (1995).

[162] J. Peatross, S. Voronov, and I. Prokopovitch *Opt. Expr.* **1,** 114-125 (1997).

[163] J. Peatross, S. Backus, J. Zhou, M. M. Murnane, and H. C. Kapteyn *J. Opt. Soc. Am. B* **15,** 186-192 (1998).

[164] V. E. Peet *Phys. Rev. A* **53,** 3679-3682 (1996).

[165] V. E. Peet and R. V. Tsubin *Opt. Comm.* **134,** 69-74 (1997).

[166] V. E. Peet and R. V. Tsubin *Phys. Rev. A* **56,** 1613-1620 (1997).

[167] V. Peet, private communication.

[168] V. Peet, private communication.

[169] A. M. Perelomov, V. S. Popov, and M. V. Terent'ev *Sov. Phys. JETP* **23,** 924-934 (1966).

[170] M. Plummer and J. F. McCann *J. Phys. B: At. Mol. Opt. Phys.* **28,** L119-L125 (1995).

[171] M. L. Pons and L. Plaja *J. Mod. Opt.* **43,** 1939-1950 (1996).

[172] R. M. Potvliege and E. Meşe, private communication.

[173] R. M. Potvliege and R. Shakeshaft *Phys. Rev. A* **38,** 4597-4621 (1988).

[174] R. M. Potvliege and R. Shakeshaft *Z. Phys. D* **11,** 93-94 (1989).

[175] R. M. Potvliege and R. Shakeshaft *Phys. Rev. A* **40,** 3061-3079 (1989).

[176] R. M. Potvliege and R. Shakeshaft, in *Atoms in Intense Laser Fields*, ed. M. Gavrila, Advances in Atomic, Molecular and Optical Physics, Supplement 1 (Academic Press, New York, 1992).

[177] R. M. Potvliege and P. H. G. Smith, in *Super-Intense Laser-Atom Physics*, B. Piraux, A. L'Huillier and K. Rzazewski, eds., Vol. B316 of NATO ASI Series (Plenum Press, New York, 1993).

[178] R. M. Potvliege and P. H. G. Smith *J. Phys. B: At. Mol. Opt. Phys.* **24,** L641-L646 (1992).

[179] R. M. Potvliege and P. H. G. Smith *J. Phys. B: At. Mol. Opt. Phys.* **25,** 2501-2516 (1992).

[180] R. M. Potvliege and P. H. G. Smith *Phys. Rev. A* **49,** 3110-3113 (1993).

[181] R. M. Potvliege, *STRFLO: A code for two-colour Sturmian-Floquet calculations*, submitted to *Comp. Phys. Comm.*, (1998).

[182] R. M. Potvliege, private communication.

[183] W. H. Press, B. P. Flannery, S. A. Teukolsky, and W. T. Vetterling, *Numerical Recipes: The Art of Scientific Computing (FORTRAN)*, (Cambridge University Press, 1989).

[184] S. G. Preston, A. Sanpera, M. Zepf, W. J. Blyth, C. G. Smith, J. S. Wark, M. H. Key, K. Burnett, M. Nakai, D. Neely, and A. A. Offenberger *Phys. Rev. A* **53,** R31-R34 (1996).

[185] S. G. Preston, D. M. Chambers, R. S. Majoribanks, P. A. Norreys, D. Neely, M. Zepf, J. Zhang, M. H. Key, and J. S. Wark *J. Phys. B: At. Mol. Opt. Phys.* **31,** 1069-1082 (1998).

[186] M. Protopapas, D. G. Lappas, C. H. Keitel, and P. L. Knight *Phys. Rev. A* **53,** R2933-R2936 (1996).

[187] S. C. Rae and K. Burnett *Phys. Rev. A* **46,** 1084-1090 (1992).

[188] S. C. Rae and K. Burnett *J. Phys. B: At. Mol. Opt. Phys.* **26,** 1509-1518 (1993).

[189] S. C. Rae, K. Burnett and J. Cooper *Phys. Rev. A* **50,** 3438-3446 (1994).

[190] U. W. Rathe, C. H. Keitel, M. Protopapas, and P. L. Knight *J. Phys. B: At. Mol. Opt. Phys.* **30,** L531-L539 (1997).

[191] J. F. Reintjes, *Nonlinear Optical Parametric Processes in Liquids and Gases,* (Academic Press, New York, 1984).

[192] H. R. Reiss and V. P. Krainov *Phys. Rev. A* **50,** R910-R912 (1994).

[193] D. Richards *J. Phys. B: At. Mol. Opt. Phys.* **29,** 2925-2949 (1996).

[194] J. Rosen *Opt. Lett.* **19,** 369-371 (1994).

[195] J. Rosen, B. Salik, and A. Yariv *J. Opt. Soc. Am. A* **12,** 2446-2457 (1995).

[196] S. Ruschin *J. Opt. Soc. Am. A* **11,** 3224-3228 (1994).

[197] P. Saari and K. Reivelt *Phys. Rev. Lett.* **79,** 4135-4138 (1997).

[198] Y. I. Salamin and F. H. M. Faisal *Phys. Rev. A* **54,** 4383-4395 (1996).

[199] Y. I. Salamin and F. H. M. Faisal *Phys. Rev. A* **55,** 3964-3967 (1997).

[200] P. Salières, A. L'Huillier, and M. Lewenstein *Phys. Rev. Lett.* **74,** 3776-3779 (1995).

[201] P. Salières, A. L'Huillier, P. Antoine, and M. Lewenstein, (Los Alamos preprint), to be published in Advances in Atomic, Molecular and Optical Physics, (1998).

[202] P. Salières and M. Lewenstein *Physics World* **11,** 26-27 (1998).

[203] Y. R. Shen, *The Principles of Nonlinear Optics,* (John Wiley, New York, 1984)

[204] P. L. Shkolnikov, A. E. Kaplan, and A. Lago *J. Opt. Soc. Am. B* **13,** 412-423 (1996).

[205] W. Sibbett in *Laser Sources and Applications,* ed. A. Miller and D. M. Finlayson, Proceedings of the 47th Scottish Universities Summer School in Physics, (IOP Publishing, Bristol, 1995).

[206] E. Sidick, A. Knoesen, and A. Dienes *J. Opt. Soc. Am. B* **12,** 1704-1712 (1995).

[207] A. E. Siegman, *Lasers,* (University Science, Mill Valley, 1986).

[208] A. E. Siegman *Proc. SPIE* **1124,** 2 (1990).

[209] J. Sochacki, Z. Jaroszewicz, L. R. Staroński, and A. Kolodziejczyk *J. Opt. Soc. Am. A* **10,** 1765-1768 (1993).

[210] J. Sochacki, A. Kolodziejczyk, Z. Jaroszewicz, and S. Bará *Appl. Opt.* **31,** 5326-5330 (1992).

[211] H. Sõnajalg and P. Saari *Opt. Lett.* **21,** 1162-1164 (1996).

[212] C. Spielmann, N. H. Burnett, S. Sartania, R. Koppitsch, M. Schnürer, C. Kan, M. Lenzner, P. Wobrauschek, and F. Krausz *Science* **278,** 661-664 (1997).

[213] B. Sundaram and P. W. Milonni *Phys. Rev. A* **41,** 6571-6573 (1990).

[214] A. T. Stelbovics and R. S. Watts, *Multidimensional Numerical Integration with Diophantine Point Sets*, The Flinders University of South Australia, FIAS-R-98, (1982).

[215] K. T. Taylor, J. S. Parker, D. Dundas, E. Smyth, and S. Vivirito, in *Multiphoton Processes 1996*, ed. P. Lambropoulos and H. Walther, Proceedings of the 7th International Conference on Multiphoton Processes, (IOP Publishing, Bristol, 1997).

[216] D. A. Telnov, J. Wang, and S. Chu *Phys. Rev. A* **52,** 3988-3996 (1995).

[217] S. P. Tewari, H. Huang, and R. W. Boyd *Phys. Rev. A* **51,** R2707-2710 (1995).

[218] S. P. Tewari, H. Huang, and R. W. Boyd *Phys. Rev. A* **54,** 2314-2325 (1996).

[219] J. W. G. Tisch, T. Ditmire, D. J. Fraser, N. Hay, M. B. Mason, E. Springate, J. P. Marangos, and M. H. R. Hutchinson, in *Multiphoton Processes 1996*, ed. P. Lambropoulos and H. Walther, Proceedings of the 7th International Conference on Multiphoton Processes, (IOP Publishing, Bristol, 1997).

[220] J. W. G. Tisch, T. Ditmire, D. J. Fraser, N. Hay, M. B. Mason, E. Springate, J. P. Marangos, and M. H. R. Hutchinson *J. Phys. B: At. Mol. Opt. Phys.* **30,** L709-L714 (1997).

[221] Vachaspati *Phys. Rev.* **128,** 664 (1962).

[222] P. Vahimaa, V. Kettunen, M. Kuittinen, J. Turunen, and A. T. Friberg *J. Opt. Soc. Am. A* **14,** 1817 (1997).

[223] A. Vasara, J. Turunen, and A. T. Friberg *J. Opt. Soc. Am. A* **6,** 1748-1754 (1989).

[224] V. Véniard, R. Taieb, and A. Maquet *Phys. Rev. A* **54,** 721-728 (1996).

[225] L. Vicari *Opt. Comm.* **70,** 263-266 (1989).

[226] C. G. Wahlström, J. Larsson, A. Persson, T. Starczewski, S. Svanberg, P. Salières, P. Balcou, and A. L' Huillier *Phys. Rev. A* **48,** 4709-4720 (1993).

[227] J. B. Watson, A. Sanpera, and K. Burnett *Phys. Rev. A* **51,** 1458-1463 (1995).

[228] J. B. Watson, A. Sanpera, K. Burnett, and P. L. Knight *Phys. Rev. A* **55,** 1224-1233 (1997).

[229] J. B. Watson, A. Sanpera, X. Chen, and K. Burnett *Phys. Rev. A* **53,** R1962-R1965 (1996).

[230] F. A. Weihe, S. K. Dutta, G. Korn, D. Du, P. H. Bucksbaum, and P. L. Shkolnikov *Phys. Rev. A* **51,** R3433-R3436 (1995).

[231] T. Wulle and S. Herminghaus *Phys. Rev. Lett.* **70,** 1401-1404 (1993).

[232] D. Xenakis, O. Faucher, D. Charalambidis, and C. Fotakis *J. Phys. B: At. Mol. Opt. Phys.* **29,** L457-L463 (1996).

[233] R. Zerne, C. Altucci, M. Bellini, M. B. Gaarde, T. W. Hänsch, A. L'Huillier, C. Lynga, and C.-G. Wahlström *Phys. Rev. Lett.* **79,** 1006-1009 (1997).

[234] J. Zhou, J. Peatross, M. M. Murnane, H. C. Kapteyn, and I. P. Christov *Phys. Rev. Lett.* **76,** 752-755 (1996).

[235] T. Zuo, A. D. Bandrauk, M. Ivanov, and P. B. Corkum *Phys. Rev. A* **51,** R3991-R3998 (1995).

[236] T. Zuo, S. Chelkowski, and A. D. Bandrauk *Phys. Rev. A* **48,** 3837-3844 (1993).

[237] L. J. Zych and J. F. Young *IEEE J. Quant. Electr.* **14,** 147-149 (1978).